Ph.D. Thesis

Development and Validation of a Frequency Domain Based Methodology for the Preliminary Design of Floating Offshore Wind Semi-Submersible Platforms

Presented by:
María Alonso Reig

Thesis Advisors:
Prof. Dr.-Eng. Victor Petuya Arcocha
Dr. Iñigo Mendikoa Alonso

November 2023

Dedicated to my beloved parents and brother

"Lana da bertute guztien ama"

Acknowledgments

I would like to begin by expressing my gratitude for the support and guidance of my thesis advisor and co-advisor, Victor Petuya and Iñigo Mendikoa. Victor, thank you for your practical insights, which have helped me countless times to stay on course and complete this thesis. Iñigo, thank you for sharing this time throughout these years, for your patience, and for your unwavering support at all times.

I want to thank the Basque Government for promoting the development of doctoral theses and thus increasing talent within the Basque Country, through scholarships such as BIKAINTEK, which has been a significant part of the funding for this thesis. Thanks also to TECNALIA, and particularly to the Offshore Renewable Energies Team, for sharing your experience and knowledge with me over these years, which has been essential in carrying out this work. Particularly, I want to thank Vincenzo Nava for always assisting me when I turned to you, both in the technical development of the research and in reviewing publications, and Imanol Touzón for your availability and your critical perspective, which has consistently improved my work. Thanks also to Jose Luis Villate for your trust and support, as well as for always providing a quick response to everything I needed. I also want to express my gratitude to SENER, especially to Alfonso Acuñas for infecting me with enthusiasm at work and for believing in me. Jorge Peña, and Iñaki Zabala, who have guided me during these years and have contributed to the industrial and practical focus of the thesis. I must not forget Juan Ruiz de Gopegui, who encouraged me to make the decision to pursue this Ph.D. thesis and Xabier Lekube, whose call was the beginning of this journey. I am thankful to Henrik Bredmose and Antonio Pegalajar for welcoming me to DTU. Their critical thinking and demand for results have been a valuable lesson and a methodology I have learned for the rest of my life.

Of course, this thesis would not have been possible without the constant support of my friends. My "Mordor" girls, who are the best I could have, and I could not be prouder. You are an example of friendship, integrity, effort and improvement. Luci, your talent and creativity have resulted in a very special cover for this project. Not to mention "La Velada," who have always made every moment with them worthwhile. And thanks also to my friends from the university, who have always been a source of inspiration, growth, and, all while having a great time. Javi, thank you for being with

me from the beginning and for giving me strength and confidence when I needed it most.

Last but not least, I want to thank my family. To my aunt María, who is part of every stage of my life. Abu Esther, I remember you every day. And especially my parents, Marta and Iosu, and my brother, Jorge. You have always been in the front lines. Thank you very much for your advice, always thinking about what is best for me. How lucky I am to have such strong pillars like you.

María

Agradecimientos

Me gustaría empezar agradeciendo el apoyo y supervisión de mi director y co-director de tesis, Victor Petuya e Iñigo Mendikoa. Victor, gracias por tu punto de vista práctico, que me ha ayudado tantas veces a retomar el camino para terminar esta tesis. Iñigo, gracias por acompañarme durante estos años, por tu paciencia, y por tu gran disposición en todo momento.

Quiero agradecer al Gobierno Vasco por fomentar el desarrollo de tesis doctorales, y así aumentar el talento dentro del País Vasco, mediante becas como BIKAINTEK, que ha sido gran parte de la financiación para el desarrollo de esta tesis. Gracias también a TECNALIA, y particularmente al equipo de Energías Renovables Offshore, por haber compartido vuestra experiencia y conocimientos conmigo durante estos años, que ha sido fundamentales para llevar a cabo este trabajo. Concretamente, quiero agradecer a Vincenzo Nava por haberme ayudado siempre que he acudido a ti tanto en parte del desarrollo técnico de la investigación como en la revisión de las publicaciones, a Imanol Touzón por tu disposición y por tu punto de vista crítico que ha resultado en una mejora siempre de mi trabajo. Gracias también a Jose Luis Villate por tu confianza y apoyo, además de darme siempre un respuesta rápida a todo lo que he necesitado. También, quiero agradecer a SENER, que siempre me ha hecho sentir como en casa. Especialmente, gracias a Alfonso Acuñas, por contagiarme de entusiasmo en el trabajo y confiar en mi. A Jorge Peña e Iñaki Zabala, que me han guiado durante estos años y han contribuido al enfoque industrial y práctico de la tesis. Tampoco quiero dejarme a Juan Ruiz de Gopegui, quien me dio el empujón para tomar la decisión de hacer esta tesis doctoral y a Xabier Lekube, que su llamada fue el inicio de este camino. Agradezco a Henrik Bredmose y a Antonio Pegalajar por haberme acogido en DTU. El sentido crítico y la exigencia de los resultados han sido de gran lección y una metodología aprendida para el resto de mi vida.

Por supuesto, esta tesis no hubiera sido posible sin el apoyo constante de mis amigos. Mis chicas de "Mordor", que son las mejores que puedo tener y no puedo estar más orgullosa. Sois un ejemplo de amistad, integridad, esfuerzo y superación. Luci, tu talento y creatividad han dado resultado a una portada muy especial para este trabajo. Sin olvidar también a *La Velada*, que siempre han conseguido que cada momento con ellos merezca la pena. Y gracias también a la cuadrilla de la Uni, que siempre ha supuesto un contagio de exigencia, crecimiento y, sin dejar la risas de lado. Javi,

gracias por haberme acompañado desde el principio. Me has dado la fuerza y la confianza cuando más lo necesitaba.

Por último, y no por ello menos importante, quiero dar las gracias a mi familia. María, acompañándome en cada etapa de mi vida. Abu Esther, me acuerdo de tí todos los días. Especialmente agradecer a mis padres, Marta y Iosu, y a mi hermano, Jorge. Vosotros habéis estado siempre en primera línea. Muchas gracias por vuestros consejos, siempre pensando en lo mejor para mi. Me siento afortunada de tener unos pilares tan fuertes como vosotros.

María

Abstract

Global efforts to combat climate change involve increasing renewable energy use, with a focus on wind energy. While onshore wind is reaching its limits, offshore wind, and particularly Floating Offshore Wind (FOW), is gaining huge interest. Moreover, FOW gives access to deeper waters, unlocking 80% of marine wind resources, leading to install larger and more powerful wind turbines. Among the floating substructures used to support the wind turbines, semi-submersible configuration offers several advantages, including access to various water depths, easy onshore turbine assembly and tow-out, and simple installation. While it is still an emerging technology, there is growing interest regarding this platform type, and a large variety of platform concepts are currently in design stage, driving the need for optimisation.

The behaviour of Floating Offshore Wind Turbines (FOWT) is influenced by structural dynamics, aerodynamic, hydrodynamic, and mooring dynamics, with control systems managing their interactions. Modelling these complex coupling effects is challenging, so fully-coupled time-domain numerical tools are commonly utilised to address both linear and non-linear loads. However, due to the high computational effort required for these type of analyses, in the preliminary design stages frequency domain based tools are often employed.

In this Thesis, an efficient frequency domain numerical tool for the preliminary design of the floating offshore wind substructures has been developed, investigated and validated against a time domain state-of-the-art method. Since it is focused on the design of the floating substructures, and particularly applied to semi-submersible platforms, the acceleration of the design process is sought. The large number of platform assessment requires high computational cost, and therefore, a novel method to obtain the hydrodynamic coefficients is here presented. This method has demonstrated to estimate the hydrodynamic coefficients with reasonable accuracy and, as the main advantage, it performs the calculation at least five times faster than the conventional methods.

Additionally, another novel method has been developed, that predicts the second-order hydrodynamic loads at linear cost, in computational terms. These loads are not commonly considered in the initial stages of design, however, it is known they are significant for the mooring design, especially when catenary mooring systems are used. This method has shown

to provide accurate results, despite the simplifications that have been adopted. Similarly to the first method, the main advantage this one presents is the important reduction of the computational cost achieved, making it suitable for the preliminary design stage of FOW substructures. Both developed methods have been validated against radiation-diffraction analysis and have been integrated into the frequency domain simplified response model. The proposed tool has shown to provide similar results regarding the dynamic behaviour of FOWT structures and enables to identify the most suitable platform designs to be assessed in a more advance phase of design, narrowing down the number of potential platform solutions.

Moreover, the notable efficiency of the proposed tool makes it suitable for sensitivity analyses, in order to have a better understanding of the FOWT dynamic behaviour and quantify the influence of the different parameters on the platform design. For instance, in this Thesis, two sensitivity studies have been carried out. On one hand, how the platform dimensions change when a larger wind turbine aims to be installed has been discussed, resulting that the diameter of the columns is the design parameter that most changes. And, on the other hand, how the mooring system affects to the platform design, as well as the importance of including the second-order loads is highlighted.

Resumen

Los esfuerzos globales para combatir el cambio climático implican un aumento en el uso de energía renovable, estando la energía eólica entre las más prometedoras. Mientras que la energía eólica en tierra está alcanzando sus límites, la energía eólica marina, y en particular la energía eólica flotante, está generando un gran interés. Además, esta última proporciona acceso a aguas más profundas, desbloqueando el 80% del recurso eólico marino, lo que permite la instalación de aerogeneradores más grandes y de mayor potencia. Entre las subestructuras flotantes utilizadas para soportar las turbinas, las plataformas semi-sumergibles ofrecen varias ventajas como el acceso a emplazamientos con diferentes profundidades de agua, sencilla instalación en tierra y posible remolque desde el puerto. Aunque aún es una tecnología emergente, existe un creciente interés por esta configuración de plataforma, y actualmente se encuentran en fase de diseño una amplia variedad de conceptos de plataformas semi-submergibles, lo que impulsa la necesidad de su optimización.

El comportamiento de este tipo de estructuras está influenciada por la dinámica estructural, la aerodinámica, la hidrodinámica y la dinámica del sistema de fondeo, junto con los sistemas de control que gestionan sus interacciones. Se trata de un sistema complejo con importantes efectos de acoplamiento, cuya modelización supone un gran desafío. Es por ello que son las herramientas basadas en el dominio del tiempo que permiten analizar sistemas acoplados las que se utilizan comúnmente. Sin embargo, su análisis requeire un al alto esfuerzo computacional que para las fases iniciales de diseño son inasumibles. Por tanto, durante el diseño preliminar se emplean herramientas basadas en el dominio de la frecuencia, dada su mayor eficiencia.

En esta tesis, se ha desarrollado, investigado y validado una herramienta basada en el dominio de la frecuencia para el diseño preliminar de subestructuras de eólica marina flotante, cuya ventaja principal reside en su bajo coste computacional. Se centra en el diseño de las subestructuras flotantes, y en particular en las plataformas semisumergibles, y se busca acelerar el proceso de diseño reduciendo significativamente el número de diseños válidos desde la fase inicial. La gran cantidad de plataformas a evaluar durante la fase inicial de diseño implica un alto coste computacional, por esta razón se ha desarrollado un método eficiente de cálculo de la respuesta de las plataformas que incluye diferentes herramientas. Por un lado un método novedoso para obtener los coeficientes hidrodinámicos de

cada uno de los flotadores. Este método ha demostrado estimar los coeficientes hidrodinámicos con una precisión adecuada para esta fase de diseño preliminar y, como principal ventaja, realiza el cálculo al menos cinco veces más rápido que los métodos convencionales.

Por otro lado, se ha desarrollado otro método pionero que predice las cargas hidrodinámicas de segundo orden de manera mucho más rápida que los métodos del estado del arte. Estas fuerzas no lineales no suelen considerarse en las etapas iniciales de diseño por el alto coste computacional que requiere su análisis; sin embargo, es sabido que son de gran importancia para el diseño del fondeo, especialmente cuando se utilizan sistemas de amarre de tipo catenaria. Este método ha demostrado proporcionar resultados razonablemente precisos, a pesar de las simplificaciones adoptadas, con la principal ventaja de haber logrado una reducción del coste computacional significativa. De esta manera, este método acelerado ha demostrado ser una buena alternativa para implementar el cálculo de fuerzas hidrodinámicas de segundo orden durante el diseño preliminar de subestructuras flotantes de eólica marina. Ambos métodos han sido validados mediante análisis de radiación-difracción con herramientas comerciales y se han integrado en el modelo simplificado de respuesta basado en el dominio de la frecuencia. La herramienta propuesta ha demostrado proporcionar resultados similares en cuanto al comportamiento dinámico de las estructuras de FOWT y permite identificar los diseños de plataforma más adecuados que deben evaluarse en una fase más avanzada del diseño, reduciendo así la cantidad de soluciones potenciales de plataforma.

Además, la notable eficiencia de la herramienta propuesta la convierte en idónea para realizar análisis de sensibilidad, con el fin de tener una mejor comprensión del comportamiento dinámico de los aerogeneradores flotantes y cuantificar la influencia de diferentes parámetros en el diseño de las subsestructuras que soportan las turbinas. Por ejemplo, en este trabajo se han llevado a cabo dos estudios de sensibilidad. Por un lado, se ha discutido cómo cambian las dimensiones de la plataforma cuando se pretende instalar un aerogenerador más grande, resultando ser el diámetro de las columnas el parámetro más influyente. Y, por otro lado, cómo afecta el sistema de fondeo al diseño de la plataforma, así como la importancia de las fuerzas hidrodinámicas de segundo orden desde las fases iniciales de diseño.

Contents

List of Figures **xvii**

List of Tables **xxiii**

Nomenclature **xxv**

1 Introduction **1**
1.1 Motivation 1
1.2 Challenges for the Design and Analysis of Floating Offshore Wind Substructures 2
1.3 Aim, Scope and Limitations 5
1.4 Thesis Organisation 7

2 State of the Art **9**
2.1 Floating Offshore Wind Substructures 9
2.2 Semi-submersible Platform Designs 13
2.2.1 Current Designs 13
2.2.2 Nautilus Semi-Submersible Platform 15
2.2.3 Up-scaling Platforms for Bigger Turbines 16
2.3 Modelling and Analysis of FOW Platforms 17
2.3.1 FOWT Components and Environmental Conditions 18
2.3.2 Modelling Approaches for FOWT 19
2.4 Hydrodynamic Analysis in the Early Design of FOW Substructures 26
2.4.1 First-Order Hydrodynamic Analysis 27
2.4.2 Second-Order Hydrodynamic Analysis 28

3 Preliminary Design and Modelling of FOWT **31**
3.1 Site and Environmental Conditions Assessment 31
3.1.1 Wind and Wave Excitation 32
3.1.2 Site Description 33
3.1.3 Design Load Cases 35

3.2 Design of FOWT 36
3.2.1 Wind Turbine 36
3.2.2 Tower 37
3.2.3 Semi-Submersible Platform 38
3.2.4 Mooring System 43
3.3 Frequency Domain Model Framework 43
3.3.1 Structural Model 44
3.3.2 Aerodynamic Model 48
3.3.3 Hydrodynamic Model 51
3.3.4 Mooring System Model 55
3.3.5 Frequency Domain Model Assembly 57
3.3.6 Overall System Properties 59

4 Linear Hydrodynamic Coefficients Estimation Methodology 63
4.1 Hydrodynamic Analysis on Aggregated Components (*HAAC*) 64
4.1.1 Basic Steps: Database - Interpolate - Scale 64
4.1.2 Additional Contributions to the Methodology 68
4.1.3 Last Step: Superposition 74
4.2 Validation of the *HAAC* methodology 74
4.2.1 Full Floater Hydrodynamic Coefficients 74
4.2.2 Computational Effort Reduction 79
4.3 Integration of *HAAC* into the Frequency Domain Model . . 80
4.3.1 System Natural Periods 81
4.3.2 Dynamic Response of the FOWT 82

5 Approach for the Second-Order Hydrodynamic Loads Calculation of Semi-Submersible Platforms 91
5.1 Accelerated Method for Second-Order Loads on Semi-Submersible Floaters 92
5.1.1 Definition of the Non-Dimensional Parameters . . . 94
5.1.2 Second-Order Loads on Vertical Cylinders 95
5.1.3 Second-Order Loads on Horizontal Member with Longitudinal Axis Perpendicular to the Wave Propagation Direction 98
5.1.4 Second-Order Loads on Horizontal Member with Longitudinal Axis Aligned to the Wave Propagation Direction 101
5.2 Validation of the Accelerated Method on Semi-Submersible Platforms 103
5.2.1 Parametric Studies and Results for the Columns . . 104
5.2.2 Results for the Pontoon Members 109
5.2.3 Results for the Nautilus Semi-Submersible Floater . 112

5.2.4 Computational Cost 116
5.2.5 Sensitivity of the Method with the Platform Design Parameters 117
5.3 Integration of the Accelerated Method on the Frequency Domain Model 121

6 Validation of the Preliminary Design Tool for FOWT 127
6.1 Description of the Validation Procedure 127
6.1.1 Set-up of the Time Domain Simulations in OpenFAST 129
6.1.2 Assessment of the Non-Linearity Level of the Fully-Coupled Model 131
6.1.3 Maximum Dynamic Response Factor Calibration . . 133
6.1.4 Platform Cost Estimation 135
6.2 Dynamic Response Analysis: *FD Tool* vs SoA Methods . . 136
6.2.1 Comparative Analysis of the FOWT Maximum Response 136
6.2.2 Selection of Set of Suitable Designs 146
6.3 Computational Cost Reduction 149

7 Sensitivity Studies with the *FD Tool*: Defining Design Guidelines 151
7.1 Designing Platforms to Support Larger Wind Turbines . . . 152
7.1.1 Platform Design Space for the IEA 15 MW WT . . 152
7.1.2 Dynamic Response Assessment 153
7.1.3 Selected Platform Solutions 158
7.2 Influence of the Mooring System on the Floaters Design . . 159
7.2.1 Assessment of the Response for the Different Mooring Systems 161
7.2.2 Effect of the Second-Order Hydrodynamic Loads on the Platform Response 165

8 Conclusion and Future Work 169
8.1 Conclusions 169
8.1.1 Conclusions Related to *HAAC* 170
8.1.2 Conclusions Related to the *Accelerated Method* . . . 172
8.1.3 Conclusions Related to the *FD Tool* 174
8.1.4 Conclusions Related to the Sensitivity Studies . . . 177
8.2 Future Work 179

Bibliography 181

Main Outcomes of the Thesis 189

List of Figures

1.1 Overview of the proposed *FD Tool*. Dashed lines indicate the novel modules developed in this Thesis. 5

2.1 Types of floating platforms (source: NREL). 10
2.2 Typical frequency diagram for a floating offshore wind turbine. 11
2.3 Forecasted installed power capacity in MW for 2030 and the types of foundations [1]. 13
2.4 Semi-submersible platforms: (a) OO-Star [2] (b) SPIC [3] (c) Windfloat (edp.com) (d) DUT Semi [4]. (e) Nautilus (nautilusfs.com) (f) HiveWind (hivewindenergy.com) 14
2.5 Nautilus semi-submersible platform [5]. 15
2.6 FOWT system main components and rigid motions in 6 DoFs. 18

3.1 Data from the NOAA buoy EO1 at 4 m from MSL: (a) Annual probability distribution (%) for 10-minute mean wind speed. (b) Wind rose of GoM. Data from [6]. 34
3.2 Scatter diagram for the Gulf of Main [6]. 35
3.3 DTU 10 MW WT clamped tower fore-aft normalised modal displacements. (a) 1^{st} mode (b) 2^{nd} mode. 38
3.4 Nautilus semi-submersible platform. (a) LIFES50+ [2] FOWT (b) Parameterisation. 40
3.5 Simplified FOWT model 44
3.6 Aerodynamic damping ratio for surge, pitch and tower first fore-aft mode as a function of mean wind speed. 50
3.7 Platform horizontal displacement versus wind thrust acting on the DTU 10 MW WT and on the IEA 15 MW WT. . . . 56
3.8 Mooring stiffness in the surge motion corresponding to a given wind speed for the DTU 10 MW WT and for the IEA 15 MW WT. 56

3.9 Overview of the frequency domain simplified model, *FD Tool*, and the numerical approaches used for each of the dynamic analysis. 58
3.10 Surge natural periods for the different platform designs. . . 59
3.11 Heave natural periods for the different platform designs. . . 60
3.12 Pitch natural periods for the different platform designs. . . 60
3.13 Tower fore-aft deflection natural periods for the different platform designs. 61
3.14 Campbell diagram for the DTU 10 MW WT and the FOWT tower first fore-aft bending natural frequency range. 61

4.1 *AQWA* model of a semi-submersible platform: (a) Original (b) Decomposed into members. 65
4.2 *AQWA* model for the pontoon database: (a) front view (b) top view. 66
4.3 *AQWA* model of two columns separated a distance s along the x-axis. 69
4.4 Error for the added mass (A), radiation damping (B) and the excitation loads (X) for the surge (1), heave (3) and pitch (5) motions of two cylinders with different s/D ratio. *AQWA* vs *HAAC* (assuming no interaction). 70
4.5 Pitch radiation damping from *AQWA* and *HAAC* with (purple) and without (yellow) interaction for an array of cylinders of 10.5 m diameter, 17 m draft and separated a distance of 50 m. (a) 2 cylinders (b) 3 cylinders (c) 5 cylinders. 71
4.6 Pitch radiation damping from *AQWA* and *HAAC* for an array of two cylinders of 10.5 m diameter, 17 m draft and separated a distance (a) 15 m (b) 50 m (c) 75 m (d) 150 m. 72
4.7 Pitch hydrodynamic coefficients for a pontoon 10 m wide and 45 m long and 25 m depth. *AQWA* vs *HAAC* with (purple) and without (yellow) considering the depth variation.(a) Added mass (b) Radiation damping (c) Excitation load amplitude. 73
4.8 Added mass for D12 platform. (a) Surge (b) Pitch. 76
4.9 Radiation damping for D12 platform. (a) Surge (b) Pitch. . 76
4.10 Excitation force magnitude for D12 platform. (a) Surge (b) Pitch. 76
4.11 Added mass for D26 platform. (a) Surge (b) Pitch. 77
4.12 Radiation damping for D26 platform. (a) Surge (b) Pitch. . 77
4.13 Excitation force magnitude for D26 platform. (a) Surge (b) Pitch. 77
4.14 Added mass for D29 platform. (a) Surge (b) Pitch. 78

4.15 Radiation damping for D29 platform. (a) Surge (b) Pitch. . 78
4.16 Excitation force magnitude for D29 platform. (a) Surge (b) Pitch. 78
4.17 Scheme diagram for *HAAC* validation process. 80
4.18 Error obtained for the natural periods between *HAAC* and *AQWA*. Negative sign means under prediction through *HAAC*. 81
4.19 Response standard deviation for each design under SS1 (a) Surge [m]. (b) Heave [m] (c) Pitch [deg] (d) Nacelle Acceleration [m/s^2]. 87
4.20 Response standard deviation for each design under SS2 (a) Surge [m]. (b) Heave [m] (c) Pitch [deg] (d) Nacelle Acceleration [m/s^2]. 88
4.21 Response standard deviation for each design under SS3 (a) Surge [m]. (b) Heave [m] (c) Pitch [deg] (d) Nacelle Acceleration [m/s^2]. 89
4.22 Response standard deviation for each design under DLC8 (a) Surge [m]. (b) Heave [m] (c) Pitch [deg] (d) Nacelle Acceleration [m/s^2]. 90

5.1 Semi-submersible platform and global reference frame. . . . 93
5.2 Horizontal members with the longitudinal axis perpendicular (left) and aligned (right) to the wave propagation direction. 99
5.3 Standard deviation error. Accelerated method vs *AQWA*. Analysis of the error using different number of modes in the modal truncation and different diameter-to-draft ratio (see legend) under SS2 conditions. 105
5.4 Standard deviation error. Accelerated method vs *AQWA*. Analysis of the error using different number of modes in the modal truncation and different diameter-to-wave-length ratio studied for three cylinders with a diameter of 10.5 m and a draft of (a) 17 m (b) 77 m. (c) 137 m. 108
5.5 SS2 - Second-order loads on cylinder D = 10.5 m and draft = 17 m *AQWA* and Accelerated Method (128 modes). . . . 110
5.6 SS2 - Second-order loads on cylinder D = 10.5 m and draft = 77 m. *AQWA* and Accelerated Method (128 modes). . . 110
5.7 SS2 - Hydrodynamic loads on pontoon member with the longitudinal axis perpendicular to wave propagation direction. *AQWA* and Accelerated Method (128 modes) .(a) first-order, (b) second-order. 113

5.8 SS2 - Hydrodynamic loads on pontoon member with the longitudinal axis aligned to wave propagation direction *AQWA* and Accelerated Method (128 modes) .(a) first-order, (b) second-order. 114
5.9 SS2 - Hydrodynamic loads for the full floater.(a) first-order, (b) second-order (128 modes). 115
5.10 Second-order loads standard deviation on each platform design under SS2. *AQWA+DM* and *Accelerated Method* (128 modes). (a) Surge force [N] (b) Heave force [N] (c) Pitch moment [Nm] 119
5.11 SS2 - Second-order hydrodynamic loads for the designs: (a) D23 (b) D25 120
5.12 Scheme diagram for *Accelerated Method* validation process. 121
5.13 Response standard deviation for each design under SS2. (a) Surge (b) Heave (c) Pitch (d) Nacelle Acceleration 124
5.14 Response standard deviation for each design under SS3. (a) Surge (b) Pitch 125
5.15 Response standard deviation for each design under DLC8. (a) Surge (b) Pitch 126

6.1 Overview of the validation procedure. 128
6.2 Frequency distribution for D2 under DLC1 conditions (a) Surge, (b) Pitch, (c) Nacelle acceleration. 132
6.3 Steel mass for the different platform concepts from table 3.8. 136
6.4 Surge maximum displacement under DLC2 for the different platform designs supporting the DTU 10 MW WT. 138
6.5 Heave maximum displacement under DLC2 for the different platform designs supporting the DTU 10 MW WT. 138
6.6 Pitch maximum angle under DLC2 for the different platform designs supporting the DTU 10 MW WT. 139
6.7 Nacelle maximum acceleration under DLC2 for the different platform designs supporting the DTU 10 MW WT. 139
6.8 Surge maximum displacement under DLC8 for the different platform designs supporting the DTU 10 MW WT. 141
6.9 Heave maximum displacement under DLC8 for the different platform designs supporting the DTU 10 MW WT. 141
6.10 Pitch maximum angle under DLC8 for the different platform designs supporting the DTU 10 MW WT. 142
6.11 Nacelle maximum acceleration under DLC8 for the different platform designs supporting the DTU 10 MW WT. 142
6.12 Surge maximum displacement under DLC9 for the different platform designs supporting the DTU 10 MW WT. 144

6.13 Heave maximum displacement under DLC9 for the different platform designs supporting the DTU 10 MW WT. 144
6.14 Pitch maximum angle under DLC9 for the different platform designs supporting the DTU 10 MW WT. 145
6.15 Nacelle maximum acceleration under DLC9 for the different platform designs supporting the DTU 10 MW WT. 145
6.16 Pitch maximum angle under DLC8 for the different platform designs supporting the DTU 10 MW WT and threshold range. 147
6.17 Nacelle maximum acceleration under DLC8 for the different platform designs supporting the DTU 10 MW WT and threshold range. 147
6.18 Improvement of the computational efficiency for the dynamic response analysis through the *FD Tool* with respect to the SoA tool. 150

7.1 Pitch maximum angle under DLC2 for the different platform designs supporting the IEA 15 MW WT and threshold range. 154
7.2 Nacelle maximum acceleration under DLC2 for the different platform designs supporting the IEA 15 MW WT and threshold range. 154
7.3 Pitch maximum angle under DLC5 for the different platform designs supporting the IEA 15 MW WT and threshold range. 155
7.4 Nacelle maximum acceleration under DLC5 for the different platform designs supporting the IEA 15 MW WT and threshold range. 155
7.5 Pitch maximum angle under DLC8 for the different platform designs supporting the IEA 15 MW WT and threshold range. 156
7.6 Nacelle maximum acceleration under DLC8 for the different platform designs supporting the IEA 15 MW WT and threshold range. 156
7.7 Pitch maximum angle under DLC9 for the different platform designs supporting the IEA 15 MW WT and threshold range. 157
7.8 Nacelle maximum acceleration under DLC9 for the different platform designs supporting the IEA 15 MW WT and threshold range. 157
7.9 Stiffness for five mooring systems as a function of the mean wind speed at equilibrium position under no excitation. (a) Surge (b) Pitch 160
7.10 Natural periods (s) for the different platform designs and mooring systems. 162

7.11 Stiffness for five mooring systems as a function of the mean wind speed at equilibrium position under no excitation. (a) Surge (b) Pitch 163
7.12 Surge mooring stiffness vs FOWT horizontal displacement for three DLCs. 165
7.13 Mooring stiffness versus FOWT offset in the surge DoF with (blue) and without (yellow) second-order hydrodynamic loads. 166
7.14 Surge maximum displacement for the different designs using the stiffest mooring system $Moor_1$ under DLC9. 167
7.15 Surge maximum displacement for the different designs using the original mooring system from section 3.2.4 $Moor_3$ under DLC9. 167
7.16 Surge maximum displacement for the different designs using the softest mooring system $Moor_5$ under DLC9. 168

List of Tables

2.1 Representative natural frequencies (Hz) of the three main floating substructure concepts [7]. 11
2.2 Nautilus platform dimensions (m). 16
2.3 Aero-servo-hydro-elastic tools used in offshore wind. 25

3.1 DLCs for the GoM defined by the mean wind speed (m/s), and the wave significant height (m) and peak period (s). . . 35
3.2 Wind turbines mass and inertia properties. (Units: kg, m) . 36
3.3 Tower structural properties. (Units: kg, m, s) 37
3.4 Steel material properties. (Units: kg, m, s) 37
3.5 Platform design parameters definition and nomenclature. . 39
3.6 Weight densities (kg/m^3) for the platform structural steel. . 40
3.7 Thresholds defined for the FOWT response. * h: water depth. ** Value extracted from COREWIND project. g: gravity acceleration. 41
3.8 Platform design space. Values of diameter (D), separation between columns (s) and draft (d) (Units: m). 42
3.9 Mooring system properties for each FOWT. (Units: kg, m, deg) 43

4.1 Sea states used for the *HAAC* validation. (Units: m, s) . . 83

5.1 Accelerated method error (%) for different number of modes with respect to the loads from *Slender* (5.12) and from *AQWA*. Cylinders of D = 10.5 m and drafts 17 m and 77 m under SS2 conditions. 106
5.2 SS2 - Pontoon perpendicular member second-order loads error (%) vs number of modes using the loads from the *Slender* (5.12) and the *AQWA* as reference signals. 111
5.3 SS2 - Pontoon aligned member second-order loads error (%) vs number of modes using the loads from the *Slender* (5.12) and the *AQWA* as reference signals. 112

5.4 SS2 - Second-order loads error (%) for each member separately and for the full Nautilus floater with 128 modes. . . . 116
5.5 Computational time (s) for the accelerated method to calculate second-order loads on the Nautilus floater for a 1-hour sea state, using different number of modes. 117

6.1 OpenFAST ElastoDyn output parameters corresponding to the DoFs considered in the simplified structural model in section 3.3.1. 130
6.2 Gumbel maximum response under DLC9 conditions from the OpenFAST simulations. (Units: m, deg, s) 134
6.3 Maximum response under DLC9 conditions using eq. (6.4) with the mean and standard deviation derived from the SoA tool. (Units: m, deg, s) 134
6.4 Maximum response under DLC9 conditions using eq. (6.4) with the mean and standard deviation from the *FD Tool*. (Units: m, deg, s) 134
6.5 Sorted list of platforms that meet design requirements and the response from the FD Toll and TD SoA tool. (Units: kg, m, deg, s) 148

7.1 New platform design space for IEA 15 MW WT. Values of diameter 'D', separation between columns 's' and draft 'd' (Units: m). 153
7.2 Sorted list of platforms that meet design requirements and the maximum response estimated by the *FD Tool* for the IEA 15 MW WT. (Units: kg, m, deg, s) 158

Nomenclature

Abbreviations and Acronyms

BEM	Blade Element Momentum
CFD	Computational Fluid Dynamics
CM	Centre of Mass
CoB	Centre of Buoyancy
CoG	Centre of Gravity
DLC	Design Load Case
DoF	Degree of Freedom
DTU	Technical University of Denmark
EoM	Equation of Motion
FA	Fore-Aft
FD	Frequency Domain
FEM	Finite Element Methods
FFT	Fast Fourier Transform
FLS	Fatigue Limit State
FOW	Floating Offshore Wind
$FOWT$	Floating Offshore Wind Turbine
GoM	Gulf of Maine
$HAAC$	Hydrodynamic Analysis on Aggregated Components

$HAWT$	Horizontal Axis Wind Turbine
IEA	International Energy Agency
IEC	International Electrotechnical Commission
$iFFT$	Inverse Fast Fourier Transform
$LCOE$	Levelised Cost Of Energy
ME	Morison Equation
MSL	Mean Sea Level
$NREL$	National Renewable Energy Laboratory
PDF	Probability Density Function
PF	Potential Flow
PM	Peirson-Moskowitz
PoF	Point of Flotation
PSD	Power Spectral Density
QS	Quasi-Static
QTF	Quadratic Transfer Function
$QuLAF$	Quick Load Analysis of Floating Wind Turbines
RNA	Rotor and Nacelle Assembly
SoA	State of the Art
STD	Standard Deviation
TD	Time Domain
TLP	Tension Leg Platform
TRL	Technology Readiness Level
TT	Tower Top
ULS	Ultimate Limit State
WT	Wind Turbine

Greek Letters

α	Power law coefficient for wind speed profile
$\bar{\xi}$	Mean response
ϵ_T	Error definition for the natural periods
ϵ_σ	Error definition for the response standard deviation
ϵ_{coef}	Error definition for the hydrodynamic coefficient estimation
η	Wave amplitude
$\hat{\xi}$	Amplitude of the frequency domain response motion
κ	Non dimensional wave number
λ	Eigenvalue
$\mathcal{T}_\phi$	Transfer function of the second-order velocity potential
∇	Platform displaced water volume
Ω	Non dimensional angular frequency
ω	Angular frequency
ϕ	Eigenvector or tower mode shape
$\phi^{(1)}$	First-order velocity potential
$\phi^{(2)}$	Second-order velocity potential
ϕ_{hub}	Tower first fore-aft mode shape at the hub height
$\phi_{z,hub}$	First derivative of the tower first fore-aft mode shape at the hub height
$\phi_{zz,hub}$	Second derivative of the tower first fore-aft mode shape at the hub height
ρ_w	Water density
ρ_{air}	Air density
σ	Standard deviation
σ_s	Estimated standard deviation

σ_u	Wind standard deviation
σ_ξ	Response standard deviation
σ_{ref}	Reference standard deviation
$\tilde{\rho}$	Tower mass per unit length
ς_{aero}	Aerodynamic damping coefficient
ξ	Response
$\zeta_{str,tw}$	Tower structural damping ratio for the first fore-aft mode shape

Roman Letters

$\overline{GM}$	Metacentric height from the centre of gravity
$\mathbf{V}_j$	Eigenvector used in the accelerated method
A	Added mass matrix
a	Pontoon width
A_x	Floater area projected on the YZ plane
A_z	Floater area projected on the XY plane
A_{inf}	Infinite added mass matrix
a_{sc}	Width of the scaled pontoon
B	System damping matrix
B_{aero}	Aerodynamic damping matrix
b_{aero}	Aerodynamic damping coefficient
B_{rad}	Radiation damping matrix
B_{rad}^{int}	Radiation damping matrix including interaction between columns
B_{str}	System structural damping matrix
B_{vis}	Viscous damping matrix
C	System stiffness matrix
C_D	Drag coefficient

C_{hst}	Hydrostatic stiffness matrix
$C_{m,x}$	Inertia coefficient along x-direction.
$C_{m,z}$	Inertia coefficient along z-direction.
C_{ma}	Inertia coefficient along the pp vertical direction.
C_{mb}	Inertia coefficient along the pa vertical direction.
C_{mc}	Inertia coefficient along pontoon horizontal direction.
C_{moor}	Mooring stiffness matrix
C_{str}	System structural stiffness matrix
C_{tw}	Tower structural stiffness
CM^{TT}	Centre of mass of referred to the tower top.
D	Diameter of the platform columns
d	Platform draft and pontoon depth
d_{db}	Draft of the cylinders from the database
D_{sc}	Diameter of the scaled cylinders
d_{sc}	Depth of the scaled submerged pontoon
EI	Bending stiffness
f	Frequency
$F_{aero,tw}$	Tower aerodynamic drag force
$F_{aero,x}$	Aerodynamic thrust
$F_{aero,z}$	Aerodynamic vertical force
F_{aero}	Aerodynamic loads
F_{buoy}	Buoyancy force
$F_c^{(2)}$	Second-order force on vertical cylinders
F_{hst}	Hydrostatic load
F_{hyd}	hydrodynamic loads

$F_{pa}^{(2)}$	Second-order force on aligned pontoon member
$F_{pp}^{(2)}$	Second-order force on perpendicular pontoon member
F_{rad}	Hydrodynamic radiation load
F_{vis}	Hydrodynamic viscous load
$F_{w}^{(1)}$	Hydrodynamic first-order wave load
$F_{w}^{(2)}$	Hydrodynamic second-order wave load
$F_{z}^{(AM)}$	Added mass second-order heave force
$F_{z}^{(FK)}$	Froude-Krylov second-order heave force
g	Gravity acceleration
H	Mechanical transfer function
h	Water depth
h_c	Platform column height
h_d	Platform deck height
h_p	Platform pontoon height
H_s	Significant wave height
h_{hub}	Hub height above mean sea level
h_{lc}	Platform lower column height
h_{tw}	Tower height
h_{uc}	Platform upper column height (freeboard)
h_{wb}	Columns water ballast height
I	Wind Turbulence Intensity
I_{tot}^{O}	System inertia with respect to the PoF
I^{TT}	Inertia referred to the tower top.
I_{y,A_z}	Second moment of area about the y-axis
k	Wave number

KC	Keulegan Carpenter Number
L	Pontoon length
L_u	Integral scale parameter in the wind speed horizontal direction
L_w	Wave length
L_{db}	Length of the pontoon from the database
m	Mass of the system.
$M_{aero,y}$	Aerodynamic tilt moment about y-axis on the tower top.
m_f	Floater mass
m_{moor}	Mooring system mass
m_{rn}	Rotor and nacelle mass
M_{str}	System structural mass matrix
m_{tot}	System total mass. Considering the RNA, tower, platform and mooring system
M_{tw}	Tower mass
$M_y^{(2)}$	Second-order moment about y-axis
$p(2)$	Second-order pressure
Re	Reynolds Number
s	Distance between the platform column axes
S_u	Wind speed Kaimal spectrum
$S_{y,A}$	First moment of area about the y-axis
sc_c	Scaling factor for the cylinder
sc_p	Scaling factor for the pontoon
t	Time
T_p	Wave peak period
T_s	Estimated natural period
T_{ref}	Reference natural period period

U	Wind Speed
$u^{(1)}$	First-order horizontal velocity of the water particle
$u^{(2)}$	Second-order horizontal velocity of the water particle
u_b	Body horizontal velocity
u_f	Fluid horizontal velocity
U_{ref}	Wind speed at reference height
u_{rep}	Representative horizontal velocity of the water particle
v	Generalised coordinate
w	Vertical velocity of the water particle
$w^{(1)}$	First-order vertical velocity of the water particle
$w^{(2)}$	Second-order vertical velocity of the water particle
w_d	Platform deck width
w_{rep}	Representative vertical velocity of the water particle
X	Wave excitation coefficient
z	Vertical distance from the ground or from the MSL
z_{tot}^{CM}	Vertical position of the centre of mass of the FOWT with respect the MSL
z_{ref}	Vertical distance to the reference height from the ground or from the MSL

Chapter 1

Introduction

In this chapter, the introduction to the content presented in this document is provided. First, in section 1.1, the motivation behind this study is explained, offering a brief description of the current status of floating offshore wind worldwide and highlighting the future perspectives. Following that, in section 1.2, the main existing challenges related to the design and modelling of floating offshore wind systems are exposed, along with an exploration of how this work addresses these challenges. The primary objectives, as well as the scope and limitations of the proposed methods, are detailed in section 1.3. Finally, in section 1.4, the description of the document's structure is given.

1.1 Motivation

Since the last years, there is a worldwide commitment to climate change mitigation through the reduction of the greenhouse gas emissions. This can be achieved by means of increasing the deployment of renewable energy technologies [8]. Among the renewable energy sources, wind energy has achieved a matured stage using the three blade Horizontal Axis Wind Turbine (HAWT). Onshore sites with good wind resource are now approaching their limits and offshore wind increases the potential of the wind energy generation [8, 9]. To date, bottom-fixed foundations have been used for the installation of offshore wind turbines and they are generally the cheapest way to build offshore wind farms. Per contra, this technology is limited to shallow waters (< 60 m) due to economical aspects. Previous research [8] show that moving towards deeper waters gives access to the 80% of the marine wind resource, thus, Floating Offshore Wind (FOW) is attracting increasing interest among stakeholders due to its numerous advantages including access to sites with higher capacity factors and the potential to

install larger turbines, resulting in an increased nominal power generation.

When it comes to floating platforms, they can be classified into four types, based on their stability mechanism: the spar-buoy, which is ballast stabilised; the semi-submersible and the barge, which are buoyancy stabilised; and the Tension Leg Platform (TLP), which is mooring stabilised.

It is expected floating technology to be more cost effective than bottom-fixed in the near future. Currently, there are four floating offshore wind farms operating in Europe: Kincardine, Hywind Scotland, WindFloat Atlantic and Hywind Tampen. All of them are proving the feasibility of the floating technology, able to perform as well as bottom-fixed solutions or even better [10]. There is an important issue with FOW and it is the high cost of the foundation due to the immaturity of technology. It is one of the main drivers of the total cost, after those related to the operation and maintenance, and the most expensive structural component [11]. Therefore, technology optimisation, standardisation, and scaling of the foundations would have a direct impact on the total cost of FOW [10].

Among the mentioned types of floating substructures, semi-submersible configuration have attracted great interest among designers [12, 7]. Today there are many different solutions for semi-submersible platforms and still it is not clear which of them will predominate in the market. In fact, this large potential in the market can become a threat due to the high degree of competition among designs. Since this is an emerging technology, so far the knowledge from bottom-fixed offshore structures has enabled the development of a great variety of floating platforms [13]. Furthermore, the current design process requires long term simulations and the cost prediction brings a lot of uncertainty, since there is no experience yet. Therefore, there is a lack of efficient and versatile design tools specific for FOW substructures that enable a quick optimisation process, especially for the initial stages of design.

In addition, wind turbine size is increasing with accelerated pace and consequently, larger structures need to be designed. For this reason, analysing the influence of the design parameters through sensitivity analyses holds great significance. This knowledge empower designers to make informed decisions and fine-tune the designs accordingly, ensuring optimal performance and stability.

1.2 Challenges for the Design and Analysis of Floating Offshore Wind Substructures

The floating substructure is one of the main drivers of the total cost of a floating wind farm. These costs include the material and design, construc-

tion, installation, operation and maintenance, and decommissioning. The main objective when designing a floating platform is to generate electricity at the lowest cost, provided that optimal performance and stability are ensured. Material and construction costs related to the platform are around 17% of the total cost [11], being the component with the highest contribution. These costs depend on the substructure design and, therefore, by means of its quick optimisation from the early design stage, a reduction of the total costs can be achieved.

Floating offshore wind turbines (FOWT) are composed of four main subsystems: the wind turbine, the tower, the floating platform and the mooring system, which is anchored to the seabed. They are complex systems since they are subjected to many load interactions, such as wind, wave, current, or ice, and their design involve a large number of variables. In order to assess the dynamic behaviour of these structures, tools capable of modelling the coupled hydro-aero-servo-elastic effects on the whole system are required. In the preliminary design stages, usually simplified models based on the frequency domain are used, because of its high computational efficiency. These reduced models consider just a few Degrees of Freedom (DoF) that represent the main motions of the structure. In the more advanced stages of design, time domain fully coupled aero-servo-hydro-elastic models are analysed with a large number of DoFs. In order to account for the non-linear effects, time domain based numerical analyses are performed, although they are very time consuming. Among designers, the most commonly used time domain numerical tools are FAST [14] developed by NREL, HAWC2 [15] by DTU, and BLADED [16] by DNV.

In literature, several frequency domain based simplified models can be found. Generally, the wind turbine is represented by a lumped mass, the tower is the only flexible member, the platform is considered a rigid body and the mooring system is represented by a stiffness matrix. The non-linearities inherent in the wind turbine control system, makes the frequency domain analysis more complex, and thus, the aerodynamic loads are usually cascaded to the simplified model from advanced models. Similar procedure is followed for the calculation of the hydrodynamic loads, which are commonly obtained though radiation-diffraction analysis. When looking for the optimum semi-submersible platform design, tens of platform solutions are assessed where a wide range of values for the design parameters are combined, such as columns diameter, separation between the columns or platform draft. This requires to perform a hydrodynamic analysis for each of the platforms of the design space. As in every floating body, the dynamics will be affected by the radiation-diffraction loads, which are usually computed in commercial software, such as AQWA or WAMIT, that are

based on the potential flow theory. From these type of analysis, the first- and second-order hydrodynamic loads can be obtained.

On one hand, first-order hydrodynamic loads are obtained by means of the linear hydrodynamic coefficients, which are the added mass, radiation damping and wave excitation coefficients. These are usually considered in the preliminary design stages of offshore wind substructures. Sometimes, they are simplified into constant coefficients, but it is not very recommended when analysing large and complex structures. The radiation-diffraction analysis adopted in panel code software is often used since it provides a reasonable accuracy, although, as before mentioned, it can become a long process if many platform solutions are aimed to be assessed.

On the other hand, second-order hydrodynamic loads play a crucial role in catenary moored structures because they are highly sensitive to low-frequency stimulation. Yet, computing these loads involves a significant computational workload, requiring two time-intensive steps. Initially, obtaining the Quadratic Transfer Functions (QTFs) from radiation-diffraction analysis increases the time needed for this analysis compared to calculating linear loads. Subsequently, a double summation is necessary to compute the loads for a specific wave spectrum, particularly time consuming when employing long time series. Consequently, during the preliminary design stages of floating platforms, these loads are often disregarded. Nonetheless, integrating them into the design process from the outset would result in more precise platform designs and facilitate the adoption of a more appropriate mooring design, mitigating structural resonance.

FOW technology is continually advancing, and while onshore wind technology is well-established, there remains considerable ground to cover in understanding the dynamic behaviour, modelling, and design of floating systems. It is pivotal to develop efficient tools that can parameterise the structure, swiftly conduct sensitivity analysis, and enhance comprehension of the impact of various parameters on the dynamic behaviour of FOWT substructures. This approach empowers designers to refine their platforms effectively while significantly reducing the time invested in the process.

This Thesis addresses the design and analysis of semi-submersible platforms in order to accelerate the substructure preliminary design phase and provide a better understanding of the dynamic behaviour of the system and the effects of the design parameters, which would enable the definition of certain design guidelines, such as scaling laws with wind turbine power or design driving load cases identification. By addressing these challenges, it is aimed to propel floating offshore wind technology towards a more competitive and sustainable future in the renewable energy sector.

1.3 Aim, Scope and Limitations

In this Thesis, it is sought to address the challenges regarding the preliminary design phase of the floating offshore wind platforms described above. For that purpose, and in view of the related work found in literature, a novel design tool was developed, including two standalone modules for the hydrodynamic analysis of FOW floating platforms, as main contribution in this research field. These developed methods are the alternative to the commonly used radiation-diffraction analyses and significantly accelerate the floating platform design process. Furthermore, as before mentioned, in the initial stages of the platform design, a large number of potential solutions are assessed, where a wide range of platform dimensions are considered.

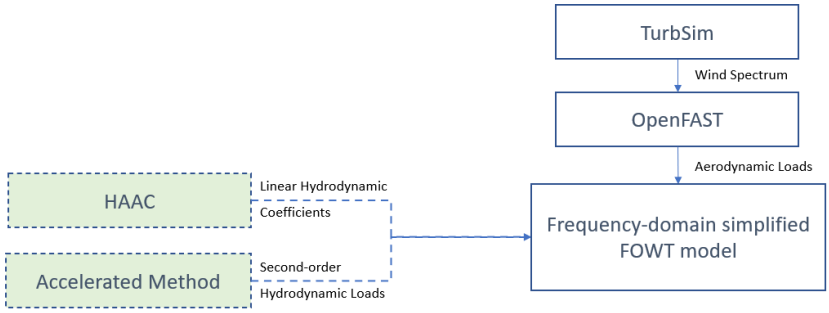

Figure 1.1: Overview of the proposed *FD Tool*. Dashed lines indicate the novel modules developed in this Thesis.

The main objective of the proposed tool is to narrow down the number of suitable solutions that meet the design requirements in the floater preliminary design stage. For that purpose, the developed methods were integrated into a simplified frequency domain response model, as shown in fig. 1.1. The aerodynamic loads were cascaded from the advanced state-of-the-art tool, OpenFAST. The turbulent wind time series were generated in TurbSim [17], also developed by NREL. This tool is denoted *FD Tool* and in this Thesis is shown that it significantly accelerates the overall FOWT design process, allowing to assess a larger number of designs from the beginning and, thus, accelerating the possibility of finding the optimal design and, consequently, achieving the final goal which is the reduction of the costs associated to the substructure. Moreover, this tool has the advantage that it can be further integrated with automatic optimisation algorithms, or be used to perform sensitivity analyses in order to gain a better understanding of FOWT dynamic behaviour, taking advantage of its high efficiency. Regarding this point, several sensitivity analyses were performed, such as how the scaling-up of the wind turbines influences on the platform design, the

effects of the mooring design on the definition of the platform concept, or the importance of the second-order loads during the initial phase of design.

Due to the increasing interest of the designers, this Thesis is focused on the semi-submersible platforms, consisting of a pontoon and vertical columns. However, it can readily be adapted to other types of floating structures, such as spars or TLPs, albeit with some necessary adjustments in the formulation. The core theoretical principles would remain consistent. Regarding the structural model, the present tool has been validated for the application on two-plane symmetric semi-submersible platforms, and consequently, only the surge, heave and pitch motions were evaluated. In case of asymmetric platforms, these aspects would need to be incorporated. It is worth noting that the scope of this study solely encompasses wind and wave excitation when they are aligned. Moreover, current, ice or wind gust loads are not here considered, since these type of excitation are usually accounted in more advanced stages of design rather than for the preliminary phases.

It should also be kept in mind that the proposed methods for the first- and second-order hydrodynamic analyses suffer several simplifications in order to achieve the computational cost reduction. For instance, since semi-submersible platforms are large and complex structures, they are split into simple members. Then, the hydrodynamic radiation and diffraction loads are estimated for each of the members, and superposition is further applied. The fact of neglecting cross-interaction is an assumption that will derive into inaccuracies, especially when the platform members are relatively closed from each other.

Moreover, regarding the second-order hydrodynamic load calculation method, it is based on the Morison and Rainey force model, which is based on slender body theory. A semi-submersible platform is not slender, and for that reason it is split into columns and pontoon bodies. However, some of the simple members are not even slender, which also leads to certain inaccuracies.

In this work, only a linear drag force is considered through the viscous damping, but it was neglected for the second-order hydrodynamic loads. Despite, it could be introduced through the Morison drag force equation. The maximum values for the platform response motions estimated from this frequency domain tool were adjusted by means of three hours time domain simulations using three seeds and three different platform designs supporting the DTU 10 MW WT. Therefore, the estimation of the maximum value as a function of the mean and standard deviation applied for a different wind turbine might suffer slight variations.

1.4 Thesis Organisation

In this section, the structure of the Thesis is outlined. In chapter 2, an examination and presentation of the current state-of-the-art in various aspects related to the research work are provided. Moving on to chapter 3, the Thesis delves into the description of FOWT, offering insights into the design of each primary component and detailing the proposed frequency domain response model, *FD Tool*.

Following this, chapter 4 and chapter 5 introduce the novel hydrodynamic methods used for estimating hydrodynamic coefficients, and calculating the second-order hydrodynamic loads, respectively. Each method's formulation is elucidated, along with an explanation of the validation results. Additionally, a discussion on the reduction of computational costs achieved through these methods is included.

Subsequently, chapter 6 focuses on the validation of the new *FD Tool* and overall platform design methodology, and conducts a comparative analysis of FOWT responses under various Design Load Cases (DLC). Once the proposed tool has been successfully validated, chapter 7 presents the sensitivity studies conducted using this tool, such as the influence of the wind turbine scaling up on the platform design, and the effect of the mooring system on the floater definition.

Finally, chapter 8 concludes by summarising the key findings of this Thesis and mentioning avenues for future research.

Chapter 2

State of the Art

In this chapter, the state of the art of the floating offshore wind substructures is given. First, the different types of floating platforms used to support Floating Offshore Wind Turbines (FOWT) are described, mentioning their advantages and disadvantages, in section 2.1. Since this Thesis is focused mainly on the design of the semi-submersible configuration, although it can be extender or adapted to other types, a more detailed section regarding this topic is found in section 2.2. Here, the current existing semi-submersible platforms are compared. Also, the case study used in this Thesis, the Nautilus platform, is described and all the necessary data for the development of this work is given. Moreover, a brief literature review of the platform scaling procedures in order to support larger wind turbines is given. In section 2.3, the FOWT components are described and the different ways they can be modelled are exposed, based on other researchers. There is a special section dedicated to the existing hydrodynamic modelling and analysis methods in section 3.3.3, as is the main contribution of this Thesis. Here, the literature gaps found are highlighted and an brief summary of what this work presents is given.

2.1 Floating Offshore Wind Substructures

Floating Offshore Wind (FOW) has increased the interest of designers since it offers several advantages with respect to the bottom-fixed technology, such as the access to deep water areas, which covers almost the 80% of the ocean surface. Floating platforms can be classified into three main types, based on their primary stabilising mechanism [11, 7]:

- **Spar type - Ballast stabilised**: they are large draft cylindrical structures that have a ballast at the bottom in order to locate the

Centre of Gravity (CoG) below the Centre of Buoyancy (CoB). These structures have a large inertial resistance to pitch and roll and due to the small water plane area makes it highly resistant to wave and wind loads. The large draft limits site location with water depths above 100 m.

- **Semi-submersible - Buoyancy stabilised**: structures with a large waterplane area in order to achieve a stabilising restoring moment in case of rotational displacement. They are commonly composed of buoyant columns connected to other elements, such as pontoons. These are large and weighted platforms with smaller draft than the spar configuration, making it suitable for water depths above 40 m. The barge type are similar to the semi-submersible platforms, with the difference that they have a unique hull, usually with a moonpoon in between to increase the stability in hard sea states.
- **Tension Leg Platform (TLP) - Mooring stabilised**: the platform is moored to the seabed using tendons that are constantly under tension, thus they are more expensive than other floating technologies.

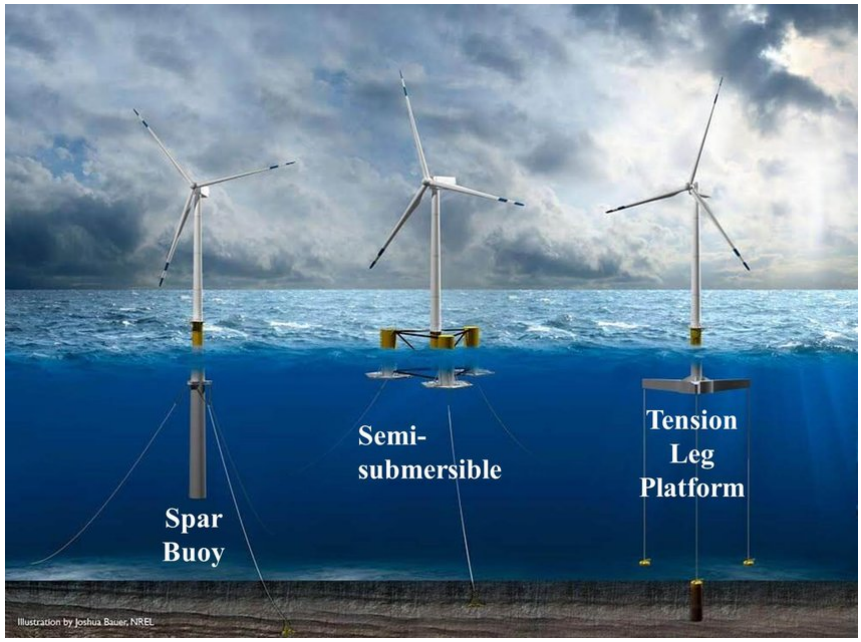

Figure 2.1: Types of floating platforms (source: NREL).

In fig. 2.1 the different platform configurations are shown. The semi-submersible, barge and spar types usually are catenary-moored systems.

The natural frequencies for these structures are below the wave frequency range, although they can be excited resonance by the slow-drift wave excitation. The TLPs, however, have natural frequencies above the first order wave load frequencies. In table 2.1 the usual natural frequencies for each type of floater are given.

DoF	Spar	Semi-submersible	TLP
Surge	0.02	0.02	0.04
Heave	0.07	0.07	0.44
Pitch	0.05	0.05	0.43

Table 2.1: Representative natural frequencies (Hz) of the three main floating substructure concepts [7].

When designing any type of foundation, it is important to place the natural frequencies far enough from the wave excitation frequency and the wind turbine's rotational frequencies. It is common to classify the structure as soft or stiff, based on the rotor frequency, f_{1p}, and the blade passing frequency, f_{3p}. In fig. 2.2 the traditional frequency diagram for a FOWT is given. While the floating substructures are usually described as soft-soft, the tower bending frequency is designed as soft-stiff.

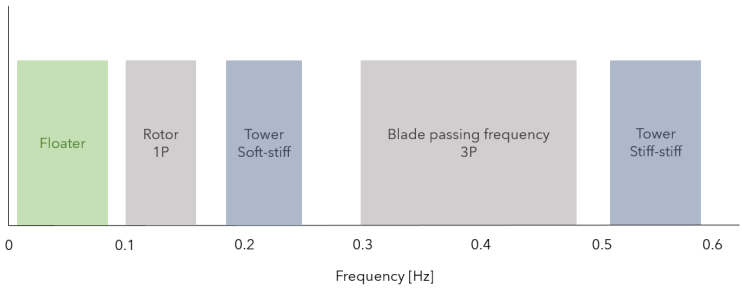

Figure 2.2: Typical frequency diagram for a floating offshore wind turbine.

Each of the floating platforms have their advantages and disadvantages, thus, depending on the site, including factors such as the type of seabed, the water depth, the distance to shore or the metocean conditions, a platform configuration that is most suitable would be determined accordingly. The spar is very easy to manufacture and provides low operational risk. However, they are limited to very deep waters and high fatigue loads occur in the tower base. In addition, there is currently no global market for the spar type, despite having a high Technology Readiness Level (TRL). Contrary to the spar, there's significant market competition observed with the semi-submersible floater. Designers have shown considerable interest in this type due to its potential for cost reduction through mass production, independ-

ence regarding depth, and easy installation, thereby achieving high TRL levels. However, since they are large and complex substructures, they suffer large motions and are very sensitive to wave loads, resulting in important effects on the turbine. As for the TLPs, it is an interesting option for their high stability and suitability under high sea state conditions, but with the drawback of being a highly stressed structure which requires a complex and risky installation. For this reason, the TRL is still very low and no global market has been developed. According to a review in [7], a set of criteria was established considering the Levelised Cost of Energy (LCOE), durability, performance, flexibility and other considerations, and a set of ten floaters were assessed. Among them, the semi-submersible with active ballast system resulted in third place, after two spar types. Furthermore, the former platform showed the highest confidence.

Semi-submersibles platform are the most expensive type of floating foundation, being up to seven times the cost of a single TLP and twice the cost of a spar, although it holds the lowest installation cost [18]. The cost of the foundation is highly related to its size, therefore the optimisation of the floater would have a great impact on the foundation cost and, therefore, on the LCOE. For that purpose, efficient computer software tools developed specifically for the design of floating offshore wind support structure are required.

In Europe currently there are six floating wind farms connected to the grid with an overall power capacity of 115 MW. Hywind Scotland was the world's first floating offshore wind farm, located off-coast of Aberdeen where the water depth is 108 m. Spar foundations support each of the five 6 MW Vestas wind turbines. In the next years it is expected that semi-submersible configuration will be the leading floating substructure, achieving a global market share of almost 80 % according to [19] and almost 100 % according to [1], as can be observed in fig. 2.3. In view of this forecast regarding floating offshore wind substructures, the semi-submersible configuration shows numerous advantages compared to the other floating platform technologies, such as the access to sites of a wide range of water depths, onshore wind turbine assembly and tow-out and easy installation [19, 11]. Moreover, there is a huge potential to achieve an optimal design due to the large variety of platform concepts, using the platform members and dimensions as design parameters. It is still an emerging technology, but designers have shown great interest for this type of platform, therefore, there is a general need for its optimisation. Furthermore, hybrid structures that merge the semi-submersible low draft characteristic with favourable attributes of the other configurations, as well as industrialisation, are two emerging topics that will potentially reduce the FOWT costs [19].

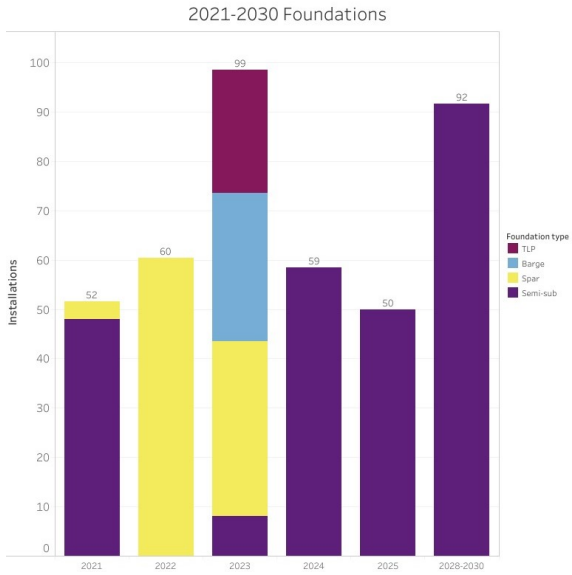

Figure 2.3: Forecasted installed power capacity in MW for 2030 and the types of foundations [1].

2.2 Semi-submersible Platform Designs

2.2.1 Current Designs

Semi-submersible platforms are one of the most feasible floating substructures for offshore wind, and currently, more than thirty different concepts are in design stage, and the question of which concept will emerge as the market leader remains unanswered.

This type of floater sets its origins in the oil and gas industry, and it is commonly composed of three or four columns that are connected to each other by means of braces or a pontoon base. In fig. 2.4, some of the existing semi-submersible platforms are shown, and the wide variety of concepts is notable. The use of a pontoon base is more suitable to reduce fatigue loads, since these structures have static stability and the large water plane area associated to these connections increases the hydrodynamic stability, because of the high hydrostatic stiffness [20]. The advantages of the semi-submersible floaters have already been discussed in section 2.1. Nevertheless, their complex dynamic response due to the coupled interaction effects of wind and wave loads, makes their design very challenging.

The first project aimed to assess the feasibility of the semi-submersible floaters for offshore wind was Fukushima-FORWARD, supporting a 2 MW wind turbine in Japan. Then, the WindFloat1 project emerged, a three column configuration with a 2 MW commercial wind turbine mounted on

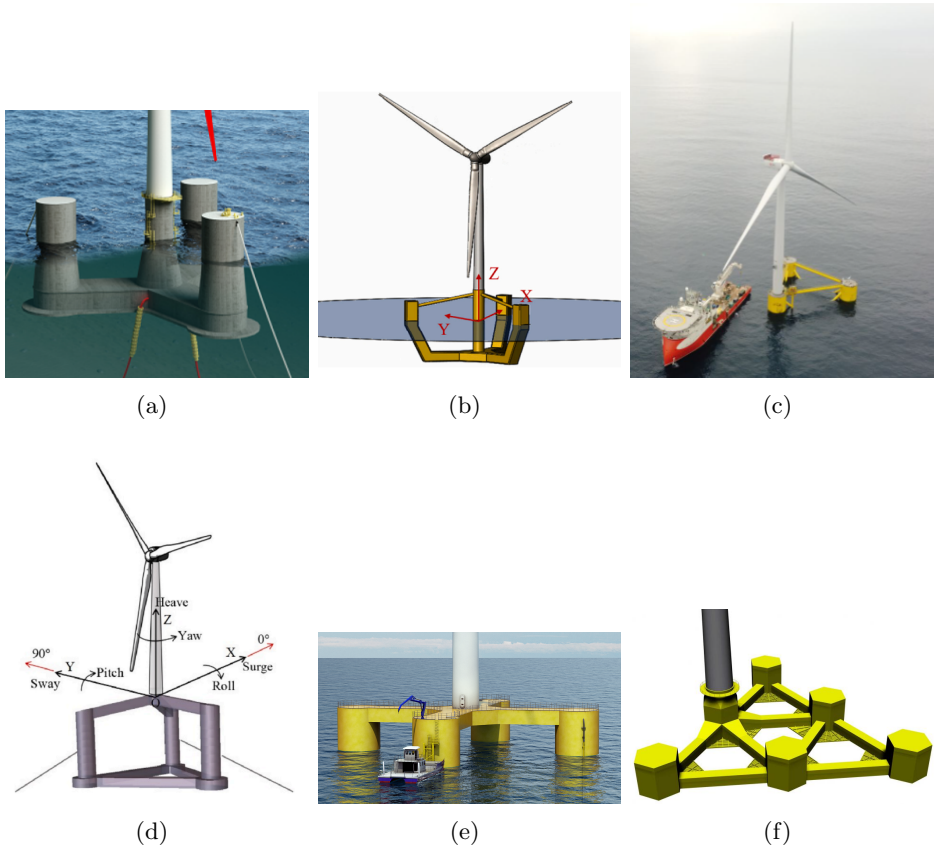

(a) (b) (c)

(d) (e) (f)

Figure 2.4: Semi-submersible platforms: (a) OO-Star [2] (b) SPIC [3] (c) Windfloat (edp.com) (d) DUT Semi [4]. (e) Nautilus (nautilusfs.com) (f) HiveWind (hivewindenergy.com)

one of them in the Atlantic Ocean in 2011. It evolved to WindFloat Atlantic project and now this semi-submersible concept has achieved the precommercial phase with the deployment of three 8 MW wind turbines in Ferrol (Spain) in 2019. Olav Olsen developed in 2011 the conceptual design OO-Star Wind Floater Semi which also achieved a TRL 5 with its installation and commission at MetCentre (Norway). Zhao et al. [4] proposed a novel concept of semi-submersible platform to support the DTU 10 MW wind turbine [21], DUT Semi. It consists of a steel substructure with three columns connected by a tripod that supports the wind turbine and a horizontal pontoon, which reduces fatigue sensitivity, and welding process. Their results show that the proposed design has a reasonably good stability, particularly in the heave motion. Cao et al. [3] put forward SPIC, a new semi-submersible platform to support the DTU 10 MW wind tur-

bine, which is composed of three partially inclined side columns designed for an intermediate water depth of 60 m. This concept demonstrated to achieve great stability under design environmental conditions and proved to have smaller responses under extreme conditions than the standard limited values.

2.2.2 Nautilus Semi-Submersible Platform

Herein, the Nautilus semi-submersible platform is described since it has been the reference configuration for the novel methods developed in this Thesis for the the preliminary design.

The Nautilus platform was developed by Nautilus Floating Solutions [5], which started as a spin-off company of TECNALIA, one of the reference applied research centres in Europe. This platform is composed of four columns symmetrically located on top of a squared ring pontoon base (see fig. 2.5). The transition piece is connected to the platform through the main deck, which is crossed-shape. The columns have a diameter of 10.5 m with a separation between their axes of 54.75 m. The width of the pontoon equals to the diameter of the columns and the height is 1.5 m. The main deck is 3 m height and 10.5 m wide. The total height of the platform is 26 m and, fully charged with water ballast, it drafts 17 m.

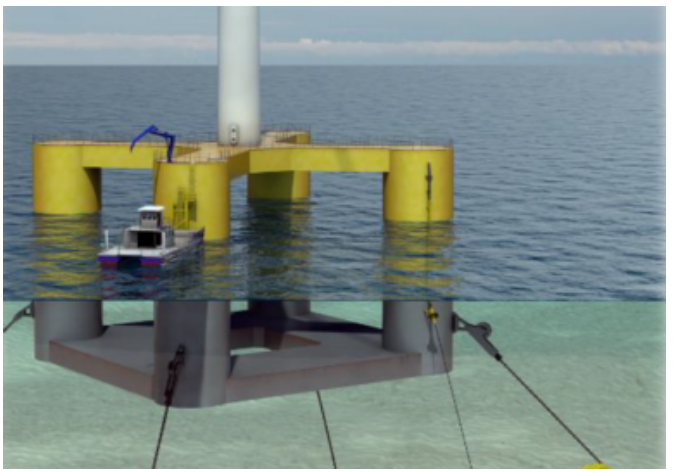

Figure 2.5: Nautilus semi-submersible platform [5].

The structure is made of structural steel S-275 J2 and S-355. It employs an active ballast system to counteract the overturning moment produced by the wind action, which modifies the platform mass, CoG position and mass moment of inertia according to the mean wind speed and direction [2]. It has an overall mass of 7781 t including water ballast in the pontoon

and inside the columns.

Platform Dimensions	
Column diameter	10.50
Column height	26.00
Distance between columns	54.75
Pontoon width	10.50
Pontoon height	1.50
Deck height	3.00
Deck width	10.50
Platform draft	17.00

Table 2.2: Nautilus platform dimensions (m).

2.2.3 Up-scaling Platforms for Bigger Turbines

The stronger and steadier wind speeds, which typically feature offshore sites, favours the installation of larger wind turbines. Currently, there is a dominant trend to increase the power capacity generation in order to reduce project costs by means of increasing the size of the wind turbines. For instance, the three leading wind turbine manufacturers (Siemens Gamesa, Vestas and General Electric) are developing 15 MW wind turbines with the intention to be available by 2024 [19]. The largest wind turbines are operating in Europe, the two 14 MW machines developed by Siemens Gamesa and General Electric, respectively. The Chinese wind turbine manufacturer Ming Yang recently presented a 22 MW wind turbine model, which is set for development between 2024 and 2025. This turbine will have a 310 m diameter rotor. In view of the anticipation of larger turbines in the coming years, understanding the dynamics of floating wind turbines, and analysing the influence of the platform design parameters holds great significance.

The scaling of wind turbines has reached a mature phase, having been extensively researched in onshore technology. However, the scaling of floating substructures to support these continually larger turbines remains unclear, and multiple approaches have been suggested: Sergiienko et al. [22] investigated the deviation between the theoretical and real scaling of the semi-submersible floating platforms and assessed the influence on the dynamic behaviour of the substructure. The relationship between both scaling of the rotor and scaling of the platform is of great importance, and especially how this ratio affects the loads, mass and stability of the FOWT system. The length scale of the wind turbine is defined by the rotor diameter, whereas the length scale of the platform can be defined by the column diameter, distance between the columns, draft, or any other platform characteristic length. Islam et al. [23] presented the design of a

semi-submersible floater aimed to support the DTU 10 MW WT based on the WindFloat design developed for the NREL 5 MW WT. They used the same geometrical scaling factor for both the up-scaling rotor and floater. For the hydrodynamic loads and induced responses, the Froude scaling laws were used. The scaled design was over estimated, showing a large displaced mass and further detail stability calculation is recommended in order to get a more adjusted design. Roddier et al. [24] up-scaled the WindFloat semi-submersible platform from 7 MW WT to 10 MW using the Froude scaling laws. Xu et al. [25] also analysed the dynamics of a scaled OC3-Hywind Spar-type FOWT supporting the DTU 10 MW wind turbine, however, the large and strong non-linear motions of the platform, as well as the coupling effects between the mooring system and support structure need still thorough research. In [2] the Nautilus platform was assessed and up-scaled from the initial concept for 5 MW wind turbine to the DTU 10 MW reference wind turbine. Zhao et al. [26] up-scaled a blaceless semi-submersible platform from the NREL 5 MW wind turbine to the DTU 10 MW in moderate water depths and compared the motion responses and structural dynamics, which were both increased, and especially the former in a reasonable range, proving the feasibility of the up-scaling process. Leimester et al. [27] developed a procedure for up-scaling the OC4-DeepCwind semi-submersible platform which was originally design for the NREL 5 MW wind turbine and was modified to support the IWT-7.5-164 WT. They also concluded that the up-scaled systems resulted too conservative, requiring a more detailed stability analysis afterwards. Furthermore, they recommended to use different scaling factors for each platform component in order to get a more optimised procedure.

2.3 Modelling and Analysis of FOW Platforms

In this section, the modelling and analysis for the design of FOW platforms is exposed. For that purpose, the main components of a FOWT are first described in section 2.3.1 and the typical modelling approaches used for each of them are summarised in section 2.3.2. In particular, the challenges in the hydrodynamic analysis methods will be highlighted since it is where the main research contribution of this Thesis is focused on, and it will serve as an introduction for the next section section 3.3.3, which describe the new tools developed. In addition, the most popular aero-hydro-servo-elastic models used for the design and analysis of FOWT are described, specifically for the initial phases of design.

2.3.1 FOWT Components and Environmental Conditions

The complete system of a FOWT is composed mainly of four components: the wind turbine, the tower, the platform and the mooring system, as shown in fig. 2.6. The global reference system is usually located at the Point of Flotation (PoF), which has the origin at the Mean Sea Level (MSL), the x-axis is aligned with the wave propagation in the zero direction, the z-axis is pointing upwards and the y-axis direction results from the right-hand thumb rule.

The rigid body motions of a FOWT are surge, sway and heave for the traslational motions in the x, y, and z directions, respectively. And the rotational motions around those axes are defined as the roll, pitch and yaw, respectively.

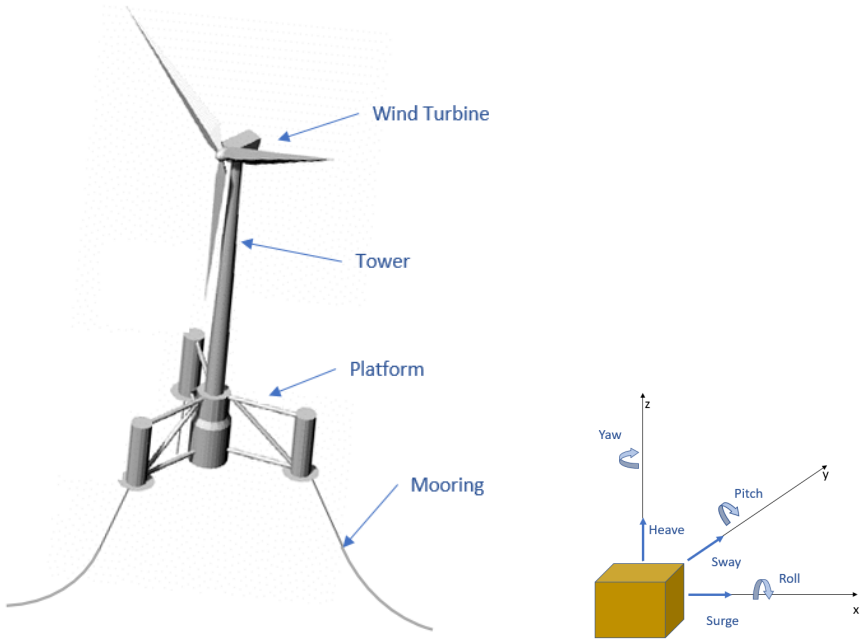

(a) (b)

Figure 2.6: FOWT system main components and rigid motions in 6 DoFs.

FOWTs are deployed offshore, thus they are exposed to hard environmental conditions mainly due to wind and marine loads. The wind acts mainly on the Rotor and Nacelle Assembly (RNA), being the thrust aerodynamic force the responsible for the power generation, and also drag forces on the tower take place. Regarding the marine loads, the wave loads are the main action on the platform and on the mooring lines, although current

and tides might have an important effect on the response.

2.3.2 Modelling Approaches for FOWT

The modelling and analysis of a FOWT will depend on the stage of design, as well as the numerical tool to use, since the level of fidelity, accuracy and computational efficiency varies along the whole design process. During the initial phases of design, where a wide design space is explored, simplified frequency domain based models are frequently used. However, once the preliminary design is defined, time domain coupled numerical tools are used in order to assess the performance under a wide range of environmental conditions.

During the preliminary design phase, simplified frequency domain based response models are usually used, due to the high computational efficiency. These models only consider a few DoFs, that represent the main motions of the structure and are set up with cascading techniques, which consist in pre-computing some information in the advanced models to improve the accuracy of the simplified models. Then, in more advanced stages of design, fully coupled aero-servo-hydro-elastic models are used. These models represent a large number of DoFs and, in order to account for the non-linear effects and transitory periods, time domain based numerical analysis are performed. These advanced models offer a very high level of accuracy, at the expense of high computational cost.

The dynamics of a FOWT are affected mainly by the structural dynamics, the aerodynamics, the hydrodynamics, and the mooring dynamics, and the coupled effect will be considered by the control. The coupling effects between these dynamics are complex to model, so, in order to account for both linear and non-linear loads, fully coupled time domain based numerical tools are commonly used. Each of these effects can be modelled with a different level of fidelity, therefore, in the following subsections, the literature review regarding the different modelling options is detailed. Furthermore, the most popular fully coupled aero-servo-hydro-elastic models are described.

Structural Dynamics

Structural dynamics can be assessed through low, mid or high-fidelity models, depending on the number of degrees of freedom considered, as well as on the consideration of the structure motions and deformations. The simplest representation is considering the FOWT as a rigid body six DoFs: surge, sway and heave translational motions, and roll, pitch and yaw rotational motions. This approach can be suitable for stability analyses during the

early design stage, but not appropriate for representing deformations or non-linear behaviours. Borg et al. presented a method that included the flexibility of a spar foundation in the aero-hydro-servo-elastic simulations adopted in HAWC2 and resulted that the substructure bending mode did not have a significant effect on the motion of the global structure but relevant sectional loads within the platform could depend on the bending motion [28]. It is also quite common to combine system elements with rigid body properties and other with flexible properties. For instance, the platform is commonly modelled as a rigid body, whereas the tower is considered flexible. Pegalajar-Jurado et al. developed the QuLAF (Quick Load Analysis of Floating Wind Turbines) model [29] where they considered the platform as a rigid body, the RNA is represented by a lumped mass and the tower is the only flexible member. Also, Backinsky used a simplified model for a TLP assuming the platform hull as a rigid body and considering the flexibility of the blades, tower and platform tendons [30]. In these cases, modal analysis is performed in order to obtain the mode shapes of certain flexible DoFs, such as the modal deflection of the tower or blades. For that purpose, Finite Element Method (FEM) models are usually used, where the eigenvalue problem is solved, such as ANSYS, ADAMS or BModes, the standalone tool developed by NREL [31]. Furthermore, sometimes relevant non-linear dynamic properties are considered and included in linear models, instead of quasi-static analysis since they trend to under predict restoring forces, although they are computationally more efficient.

In the initial design phases, also reduced DoFs models are used, where only the DoFs of interest are considered. The frequency domain based model QuLAF [29] uses four DoFs, the surge, heave and pitch platform motions and the tower deflection due to the first tower fore-aft bending mode, since it is considered a 2D model. Karimi et al. [32], which also developed a fully coupled frequency domain simplified model, however, does not account for the flexibility of the tower and blades for simplicity, and considered the FOWT as a rigid body of six DoFs. Reduced models have also used for time domain simulations, Sandner et al. [33] used a simplified model of the OC3-Hywind FOWT, representing the structure with four rigid bodies, the wind turbine, tower, platform and station keeping system, and nine DoFs, which demonstrated to reproduce reliably the overall behaviour of the system.

After a wide overview of the existing frequency domain based structural models in literature, the QuLAF, developed by Pegalajar et al. [29], was chosen as reference for the development of the tool presented in this Thesis. The reason for this, was that it is a very simple model, easy to reproduce and the results obtained agreed very well with the time domain simulations

adopted in OpenFAST, the NREL reference tool [14].

Aerodynamics

The aerodynamic analysis is a critical aspect on the design of FOWT. The complex interactions between the turbine blades and the offshore environment results in dynamic loads that can cause fatigue and structural damage. For this reason, accurate modelling and analysis of these loads are essential for optimising power production and ensuring safety and reliability of floating wind turbines. Advanced simulation tools and experimental testing methods are used to model and analyse the effects of the aerodynamic loads, but still are generally difficult to obtain with high accuracy. Similarly to the structural dynamics, here also low to high-fidelity tools for the aerodynamic assessment can be found in literature. The most widely-used approach is the Blade Element Momentum (BEM) theory developed by Glauert [34], based on the actuator disk theory and combines the Blade Element Theory and the Momentum Theory to determine, through an iterative process, the aerodynamic forces and the induced velocities near the rotor. In practice, wind turbine blades are split into a finite number of elements along the span. Due to the rotational motion of the blades, each element forms an annular region where conservation of angular momentum takes place. Therefore, by means of the balance between the axial thrust on the turbine and the change of momentum of the flow passing through the swept annulus, and the balance between the turbine torque with the change of angular momentum in the flow, the induction factors are determined [35]. The computational efficiency of the BEM method is achieved through simplifications that also introduce some limitations. These include static calculations for each iteration, no consideration of the aerodynamic interaction between blade sections, assumes that forces on the blades are determined uniquely by the lift and drag coefficients. Further, momentum balance is assumed to occur only in the plane parallel to the rotor plane. However, corrections such as tip loss and hub vortex models have been developed to address these limitations. Nevertheless, BEM theory is widely used and considered reliable for the calculation of the induced velocity and elemental aerodynamic loads on wind turbine blades.

Several tools use the BEM theory to perform the aerodynamic analysis. AeroDyn [36], developed by NREL, consists of a series of routines that perform the aerodynamic calculations for aero-elastic simulations of HAWT configurations. The lift, drag and pitching moment of the airfoil sections along the wind turbine blades are calculated. Then, considering the turbine geometry, operating conditions and blade-element velocity and location, the inflow wind and the aero-elastic effects, it obtains the distrib-

uted forces along the blades. The most important models used in AeroDyn are the wake models, that calculate the effect of the wake on the turbine rotor aerodynamics. In AeroDyn v14, two different options are available: the widely-used approach BEM theory or the more recently developed Generalised Dynamic Wake model. The latter is not included in the last versions of AeroDyn [37].

High-fidelity aerodynamic methods are based on CFD or Potential Flow (PF), which solve the Navier-Stokes equation numerically and thus, the analysis requires significant computational cost. Sanderse et al. [38] provided a comprehensive review of the CFD methods used for wind turbines.

Hydrodynamics

Herein, just a brief summary of the current mid and high-fidelity methods for the hydrodynamic analysis of the floating structures is given since a more detailed literature review is given in section 3.3.3.

For a very initial stage of design, a stability analysis can be enough, considering just the hydrostatic loads. This is achieved through the Archimedes Law [39]. In order to analyse the dynamic behaviour of the floating body, the hydrodynamic loads are required. These loads are the dynamic forces and moments and can be divided into radiation and diffraction loads and both can be solved separately. The former correspond to the loads caused by the fluid on an oscillating body in still water, and waves are radiated from the body. The latter refers to the loads due to wave action on a fixed body. Airy wave theory is widely used to describe the incident wave field and the wave kinematics can be expressed by means of the wave potential.

The most widely used mid-fidelity methods used for the first and second order hydrodynamic analysis are PF theory base tools and the Morison Equation (ME), or a combination of both. On one hand, PF consist on the calculation of the radiation-diffraction loads acting on the submerged part of the floater. They are solved in the frequency domain and use panel methods, where the number of panels is adjusted to achieve the desired accuracy and computational efficiency. From this analysis, the hydrodynamic coefficients are obtained, which correspond to the radiation damping and added mass, and to the linear wave excitation coefficient. Since potential flow is applied, mooring reactions, aerodynamic loads and viscous loads are not included in this analysis [39]. The most widely used numerical tools where radiation-diffraction analyses can be adopted are WAMIT [40], ANSYS-AQWA [41] or NEMOH [42].

On the other hand, the ME is based on the slender body theory, thus it is limited to slender cylindrical structures which fulfil $D/L_w < 0.2$, being L_w the wave length. This force is decomposed into a drag force proportional

to the velocity and a virtual mass force proportional to the acceleration [43], as given in (2.1) for a differential section of the cylindrical structure.

$$dF = \left(\rho_w (C_a + 1) A (\dot{u_f} - \dot{u_b}) + \frac{1}{2} \rho_w C_D D (u_f - u_b) |u_f - u_b| \right) dz \quad (2.1)$$

where ρ_w is the water density, A is the cross-sectional area of the cylinder, D is the diameter, u_b is the cylinder horizontal velocity and u_f the fluid particle velocity. C_a and C_D are the inertia and drag coefficients that depend on the local flow conditions and mainly on the Keulegan Carpenter Number, KC, which relates the structure diameter with the wave amplitude and period, and on the Reynolds Number, Re. In [44] provide useful tables to obtain these coefficients. In (2.1), the first term corresponds to the inertia term, which includes the Froude-Krylov force and the added mass term. The former, is related to the pressure in the undisturbed wave field; and the latter, represents the force required to accelerate the flow around the cylinder. Th second term in (2.1) corresponds to the drag force that includes the viscous effects. The Morison Equation can sometimes be simplified to a single term, depending on the inertia or drag dominance. The KC number is a useful indicator of the importance of drag versus inertia forces. If $KC < 3$, the inertia force is dominant and the drag term can be neglected. If $3 < KC < 15$ the drag is dominant and it can be linearised [39]. However, there are other situations of KC where none of the terms can be neglected. For semi-submersible structures usually inertia forces dominate over the drag forces, although it depend on each flow situation. The main limitation of the Morison Equation application is that it can only be accurately applied to slender bodies ($D/L_w < 0.2$). For $D/L_w > 0.2$ MacCamy and Fuchs solution can be used [45]. The radiation-diffraction analysis, however, accounts for the whole D/L_w spectra. Furthermore, the ME does not account for the alteration of the incident wave field by the platform.

It is common to combine PF theory with the ME, when viscous effects that can not be neglected, by including a drag term. These methods have shown to provide a good balance between accuracy and computational effort.

Again, high-fidelity CFD tools can be used in order to assess a specific non-linear problems, such a slamming or vortex shedding. Nevertheless, CFD models are computationally very expensive, and therefore are nor suitable for a general analysis of the floater, but more for specific parts.

Mooring Dynamics

The station keeping system or mooring system is what pushes the structure towards its equilibrium position through restoring forces when it is displaced from it. There are different types of mooring systems, although the most common for the semi-submersible platforms is based on catenary lines with drag anchors. The mooring system adds mainly stiffness to the FOWT, with a slight contribution of mass due to the lines weight. The stiffness of the mooring lines is dependent of the catenary shape, and therefore, it is a non-linear matrix. Mid-fidelity methods use quasi-static analysis (QS) due to their computational efficiency, and they have shown to agree very well with the true system dynamics for small displacements around the equilibrium position and small wave amplitudes. The QS analysis works better for taut mooring systems since the restoring force is proportional to the axial strain, however, it can also be applied to catenary moored configurations assuming certain simplifications. Despite, this method is quite useful for the preliminary design stage adopted in the frequency domain. When the platform displacements and velocities become important, the dynamic effects, such as inertia and hydrodynamic drag and added mass loads on the lines, might be necessary in order to have an accurate prediction of the structure behaviour. Furthermore, dynamic effects on the mooring lines are of high importance for fatigue loads and ultimate loads assessment. In that case, FEM models are commonly used, particularly, the mooring lines are discretised into finite elements and the equations of the catenary are solved using, for example, the equations given by Faltinsen [46] for each floater position. Hall et al. [47] evaluated the importance of the mooring system approaches and concluded that the QS methods provide reasonably accurate response of the platform, but lead to important inaccuracies on the FOWT structure dynamics under extreme load conditions. There are currently several commercial and open tools that perform dynamic analysis of the mooring systems, such as OrcaFlex or the standalone open source codes from NREL, MoorDyn And MAAP+.

Aero-hydro-servo-elastic Tools

FOWT are complex systems where the above explained four main dynamics interact together and coupled effects occur. Depending on the design phase, mid-or high-fidelity methods are used, and a wide combination of fidelity levels can be assessed together. During the initial design stage, it is common to use reduced structural FOWT models combined with cascading techniques, where simplified models are fed with accurate data obtained from high-fidelity methods. The main objective is to accurately capture

the most important physical phenomena, while keeping the compromise with a reasonable computational cost. Then, for more advanced design phases, time domain simulations are commonly used. These techniques are generally mid-fidelity software and the most popular among designers are FAST, also OpenFAST, developed by NREL in the United States of America [14], which is an open source code composed of several modules able to solve the coupled non-linear aero-hydro-servo-elastic and mooring analysis; HAWC2 [15] developed by the Technical University of Denmark (DTU) which is an aero-elastic model coupled with a hydrodynamic model in the time domain; and, BLADED [16] that was developed by Det Norske Veritas (DNV), which coupled with the hydrodynamic and mooring modules from SIMA [48], analyse the global dynamics of the FOWT [49]. Both FAST and BLADED use frequency domain tools to perform the hydrodynamic analysis, such as the PF solvers ANSYS-AQWA [41], WAMIT [40] or NEMOH [42]. These commercial software tools are considered mid-fidelity solvers and the time domain simulations enable to account for the non-linear effects, however, this leads to longer simulations and higher computational effort. The level of accuracy of these type of solvers might not be necessary for the initial stages of FOWT design, thus, the choice of the numerical tool will depend on the trade-off between accuracy, fidelity and computational cost. In table 2.3 a summary of the most used aero-hydro-servo-elastic tools used in offshore wind are given.

Code	**Developer**	**Structural**	**Aero**	**Hydro**	**Moor**
FAST /OpenFAST	NREL	Modal /FEM	BEM	PF/ME	QS/Dyn
HAWC2	DTU	Modal /FEM	BEM	PF/ME	QS/Dyn
BLADED	DNV-GL	Modal /FEM	BEM	PF/ME	QS/Dyn
SIMA	SINTEF	FEM	BEM	PF/ME	QS/Dyn

Table 2.3: Aero-servo-hydro-elastic tools used in offshore wind.

During the preliminary stages of design, usually low-fidelity models are used to examine operational and extreme conditions. In literature, several numerical tools can be found for the initial stage of the FOWT design [49]. For instance, Hegseth and Bachynski [50], Karimi et al. [51] and Pegalajar-Jurado et al. [29] developed in-house frequency domain models that are publicly available. Hegseth and Bachynski [50] developed an efficient design method for the evaluation of two spar designs for floating wind that was validated against results derived from time domain analysis. A simplified model of three DoFs was used: the platform surge and pitch and the first tower bending mode. The aerodynamic loads were obtained from time domain simulations and the hydrodynamic loads, due to the simplicity of the spar geometry, were approached using the MacCamy-Fuchs Theory

[45]. The frequency domain model showed reasonable agreement with the fully coupled non-linear time domain model for both fatigue and extreme response. Karimi et al. [51] also developed a frequency domain model considering a flexible moored platform and rigid tower and blades, although the model has the capability to include the structural DoFs. Again, the aerodynamic loads were obtained using the time domain numerical tool FAST and this time WAMIT was used for the hydrodynamic characteristics of the floater. This frequency domain model was used for evaluating the cost of the different classes of floating platforms. Pegalajar-Jurado et al. [29] developed a similar frequency domain model representing four DoFs: the platform surge, heave and pitch motions and the first tower fore-aft bending mode. The model was denoted QuLAF, which is been previously mentioned in section 2.3.2, and it consists of a planar model that assumes aligned wind and wave conditions. The aerodynamic loads were also obtained from time domain simulations adopted in FAST and the hydrodynamic loads were obtained from the frequency domain based PF solver, WAMIT. For the validation of the model, the semi-submersible floating wind turbine used in the LIFES50+ project [2] was used, supporting the DTU 10 MW WT, and the structure motions were compared to those obtained with FAST. The existing frequency domain numerical tools still need to cascade some inputs from the validated state of the art numerical software: the aerodynamic loads from BEM based tools and the hydrodynamic loads from the PF solvers. In the preliminary design stages, a wide design space of platform concepts are analysed and, therefore, a large number of simulations need to be performed. This process can be very time consuming and, as an alternative to the high computational cost demanded by the time domain analyses, usually frequency domain numerical approaches are used to evaluate the FOW structures response. However, many inputs on the frequency domain methods are obtained by means of other more advanced tools which require high computational effort, and thus, make the whole design process less efficient [29], [32], [52].

2.4 Hydrodynamic Analysis in the Early Design of FOW Substructures

When designing a FOW platforms, a correct characterisation of platform hydrodynamic properties is required. In the initial stages of design, generally only the first-order wave excitation loads are considered, in order to save computational effort. However, it is known that the second-order wave loads, specially low-drift forces, can be significant for catenary-moored structures, such as semi-submersible platforms. In this section, a more de-

tailed literature review is provided regarding the methods used for the first- and second-order hydrodynamic loads calculation in the early design phase of the FOW substructures.

2.4.1 First-Order Hydrodynamic Analysis

As in every floating body, hydrodynamics will be affected by the radiation and diffraction loads. In the initial stages of design, usually only the first-order loads are considered. These are also known as the hydrodynamic coefficients, which are the added mass, radiation damping, and linear excitation loads. They are frequency-dependent values, thus, the analysis of the FOWT response in the frequency domain can be easily adopted. It has already been mentioned in section 2.3.2 that the radiation-diffraction loads are usually obtained through PF theory based tools such as *AQWA, WAMIT* or *NEMOH*. In addition, the Morison Equation can be used for slender structures, or combined with the latter in order to include viscous effects. Regarding to chose which method to employ, designers constantly look for the trade-off between accuracy and computational cost, striving to develop effective and trustworthy tools that can be used during the preliminary design stages. Optimisation routines are commonly implemented to analyse the platform response so as to get the optimal design in terms of cost. It is common practise to integrate panel codes to perform the hydrodynamic analysis to obtain the dynamics of each platform solution. Consequently, this process can result in lengthy simulation times, particularly when looping a significant number of platform designs. Karimi et al. [53] developed a multi-objective optimisation function using a frequency domain dynamic model that was fed with the hydrodynamic data obtained from *WAMIT* [40]. Also, Hall et al. [39] developed a basis function approach that represents the design space in terms of hydrodynamic performance instead of geometric details. However, this function demonstrated its validity for similarly-shaped geometries only and it also required a previous processing of the coefficients in *WAMIT*. In order to address the high computational cost of including the potential flow solver in the optimisation loop, Ferri et al. [54] evaluated off-line a grid of platforms varying the column diameter, draft and radius of the platform to be interpolated online, achieving an important computational cost reduction, although still 784 platforms were evaluated in *AQWA* [41] for the accurate definition of the fitted multidimensional functions, which can take days of simulation.

In literature, efforts have been usually focused on efficiently calculating hydrodynamic forces on isolated vertical cylinders, whereas comparatively little research has been developed regarding neighbouring cylinders and their impact on wave loading, which is important for offshore structures

with multiple cylindrical supports. P. McIver and D.V. Evans [55] published a large-spacing approximation for the estimation of wave forces on a group of columns of fixed vertical cylinders, where the scatter diverging waves are replaced by plane waves. Similarly and applied to both diffraction and radiation loads, A. N. Williams et al. [56, 57] examined the hydrodynamic interactions of an array of cylinders simulating a TLP using equivalent plane waves and non-planar correction terms, allowing for the determination of the hydrodynamic interactions using only the characteristics of an isolated cylinder. These approaches still require solving the velocity potential integrals, which have an expensive computational cost.

2.4.2 Second-Order Hydrodynamic Analysis

Second-order hydrodynamic loads on semi-submersible floaters are commonly obtained through radiation-diffraction analysis by means of panel codes, but they require high computational effort for the calculation of the full quadratic transfer functions (QTF). In addition, once the QTFs are obtained, their application to obtain the load time series for a certain wave spectrum requires the evaluation of a double sum at cost $O(N^2)$, with N being the number of frequencies. This calculation can lead to a high computational effort when long time series are assessed, which is acceptable for a validation process and for the loads calculation of a known design, but is not feasible for preliminary design optimisation. For this reason, usually, second-order loads are not included in the numerical models used in preliminary analysis. To simplify and accelerate the calculation of the second-order hydrodynamic loads, several approximations have been developed. The majority of them consider simplifications of the full QTF computation. The Newman approximation [58] is one of the most known, used for modelling the slow drift problem of moored floating vessels. For instance, Coulling et al. [59] obtained the second-order wave forces on a semi-submersible through Newman approximation and observed very good prediction of the response in surge. However, it is not always accurate, compared to the full QTF approaches, especially in shallow waters. See for example Duarte et al. [60]. Another approach is the white noise approximation proposed by Crandall and Mark [61], which has shown to agree very well with the full QTF computation. The main condition to ensure its accuracy is that the second-order motion spectrum must be narrow banded. Through this methodology, the force spectrum must be computed just for the pairs of frequencies whose difference is equal to the natural frequency of the drift motion. These methods provide a substantial reduction of the computational effort, although the QTFs still need to be obtained through radiation-diffraction analysis which is usually time consuming. As an al-

ternative and fast method, hydrodynamic loads have been commonly evaluated through the Morison's equation under the assumption of slender body theory. To this end, a semi-submersible floater must be decomposed into its individual members. Ishihara et al. [62] used an augmented Morison's equation to evaluate the dynamic response of a semi-submersible FOWT and observed that Morison's equation still needed further improvements. Consequently, they determined correction factors for that specific floater for the inertia and drag coefficients from force oscillation tests to account for the interaction between members. This method, however, is not valid for a generic floater since the correction factors were obtained for that specific floater geometry. H. Bredmose and Pegalajar-Jurado also developed a fast method for calculating the second-order hydrodynamic loads on slender bodies. This method was applied to a vertical cylinder [63, 64] , and the second-order surge force and pitch moment were accurately predicted. The method is based on the Morison and Rainey force model, and thus it is limited to slender bodies. The main advantage of the method resides on the reduction of computational cost in the second-order hydrodynamic load calculation through the eigenvalue decomposition of the QTF, and further modal truncation. Through this method, with only 8 modes the second-order surge force was accurately obtained between 400-800 times faster than the conventional methods. This method, referred to as accelerated method, has been extended in this Thesis for the application on semi-submersible platforms. For that purpose, new formulation was developed and it will be detailed in chapter 5.

Second-Order Hydrodynamic Loads and Mooring Design

The action of the waves on a floating structure is non-linear and it can be described based on a perturbation method considering effects in different orders of magnitude with respect to the wave amplitude. This procedure is valid as long as wave amplitude and structure motions are small enough. The analysis of offshore systems response is normally performed considering only first- and second-order effects. Since the second-order forces are significantly smaller than those related to first order, their effects are only relevant when they are amplified by a resonant motion such as a floating platform horizontal motion in surge, sway, and yaw degrees of freedom. For a floating semi-submersible platform moored by catenary lines, the natural period of platform horizontal motion is usually quite higher than those of wave components with significant energy and, therefore, only the second-order forces related to difference-frequency, or low-frequency components, are relevant ('slow-drift' forces). These forces are due to the interaction between waves of different frequencies, and when the difference-frequency

of a pair of sinusoidal wave components with significant energy is close to a natural frequency of the moored platform motion (typically the above mentioned horizontal motions), this platform motion is amplified and the mooring system will receive higher forces, in addition to the zero-frequency effects also induced by waves ('mean drift' forces). This means that second-order loads must be considered when designing a mooring system of the floating platform, and the platform horizontal motion response is the result of these second-order wave loads and the mooring system stiffness in these horizontal degrees of freedom [65]. Zhang et al. [66] examined the effect of the second-order hydrodynamic loads on the response of three different semi-submersible platforms supporting the NREL 5 MW WT. They confirmed that the second-order difference wave loads can excite the resonance, especially in the platform pitch motion. Xu et al. [67] also studied the effect of the low-drift forces on the response of semi-submersible platform and concluded that they were one of the main focusing points in the platform motion, together with the water depth. They found that the platform motion response generally increased when the second-order difference-frequency loads used full QTF methods. Furthermore, they found that the wave frequency and low-frequency dynamic behaviour were not strong compared to the mean static force due to wind and wave. Despite, the second-order wave forces could induce resonant motions and increased the response maximum values and standard deviations.

Chapter 3

Preliminary Design and Modelling of FOWT

In the present chapter, the proposed frequency domain based method for the preliminary design of Floating Offshore Wind (FOW) substructures is described, which is denoted as *FD Tool*. First, the site assessment and environmental conditions are detailed in section 3.1. Then, each of the components of the Floating Offshore Wind Turbine (FOWT) are described, as well as the floater parameterisation utilised in this work, in section 3.2. Finally, in section 3.3 the structural, aerodynamic, hydrodynamic and mooring models used in this study are explained. In addition, it is provided a visual scheme that introduces the two novel methods developed in this Thesis, which are focused on the hydrodynamic analysis, and how they are assembled to the frequency domain response model is explained.

3.1 Site and Environmental Conditions Assessment

The site where a floating offshore wind farm plans to be deployed determines the environmental conditions to which the FOWTs will be subjected. Offshore sites are quite hard environments, thus it is important to carry out a deep assessment in order to define an appropriate design according to the expected conditions. Furthermore, having a thorough grasp of wind and wave phenomena enables the implementation of a precise modelling approach. A brief explanation of the wind and wave physical characteristics are given in section 3.1.1. Every location exhibits distinct wind and wave conditions due to factors such as proximity to land, the presence of mountains, local atmospheric patterns, water depth, seabed topography, ocean currents, and other site-specific characteristics. These factors contribute to specific probabilities regarding the direction and intensity of both wind

and waves. In this context, a particular site has been selected for the case study, and essential site-specific information is presented in section 3.1.2. These wind and wave conditions have a direct impact on the external forces acting on the floating structure and the power generation of the offshore wind farm. Each site may experience various wind and wave combinations, such as operational conditions and ultimate scenarios. The Design Load Cases (DLCs) used for the evaluation of the response of the FOWT, and consistently used throughout this study, are detailed in section 3.1.3.

3.1.1 Wind and Wave Excitation

Wind is considered an ergodic process, what means that it can be represented through statistic measures. The wind speed has three components: longitudinal, lateral and vertical direction. The former is the main propagation direction, whilst the remaining two have generally significantly lower values. In this Thesis, the lateral and vertical components were neglected. The wind speed suffers important variations with time and it can be quite different depending on the time scale. For this reason, it is important to report the wind speed for a specific period of time. Commonly, 10-minute or 1-hour periods are used. Wind rarely blows with a steady wind velocity, it is not but a simplification. However, wind is a turbulent flow and it is usually represented by its mean speed and the standard deviation of the fluctuating values. The ratio of these two variables results in the turbulence intensity, I, as given in (3.1).

$$I = \sigma_u / \bar{U}_{ref} \tag{3.1}$$

where σ_u is the standard deviation of the wind speed and $\bar{U}_{ref}$ is the mean wind speed at a reference height. This relation of the wind speed with height, z, is also another characteristic of the wind process, it is called wind shear and it is due to the effects of the viscous boundary layer. In order to get the mean wind speed at a certain height from the ground, two formulations are usually used: the logarithmic and power law. In this study, the latter formulation has been applied and, thus, it is given below.

$$\bar{U}(z) = \bar{U}_{ref} \left(\frac{z}{z_{ref}} \right)^{\alpha} \tag{3.2}$$

Here, $\bar{U}(z)$ is the mean wind speed at height z from the ground, or from the Mean Sea Level (MSL) for offshore conditions, and U_{ref} the mean wind speed at the reference vertical distance z_{ref}. The power law coefficient used is the one recommended for offshore sites, which is denoted with α and has the value of 0.14.

There are several wind spectra definitions for the design of structures subjected to wind loads. However, not all of them are suitable for offshore conditions, particularly, Davenport or Harris spectra have shown to have questionable application in floating structures [68]. Alternatively, for large floating structures, the use of Kaimal or API spectra are recommended. In this work, the Kaimal spectrum was applied for the calculation of the wind excitation, and it is given by (3.3).

$$S_u(f) = \frac{4\sigma_u^2 L_u/\bar{U}_{ref}}{(1+6fL_u/\bar{U}_{ref})^{5/3}} \tag{3.3}$$

Where $S_u(f)$ is the wind Kaimal spectrum, L_u is the integral scale parameter, and f is the frequency.

TurbSim tool, developed by NREL [17], was used to generate the turbulent wind speed signals. This tool is a stochastic full-field turbulent wind simulator and provides the time series of the three-component wind speed vectors at a given height, for the given time step and simulation time. The TurbSim output file is read by InflowWind, used for the calculation of the wind loads through AeroDyn [36].

Waves can be generated in many different ways, such as wind, although there are other types of waves that are composed of multiple non-linear waves together, each of them propagating in different directions. The waves generated by wind can be represented as a combination of regular waves of different amplitude and period values, propagating in different directions. Real waves are very complex to model, thus several simplifications can be considered. The most common way of studying waves is through Airy's theory, which assumes linear relationship between the wave kinematics and the wave height. In addition, unidirectional waves are usually considered, where all the combination of regular waves are assume to propagate in the same direction.

Irregular waves are assume to follow an ergodic Gaussian process, thus they can be defined through a spectrum. The most used wave spectra are the Jonswap and the Peirson-Moskowitz (PM) spectra, which both are characterised by the significant wave height (H_s) and the wave peak period (T_p). The main difference between both spectra resides in the peakness parameter, which is equal to unity for the PM spectrum, resulting in a lower peak of energy at the wave peak period.

3.1.2 Site Description

For this study, the Gulf of Maine (GoM), located at the North Atlantic ocean, was chosen for the installation of the FOWT case study. A relevant source of information is available due to the presence of three measurement

buoys which provide wave and wind climate data, such as the wave height and wave period every half-hour, and 10-minute mean wind speed values, wind direction and gust. Furthermore, current mean values and other environmental characteristics can be obtained (e.g.,water temperature, salinity, density and air temperature), and it is a realistic site for the deployment of a floating offshore wind farm [6]. It represents medium metocean conditions with a 50-year significant wave height of 10.9 m and peak periods between 9-16 s. It has a mean water depth of 130 m with sand-mud-rock seabed. The average wind speed at 100 m height is 9.8 m/s, making it suitable for the DTU 10 MW WT, which has a rated wind speed of 11.4 m/s, and also an appropriate site for the IEA 15 MW WT, whose rated wind speed is 10.59 m/s. The water density can be assumed 1025 kg/m^3.

In fig. 3.1 the probability distribution of the annual mean wind speed at the measuring buoy which is at 4 m above from the MSL, is shown. The long-term probability distribution can be represented by a Weibull distribution with a scale coefficient of 6.214 and shape coefficient of 1.701. The annual average wind speed at the DTU 10 MW WT hub height (119 m) is 10.02 m/s. Kaimal spectrum model is considered as the most suitable for the wind spectral density characteriSation [10].

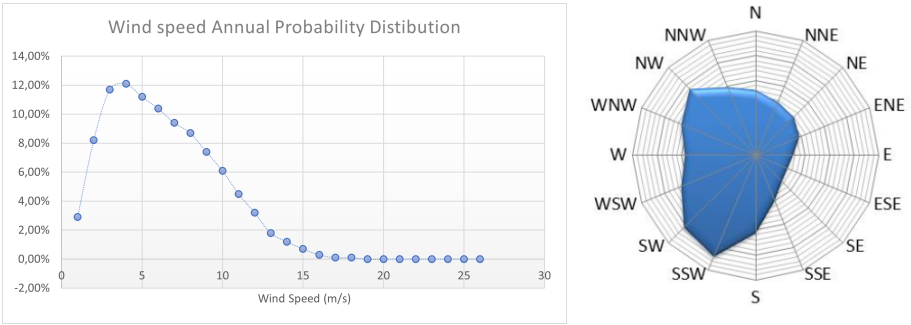

(a) (b)

Figure 3.1: Data from the NOAA buoy EO1 at 4 m from MSL: (a) Annual probability distribution (%) for 10-minute mean wind speed. (b) Wind rose of GoM. Data from [6].

Regarding the marine conditions at the GoM, in fig. 3.2 the scatter diagram obtained from the data found in [6] is given, which represents the probability of occurrence of each certain significant wave height and wave peak period combinations. The most accurate wave spectrum for this site is the PM model, since is was observed that the wave climate is not very bound to the wind conditions, being the swell sea the wave climate driver. Taking into account the scatter diagrams regarding the combined wind and

wave conditions, a 3^{rd} order polynomial equation was found to be the best approach for the wind-wave correlation in GoM [6].

		Tp (s)								
		1<Tp<2	2<Tp<3	3<Tp<4	4<Tp<5	5<Tp<6	6<Tp<7	7<Tp<9	9<Tp<11	Tp>11
Hs (m)	<1	0,03%	4,69%	7,29%	7,02%	3,91%	5,91%	13,49%	6,27%	0,08%
	1<Hs<2		0,00%	0,92%	6,64%	6,85%	7,32%	7,90%	8,36%	0,16%
	2<Hs<3			0,00%	0,09%	0,55%	2,71%	2,91%	3,31%	0,15%
	3<Hs<4				0,00%	0,01%	0,12%	1,11%	1,04%	0,08%
	4<Hs<5						0,00%	0,19%	0,47%	0,04%
	5<Hs<6							0,02%	0,21%	0,01%
	<Hs<7								0,08%	0,01%
	7<Hs<8								0,02%	0,01%
	Hs>8								0,00%	0,00%

Figure 3.2: Scatter diagram for the Gulf of Main [6].

3.1.3 Design Load Cases

When designing FOWTs, it is of great importance to know which are the driving load cases. The International Electrotechnical Commission (IEC) defines in [69] the combined wind and wave conditions and wind turbine operation condition for FOWT design. In this Thesis, a set of representative load cases were defined based on the LIFES50+ project [2], used to assess the dynamic response of the case study FOWT. These are given in table 3.1, where six of them correspond to normal operation conditions, while the other correspond to ultimate conditions. The turbulent wind was modelled with the Kaimal spectrum and the irregular waves follow the PM spectrum. The wave conditions for ultimate load cases correspond to 50-year significant wave height and the upper limit of the wave peak period. The wind speed values refer to the mean speed at the wind turbine hub height.

ID	U_{ref}	H_s	T_p	**Condition**
DLC1	7.1	1.67	8.0	Operational
DLC2	10.3	2.20	8.0	Operational
DLC3	13.9	3.04	9.5	Operational
DLC4	17.9	4.29	10.0	Operational
DLC5	22.1	6.20	12.5	Operational
DLC6	25.0	8.31	12.0	Operational
DLC7	7.1	10.90	16.0	Ultimate
DLC8	12.0	10.90	16.0	Ultimate
DLC9	22.1	10.90	16.0	Ultimate

Table 3.1: DLCs for the GoM defined by the mean wind speed (m/s), and the wave significant height (m) and peak period (s).

3.2 Design of FOWT

In this section, each of the FOWT components, which have been previously briefly introduced through fig. 2.6, are here thoroughly described and the platform design space, as well as the parameterisation employed in this work, are outlined. FOWT are composed of four main components: the wind turbine, the tower, the floating platform and the mooring system anchored to the seabed. They are complex systems since they are subjected to the offshore hard conditions where many load interaction effects take place, such as wind, wave, current or ice. Subsequently, the design procedure and parameters considered in this work for each of the FOWT components are comprehensively presented.

3.2.1 Wind Turbine

In this Thesis, two wind turbines are examined: the DTU 10 MW WT and the IEA 15 MW WT. The former, designed as a scaled-up version of the NREL 5 MW WT, offers ample information as documented in [21]. Additionally, this turbine played a pivotal role in the LIFES50+ project's inception [2], which served as the foundation for this study's development. The latter results from a collaborative effort between the IEA, NREL, and DTU, serves as a benchmark wind turbine for both the industry and research community, anticipating the next generation of larger wind turbines [70].

Both wind turbines serve as reference models, and there is publicly available information detailing their dimensions, structural characteristics, and performance. The essential data regarding the wind turbines required for this study is condensed in table 3.2. In this context, RNA stands for the Rotor and Nacelle Assembly, CM^{TT} represents the centre of mass relative to the tower top (TT), and I^{TT} denotes the moment of inertia around the TT axis indicated in the subscript.

Parameter	**DTU 10 MW**	**IEA 15 MW**
RNA mass	676 723	949 781
RNA CM^{TT}	[-0.939, 0, 2.789]	[-6.500, -0.090, 4.517]
RNA I^{TT}_{xx}	1.659×10^8	3.780×10^8
RNA I^{TT}_{yy}	1.062×10^8	2.560×10^8
RNA I^{TT}_{zz}	1.014×10^8	2.370×10^8
H_{hub}	119	150

Table 3.2: Wind turbines mass and inertia properties. (Units: kg, m)

The DTU 10 MW WT played a central role in the majority of the work. It served as the validation benchmark for each of the hydrodynamic mod-

ules, elaborated in chapter 4 and chapter 5. Additionally, it was utilised to validate the comprehensive frequency domain design tool in chapter 6, and to evaluate the effect of the mooring system on the platform design in section 7.2. The IEA 15 MW WT was selected as a case study to investigate the impact of up-scaling wind turbines on the design of the floating platforms in section 7.1, with the DTU 10 MW WT as reference for the comparison.

3.2.2 Tower

Here, a description of the towers utilised to support each of the wind turbines mentioned in the previous section is provided. The tower properties for the DTU 10 MW WT align with those employed in the LIFES50+ project, as outlined in [2]. As for the tower supporting the IEA 15 MW WT, the data from the floating tower utilised in the Volturn US-semi-submersible platform was extracted, as documented in [71]. It is worth noting that both towers employed in this study deviate from the literature due to variations in the outer and inner diameter along the tower's height, which were determined through linear interpolation. A concise summary of the properties necessary for the implementation of this research can be found in table 3.3.

Parameter	**DTU 10 MW**	**IEA 15 MW**
Tower Mass	879 381	1 263 000
Tower Centre of Mass	[0, 0, 54.908]	[0, 0, 70.000]
Tower Height	107.000	129.386
Tower Top Height	114.667	144.386
Tower Base Height	7.667	15.000
Tower Top Diameter	5.500	6.500
Tower Base Diameter	10.500	10.500
Tower Top Thickness	0.037	0.021
Tower Base Thickness	0.040	0.082
Damping ratio 1^{st} fore-aft mode	0.019	0.010
1^{st} fore-aft natural frequency	0.405	0.496
1^{st} side-to-side natural frequency	0.400	0.483

Table 3.3: Tower structural properties. (Units: kg, m, s)

Parameter	**Symbol**	**Value**
Steel Density	ρ	8500
Young Modulus	E	2.10×10^{11}
Shear Modulus	G	8.08×10^{10}

Table 3.4: Steel material properties. (Units: kg, m, s)

The natural frequencies given in table 3.3 correspond to the clamped

tower configuration and in fig. 3.3 the first and second fore-aft mode shapes of the DTU 10 MW WT floating tower are shown. Note that they are normalised with respect to the tower top modal displacement. The eigenvalue problem was solved using BModes, the NREL developed FEM code for the calculation of dynamically coupled modes in beams [31]. For that purpose, some of the tower distributed properties were required, such as the inertia and the stiffness of each discretised section. The tower top mass properties were set according to the wind turbine described in section 3.2.1. Note that the values given in table 3.3 do not include the effects of the floating substructure, since the mode shapes used in this Thesis correspond to the condition of clamped tower.

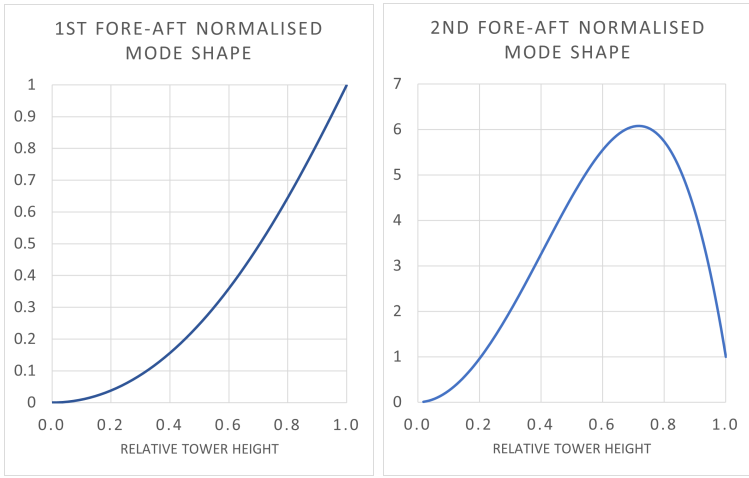

(a) (b)

Figure 3.3: DTU 10 MW WT clamped tower fore-aft normalised modal displacements. (a) 1^{st} mode (b) 2^{nd} mode.

The number of sections into which discretise the tower would be decision of the designer. In this particular study, 56 sections were used for both towers and the distributed mass and inertia, and stiffness properties were obtained for each section. These distributed properties align with the specifications needed for the tower input file utilised by OpenFAST, specifically the ElastodynTower module.

3.2.3 Semi-Submersible Platform

In this Thesis, a wide platform design space was defined in order to perform a comparative analysis of the dynamic response of each FOWT, which served to validate the present frequency domain design tool. As a refer-

ence case study, the Nautilus semi-submersible platform described in the LIFES50+ project [2] was used, which has been previously described in section 2.2.2. It is a symmetric floating substructure composed of four columns connected through a square-shaped ring pontoon at the columns base and by a X-shaped main deck at the columns top. The transition piece that connects the platform to the tower is embedded in the main deck central position, as shown in fig. 3.4. The floater is characterised by the columns diameter, D, by its draft, d and by the distance between the columns, s. The columns have a total length of h_c, without considering the pontoon height, where the submerged part of the columns is defined as the *lower column*, h_{lc}, and the freeboard is defined as the *upper column*, h_{uc}. The main deck is defined by the width of the rectangular braces, w_d, and its height h_d. The pontoon base is characterised by its width a and by its length measured through the distance between the width central axes, s, and by its height h_p. To attain hydrostatic stability, the pontoon is filled partially or completely with water, and, as needed, a portion of the columns is also filled with water to serve as ballast. The height of the water that enters the columns is denoted as h_{wb}, as shown in fig. 3.4. In table 3.5 the description and nomenclature of the design parameters required for the platform structural properties calculation are given.

Symbol	**Parameter**
h_d	Main deck height
w_d	Main deck width
l_d	Main deck length
D	Column diameter
s	Distance between column axes
h_{uc}	Upper column height or freeboard
h_{lc}	Lower column height
h_c	Column total height
h_p	Pontoon height
l_{out}	Pontoon outer length
l_{in}	Pontoon inner length
a	Pontoon width

Table 3.5: Platform design parameters definition and nomenclature.

The structural properties of the platforms, such as mass and inertia, and the hydrostatic stiffness were computed in a calculation spreadsheet taking into account the steel mass of each platform member, based on steel weights per volume given in table 3.6. Then, the amount of water ballast was determined in order to achieve hydrostatic stability. The centre of mass of the platform was defined considering the overall mass.

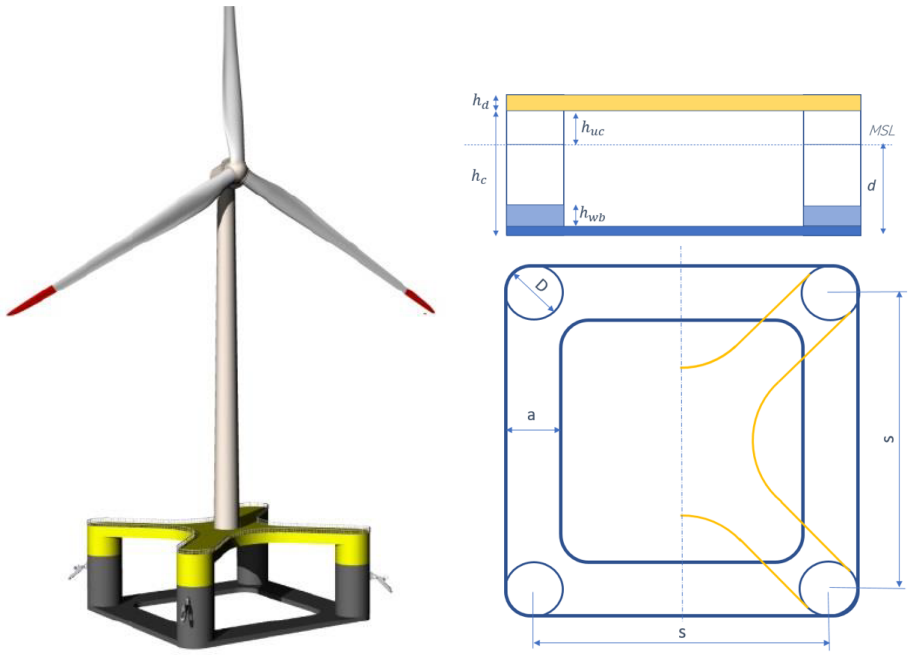

(a) (b)

Figure 3.4: Nautilus semi-submersible platform. (a) LIFES50+ [2] FOWT (b) Parameterisation.

Parameter	Symbol	Value
Upper Column and deck	ρ_{uc}	120
Lower Column	ρ_{lc}	185
Pontoon	ρ_p	230

Table 3.6: Weight densities (kg/m^3) for the platform structural steel.

To simplify the design process and streamline the number of parameters involved, several key assumptions and relationships were implemented. Firstly, the height of the pontoon, the height of the main deck, and the freeboard of the columns were maintained as constant values across all design configurations. Furthermore, the columns were placed at the corners of each pontoon base, which allowed for the spacing between columns to be linked to the length of the pontoon. Additionally, the diameter of the columns was set equal to the width of the pontoon. These simplifications and interrelated parameters served to facilitate the design process, and for the validation of the present design tool. Below, the mentioned relationships and assumptions are summarised.

$$
\begin{aligned}
h_d, h_p, h_{uc} &= constant \\
w_d = w_p &= D \\
l_d &= \frac{\sqrt{2}}{2}(s - D) \\
l_{out} &= s + D \\
l_{in} &= s - D \\
d &= h_{lc} + h_p
\end{aligned}
$$

Definition of the Platform Design Space

To establish a practical and realistic design space, conventional design criteria have been taken into careful consideration. Considering the primary objective of designing a FOW substructure, which is to endure challenging offshore conditions while maintaining cost competitiveness (e.g., minimising the LCOE), the defined requirements prioritise the reduction of construction and material costs while simultaneously maximising power production. To achieve this goal, efforts are made to minimise factors such as steel mass, tendon pretension, and displacements. It is worth noting that in this study, certain simplifications have been made regarding cost considerations, but they suffice for validating the proposed methodology. For instance, installation costs are assumed to be uniform across all designs, and material costs are essentially represented by the platform's steel mass. These simplifications help streamline the design process while ensuring robustness in the face of offshore challenges. The design criteria that the FOWT must fulfil have been defined according to the common standards used for the FOWT design [72, 73, 74]. Since this methodology is aimed for the preliminary design stages, conservative thresholds have been chosen regarding the maximum response motions. Below, the design requirements are listed. The following design requirements are applied, based on the data found in literature:

Design Thresholds		
$0.3h$	m	Maximum surge displacement in operational conditions.*
10	deg	Maximum pitch angle in operational conditions.
$0.18g$	m/s^2	Maximum nacelle acceleration in operational conditions.**

Table 3.7: Thresholds defined for the FOWT response.
* h: water depth.
** Value extracted from COREWIND project. g: gravity acceleration.

In Ghiogo et at. [73] also the material cost and a cost function for a preliminary design phase are given: for a S355 steel with density 8500

kg/m^3, the cost is 3000 Eur/t. However, in this work the cost of the platform will be referred in terms of steel mass since the main objective is to compare the different platforms from the design space. A more detailed insight of the factors influencing the FOWT cost is out of the scope of this Thesis.

In table 3.8, the design space of the semi-submersible platforms based on the reference Nautilus floater are defined. Each table corresponds to the platform designs with the same column diameter values. As before mentioned, there are some parameters whose dimensions remain constant for all the platforms considered. These values correspond to the platform deck height of 2 m, the columns freeboard with 6 m and the pontoon height of 1.5 m.

According to the constraints above defined, the evaluation of the various platform solutions was based on three key parameters: the column diameter, the spacing between columns, and the platform draft. A comprehensive comparison was conducted, encompassing a total of thirty-three distinct platform configurations. These configurations are generated by combining different ratios of column diameter to draft and column diameter to the distance between columns, providing a comprehensive assessment of the design space.

ID	**D1**	**D2**	**D3**	**D4**	**D5**	**D6**	**D7**	**D8**	**D9**	**D10**	**D11**	**D12**
D	10	10	10	10	10	10	10	10	10	10	10	10
s	50	50	50	55	55	55	60	60	60	70	70	70
d	11	15	20	11	15	20	11	15	20	11	15	20

ID	**D13**	**D14**	**D15**	**D16**	**D17**	**D18**
D	11	11	11	11	11	11
s	50	50	50	55	55	55
d	11	15	20	11	15	20

ID	**D19**	**D20**	**D21**
D	12	12	12
s	50	50	50
d	11	15	20

ID	**D22**	**D23**	**D24**	**D25**	**D26**	**D27**
D	13	13	13	13	13	13
s	50	50	50	70	70	70
d	11	15	20	11	15	20

ID	**D28**	**D29**	**D30**	**D31**	**D32**	**D33**
D	15	15	15	15	15	15
s	50	50	50	70	70	70
d	11	15	20	11	15	20

Table 3.8: Platform design space. Values of diameter (D), separation between columns (s) and draft (d) (Units: m).

3.2.4 Mooring System

The mooring system used for the case study of this Thesis is here defined. Two distinct mooring systems were employed, with each tailored to the specific wind turbine. As the height of the turbine increases, so do the dimensions of the substructure, resulting in increased drift forces that necessitate varying mooring stiffness for each structure. For that purpose, two catenary mooring systems were defined. On one hand, the mooring based on the original station keeping system of the LIFES50+ project from [2] for the Nautilus semi-submersible platform supporting the DTU 10 MW WT. And, on the other hand, the original mooring system from the Volturn US semi-submersible floater reported in [71]. The mooring system properties are summarised in table 3.9.

Parameter	DTU 10 MW	IEA 15 MW
Number of lines	4	4
Angle between adjacent lines	90.00	90.00
Chain diameter	0.097	0.185
Mass per unit length	188.18	685.00
Anchor depth (below MSL)	130.00	100.00
Fairlead depth (above MSL)	6.00	14.00
Line length	833.00	400.00
Line pretension	448 790	800 000

Table 3.9: Mooring system properties for each FOWT. (Units: kg, m, deg)

3.3 Frequency Domain Model Framework

This section introduces the simplified frequency domain modelling approach employed in this Thesis, which was implemented in Python code. The input for wind and wave excitation was fed in the form of spectra, and the resulting response motion in the frequency domain was derived using the system's transfer function. This transfer function incorporated the mass, damping, and stiffness matrices. Subsequent sections will detail the process of linearising and adapting each of these inputs, many of which typically exhibit non-linear characteristics in the time domain, for representation in the frequency domain.

To switch a signal from the time domain to the frequency domain, the Fast Fourier Transform (FFT) is used. Conversely, the Inverse FFT (iFFT) is employed to obtain a time series from a frequency-dependent signal. These transformations have been consistently utilised in the study, and their application will be elaborated further.

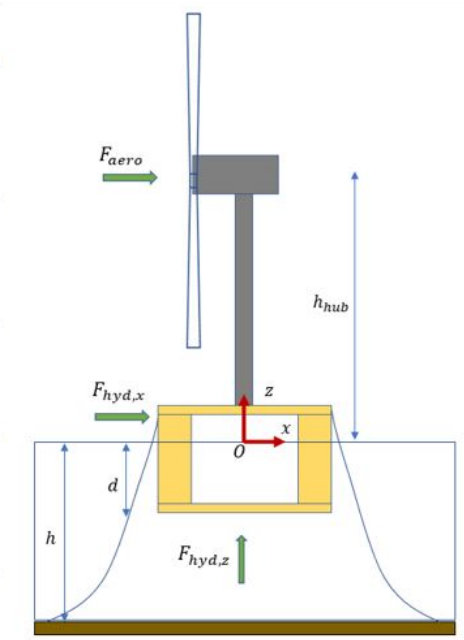

Figure 3.5: Simplified FOWT model

In fig. 3.5, an overview of the simplified model used throughout this Thesis is shown. The four main components can be identified, as well as the wind and wave excitation acting on the structure. The global frame is also represented with the red arrows located at the Point of Flotation (PoF). Since the dynamics of a FOWT are mainly affected by the structural dynamics, the aerodynamics, the hydrodynamics and the mooring dynamics, each of the corresponding models are described in the following subsections. First, the structural model is defined in section 3.3.1, as well as the Degrees of Freedom (DoFs) considered, and the representation of each of the FOWT members. Then, the aerodynamic model is presented in section 3.3.2, where it is described the way the aerodynamic damping and the aerodynamic loads are obtained and how to include them in the equation of motion. Next, in section 3.3.3, the hydrodynamic model is detailed, which provides the hydrodynamic radiation-diffraction loads and accounts for the viscous effects. In section 3.3.4, how the mooring system is represented is described. Finally, how each of the models are assembled together into the frequency domain response model is explained in section 3.3.5.

3.3.1 Structural Model

The Equation of Motion (EoM) in the frequency domain for a single DoF system is given in (3.4).

$$\hat{\xi}(\omega) = \frac{\hat{F}(\omega)}{-\omega^2 m + i\omega b + c} \tag{3.4}$$

where $\hat{\xi}(\omega)$ is the response amplitude, $\hat{F}(\omega)$ is the excitation force amplitude, both frequency-dependent values, being ω the angular frequency. m is the system mass, and b and c are the damping and restoring coefficients, respectively.

Numerous simplified models for FOWT design can be found in literature. In this study, the starting point for the development of an efficient tool for FOWT design was the before mentioned QuLAF model, by A. Pegalajar-Jurado et al. [29]. The ways it could be improved for the FOW substructures' design was analysed and the relevant modifications were implemented. Particularly, the areas of improvement were related to the calculation of the hydrodynamic loads. In this model, the wind turbine was represented using a lumped mass, the tower was the sole flexible component, the platform was treated as a rigid body, and the mooring was characterised by a non-linear stiffness matrix that adjusts with changes in the platform's surge displacement. It consisted of a planar model, which did not take into account wind and wave misalignment conditions. Factors such as current, tides, or ice were omitted from consideration, as they are typically more pertinent in advanced design phases rather than preliminary ones. The FOWT was reduced to 4 DoFs: the surge, heave and pitch platform motions, and the first tower fore-aft (FA) modal deflection. This simplification enabled the computation of nacelle acceleration, which holds particular significance for fatigue analysis. The response vector according to the DoFs considered is given in (3.5), where the lower index correspond to the four DoFs, respectively.

The sign convention is positive surge and tower deflection in the downwind direction, positive heave upwards, and positive pitch clockwise about the PoF, which is the global reference frame origin.

$$\hat{\xi}(\omega) = \begin{bmatrix} \hat{\xi}_1(\omega) \\ \hat{\xi}_2(\omega) \\ \hat{\xi}_3(\omega) \\ \hat{\xi}_4(\omega) \end{bmatrix} \tag{3.5}$$

The equation of motion of a FOWT in the frequency domain can be written in matrix form as follows:

$$\hat{\ddot{\xi}}(\mathbf{M} + \mathbf{A}) + \hat{\dot{\xi}}\mathbf{B} + \hat{\xi}\mathbf{C} = \hat{F}_{aero} + \hat{F}_{hyd} \tag{3.6}$$

Where $\mathbf{M}$ is the system structural mass matrix, $\mathbf{A}$ is the hydrodynamic added mass matrix, $\mathbf{B}$ is the system damping matrix and $\mathbf{C}$ the system

stiffness matrix. $\hat{F}_{aero}$ is the FFT amplitude of the wind excitation load and $\hat{F}_{hyd}$ is that of the wave excitation load to which the FOWT is subjected. The total load acting on the FOWT is the sum of the aerodynamic and hydrodynamic forces.

In this model, the tower's flexibility is taken into account because the tower deflection at the RNA position is of particular interest, especially for fatigue analyses. To incorporate the tower's flexibility, modal analysis is employed, where the structural deformation is approximated using a linear combination of mode shapes. To facilitate this, the tower is assumed to be clamped, resembling an onshore wind turbine setup, and it is divided into small longitudinal sections. Each section is associated with height-dependent properties, including mass (m) and bending stiffness (EI). By solving the eigenvalue problem (3.7), the vibration modes are determined for each natural frequency. Here, the subscript $_{zz}$ signifies the second derivative concerning the vertical coordinate z.

$$m\ddot{v} + (EIv_{zz})_{zz} = 0 \tag{3.7}$$

The eigenvector and eigenvalues derived from (3.7) correspond to the mode shape, ϕ, and natural frequencies, λ, of the tower, respectively. As the mode shapes are orthogonal, superposition can be applied and the deflection, v, can be written as follows:

$$v(z,t) = \sum_{i=1}^{\infty} \phi_i(z)\lambda_i(t) \tag{3.8}$$

Generally, not all the modes are used to represent the deflection of the structure. Only those that correspond to the natural frequencies close to the excitation frequency range are considered. In this Thesis, only the first fore-aft mode shape was employed, although using a larger number of modes, a higher accuracy on the deflection representation would be achieved. However, this decision depends on the relevance of each of the tower mode shapes on the structure dynamic behaviour.

The mode shapes and natural frequencies of the flexible tower were obtained using BModes [31], the NREL tool that solves the eigenvalue problem. When designing the substructure for FOW, the wind turbine and the tower are already defined, thus the mode shapes were computed in advance and stored to set as the input of the structural model.

Once the tower mode shapes were computed, then, the system structural matrices can be obtained. Since the present system is represented with four DoFs, the matrices size 4x4. The mass and inertia matrix were defined the same way as done by Pegalajar et al in [29], based on the force necessary to produce unit acceleration for each DoF:

$$M_{str} = \begin{bmatrix} m_{tot} & 0 & m_{tot} z_{tot}^{CM} & m_{rn}\phi_{hub} + \sum_{i=1}^{N_t} \tilde{\rho}_i \phi_i \Delta z_i \\ & m_{tot} & 0 & 0 \\ & & I_{tot}^{O} & m_{rn}\phi_{hub} h_{hub} + I_{rn}^{TT}\phi_{z,hub} + \sum_{i=1}^{N_t} \tilde{\rho}_i \phi_i z_i \Delta z_i \\ & & & m_{rn}\phi_{hub}^2 + I_{rn}^{TT}\phi_{z,hub}^2 + \sum_{i=1}^{N_t} \tilde{\rho}_i \phi_i^2 \Delta z_i \end{bmatrix} \tag{3.9}$$

being $m_{tot} = m_{rn} + \sum_{i=1}^{N_t} \tilde{\rho}_i \Delta z_i + m_f + m_{moor}$, which is the sum of the RNA, the tower and the floater, respectively. The tower mass is composed of the sum of the N_t sections mass into which it has been decomposed and calculated from mass per unit length $\tilde{\rho}_i$ and length Δz_i. The FOWT centre of mass (CM) vertical position with respect to the MSL is obtained by taking into account the position of the CM of each individual component:

$$z_{tot}^{CM} = \frac{m_{rn} h_{hub} + \sum_{i=1}^{N_t} \tilde{\rho}_i z_i \Delta z_i + m_f z_f^{CM}}{m_{tot}} \tag{3.10}$$

where $z_i = z_{t,i} + h_t$ is the absolute height of the tower elements with respect to the MSL, being h_t the tower base height.

The total inertia of the system, I_{tot}^{O}, is referred to the PoF and is the sum of the inertia, referred to the same point, of the RNA, platform and tower. The tower structural properties and mode shapes used in the frequency domain simplified model were the same as those used for its validation in the state of the art (SoA) model.

The structural stiffness is due to, on one hand, the negative restoring effect of the tower and rotor when the platform pitches, and on the other hand, the stiffness properties of the flexible tower.

$$C_{str} = \begin{bmatrix} 0 & 0 & 0 & 0 \\ & 0 & 0 & 0 \\ & & -m_{tot} g z_{tot}^{CM} & -m_{rn} g \phi_{hub} - \sum_{i=1}^{N_t} \tilde{\rho}_i g \phi_i \Delta z_i \\ & & & \sum_{i=1}^{N_t} EI_i \phi_{zz,i}^2 \Delta z_i \end{bmatrix} \tag{3.11}$$

And the structural damping matrix is due to the tower deflection and it is obtained as follows:

$$B_{str} = \begin{bmatrix} 0 & 0 & 0 & 0 \\ & 0 & 0 & 0 \\ & & 0 & 0 \\ & & & 2\zeta_{str,tw}\sqrt{C_{tw} M_{tw}} \end{bmatrix} \tag{3.12}$$

where $\zeta_{str,tw}$ is the structural damping ratio for the tower first fore-aft mode, and M_{tw} and C_{tw} are last diagonal elements of the system mass and stiffness matrices, respectively.

3.3.2 Aerodynamic Model

In the simplified structural model described earlier, the wind turbine was represented as a lumped mass, neglecting the flexibility of the blades and, consequently, overlooking any damping effects resulting from their motion. It is a common practice to employ cascading techniques in such scenarios to maintain accuracy in the inputs of the simplified model. Wind turbine aerodynamics involve highly intricate elements, such as rotating blades with complex profiles and variable pitch control. To account for these effects, it is advisable to pre-compute the aerodynamic loads and aerodynamic damping using more sophisticated models. In this study, following the methodology outlined by Pegalajar et al. in their work [29], the aerodynamic analysis was conducted using the state of the art reference time domain based tool, OpenFAST, using the AeroDyn module. These results were then cascaded into the simplified model. Additionally, the tower aerodynamic drag force was also included in the present model.

Aerodynamic Loads

The model assumes that the node representing the top of the tower is positioned at the centre of the rotor, without taking into account the actual distance between the tower top and the hub, as well as the overhang angle. As a result, when inputting the aerodynamic loads from the SoA model into the simplified model, it becomes necessary to transform these loads into the global reference system. It is important to note that for the simplified model, only the pure aerodynamic components are relevant, so any inertial and gravitational components should be subtracted if they are present (e.g., if they are extracted from ElastoDyn (NREL)).

$$\hat{F}_{aero}(\omega) = \begin{bmatrix} \hat{F}_{aero,x}(\omega) \\ \hat{F}_{aero,z}(\omega) \\ \hat{F}_{aero,x}(\omega) h_{hub} + \hat{M}_{aero,y}(\omega) \\ \hat{F}_{aero,x}(\omega) \phi_{hub} + \hat{M}_{aero,y}(\omega) \phi_{z,hub} \end{bmatrix} \tag{3.13}$$

To calculate aerodynamic loads in OpenFAST, all DoFs were disabled, effectively immobilising the wind turbine while keeping the controller active. Turbulent wind and calm water conditions were assumed. For each mean wind speed within the operational range, time series data were collected for the aerodynamic thrust ($F_{aero,x}$), aerodynamic vertical force ($F_{aero,z}$), and aerodynamic tilt moment around the tower top ($M_{aero,y}$). This process might involve multiple simulations, but it is important to note that these simulations need to be carried out just once for each specific wind turbine, as they are tailored to its unique characteristics. In (3.13), the aerodynamic load vector referred to the PoF is given. Because these time series were

further used as input for the simplified model, the simulations need to be as long as the maximum simulation time used in the latter. Prior to be loaded into the frequency domain model, each load time series were transformed to the frequency domain through the FFT. In this study, simulations time 5400 s were performed.

Aerodynamic Damping

The aerodynamic damping is crucial for the design of offshore wind turbines, and various researches have demonstrated that the aerodynamic damping can effectively reduce response motions and fatigue loads on the FOWT, such as Guo et al. [75] and Liu et al. [76]. Furthermore, the effects of the aerodynamic damping on the FOWT dynamic responses were explored and it is known that it is mainly related to the rigid platform motions and mooring tensions excited by the low-frequency components. Deng et al. [77] found that frequency-dependent damping enables a better understanding of the amplitude changes in FOWT's dynamic responses under operational conditions compared to constant damping, and a poor evaluation of the aerodynamic damping on decoupled models lead to an underestimation of the surge motion and over estimation of the pitch response. For this reason, it is important to carefully assess the aerodynamic damping as a function of frequency.

The rotational movement of the rotor generated by the airflow induces an aerodynamic damping effect that relies on the relative velocity. This damping is a function of the average wind speed, the rotational speed, and the oscillatory motion. Similar to the calculation of aerodynamic loads, the aerodynamic damping was obtained through time domain simulations using OpenFAST and was subsequently incorporated into the linear damping matrix of the system. To achieve this, decay tests were conducted for each DoF under steady wind conditions and calm water. To isolate the pure aerodynamic damping, any sources of damping, such as structural, radiation, and viscous damping were eliminated from the model. All DoFs except the one of interest for the decay test were deactivated, remaining the controller active to represent the wind turbine as a single DoF system. For each DoF, 600 s step test was performed in OpenFAST, jumping at each wind speed within the operational range of the FOWT. These simulations were performed for the reference Nautilus platform, described in section 2.2.2. The aerodynamic damping ratio was assumed to be the same across the different platform designs provided that the natural frequency of the FOWT does not significantly vary. From the resulting motion response time series, the local damping ratio at each peak extracted from the signal were obtained, and then it was averaged in order to get the aerodynamic

damping ratio for the corresponding DoF and mean wind speed. In fig. 3.6 the aerodynamic damping ratios corresponding to the DTU 10 MW WT for surge, pitch and tower fore-aft motion are given. The heave aerodynamic damping is zero, thus it is not shown. It is observed that the surge damping ratio became negative at rated wind speed (11.4 m/s), and as the wind speed increases, it went back to positive values. The negative damping effect could turn into critical situation, exciting resonant responses.

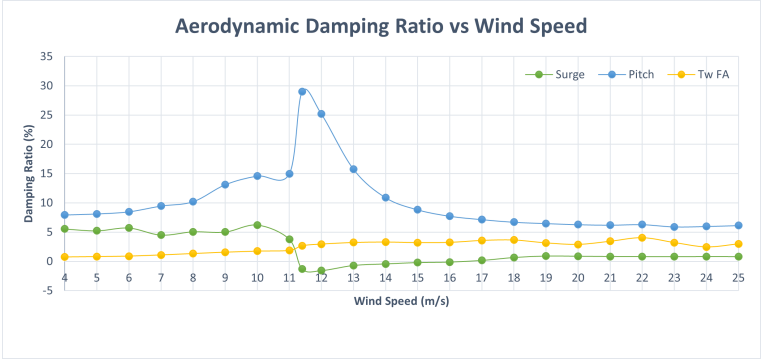

Figure 3.6: Aerodynamic damping ratio for surge, pitch and tower first fore-aft mode as a function of mean wind speed.

The aerodynamic damping ratio was converted into the aerodynamic damping coefficient using the following expression, as a function of the mean wind speed, U and the angular frequency, ω.

$$b_{aero,i}(U_j, \omega) = 2\varsigma_{aero,i}(U_j)\sqrt{C_{ii}(M_{ii} + A_{ii}(\omega))} \tag{3.14}$$

where C_{ii}, M_{ii} and $A_{ii}(\omega)$ are the diagonal terms of the restoring matrix, structural mass matrix, and added mas matrix of the FOWT system. The lower index i denotes the DoF and j each of the wind speed values. These damping coefficients were extracted from simulations in steady wind. In order to consider the wind turbulence, the probability density function (PDF) following a normal distribution was employed. This PDF was utilised to introduce the variability of wind speed into the resulting aerodynamic damping. Then, the aerodynamic damping coefficient was stored and loaded to the simplified model.

$$b_{aero,i}(\omega) = \sum_{j=1}^{N_w} PDF(U_j) b_{aero,i}(U_j, \omega) \tag{3.15}$$

Under the basis of maintaining the aerodynamic damping ratio throughout the different platform designs, since it was assumed that the natural frequencies of the FOWT are kept within a small range of values for each

DoF, the same damping ratios were used for the IEA 15 MW WT. This approach could be adopted because in this Thesis it is pursued a qualitative analysis rather than a highly accurate prediction of the response, and it was verified that the results were not substantially affected. Bear in mind, that the aerodynamic coefficient for each FOWT, where a different platform is assessed, was obtained by considering the mass and stiffness for each specific design.

Tower Aerodynamic Drag Force

The aerodynamic tower drag force is particularly significant for extreme wind conditions, where the thrust loads are small. In this work, only the horizontal component of the aerodynamic drag was considered and a single drag coefficient, C_D, was used along the whole tower height. The same element discretisation explained in section 3.2.2 was used, using 56 sections. The expression for this force is as follows:

$$F_{aero,tw}(z) = \frac{1}{2}\rho_{air} D(z) h_{tw}(z) C_{D,tw} U(z)|U(z)| \tag{3.16}$$

Here, $D(z)$ is the tower outer diameter at each vertical position, $h_{tw}(z)$ is the height of the tower section located at distance z from the MSL, and $U(z)$ is the local horizontal wind speed following the power law wind speed distribution. The tower drag coefficient, $C_{D,tw}$ was considered constant along the entire height of the tower. It is a static load, thus it will contribute to the mean response.

3.3.3 Hydrodynamic Model

The hydrodynamic forces acting on a floating offshore substructure primarily encompass hydrostatic forces F_{hst}, radiation forces F_{rad}, first-order $F_w^{(1)}$ and second-order wave forces $F_w^{(2)}$, and viscous forces F_{vis}. Additional forces can arise due to factors such as currents, tides, or other meteorological conditions, but these factors were not considered in this study. The overall hydrodynamic loads acting on the FOWT substructures are the sum of the mentioned forces, as given in (3.17). The following sections will detail the calculation methodology for each of these loads.

$$F_{hyd} = F_{hst} + F_{rad} + F_w^{(1)} + F_w^{(2)} + F_{vis} \tag{3.17}$$

Hydrostatic Loads

The hydrostatic component is related to the pressure distribution of a fluid at rest and it dictates the stability of floating structures. This force results

from the Archimedes Principle, where the equilibrium between the buoyant force and the weight of the displaced water balances. Since the platform was considered rigid body, the restoring force will depend on the water plane area, and on the position of the CoG and CoB. It is a static force and thus, obtained through the hydrostatic stiffness matrix. In this study, for the calculation of the hydrostatic stiffness small displacements were assumed, and therefore, it was obtained for the equilibrium position. Due to the two-plane symmetry of the Nautilus platform, only the diagonal terms in heave and pitch were non zero values. The stiffness matrix for the 4 DoF simplified model is given in (3.18).

$$C_{hst} = \begin{bmatrix} 0 & 0 & 0 & 0 \\ 0 & \rho_w g A & 0 & 0 \\ 0 & 0 & \rho_w g \nabla \overline{GM} & 0 \\ 0 & 0 & 0 & 0 \end{bmatrix} \tag{3.18}$$

Where ρ_w is the water density, g is the gravity acceleration, ∇ the displaced water volume and $\overline{GM}$ the metacentric distance to the CoG. This matrix is an output from the radiation-diffraction analysis, but in this work it was obtained in a spreadsheet calculation due to its geometrical properties.

From the equilibrium, it can be also defined a buoyancy force, which for the structural model of 4 DoFs has the form, being x_{CoB} the position along the x-axis of the CoB.

$$F_{buoy} = \begin{bmatrix} 0 \\ \rho_w g \nabla \\ -\rho_w g \nabla x_{CoB} \\ 0 \end{bmatrix} \tag{3.19}$$

Radiation and Wave Excitation Loads

Every floating body is subjected to radiation and diffraction loads. Radiation loads are hydrodynamic loads due to forced harmonic rigid body motions, where no incident waves occur, but the forced motion of the structure produces radiated waves. This oscillating motion of the fluid is responsible for the pressures on the structure, leading to forces and moments. Radiation loads are composed of the frequency-dependent hydrodynamic added mass, $A(\omega)$, and radiation damping, $B_{rad}(\omega)$, both functions of the structure geometry, oscillating frequency and forward speed. In this study, the forward speed was neglected, thus, the added mass and radiation damping matrices were symmetric.

Wave loads are those produced by the incident and diffracted waves acting on the structure assuming it is not moving. These loads are called wave excitation loads and are composed of the Froude-Krylov and diffraction forces and moments. The former are related to the effect of the unsteady pressure induced by the undisturbed waves, and the latter are related to the variation of this pressure field due to the presence of the structure. Similarly to radiation loads, the total frequency-dependent first-order wave excitation coefficients for each DoF were obtained through radiation-diffraction analysis. The first-order wave loads are obtained as follows:

$$F_w^{(1)}(\omega) = X(\omega)\eta(\omega) \tag{3.20}$$

Where $F_w^{(1)}$ is the linear wave load vector, η is the wave elevation, and $X(\omega)$ is the linear wave excitation coefficient per unit of wave amplitude. The hydrodynamic added mass, radiation damping and wave excitation coefficient are commonly referred to as the hydrodynamic coefficients, and are usually obtained from the radiation-diffraction analysis. The most used commercial tools are WAMIT, ANSYS-AQWA, and NEMOH, which generate these frequency-dependent coefficients for a given frequency range and for the 6 DoFs, assuming the platform as a rigid body. In this Thesis, the response model is fed with these coefficients referred to the global coordinate system, is located at the MSL with the origin at the PoF of the FOWT.

When the natural frequencies of the FOWT fall outside the range of wave excitation frequencies, it becomes relevant to consider the inclusion of second-order excitation loads. In the presence of irregular waves, which aim to replicate real offshore conditions, the interaction between different waves can lead to an excitation frequency that closely matches the natural frequencies of the structure. This is particularly significant for catenary moored structures, which typically have very low natural frequencies in surge and pitch, making them highly susceptible to low-frequency second-order hydrodynamic loads. The conventional approach to obtain the second-order hydrodynamic loads follows two steps: first, the calculation of the Quadratic Transfer Function (QTF) through radiation-diffraction analysis by means of a panel code; and second, the evaluation of the hydrodynamic loads for a certain sea state through the double sum considering the interaction between each frequency pair ω_m and ω_n. Hence, the second-order load can be expressed as

$$F_{w,k}^{(2)} = \Re\left\{ \sum_{m=1}^{N} \sum_{n=1}^{N} \hat{\eta}_m \hat{\eta}_n^* QTF_{mn,k}^{-} e^{i(\omega_m - \omega_n)t} \right\} + \Re\left\{ \sum_{m=1}^{N} \sum_{n=1}^{N} \hat{\eta}_m \hat{\eta}_n QTF_{mn,k}^{+} e^{i(\omega_m + \omega_n)t} \right\} \tag{3.21}$$

where * indicates the complex conjugate, $\hat{\eta}$ are the Fourier coefficients of the free surface elevation and $QTF_{mn,k}^{+}$ and $QTF_{mn,k}^{-}$ are the sum and difference QTFs, respectively, being k the index for the degree of freedom. The evaluation of (3.21) can lead to a high computational cost if many frequencies are involved.

It is also common practice to apply the Morison Equation for the calculation of both first- and second-order wave excitation loads, although it is limited to slender structures ($\frac{D}{\lambda} < 0.2$) [43, 78].

Viscous Loads

Radiation-diffraction analysis does not account for the drag force and viscous damping effects, thus, Morison drag force on the slender members is usually added to model.

$$F_{vis} = \frac{1}{2} \rho_w A C_{D,f} (u_f - v_b) |u_f - v_b| \tag{3.22}$$

Where $C_{D,f}$ is the floater drag coefficient, which depends on the geometry, on the KC number, on the Reynolds number and on the surface roughness. A is the drag surface, u_f is the fluid velocity and v_b the structure velocity. As it can be observed in (3.23), viscous effects depend non-linearly on the relative velocity between the fluid and the body, hence they can not be considered in frequency domain models. However, since this Thesis is focused on semi-submersible platforms design, which are large structures, drag loads can not be neglected. Therefore, a linear viscous damping was considered based on the Morison force. For sake of simplicity, small displacements and velocities relative to the fluid velocity were assumed, thus, the linear damping term resulting from (3.23) becomes:

$$F_{vis} \approx \rho_w A C_{D,f} v_b |u_f| \tag{3.23}$$

The viscous effects considered for this study were accounted in the similar way as in the QuLAF from Pegalarjar et al. [29]. The viscous damping coefficient for each DoF was derived from the Morison forces and moments in surge, heave and pitch motions. Since the drag force depends on the

submerged geometry, a linear viscous damping was defined for each platform design. The drag coefficient, however, was assumed constant. The symmetric viscous damping matrix is given as:

$$B_{vis} = \begin{bmatrix} \rho C_{Dx} A_x u_{rep} & 0 & \rho C_{Dx} S_{y,A_x} u_{rep} & 0 \\ & \rho C_{Dz} A_z w_{rep} & 0 & 0 \\ & & \rho(C_{Dx} I_{y,A_x} u_{rep} + C_{Dz} I_{y,A_z} w_{rep}) & 0 \\ & & & 0 \end{bmatrix} \quad (3.24)$$

Where C_Dx and C_Dz the global drag coefficients with values 1 and 2, respectively, since the columns oppose less resistance than the sharp corners on the bottom surface of the platform. A_x and A_z are the floater's area projected on the yz plane and xy plane, respectively, and S_{y,A_x} and S_{y,A_z} the first moment of area about the y-axis of the respective surfaces. I_{y,A_x} and I_{y,A_z} are the second moments of area about the y-axis of A_x and A_z, respectively. The representative horizontal and vertical velocities, u_{rep} and w_{rep} are obtained by averaging the fluid velocity, first over depth, and then, over time, as done in the original QuLAF [29].

3.3.4 Mooring System Model

The mooring system contributes to the FOWT with restoring forces and moments. For the case of catenary mooring lines, the provided stiffness depends on the catenary shape, which changes with the FOWT displacement. In this Thesis, a quasi-static approach was used in order to obtain the mooring stiffness and some simplifications have been adopted in order to integrate it in the frequency domain model. Following the procedure adopted in the QuLAF [29], a linearised stiffness matrix for each mean wind speed was used to represent the mooring system. This is explained by the mean thrust force produced at each mean wind speed, displacing the FOWT to a new equilibrium position. On the contrary, the displacement due to wave loads was not here considered for the calculation of the mooring stiffness.

In this Thesis, the mooring stiffness matrix was obtained through static analyses in commercial software OrcaFlex, yet this can be calculated using other tools or analytically. For the mooring systems defined in table 3.9, for the DTU 10 MW WT and for the IEA 15 MW WT, and for the site conditions defined in section 3.1, the stiffness matrices at the different equilibrium positions were obtained and stored to be loaded to the linear model. In fig. 3.7 the horizontal displacement produced by the wind thrust is shown. These values were based on the wind turbine performance curves. Another simplification in this study is that the same mooring stiffness were applied

for all the platforms from the design space, in order not to introduce differences rather than the platform properties.

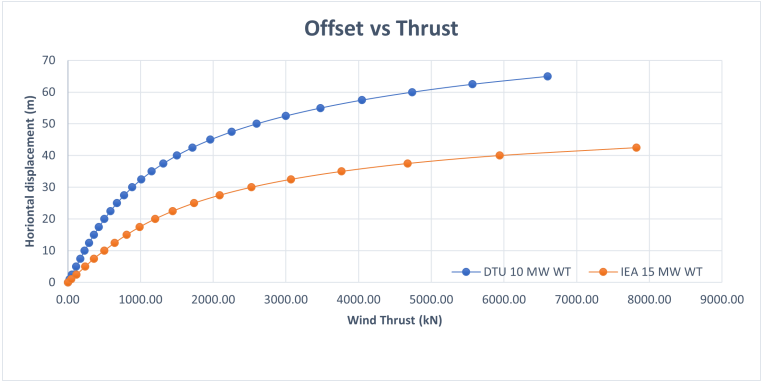

Figure 3.7: Platform horizontal displacement versus wind thrust acting on the DTU 10 MW WT and on the IEA 15 MW WT.

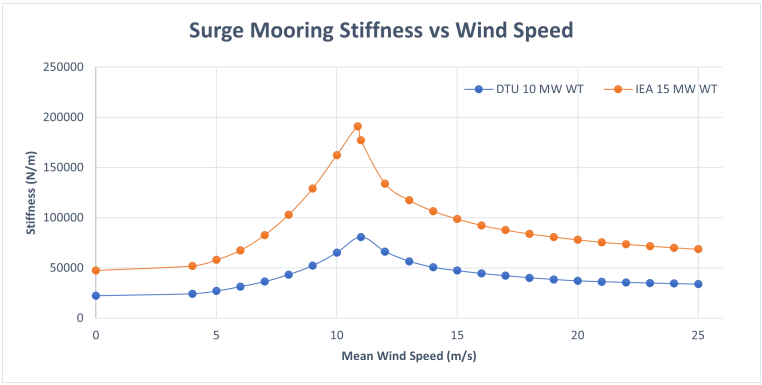

Figure 3.8: Mooring stiffness in the surge motion corresponding to a given wind speed for the DTU 10 MW WT and for the IEA 15 MW WT.

In fig. 3.8 the mooring stiffness for the surge motion is given as a function of the mean wind speed. The maximum stiffness is achieved for the rated wind speed of each corresponding turbine, since it is also associated to the maximum surge displacement. As the 15 MW WT will be subjected to a higher thrust force, due to its larger size, it will also suffer larger displacements and, thus, it requires a stiffer mooring system. The procedure followed in this work is suitable for the validation of the proposed methodology for the preliminary design phase of FOW support structures, since the focus is not yet placed on the mooring design. Otherwise, a proper evaluation of the mooring stiffness would be required, taking into account the mean drift loads and any other excitation that could produce significant displacements of the FOWT.

3.3.5 Frequency Domain Model Assembly

Putting all the previous information together, where the dynamics affecting the response of FOWTs and the modelling techniques used in this Thesis have been described, a more detailed EoM can be written as in (3.25).

$$\hat{\xi}(\omega) = \mathbf{H}(\omega)(\hat{F}_{aero}(\omega) + \hat{F}_{hyd}(\omega)) \tag{3.25}$$

$\hat{F}_{aero}(\omega)$ is the aerodynamic loads vector, $\hat{F}_{hyd}(\omega))$ are the hydrodynamic loads vector, both frequency dependent values. $\mathbf{H}(\omega)$ is the mechanical transfer function and it characterises the system, since it is a function of the mass, damping and stiffness of the FOWT. It is a complex matrix and is given in (3.26).

$$\mathbf{H}(\omega) = \frac{1}{-\omega^2(\mathbf{M_{str}} + \mathbf{A}(\omega)) + i\omega\mathbf{B}(\omega) + \mathbf{C})} \tag{3.26}$$

The total system mass and inertia matrix is the sum of the structural mass and inertia and the hydrodynamic added mass, since it is subjected to hydrodynamic loads. Regarding the damping and the stiffness matrices of the system, now that each dynamic model has been explained, they can be written as follows:

$$\mathbf{B}(\omega) = \mathbf{B_{str}} + \mathbf{B_{aero}}(\omega) + \mathbf{B_{rad}}(\omega) + \mathbf{B_{vis}} \tag{3.27}$$

$$\mathbf{C} = \mathbf{C_{str}} + \mathbf{C_{hst}} + \mathbf{C_{moor}} \tag{3.28}$$

The system damping matrix is composed of the tower structural damping ($\mathbf{B_{str}}$), the aerodynamic damping matrix ($\mathbf{B_{aero}}$), and the hydrodynamic radiation ($\mathbf{B_{rad}}$) and viscous damping ($\mathbf{B_{vis}}$). And, the restoring matrix is the sum of the structural stiffness ($\mathbf{C_{str}}$), which is due to the tower flexibility, the hydrostatic stiffness ($\mathbf{C_{hst}}$) due to the floating structure, and the stiffness that represents the mooring system ($\mathbf{C_{moor}}$).

In fig. 3.9 a simple scheme of the modelling approach is shown. As mentioned in the previous sections, cascading techniques were used in order to accurately model some of the FOWT model inputs. This is the case of the aerodynamic loads and aerodynamic damping. which were extracted from the time domain SoA tool, OpenFAST. The aerodynamic load time series, which were transformed to frequency domain thought the FFT, and the aerodynamic damping ratio foe each mean wind speed were stored and loaded to the simplified model. This aerodynamic data is employed for all the platforms from the design space that are supporting the same wind turbine, provided the system natural frequencies do not show substantial differences. The turbulent wind time series were generated using Turbsim.

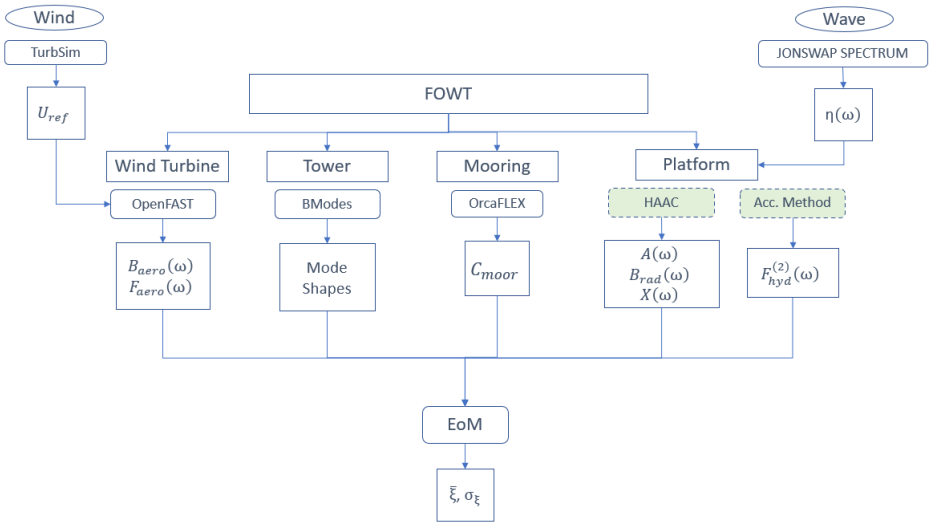

Figure 3.9: Overview of the frequency domain simplified model, *FD Tool*, and the numerical approaches used for each of the dynamic analysis.

Cascading techniques were also applied for the mooring stiffness calculation. OrcaFlex tool was employed to perform quasi-static analyses in order to obtain the mooring stiffness associated to different platform surge displacements, which at the same time are related to a specific mean thrust force. The mooring matrices were also stored to be later input into the simplified response model.

Regarding the hydrodynamic loads, it is common to perform radiation-diffraction analyses through potential flow solvers such as WAMIT or ANSYS-AQWA. However, this is not an efficient solution when a large number of platform concepts need to be assessed, as required in the initial stages of design. In order to address this, the present Thesis presents two novel standalone methods as efficient alternatives to the radiation-diffraction analysis in this design phase, providing a reasonable accuracy and with the main advantage of reducing substantially the computational cost. The first method attends to the first order hydrodynamic coefficients estimation, based on the radiation-diffraction analysis, and it has been denoted *HAAC*, making reference to *Hydrodynamic Analysis on Aggregated Components* and it is described and validated in chapter 4. The second method, focuses on the prediction of the second-order hydrodynamic wave loads based on the slender body theory, referred to it as *Accelerated Method* and it is explained and validated in chapter 5. These two methods constitute the main contribution of this Thesis, and through the integration on the frequency domain response model, their validity and usability for the preliminary design

phase of FOW platforms is demonstrated. In fig. 3.9 a simple scheme of the modelling approach is shown. The matrices obtained in the spreadsheet, such as the structural mass, stiffness and damping matrices, or the viscous damping matrix and the hydrostatic stiffness matrix are now shown in the scheme, but they are included in the EoM in (3.25). The design methodology described throughout this section, where a simplified frequency domain response model is fed with the hydrodynamic data extracted from the novel methods *HAAC* and *Accelerated Method*, was denoted *FD Tool*.

Since this methodology is based on the frequency domain, the outcome will be a mean component $\bar{\xi}$, resulting from the static analysis, and a dynamic component, represented by the standard deviation σ_ξ. The latter, is related to the area of the response spectra, according to the Parseval theorem. Therefore, the response can be obtained as the sum of the mean and standard deviation of each DoF motion. Additionally, in order to plot the time series, the iFFT is applied.

3.3.6 Overall System Properties

Herein, the natural periods of the FOWT with the floating platforms defined in table 3.8 supporting the DTU 10 MW WT are shown. The four DoFs described in the structural model section 3.3.1 were considered. For the calculation of the system natural periods, the eigenvalue problem was solved using the mass and the stiffness matrices used in the EoM (3.26).

In 3.13, 3.11 and 3.12, the natural periods for the platform surge, heave and pitch are shown. Additionally, the wave peak periods from the assessed DLCs (see table 3.1) are also depicted with dashed lines. As observed, the most crucial natural frequencies for the specified ocean conditions are associated with heave and pitch motions. The surge motion exhibited considerably longer natural periods, making it less prone to resonance under

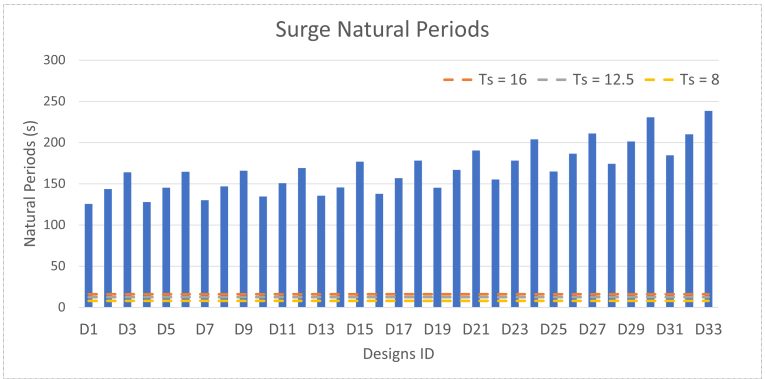

Figure 3.10: Surge natural periods for the different platform designs.

first-order wave forces, but more susceptible to low-drift loads. Among the different designs, when the diameter of the platform columns increased, the natural period also experienced an increase. Likewise, a greater platform draft or increased separation between the columns resulted in a longer natural period for the FOWT. This pattern is explained because larger platforms possess greater mass, thereby causing an extension of the natural period.

Within the FOWT designs listed in table 3.8, there were found notable cases where the natural periods for heave and pitch exhibited striking similarities. These particular designs were characterised by columns with diameters of either 13 meters or 15 meters and a separation distance of 50 meters between columns. While it is worth noting that this configuration is not commonly recommended, since 10% difference is preferred, though, it serves as a valuable example for our analysis. Furthermore, it is important to emphasise that, even though the heave motion may not be the primary concern for the floater's design, it remains crucial to consider that the nat-

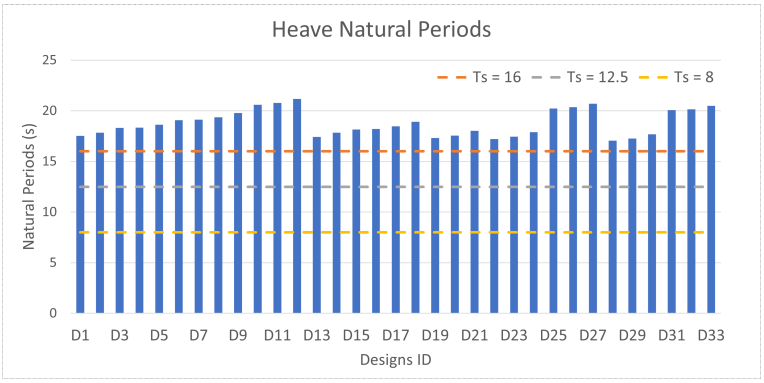

Figure 3.11: Heave natural periods for the different platform designs.

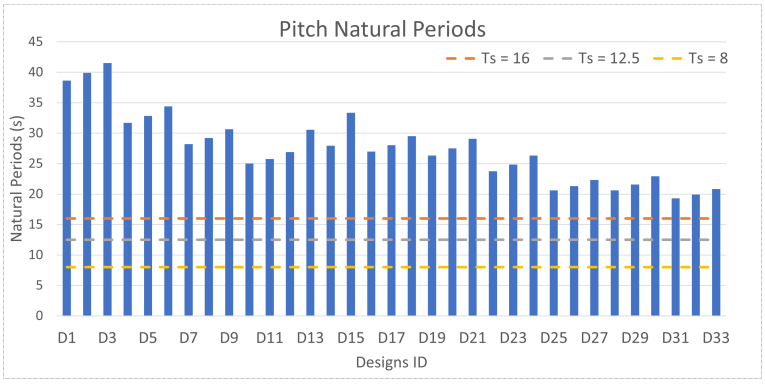

Figure 3.12: Pitch natural periods for the different platform designs.

ural period should not coincide with the interaction frequency. In fig. 3.11, it seems that certain designs closely approach the peak period associated with severe sea states, which is defined with a $T_p = 16$ s. These designs correspond mainly to those platforms with separation between the columns of 50 m.

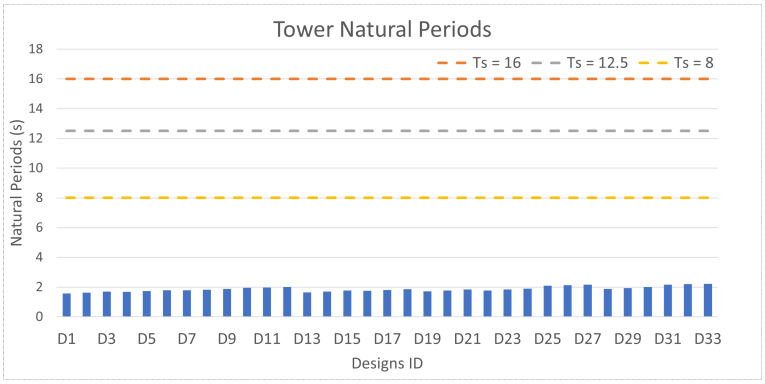

Figure 3.13: Tower fore-aft deflection natural periods for the different platform designs.

Regarding the tower's deflection caused by the first fore-aft mode is characterised by extremely short natural periods, making it more susceptible to the rotational motion of the blades. This is better explained through the Campbell diagram shown in fig. 3.14. The rotating frequencies corresponding to one to twelve passing blades are shown with the black lines. The region out of the blue shaded area corresponds to the wind turbine operation rotational speed.

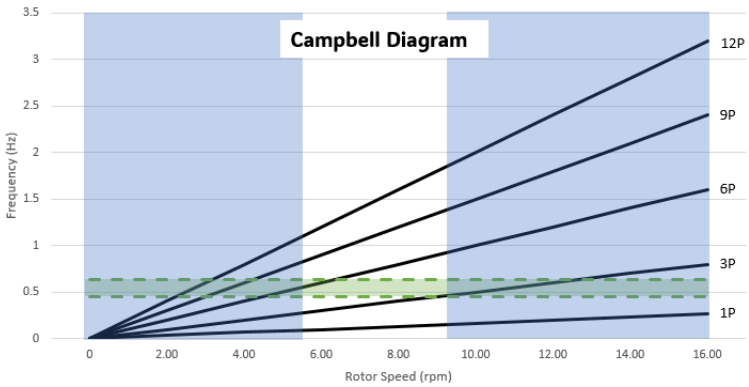

Figure 3.14: Campbell diagram for the DTU 10 MW WT and the FOWT tower first fore-aft bending natural frequency range.

The green region delimits the natural frequency range for the first fore-aft tower bending mode for the platform designs used in this study. It is

noticeable that some of the designs interfered with the 3P frequency, thus, they would probably be excited resonance, although this would be observed in the results. These designs corresponded mainly to those that have 70 m of separation between the columns. The rest of designs were far from the region to be avoided, which is from 1P to 3P. This will be later discussed, when the selection of the suitable designs is carried out in the validation of the proposed tool in chapter 6.

Chapter 4

Linear Hydrodynamic Coefficients Estimation Methodology

In the early stages of FOW substructure design, numerous substructures with varying parameters are typically analysed. As outlined in section 3.3.3, a floating body's behaviour is primarily influenced by radiation and diffraction loads. During this preliminary phase, only linear hydrodynamic loads, collectively referred to as hydrodynamic coefficients, are typically considered, which are commonly obtained through radiation-diffraction analysis using potential flow solvers. Running such analyses for each platform can be time-consuming. Given the lack of efficient and adaptable techniques for integrating into the initial FOW substructure design, this Thesis introduces an innovative methodology for estimating hydrodynamic coefficients, particularly for semi-submersible platforms. This approach significantly reduces computational demands compared to existing methods, allowing for a broader range of platform designs to be assessed. Moreover, it can be easily integrated into a response model, as described in chapter 3, facilitating swift and extensive sensitivity analyses for a better understanding of the structure's dynamics.

The proposed method breaks down the platform into simpler geometric components, calculating hydrodynamic coefficients for each separately. By summing these isolated component coefficients, the overall platform coefficients are obtained, assuming no interaction between them. This method is referred to as *Hydrodynamic Analysis of Aggregated Components*, henceforward referred to as *HAAC*. To validate *HAAC*, the estimated hydrodynamic coefficients were compared with those from *AQWA*. Furthermore, its accuracy and effectiveness in modelling the frequency domain response of various

platform designs was assessed using the simplified response model described in chapter 3. Detailed analysis of the factors affecting *HAAC*'s accuracy is discussed in subsequent sections.

This chapter is structured as follows: in section 4.1 the *HAAC* methodology is described in detail. In section 4.2 the methodology is validated comparing the hydrodynamic coefficients derived from *HAAC* against the results from the radiation-diffraction analysis of each of the platforms described in section 3.2.3 performed in ANSYS-AQWA. Then, in section 4.3, the response analysis for the different platforms is assessed, evaluating the accuracy of the method through the impact on the response calculation.

4.1 Hydrodynamic Analysis on Aggregated Components (*HAAC*)

The methodology presented here efficiently provides the hydrodynamic coefficients for FOW substructures with reasonable accuracy for the preliminary stage of platform design. The main idea is to decompose the floater into bodies of simple geometry and estimate the hydrodynamic coefficients of each member and then, apply superposition in order to obtain the coefficients of the entire floater. Using the platform from fig. 4.1 as an example, it has been decomposed into four single columns and a squared based pontoon. Regarding the latter, it has been split into four equal rectangular prisms and have been considered as a unique body, because this way the interaction effects of the pontoon are included. This can be done provided that the height of the pontoon is assumed to have negligible effect on the hydrodynamics of the full floater. Otherwise, the pontoon should be split into four isolated prisms and, analogously to the columns, the coefficients for each of them should be obtained. This approach, however, would increase the inaccuracy of the results since the interaction between the pontoon members would not be accounted for in this way.

4.1.1 Basic Steps: Database - Interpolate - Scale

HAAC is mainly based on three steps: (i) build the database, (ii) interpolate, and (iii) scale. In addition, empirical formulae have been developed to account for the interaction between the columns and consider the depth variation of the pontoon, which have been both verified against the results from radiation-diffraction analysis. This procedure is applied for any isolated member or group of members one wishes to assess, with slight differences for each individual case. The hydrodynamic coefficients are referred to the PoF, with the origin at the MSL.

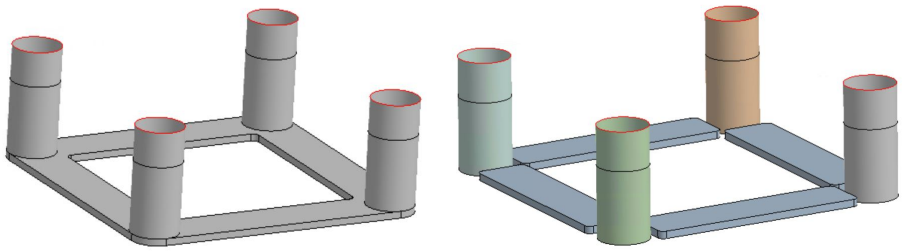

(a) (b)

Figure 4.1: *AQWA* model of a semi-submersible platform: (a) Original (b) Decomposed into members.

Step 1. Build the Database

The first step is to set the database with the hydrodynamic coefficients of a few number of cases covering a wide range of aspect ratios. The hydrodynamic analysis of these geometries can be executed in potential flow solvers, such as *AQWA* or *WAMIT*, thus setting a database based on radiation-diffraction data.

Regarding the isolated member, due to the nature of the scope of this methodology, in this work the example of vertical surface-piercing cylinders is used, like most of the columns of semi-submersible platforms. This geometry is defined by two parameters: the diameter and the draft. The hydrodynamic coefficients of a single vertical partially-submerged cylinder will depend on the diameter-to-draft ratio, assuming deep water conditions. Therefore, a database is built running simulations off-line of a small number of isolated cylinders with constant draft and different diameter values, covering a wide diameter-to-draft ratios for potential platform columns designs.

As for the group of members, such as the pontoon base (see fig. 4.2), a database is built as well for a few pontoons fully submerged at a constant depth d. The length L, height, and CoG vertical position are also set constant, and different width value a are defined. The width-to-length ratios of the database should cover the range of values of the designs one aims to assess.

Step 2. Interpolation

The second step is to interpolate the hydrodynamic coefficients using the database set in the previous step. The interpolation consists of a cubic approximation at each frequency value, and in this work particularly the

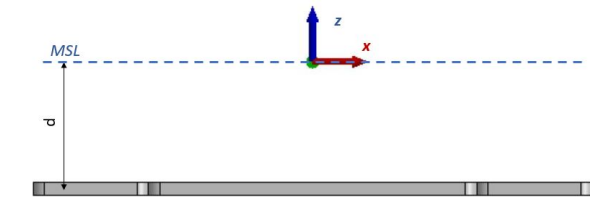

(a)

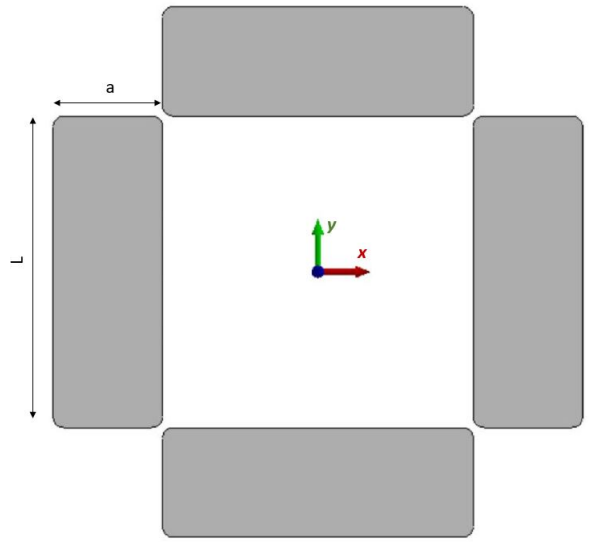

(b)

Figure 4.2: *AQWA* model for the pontoon database: (a) front view (b) top view.

interp1 function from the library Scipy [79] was used. The reason for using a cubic interpolation is that a previous check concluded that the interpolation through polynomial approximation, with degree three showed the best agreement.

In the database, only one parameter varies, while the rest are kept constant. For instance, the diameter of the cylinder is the only varying value, and in the similar way, the pontoon width. Since the geometries of interest might not have the same dimensions as the fixed values of those on the database, one should interpolate for the aspect ratio. In other words, the hydrodynamic coefficients resulting from the interpolation will correspond to geometries with the fixed dimensions of the database. The resulting isolated cylinder will have the draft of the database and, in order to keep the aspect ratio of interest, a new diameter value denoted D_{sc}. Analogously, the resulting pontoon will be submerged at the depth of the database, d_{db}

and will have the same height and length L_{db} as the database, but a new width value a_{sc}. The lower index $_{db}$ denotes the database, and $_{sc}$, scaled parameter.

$$\frac{D_{sc}}{d_{db}} = \frac{D}{d} \tag{4.1}$$

$$\frac{a_{sc}}{L_{db}} = \frac{a}{L} \tag{4.2}$$

Where D and d are the diameter and the draft of the target cylinder, and a and L the width and length of the rectangular members that form the pontoon. Bear in mind that when it comes to the cylinder, d refers to draft, whilst when it comes to the fully submerged horizontal members, it refers to as depth.

Step 3: Scaling

Finally, the hydrodynamic coefficients of the target members are calculated by means of scaling to the original dimensions through the Froude scaling factors, which depend on the units of the coefficients. The isolated cylinder is defined simply by the diameter and the draft, thus the hydrodynamic coefficients of the isolated cylinder are obtained directly by multiplying by the corresponding scaling factor the data derived from the interpolation. The scaling factor base for the cylinder is given below:

$$sc_c = \frac{d}{d_{db}} \tag{4.3}$$

The pontoon, on the contrary, depends on four design parameters: width, length, height and depth. For this reason, when multiplying the coefficients times the pontoon scaling factor, the whole pontoon is scaled, including the depth at which it is submerged. The hydrodynamic coefficients resulting from the scaled values correspond to a pontoon with the dimensions of interest at a scaled depth d_{sc}. The depth variation has an important influence on the coefficients, so it will be later explained how to consider it in the following section. The pontoon height is also scaled, although the height variation is neglected. This leads to some inaccuracies in the estimation of the surge hydrodynamic coefficients, but they have a minor effect due to the dominant role of the columns in this degree of freedom. So for the pontoon, the scaling factor and resulting scaled depth are the following:

$$sc_p = \frac{L}{L_{db}} \tag{4.4}$$

$$d_{sc} = d_{db}\frac{L}{L_{db}} \tag{4.5}$$

Note that this 'scaled depth' is not necessarily equal to the actual depth of the submerged body being analysed. As above mentioned, this is corrected as explained in the following section.

4.1.2 Additional Contributions to the Methodology

Once the hydrodynamic coefficients of an isolated column and the pontoon with the dimensions of the case study floater are estimated, superposition is applied. This is done under the assumption of negligible cross-interaction between the floater members, however, it can become important when the distance between the members is not large enough. Herein, a sensitivity analysis of the interaction between the columns and the separation distance is performed, and the verification of a developed expression to account for this interaction effect on the radiation damping is exposed.

Furthermore, the hydrodynamic coefficients of the pontoon obtained through the basic three steps correspond to that located at the scaled depth d_{sc}, due to the scaling factor applied in the third step. In order to obtain the hydrodynamic coefficients corresponding to the pontoon of the platform case study, one should consider the depth variation between the target and the scaled value. For that purpose, formulation for the added mass and for the radiation damping were developed, and are described and verified as follows.

Throughout this document, the error measure used to quantify the accuracy of the estimation of the hydrodynamic coefficients is defined below, where y and y_{ref} are the corresponding coefficients at each frequency, ω, obtained through $HAAC$ and $AQWA$, respectively.

$$\epsilon_{coef} = \frac{\int_0^\infty |y - y_{ref}|\ d\omega}{\int_0^\infty |y_{ref}|\ d\omega} \tag{4.6}$$

All the coefficients are referred to the PoF taking into account the location of each member at the platform configuration. Also, the phase change of the diffraction loads is accounted for through linear wave theory equations.

Interaction Between the Columns

HAAC assumes negligible interaction between the platform members, however, depending on the separation between them it can become significant. The way the pontoon is modelled in the database already accounts for the interaction between the four rectangular prisms, whereas the interaction between the four columns is here neglected, as well as the interaction between the columns and the pontoon base. Here in, a sensitivity analysis of the interaction between an array of columns was carried out.

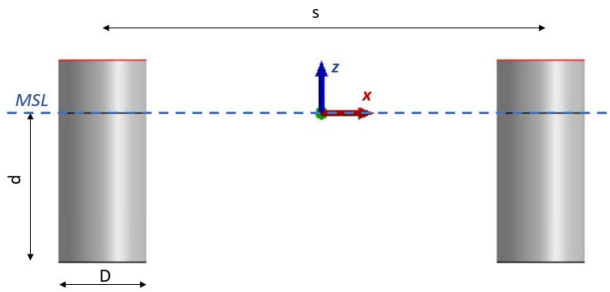

Figure 4.3: *AQWA* model of two columns separated a distance s along the x-axis.

An array of cylinders with diameter D and draft d separated along the x-axis were analysed for different separation distances, s, as shown in fig. 4.3. For that purpose, these two-cylinder models were run in *AQWA*, and the resulting hydrodynamic coefficients were compared to those obtained through *HAAC*. The error obtained for each DoF and each coefficient are given for the different s/D ratios in fig. 4.4. The excitation loads were accurately predicted under the assumption of negligible interaction, where the maximum deviation is observed for the surge force of 22%. However, this value occurred when the distance between the columns' axes was $2D$, which corresponds to a platform with the columns very close to each other. For the current semi-submersible platform configuration s/D ratios, the excitation surge force was predicted with a deviation of 12%. The added mass matched generally well, although certain peaks were not captured with the proposed methodology in the direction where the array of columns were aligned to the wave propagation direction. Still, the error was below 10% for $s > 3D$, thus the assumption of negligible interaction between the columns seems suitable for the preliminary design phase regarding the added mass and the linear excitation loads. Regarding the second-order hydrodynamic excitation loads, a similar procedure could be applied. However, second-order radiation-diffraction analyses would take a higher computational cost than the first-order analyses, and it does not add significantly higher accuracy. For this reason, second-order wave loads

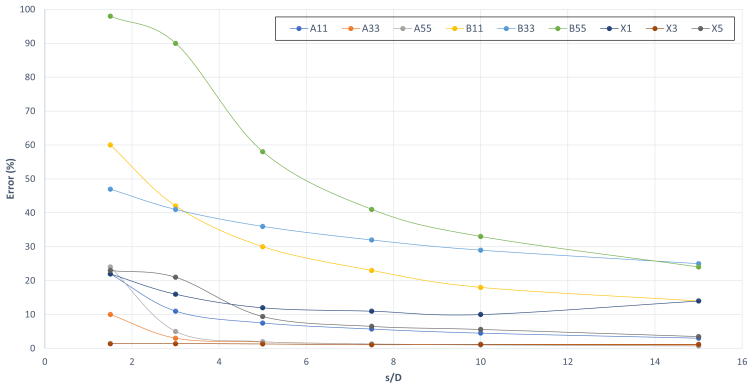

Figure 4.4: Error for the added mass (A), radiation damping (B) and the excitation loads (X) for the surge (1), heave (3) and pitch (5) motions of two cylinders with different s/D ratio. $AQWA$ vs $HAAC$ (assuming no interaction).

are obtained through the *Accelerated Method*, presented in the next chapter due to its high efficiency and reasonable accuracy.

In contrast, the interaction effects could be clearly observed in the radiation damping, achieving the largest errors. Therefore, an empirical expression was developed to estimate the radiation damping of a single cylinder within an array of cylinders, taking into account the interaction effects as a function of the distance between them. This expression accounts for the presence of the cylinders right next to the target one, and does not consider the interaction of the rest of the cylinders in the array. The expression that accounts for the interaction effects on the radiation damping is given as

$$B_{rad}^{int} = B_{rad}\left(1 + \frac{\cos ks}{2}\right)^{n} \tag{4.7}$$

where B_{rad} is the radiation damping of the isolated cylinder, B_{rad}^{int} the radiation damping of one cylinder accounting for the interaction effects due to the neighbour cylinders and k is the wave number. Moreover, it differentiates when the cylinder is located at one of the ends of the array ($n = 1$) or between two cylinders ($n = 2$).

Using (4.7), the accuracy predicting the radiation damping increased substantially, especially in surge and pitch, reducing the error to half of that neglecting the interaction effects. In order to verify this expression, the resulting radiation damping of an array of 2, 3, and 5 columns were compared to that obtained by means of $AQWA$. Since the largest error was found for the pitch motion, as shown in fig. 4.4, the hydrodynamic coefficients for the pitch radiation damping are shown in fig. 4.5. The signals correspond to the radiation damping obtained from the radiation-diffraction analysis and to

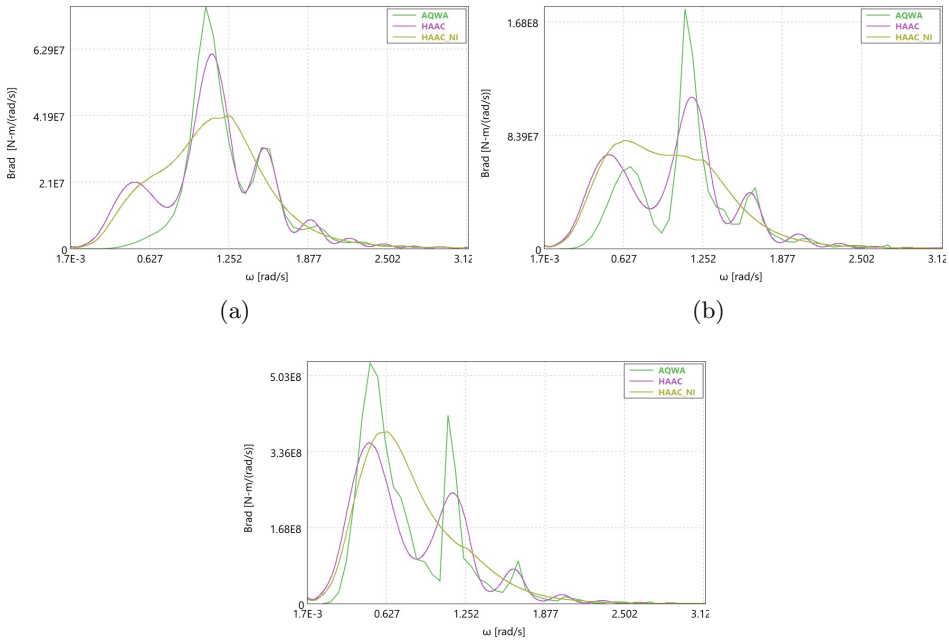

(a) (b)

(c)

Figure 4.5: Pitch radiation damping from $AQWA$ and $HAAC$ with (purple) and without (yellow) interaction for an array of cylinders of 10.5 m diameter, 17 m draft and separated a distance of 50 m. (a) 2 cylinders (b) 3 cylinders (c) 5 cylinders.

the estimated damping through $HAAC$ with and without including the interaction effects. It can be observed that the developed equation takes into account with really good accuracy the interaction effects on the radiation due to the presence of other cylinders. The accuracy seemed to improve as the number of cylinders in the array decreases, observing a better match for two cylinders than for five. This is because (4.7), as mentioned before, only accounts for the presence of the adjoining cylinders.

As shown in fig. 4.4, the accuracy of the present methodology varied with the distance between the columns, which is related to the smaller radiation and diffraction effects between the members as the separation between them increases. After applying (4.7), the prediction of the radiation damping improved and a valid region could be defined, achieving the best accuracy when the distance between the columns was from $2.5D$ to $7.5D$. In fig. 4.6, the resulting radiation damping taking into account the interaction between the columns through (4.7) is given for an array of two equal columns separated different distances. The s/D ratios of the case studies assessed in this work covered a wide range of values from 3.08 to 7,

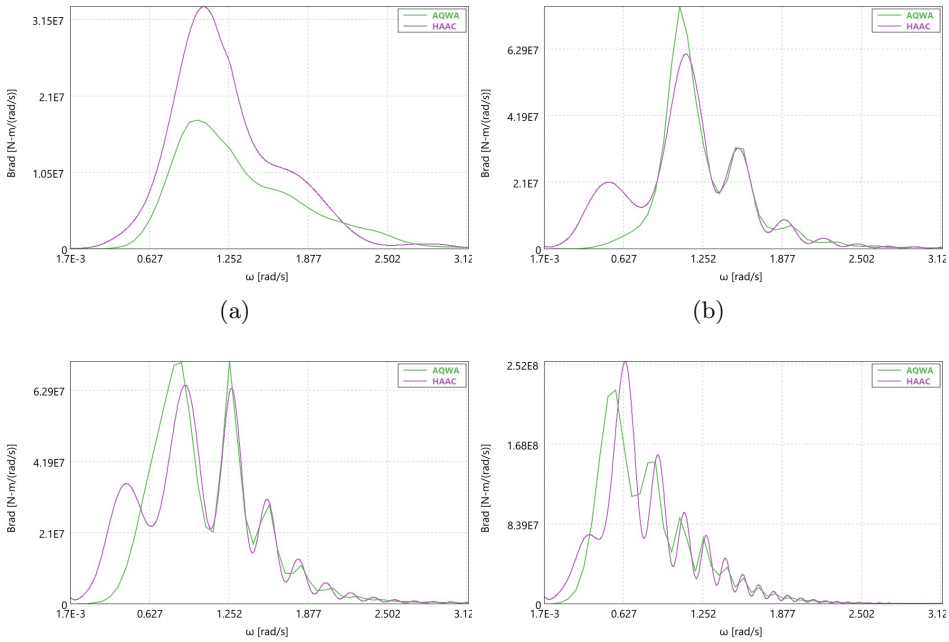

Figure 4.6: Pitch radiation damping from *AQWA* and *HAAC* for an array of two cylinders of 10.5 m diameter, 17 m draft and separated a distance (a) 15 m (b) 50 m (c) 75 m (d) 150 m.

which provided a good estimation of the radiation damping, not only for the typical dimensions of the current semi-submersible floaters but also for the potential values of the platforms supporting bigger turbines.

Depth Variation in Submerged Horizontal Bodies

The pontoon is modelled as four equal members, thus the interaction of the members is already considered in the database cases run off-line in *AQWA*. The hydrodynamic coefficients obtained after the three steps in section 4.1.1, correspond to a pontoon with the dimensions of interest but with the CoG located at the scaled depth after the third step described in section 4.1.1. Therefore, in order to obtain the added mass, radiation damping, and excitation loads of the target pontoon base, the coefficients should be transformed to the corresponding depth. Empirical formulae were developed for the added mass and radiation damping in (4.8) and (4.9), whereas the excitation loads were transformed through linear wave theory equations, as shown in (4.10).

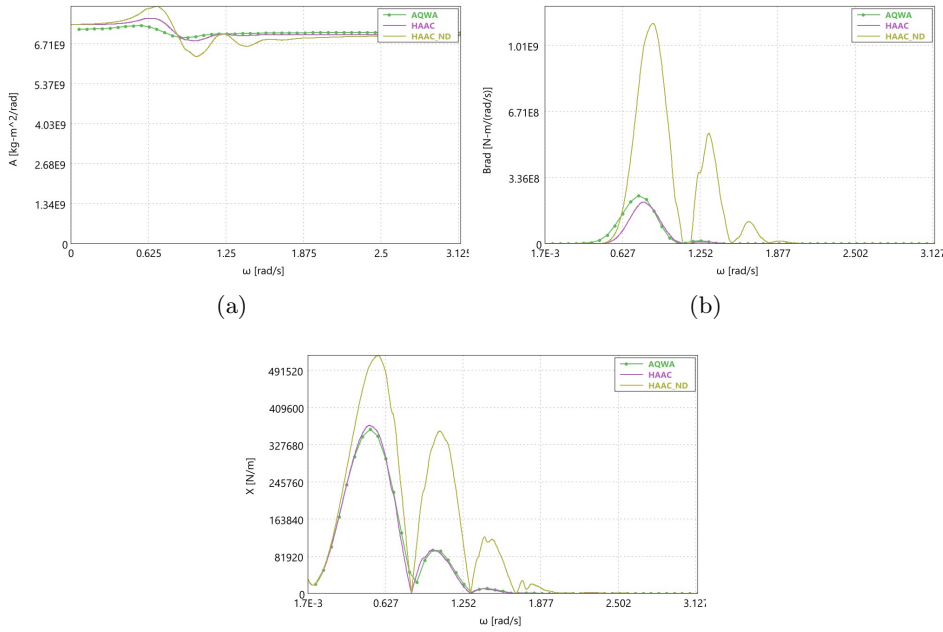

Figure 4.7: Pitch hydrodynamic coefficients for a pontoon 10 m wide and 45 m long and 25 m depth. $AQWA$ vs $HAAC$ with (purple) and without (yellow) considering the depth variation.(a) Added mass (b) Radiation damping (c) Excitation load amplitude.

$$A(\omega) = (A(\omega) - A_{inf}(\omega))e^{k(d_{sc}-d)} + A_{inf}(\omega) \tag{4.8}$$

$$B_{rad}(\omega) = B_{rad}(\omega)e^{2k(d_{sc}-d)} \tag{4.9}$$

$$X(\omega) = X(\omega)e^{k(d_{sc}-d)} \tag{4.10}$$

where k is the wave number, which was obtained through the generic dispersion relation, A_{inf} is the infinite frequency added mass matrix and d_{sc} and d are the scaled and target depths t which the pontoon is submerged.

These expressions were verified with $AQWA$ and the hydrodynamic coefficients for the pitch motion are given in fig. 4.7. The added mass was generally well predicted, while the depth variation did not seem to influence significantly. On the contrary, the depth showed to have a higher impact on the radiation damping and the excitation loads, achieving a very good match with the developed expressions. The most notable differences were found for the pitch motion, therefore, these are the results shown in this document. The surge and the heave motions were accurately predicted,

although the former has a minor contribution to the full semi-submersible platform.

4.1.3 Last Step: Superposition

Now that the additional contributions described in section 4.1.2 have been introduced, the hydrodynamic coefficients of the semi-submersible floater are obtained by means of superposition, referring the moments to the platform PoF. For that purpose, the estimated hydrodynamic coefficients of the isolated cylinder are referred to the PoF of the case study platform, considering the locations of each of the columns in the configuration. Then, the presence of the other cylinders regarding the radiation effects is accounted for through the developed expression eq. (4.7) for each of the columns and they are summed together with the coefficients of the pontoon.

4.2 Validation of the *HAAC* methodology

Up to this point, hydrodynamic coefficients related to various platform components have been discussed, and the impact of design parameters on the accuracy of the *HAAC* methodology has been explored. In this section, the proposed methodology for the hydrodynamic coefficients of semi-submersible platforms is validated. For that purpose, the hydrodynamic coefficients of the complete semi-submersible platforms defined in table 3.8 are compared against the results from the radiation-diffraction analysis performed in ANSYS-AQWA. Herein, only the most representative results are shown. According to the main motivation for the development of this methodology, the reduction in computational cost achieved compared to the conventional approach is exposed.

4.2.1 Full Floater Hydrodynamic Coefficients

The hydrodynamic coefficients, such as the added mass, radiation damping and wave excitation loads, for each of the platform designs defined in table 3.8 are here shown. The results derived from the proposed methodology are compared to those obtained through the SoA radiation-diffraction analysis in ANSY-AQWA, and henceforward, it will be denoted as *AQWA*.

The first step to take for the application of this method is to create a database for each of the platform members, as explained in section 4.1.1. In this study, the Nautilus platform was used as a case study, thus, the platform was split into four individual columns and a pontoon composed of four rectangular segments. The latter was considered as a unique body. This follows the procedure explained throughout section 4.1. The database was

built using the radiation-diffraction panel code ANSYS-AQWA. A total of 50 periods with equal spacing between 2 and 100 s were used and a constant maximum element size of 1.2 m was set, in order to maintain the analysis frequency range. Seven isolated partially submerged vertical cylinders of a constant draft of 17 m and varying diameter-to-draft ratios from 0.11 to 1.35 were modelled. Similarly, simulations of seven pontoons composed of four rectangular prisms at a depth of 13 m with a constant height of 1.5 m, constant length of 45 m, and varying width-to-length ratio from 0.066 to 0.51 were carried out. Then, as above mentioned, the hydrodynamic coefficients of the full floater were obtained through the superposition of the columns and the pontoon, all of them referred the PoF of the case study FOW platform.

Moreover, for the validation of the method, simulations in ANSYS-AQWA of the different platform designs described in table 3.8 were performed for the same frequency vector and maximum element size as in the database.

In fig. 4.8 to 4.15, the added mass, the radiation damping, and the amplitude of the excitation loads, respectively, for the semi-submersible floater D12, D26 and D29 obtained through $HAAC$ are compared against the results from $AQWA$. The reason for showing the results corresponding to these designs is that they cover the extreme values of D/d and D/s ratios, which range from 0.14 to 0.3, 0.5 to 1.36, respectively, and an intermediate one with 0.19 and 0.87. Furthermore, it was observed that the minimum error was achieved for the designs with the lowest values of D/s and D/d and vice-versa. The D/s ratio is strongly related to the superposition among the columns, occurring that as the columns were closer to each other, more significant interaction effects took place. As in $HAAC$ the cross-member interaction was neglected, worse agreement with the hydrodynamic coefficients from the conventional radiation-diffraction analysis was observed. As for the D/d, it was found that is more related to the a/d ratio, since the diameter of the columns and the pontoon width were set equal. The influence of this parameters are related to the interaction between the columns and the pontoon, noticing that when the pontoon was a large volume compared to that of the columns, the interaction between these members became more important, and therefore, neglect it resulted in higher deviations with respect to $AQWA$. Since the accuracy of the heave coefficients is implicit in the pitch moment results, only the surge and pitch motions are here shown, and its accuracy is discussed too. The remaining DoFs are not given here due to the double symmetry of the case study platform configuration.

The added mass in the surge direction showed some peaks that are due to the interaction effects of the columns, which were not captured with

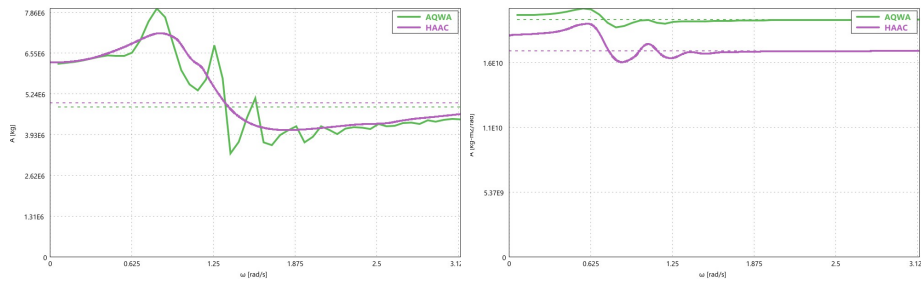

(a) (b)

Figure 4.8: Added mass for D12 platform. (a) Surge (b) Pitch.

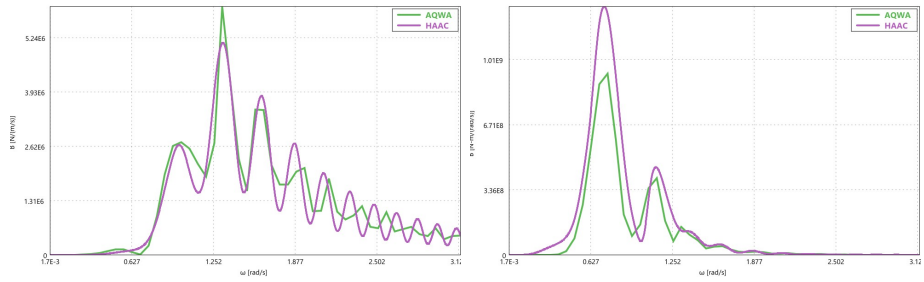

(a) (b)

Figure 4.9: Radiation damping for D12 platform. (a) Surge (b) Pitch.

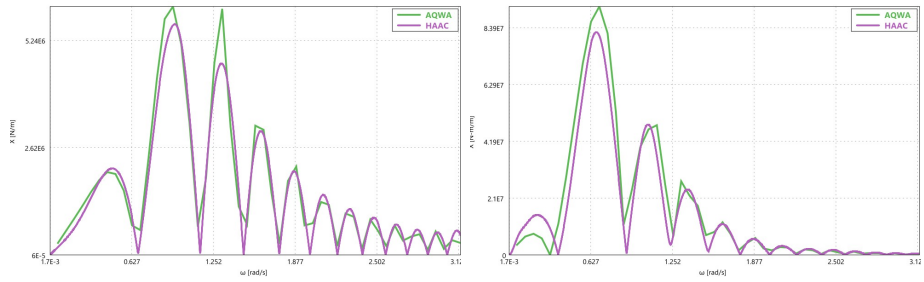

(a) (b)

Figure 4.10: Excitation force magnitude for D12 platform. (a) Surge (b) Pitch.

HAAC due to the direct superposition, although the value at zero and infinite frequency seemed to be accurately predicted. Still, the deviation in surge with respect to the results from the *AQWA* model ranged from 6-19%, using the error definition given in (4.6). The added mass in the pitch direction showed an under-prediction of 12-28%, a similar value to the deviation in the heave motion; and it is mainly related to the superposition

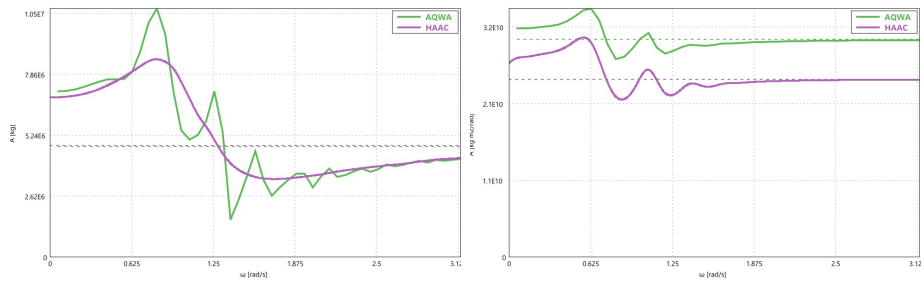

(a) (b)

Figure 4.11: Added mass for D26 platform. (a) Surge (b) Pitch.

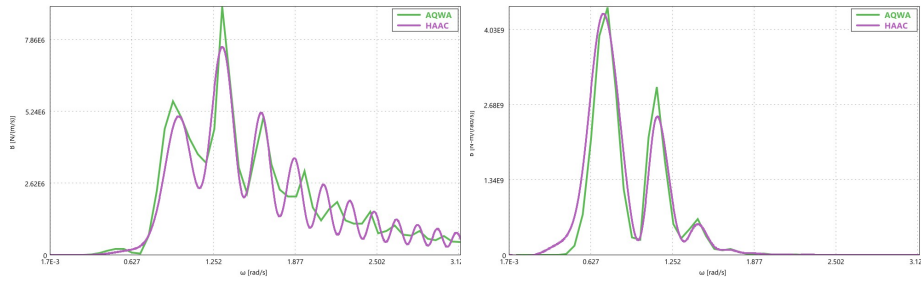

(a) (b)

Figure 4.12: Radiation damping for D26 platform. (a) Surge (b) Pitch.

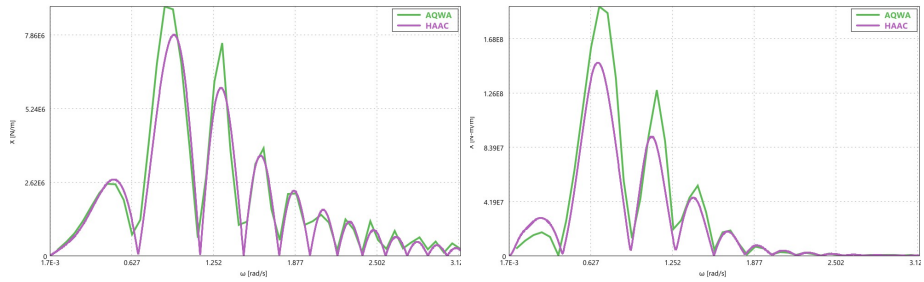

(a) (b)

Figure 4.13: Excitation force magnitude for D26 platform. (a) Surge (b) Pitch.

of the columns and the pontoon base. In addition, it was observed that considering the pontoon as four equal prisms instead of a closed structure resulted in a correlation with the lost area. However, these findings require further investigation in future work.

Regarding the radiation damping, the surge DoF seemed to be estimated with reasonable accuracy, although it was not as good as in the case of the

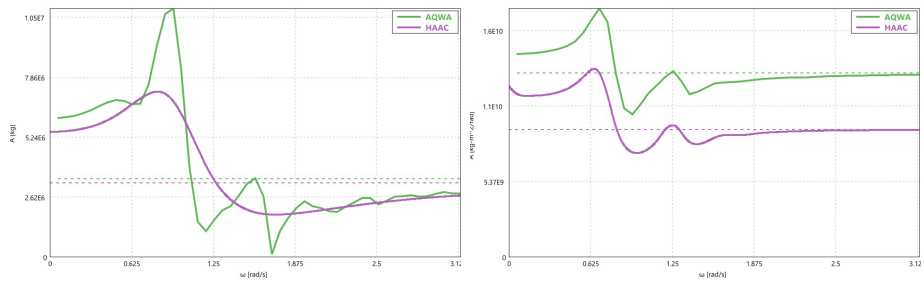

(a) (b)

Figure 4.14: Added mass for D29 platform. (a) Surge (b) Pitch.

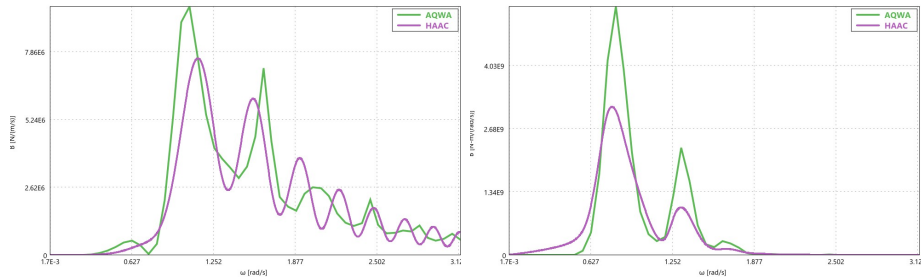

(a) (b)

Figure 4.15: Radiation damping for D29 platform. (a) Surge (b) Pitch.

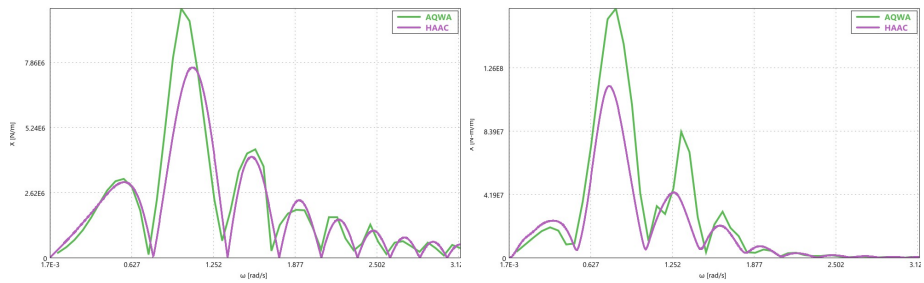

(a) (b)

Figure 4.16: Excitation force magnitude for D29 platform. (a) Surge (b) Pitch.

added mass. Nevertheless, the correction that accounts for the interaction effects by means of (4.7), provided a better match of $HAAC$ with $AQWA$, obtaining an error of 21-34% for the surge direction and 23-48% for the pitch, substantially smaller than the 30% and 58% observed for the array of two columns of the same D/s ratio in fig. 4.4.

The excitation loads showed good approach through the present meth-

odology, despite the assumption of negligible interaction between members. The surge again showed the smallest deviation with respect to the *AQWA* results, with 13-26% error. This is because the interaction has a minor effect on the surge direction due to the important role of the columns. However, larger errors were found in heave and pitch, where the interaction effects between the columns and the pontoon became more relevant, producing deviations of 15-40% and 18-38% for heave and pitch, respectively. It was observed that these errors are mainly related to the superposition. These errors might seem large, however, as it is shown in the following sections, they do not have a substantial impact on the FOWT response motions.

4.2.2 Computational Effort Reduction

The *HAAC* methodology showed to estimate the hydrodynamic coefficients of semi-submersible platforms with a reasonable accuracy for the preliminary design phase of the platforms for offshore wind. The main motivation for the development of this method is the lack of efficient tools that enable to make important decisions since the early stages of design, such as the platform configuration and main dimensions.

The time required for the radiation-diffraction analysis of the platform designs defined in table 3.8 evaluating 50 periods, from 2 s to 100 s equally spaced, varies with the size of the platform. The simulation time ranges from 13,000 s for the smallest substructure to 23,269 s, for the largest. Bear in mind that in this work the same maximum element size was used for the meshing set up in order to keep the same frequency range. The CPU used for the validation of the methodology has four cores through parallel technique in a computer with two Intel Xeon E5-2630 CPUs and Hyper-Threading active.

The present methodology estimated the hydrodynamic added mass, radiation damping, and excitation loads in less than 1 s, once the database is created. Furthermore, as it is based on the interpolation of a set of hydrodynamic coefficients, it does not depend on the geometry. The database setting for seven cylinders and seven pontoons took an overall simulation time of 60,000 s, which is between 2-5 times the time required for the radiation-diffraction analysis of a single floater design. This means that if less than five floaters aimed to be compared, it is worthy to perform a radiation-diffraction analysis in a panel code based tool, since no computational cost is saved and a higher accuracy will be obtained. However, during the preliminary design stages of the FOW substructures, generally tens of different platforms are assessed, making the present methodology suitable.

Since the computational time of *HAAC* is mainly that of the database

setting, the number of geometries and the number of frequencies to use for the interpolation would drive the computational effort reduction achieved with this method. The time required for the basic steps in section 4.1.1 is nearly negligible, thus the number of platform designs whose hydrodynamic coefficients need to be calculated does not imply a significant increase of the simulation time.

4.3 Integration of *HAAC* into the Frequency Domain Model

Once the hydrodynamic coefficients obtained through the proposed methodology have been validated against the radiation-diffraction analysis and a sensitivity of the influence of the different platform design parameters on the method's accuracy has been assessed, the impact of these differences on the FOWT response is evaluated and discussed. For that purpose, as shown in fig. 4.17, the frequency domain response model was fed with the hydrodynamic coefficients derived from both *HAAC* and *AQWA*, and the response obtained in the four DoFs were compared. Previous to the response calculation, as a part of the *HAAC* methodology's validation process, it is crucial to ensure that the natural periods for various platform designs are estimated with consistent accuracy and that the FOW structure's dynamics remain relatively unchanged. Therefore, the accuracy on the calculation of the natural periods for each FOWT was also quantified.

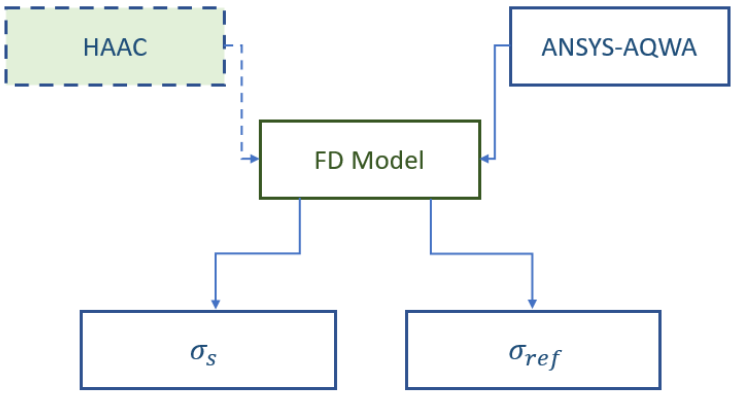

Figure 4.17: Scheme diagram for *HAAC* validation process.

4.3.1 System Natural Periods

The natural periods were determined through an eigenvalue problem, taking into account both the total mass and total stiffness at the equilibrium position of the FOWT. The hydrostatic stiffness, which is based on the platforms' geometry, was computed numerically.

The natural period values for different FOWT supported by the different platform designs were previously presented in section 3.3.6. In this section, the differences concerning the natural periods when using the hydrodynamic added mass derived from the *HAAC* methodology or from *AQWA* are examined. To facilitate this comparison, the error for each DoF was calculated and is given in fig. 4.18.

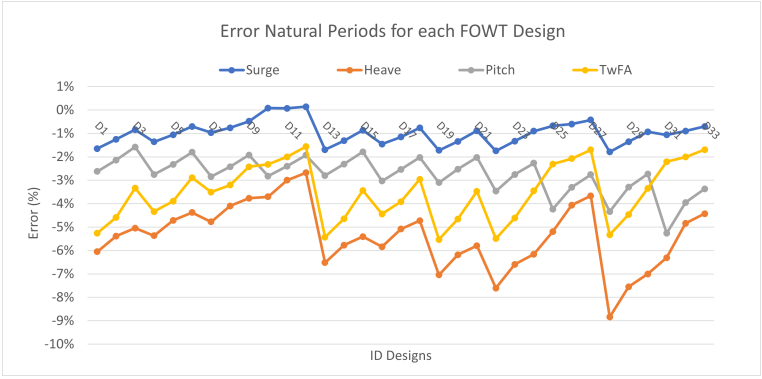

Figure 4.18: Error obtained for the natural periods between *HAAC* and *AQWA*. Negative sign means under prediction through *HAAC*.

In the previous sections, it was observed that the added mass in heave and pitch derived from *HAAC* are under estimated with respect to *AQWA*. This leads to an under prediction of the natural period in those DoFs, as it can be noticed in fig. 4.18, where except for those designs with an error close to zero, generally the sign is negative, which means under prediction of the natural period based on the definition of error used (4.11). Being T_s and T_{ref} the estimated and reference natural periods.

$$\epsilon_T = \frac{T_s - T_{ref}}{T_{ref}} \tag{4.11}$$

In general, really good agreement was observed, with deviations below 9% with respect to the reference natural periods. Surge motion natural periods showed the best agreement with *AQWA*, with deviations below 2%. The error values decreased with the diameter, with the separation of the columns and with the draft. This is related both to the columns contribution to the mass and stiffness system matrices and to the little influence

of cross-interaction. As observed in the results of the hydrodynamic coefficients, the columns seemed to show better results than the pontoon, thus, the larger the columns and the larger the distance between the them, the higher the method's accuracy. In section 3.3.6, it was observed that the incident wave peak periods were very far from the natural periods, so it is unlikely to cause resonance in this DoF.

The DoF that showed the worst match is the heave motion, although the deviations are no larger than 9% with respect to *AQWA*. Notably, this error pattern appeared less consistent than that observed in surge motion. It was primarily influenced by interaction effects, with the error decreasing substantially as the separation between the columns increased. In fact, the error was halved when transitioning from a 50-meter separation to a 70-meter separation between columns.

The natural periods for pitch motion followed a similar trend as the heave DoF, but this time they appeared to align closer with the reference values. This improved agreement can be attributed to the accurate prediction of the surge contribution to pitch motion. In cases where the platforms have very low D/s ratios, deviations below 2% can be achieved, while for scenarios where interaction effects became more significant, the error reached up to 5.5%.

Regarding the natural periods for the first tower fore-aft mode shape deflection, different contributions are taking part, such as the platform surge and pitch motions, as well as the modal deflection by the firs fore-aft model shape. For this reason, it did not always occur that the lower the D/s, the better accuracy was achieved. The influence of the surge and the pitch dynamics to the tower deflection natural frequency will be later assessed and discussed. Still, really good match was achieved between the estimated and the reference values, achieving a maximum deviation of 5.2%.

In section 3.3.6, certain designs exhibited heave natural periods quite near the wave peak period associated with the severe sea state ($T_p = 16$ s). The proximity of the natural period from the excitation period is a crucial consideration for designers. However, it is important to note that since the natural periods, as estimated using the hydrodynamic added mass from *HAAC*, were slightly under estimated, this means that for some platform designs the heave natural period may approach closer to the $T_p = 16$ s. The subsequent assessment will help determine the impact of this proximity on the response under such excitation conditions.

4.3.2 Dynamic Response of the FOWT

Given that the primary objective of this methodology is to facilitate a rapid evaluation of the dynamic behaviour and response of FOWT using various

platform designs, the focus here is on quantifying the propagation of differences observed between the radiation-diffraction analysis and the *HAAC* methodology in the response analysis. To achieve this, the hydrodynamic data from both *AQWA* and *HAAC* was incorporated into the frequency domain based response model described in chapter 3. This is shown in fig. 4.17. Since the interest here resides in evaluating the accuracy of the proposed hydrodynamic approach, only wave excitation was considered as input to the model and no wind excitation was input. While this approach may not entirely mirror real-world scenarios, especially for moderate and severe sea conditions, it does offer valuable insights into the capabilities of this methodology. Moreover, in practical situations where wind excitation is a factor, the impact of disparities between *AQWA* and *HAAC* on the response would tend to be less significant. Consequently, the response of the FOWT under the conditions specified in table 3.1 was assessed. These DLCs cover a wide range of mild, moderate and severe sea states, representing 50-year of significant wave height H_s and peak periods T_p. Below a table with the DLCs used for this validation is given:

ID	**Type**	H_s	T_p
SS1	Mild	1.67	8.0
SS2	Moderate	6.20	12.5
SS3	Severe	10.90	16.0

Table 4.1: Sea states used for the *HAAC* validation. (Units: m, s)

The response of the thirty-three platform designs considered in table 3.8 under the DLCs described in table 4.1 are shown and discussed in this section. Despite some of the disagreements observed in the previous results of the hydrodynamic coefficients, it is important not to forget the main goal of this work: to be able to reach the same conclusions regarding the dynamic behaviour of the FOWT in a comparative analysis of several platform designs as if the hydrodynamic coefficients from the radiation-diffraction analysis were used to feed the frequency-domain based response model.

Operating in the frequency domain where signals follow a Gaussian distribution, the dynamic response is expressed through the standard deviation of the response spectrum. The error definition used to measure the accuracy is given in (4.12).

$$\epsilon_\sigma = \frac{\sigma_s - \sigma_{ref}}{\sigma_{ref}} \tag{4.12}$$

where σ_s and σ_{ref} are the standard deviation of the response obtained from the frequency domain model using the hydrodynamic coefficients from *HAAC* and *AQWA*, respectively.

In fig. 4.19, 4.20, and 4.21, the standard deviation of response is given for each of the platform designs described in chapter 3 for the mild, moderate, and severe sea states, respectively. For the three sea states and the four DoF, there was found a general under prediction of the response standard deviation when the hydrodynamic coefficients from *HAAC* are fed to the frequency domain response model. This is related to the superposition, and consequently, to assume no interaction between members. Particularly, the under estimation excitation loads lead to lower displacements.

The surge displacement of the FOWT is significantly influenced by the mooring system. In this comparative analysis, it has been assumed the same mooring stiffness matrix for all designs. While this primarily affects the static response, it does result in relatively minor differences between the responses obtained using *HAAC* and *AQWA*. Additionally, it is important to note that the columns play a crucial role in the surge motion. Consequently, as the separation between the columns increases or the draft deepens, the error between the two methods decreases. Among the cases considered, the most accurate estimation of the standard deviation of the surge motion was achieved for D3, with a deviation of only 0.5% under SS2 conditions. Conversely, the least accurate case is D31, with a 15% deviation under SS1 conditions. It is worth highlighting that while this error may seem substantial, it should be viewed in the context of the relatively small standard deviation values obtained.

Similar trends to those observed in surge motion were also noticed in heave motion. In this DoF, the contribution of the pontoon to interaction effects is particularly crucial, leading to better agreement between the two methods as the pontoon length increases. Additionally, an improved match was achieved when the platform's draft increased, meaning longer columns. The most accurate prediction of the standard deviation of heave motion through the proposed method was observed for D12 under SS2 conditions, with almost zero error. Conversely, the closest match was found for D1, also under SS2 conditions, with a 19% error. Interestingly, it appeared that the sea states do not significantly affect the accuracy of the *HAAC* methodology in this context.

Regarding the pitch angle an nacelle acceleration standard deviation, very good approximation was achieved for SS1 and SS2. For mild sea states the error was nearly constant for all designs, although there was a slightly decreased as the draft of the columns increased. This is related to the major contribution of the columns to the hydrodynamic coefficients, and it has already been demonstrated that the *HAAC* methodology provided a very good estimation of arrays of columns. Furthermore, the higher are the columns with respect to the pontoon, the better accuracy was achieved. In

other words, the lower the D/s ratio, the lower deviation. The minimum error for the nacelle acceleration are found for the designs with the lowest values of D/s ratio, meaning that the interaction effect between the columns and the pontoon are less important.

On the contrary, it is noticeable that the results regarding SS3 did not agree as well as the previous results. In addition, here the results using the coefficients from $HAAC$ lead to over predict the response for cases with larger low draft columns and large width pontoons. However, this results are not realistic since usually when such moderate or severe sea states occur, they come together with wind. In order to have a more real idea of the accuracy of the proposed methodology, wind action was included to the severe sea conditions. The corresponding results are depicted in fig. 4.22, where the standard deviation of the response under SS3, but now with the excitation of turbulent wind with mean wind speed of 12 m/s. This wind speed is very close to rated speed, thus the thrust force has almost reached the maximum value. This corresponds to DLC8 described in table 3.1.

Compared to the results were only wave action was considered, when wind action is included, the differences between the response using $HAAC$ or $AQWA$ were diminished. This is explained because the wind excitation was the same for all platform designs, since they support the same wind turbine, thus it does not depend on the hydrodynamic analysis. This resulted in the damping of the inaccuracies derived from $HAAC$. Consequently, and as it was expected, as the wind loads became more important, the response signals agreed better. Now, the surge motion standard deviation was predicted with very high accuracy, with almost no difference between both signals. The heave motion achieved deviations below 10% for all cases. The platform pitch angle showed very good match between $AQWA$ and $HAAC$ in general. The platform designs with the highest D/s ratio, were those that worse agree. Despite those cases, the both methods provided similar dynamic behaviour regarding the pitch angle and the nacelle acceleration. Taking into account the main purpose of this Thesis, the good prediction of the response in these two DoF is crucial to provide confidence to the proposed design tool.

As for the nacelle acceleration, they provided the largest differences compared to the rest of DoF. This is partly related to the double derivative of the nacelle deflection, which leads to an increasing mismatch of the signals as the number of derivatives increases. In addition, those error values correspond to the cases where the maximum deviation was found. Despite this fact, it was still considered a good result since the tendency was coherent with the reference signal and, moreover, because $AQWA$ performs a frequency-domain-based analysis, whose accuracy is also limited.

It is interesting to see how the calculation of the hydrodynamic coefficients by means of the proposed methodology $HAAC$ provided the same tendency as if the potential flow problem had been solved. This is the main idea of the $HAAC$ and it has shown to provide similar results as with the radiation-diffraction hydrodynamic coefficients. Therefore, despite the slight disagreements observed in the response, they still enable us to achieve similar conclusions as the state-of-the-art tools, with much higher computational efficiency.

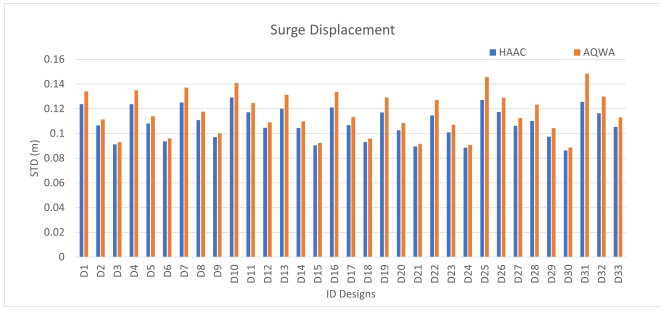

(a)

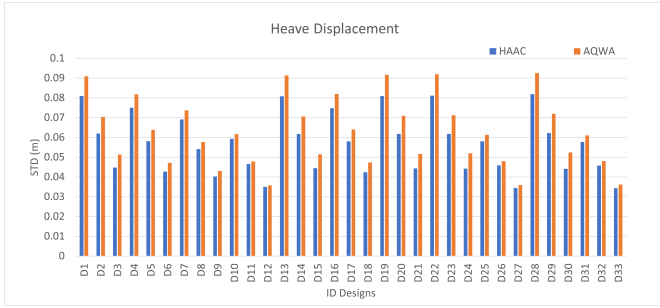

(b)

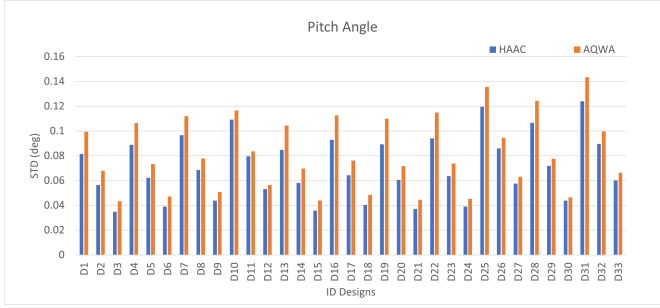

(c)

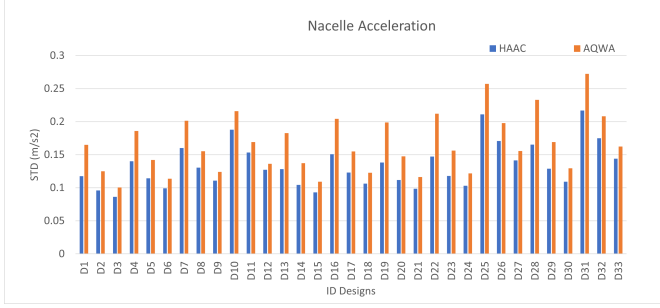

(d)

Figure 4.19: Response standard deviation for each design under SS1 (a) Surge [m]. (b) Heave [m] (c) Pitch [deg] (d) Nacelle Acceleration [m/s^2].

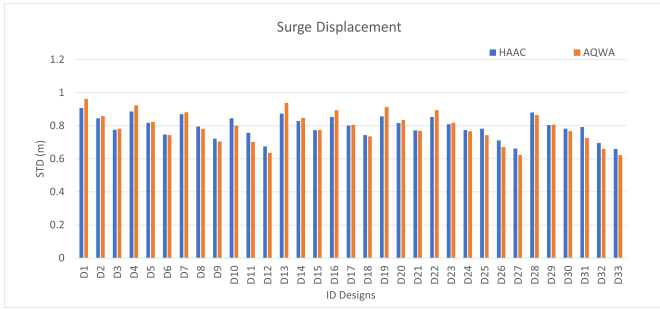

(a)

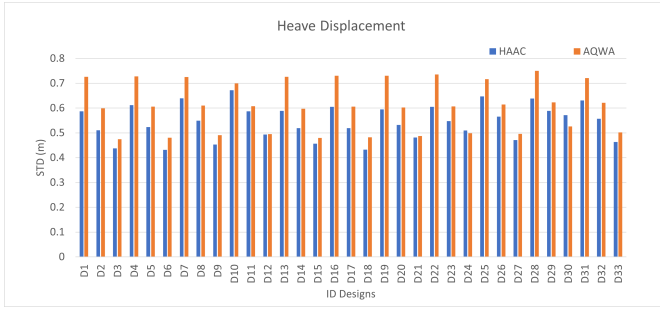

(b)

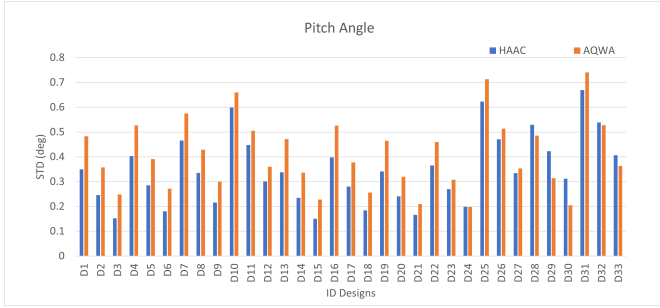

(c)

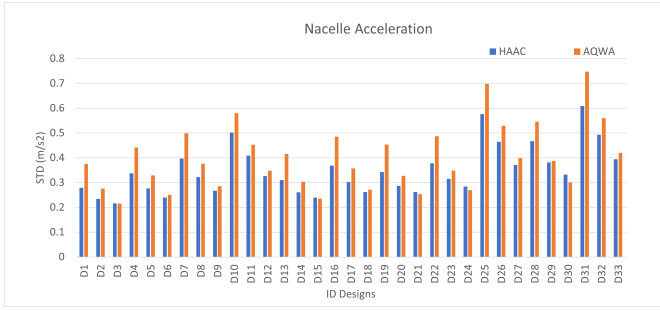

(d)

Figure 4.20: Response standard deviation for each design under SS2 (a) Surge [m]. (b) Heave [m] (c) Pitch [deg] (d) Nacelle Acceleration [m/s^2].

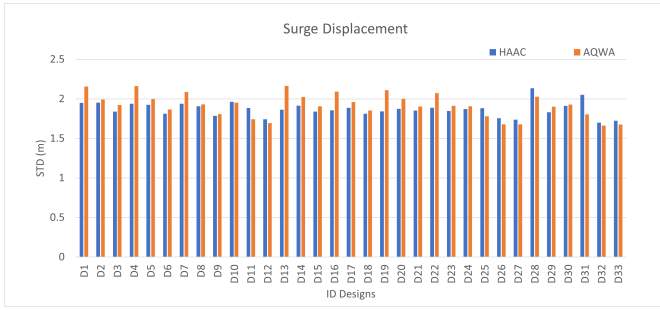

(a)

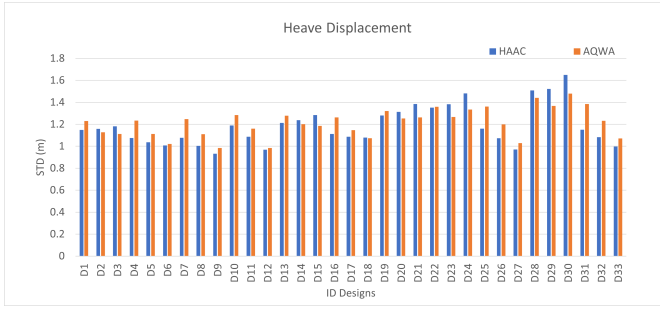

(b)

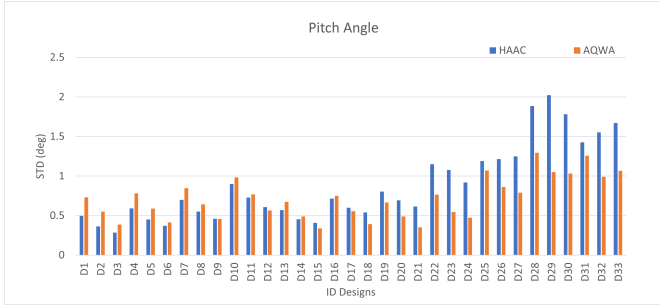

(c)

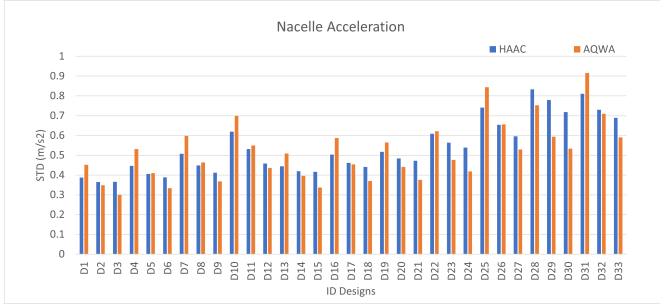

(d)

Figure 4.21: Response standard deviation for each design under SS3 (a) Surge [m]. (b) Heave [m] (c) Pitch [deg] (d) Nacelle Acceleration [m/s^2].

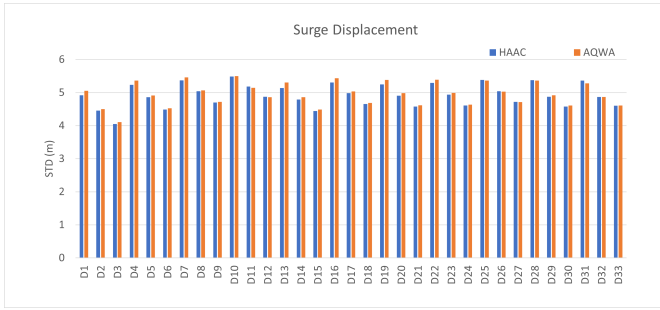

(a)

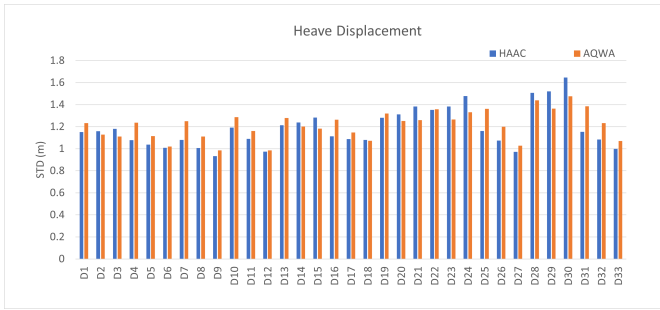

(b)

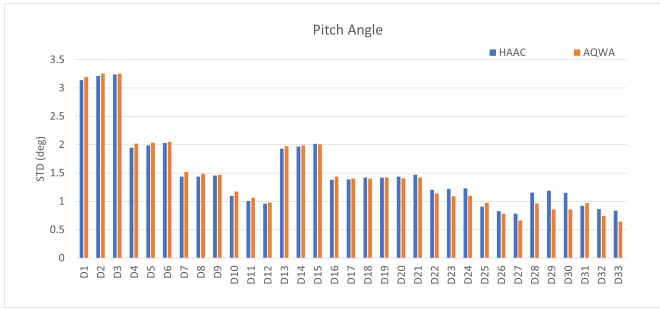

(c)

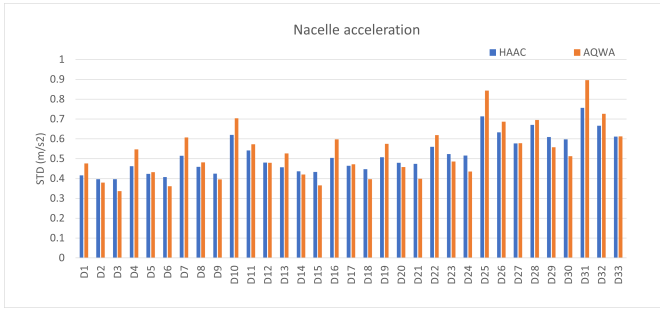

(d)

Figure 4.22: Response standard deviation for each design under DLC8 (a) Surge [m]. (b) Heave [m] (c) Pitch [deg] (d) Nacelle Acceleration [m/s^2].

Chapter 5

Approach for the Second-Order Hydrodynamic Loads Calculation of Semi-Submersible Platforms

In preceding chapters, it has been emphasised the significance of second-order hydrodynamic wave loads and discussed the existing methods for their computation. Typically, these loads are considered in advanced design stages due to their computationally intensive nature. However, this Thesis introduces an innovative approach that efficiently estimates second-order wave loads acting on semi-submersible platforms, rendering it suitable for the preliminary design phase of such substructures. This method is grounded in slender-body theory and formulates its approach based on the Morison and Rainey force model. It is important to note that the development of the accelerated method for semi-submersible platforms was carried out with the guidance and support of H. Bredmose and A. Pegalajar, as it extends their original method, which was initially implemented for an isolated slender vertical cylinder in [63, 64, 80].

Similarly to the *HAAC* methodology described in chapter 4, the method has been implemented for the Nautilus semi-submersible platform based on the LIFES50+ project [2], although it could be further tailored for other platform configurations. The accelerated method was already validated for slender vertical cylinders in previous work, such as in spars [64] or monopiles [63], but semi-submersible platforms are generally shorter columns,

leading to larger deviations with respect to the results using the conventional radiation-diffraction analysis. Therefore, some parametric studies were carried out for different cylinder diameter-to-draft ratios and diameter-to-wavelength ratios. In addition to drawing conclusions from the parametric studies conducted on the columns, a significant contribution in this work is the expansion of the accelerated method to semi-submersible platforms. To accomplish this, formulations for heave forces acting on the columns and loads on the horizontal pontoon members were developed. Furthermore, the evaluation of the validity of applying superposition, assuming negligible interaction among platform components was evaluated.

To validate the proposed approach, the estimated second-order hydrodynamic loads were compared with conventional methods commonly employed for this type of analysis. Then, for the same reasons as explained in the previous chapter, the accuracy of the method was assessed by evaluating the impact on the FOWT response analysis. For that purpose, the frequency domain response model described in chapter 3 was fed with the second-order hydrodynamic loads derived from the present method, and the response was compared against that derived from the same frequency domain response model fed with the loads obtained by means of the conventional method as in (3.21).

This chapter is structured as follows. First, in section 5.1 the proposed accelerated method for the second-order hydrodynamic load calculation is presented. Then, in section 5.2 the results obtained under certain sea states are shown and discussed. Furthermore, in section 5.3, the sensitivity of the method's accuracy is assessed by evaluating the influence on the FOWT response motions and the importance of the inclusion of the second-order hydrodynamic loads during the initial stages of the substructures' design is discussed.

5.1 Accelerated Method for Second-Order Loads on Semi-Submersible Floaters

In this section, the extension of the accelerated method originally developed by Bredmose et al. [63] for the estimation of the second-order hydrodynamic loads at linear cost on slender vertical cylinders to semi-submersible platforms is described. It is based on the Rainey (1995) [78] force model plus the standard Morison viscous force. The core of this method is that the time-consuming double sum over frequencies (see 3.21) can be bypassed by using instead the eigenvalue decomposition of the corresponding quadratic load transfer function. Since the results of the accelerated method are here bench-marked against results from a potential flow radiation-diffraction

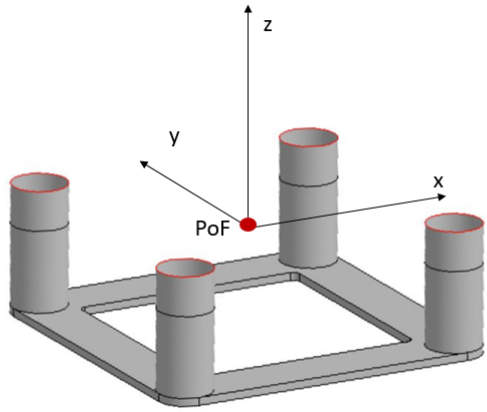

Figure 5.1: Semi-submersible platform and global reference frame.

solver, drag forces were not considered.

A semi-submersible platform its not slender itself, thus, it is split into simple members that can be considered, to a certain extent, as slender bodies. Similarly to the decomposition made for the *HAAC* methodology in chapter 4, four individual columns and, this time, also four individual rectangular prisms that form the pontoon are considered. Then, superposition is applied for the calculation of second-order loads of the full semi-submersible floater.

The coordinate system used throughout the study has its origin at the Point of Flotation (PoF), placed at the Mean Sea Level (MSL), with the z-axis pointing upwards and the x-axis pointing in the direction of the wave propagation. The y-axis follows the right-hand convention, as shown in fig. 5.1. The moments of the full platform are referred to the PoF and the contribution from surge and heave forces to the pitch moment must be considered, as well as the phases need to be referred to the global reference coordinate system.

A semi-submersible floater is usually composed of vertical members, which are commonly cylindrical columns, supported or connected by horizontal members, which can be cylinders or rectangular prisms. The Morison and Rainey force model are applied and integrated along the longitudinal axis, and depending on its orientation with respect to the wave propagation direction, the quadratic transfer functions for each member are formulated. This Thesis is focus on rectangular prisms, such as the ones shown in fig. 5.2.

As a slender-body theory-based method, the accelerated method obtains the second-order loads by means of analytical integration from the first and second-order wave velocity potential given by

$$\phi^{(1)} = \sum_{j=-N}^{N} \hat{B}_j e^{i(\omega_j t - k_j x)} \frac{\cosh k_j(z+h)}{\cosh k_j h} \tag{5.1}$$

$$\tilde{\phi}^{(2)} = i \sum_{m=-N}^{N} \sum_{n=-N}^{N} \hat{\tilde{B}}_m \hat{\tilde{B}}_n \mathcal{T}_\phi e^{i((\omega_m+\omega_n)t-(k_m+k_n)x)} \frac{\cosh{(k_m+k_n)(z+h)}}{\cosh{(k_m+k_n)h}} \tag{5.2}$$

$$\mathcal{T}_\phi = \frac{1}{2} \frac{2(\Omega_m+\Omega_n)(\Omega_m^2\Omega_n^2+\kappa_m\kappa_n)+\Omega_m(\Omega_n^4-\kappa_n^2)+\Omega_n(\Omega_m^4-\kappa_m^2)}{(\Omega_m+\Omega_n)^2-(\kappa_m+\kappa_n)\tanh{(\kappa_m+\kappa_n)}} \tag{5.3}$$

$\phi^{(1)}$ and $\tilde{\phi}^{(2)}$ are the first- and second-order velocity potentials, the former expressed in dimensional form and the latter, in non-dimensional form, see (5.6). Furthermore, Ω and κ are the non-dimensional angular frequencies and wave numbers k, also defined in (5.6). $\hat{B}$ is the Fourier amplitude of the linear velocity potential and z and h are the vertical distance along the z-axis and the water depth, respectively, and $\tilde{}$ represents a non dimensional parameter. Here a double-sided Fourier series with complex Fourier amplitudes is used for the sake of simplicity since cosine/sine and sub/super harmonics are indistinctly considered this way.

5.1.1 Definition of the Non-Dimensional Parameters

The second-order force for a vertical column can be written as a function of the following parameters

$$F = f(\rho_w, g, h, d, D, L_w, \nu, \hat{B}) \tag{5.4}$$

Where F is the force, ρ_w is the water density, g is the gravity acceleration, h is the water depth, d is the substructure's draft, D is the column diameter, L_w is the wave length, ν is the fluid viscosity and $\hat{B}$ is the Fourier amplitude of the linear velocity potential. By normalising lengths with D [81], they can be written the non-dimensional second-order force as follows

$$\tilde{F} = f(\frac{D}{d}, \frac{D}{L_w}, \frac{D}{h}, \hat{B}, \mathrm{Re}) \tag{5.5}$$

where the Reynolds number, Re, can be left out since only in-viscid loads are considered. Therefore, the parametric studies will analyse the influence on a single cylinder of two parameters: the diameter-to-draft ratio, $\frac{D}{d}$, and the diameter-to-wave-length ratio, $\frac{D}{L_p}$. The diameter-to-water-depth ratio is not studied here due to the relatively large water depth of $h = 130m$.

Therefore, the following non-dimensional variables for the analysis can be defined, as found in [63].

$$\Omega_p = \omega_p\sqrt{h/g},\ \kappa_p = k_p h,\ \tilde{\phi} = \phi\sqrt{h^3/g},\ \hat{\tilde{B}} = \hat{B}\sqrt{h^3/g} \tag{5.6}$$

where ω_p is the angular peak frequency and κ_p is the peak wave number.

5.1.2 Second-Order Loads on Vertical Cylinders

The formulation for the surge force and pitch moment of an isolated column was already developed by Bredmose et al. in [63], thus herein it has been briefly explained. In addition, the transfer function of the heave force is one of the parts of the extension of the original method, thus it is provided a detailed description of its development.

Surge and Pitch Second-Order Loads

The second-order hydrodynamic surge force is based on the formulation presented in [63], where each term is analytically integrated along the z direction, resulting in the velocity potential amplitude multiplied by the force quadratic transfer function. The surge force components acting on the vertical cylinder are four: the second-order Eulerian wave particle acceleration term, the convective acceleration term, the axial divergence term, and the free-surface term. The superscript indicates the first- (1) or second-order (2) of the wave kinematics and the second subscript c denotes the column. These forces are given by

$$F^{(2)}_{x1,c} = \int_{-d}^{0} \rho_w A_x (C_{m,x}+1) u_t^{(2)} dz \tag{5.7}$$

$$F^{(2)}_{x2,c} = \int_{-d}^{0} \rho_w A_x (C_{m,x}+1)(u^{(1)}u_x^{(1)} + w^{(1)}u_z^{(1)}) dz \tag{5.8}$$

$$F^{(2)}_{x3,c} = \int_{-d}^{0} \rho_w A_x C_{m,x} w_z^{(1)} u^{(1)} dz \tag{5.9}$$

$$F^{(2)}_{x4,c} = \rho_w A_x (C_{m,x}+1)\eta^{(1)} u_t^{(1)}|_{z=0} \tag{5.10}$$

From each of these terms, a separate quadratic transfer function is derived, as shown in [63]. The individual QTFs are added together into a single QTF, which, when multiplied by the two Fourier amplitudes of the velocity potential, gives the corresponding contribution to the second-order surge force. Expressing it in the non-dimensional form

$$\frac{F^{(2)}_{x,c}}{\rho_w A_x g h} = i \sum_{m=-N}^{N} \sum_{n=-N}^{N} \hat{\tilde{B}}_m \hat{\tilde{B}}_n e^{i((\omega_m+\omega_n)t-(k_m+k_n)x)} \mathscr{F}^{(2)}_{x,c} \tag{5.11}$$

where A_x is the cylinder cross-sectional area, $C_{m,x}$ is the added mass coefficient in the surge direction, $\mathscr{F}^{(2)}_{x,c}$ is the quadratic transfer function, and N the number of positive frequencies. The full derivation can be found in [63]. The evaluation of (5.11) involves a double sum over the number of frequencies, which would require a high computational cost for long time series. The load time series can be obtained in a much quicker way by means of eigenvalue decomposition of the quadratic transfer function, $\mathscr{F}^{(2)}_{x,c}$. First, (5.11) is given in matrix product form as follows:

$$\frac{F^{(2)}_{x,c}}{\rho_w A_x g h} = i \begin{bmatrix} \dots & \hat{\hat{B}}_m e^{i(\omega_m t - k_m x)} & \dots \end{bmatrix} \mathscr{F}^{(2)}_{x,c} \begin{bmatrix} \vdots \\ \hat{\hat{B}}_n e^{i(\omega_n t - k_n x)} \\ \vdots \end{bmatrix} \tag{5.12}$$

The quadratic transfer function $\mathscr{F}^{(2)}_{x,c}$ can be expressed as a product of eigenvalues, λ_j, and eigenvectors, V_j, where the j index corresponds to a given eigenvalue.

$$\frac{F^{(2)}_{x,c}}{\rho_w A_x g h} = i \sum_{j=1}^{2N} \begin{bmatrix} \dots & \hat{\hat{B}}_m e^{i(\omega_m t - k_m x)} & \dots \end{bmatrix} \mathbf{V}_j \lambda_j \mathbf{V}_j \begin{bmatrix} \vdots \\ \hat{\hat{B}}_n e^{i(\omega_n t - k_n x)} \\ \vdots \end{bmatrix} \tag{5.13}$$

$$\frac{F^{(2)}_{x,c}}{\rho_w A_x g h} = i \sum_{q=1}^{2N} \lambda_q \left[\sum_{m=-N}^{N} \mathbf{V}_{qm} \hat{\hat{B}}_m e^{i(\omega_m t - k_m x)} \right]^2 \tag{5.14}$$

Equation (5.13) results in the product of two identical pseudo time series that can be reformulated considering the symmetry, and that provide the force at linear cost $O(NlogN)$ via inverse Fast Fourier Transform ($iFFT$). The key equation of the accelerated method is presented in (5.14), where modal truncation has been applied. By this method, considerable computational savings are achieved, since only a few modes, q, are necessary to accurately obtain the second-order hydrodynamic load and, therefore, the load time series can be obtained at a computational cost of $O(NlogN)$.

As for the pitch moment on a single cylinder, the arm of the surge force in each position along the z-axis is introduced and the integral is solved analytically in a similar way as for the surge force. This is also detailed in [63], thus only the final formulation is given here.

$$\frac{M^{(2)}_{y,c}}{\rho_w A_x g h^2} = i \sum_{m=-N}^{N} \sum_{n=-N}^{N} \hat{\hat{B}}_m \hat{\hat{B}}_n e^{i((\omega_m + \omega_n)t - (k_m + k_n)x)} \mathscr{M}^{(2)}_{y,c} \tag{5.15}$$

where $\mathscr{M}^{(2)}_{y,c}$ is the pitch moment quadratic transfer function, with the full derivation available in [63].

Heave Second-Order Force

The formulation of the heave force is required for the load calculation on a semi-submersible floater, thus it is has been developed in this study. Following the same procedure as in section 5.1.2, the second-order axial heave force on a cylinder is the sum of Froude-Krylov (FK) and the added mass (AM) terms given by

$$F_{z,c}^{(2)} = F_{z,c}^{FK} + F_{z,c}^{AM} = p^{(2)} A_z + \rho_w C_{m,z} V_z w_t^{(2)} \tag{5.16}$$

Here $p^{(2)}$ is the second-order hydrodynamic pressure applied to the area A_z, which is the cross-sectional area of the column, $C_{m,z}$ is the inertia coefficient in heave, V_z is the corresponding volume for the motion in the heave direction, and $w_t^{(2)}$ is the second-order vertical acceleration of the water particles. It is assumed the wave kinematics and pressure remain constant over the cylinder bottom and evaluate them at the centre of the cross-sectional area.

The second-order hydrodynamic pressure, derived from the Bernoulli equation for unsteady and irrotational flow, is the sum of the contribution from the time derivative of the second-order velocity potential and the kinematic term. Under the assumption of unidirectional waves, the second-order hydrodynamic pressure is given by

$$p^{(2)} = -\rho_w \left(\phi_t^{(2)} + \frac{1}{2} \left(u^{(1)} u^{(1)} + w^{(1)} w^{(1)} \right) \right) \tag{5.17}$$

Here the time-invariant contribution to $p^{(2)}$ that relates to the Bernoulli constant is excluded, see [63], since only the dynamic second-order force is of interest. From (5.17) two separate quadratic transfer functions are obtained: one for the second-order potential term, $\mathscr{F}_{z1,c}^{(FK)}$, and another for the quadratic term, $\mathscr{F}_{z2,c}^{(FK)}$, both expressed with non-dimensional parameters. The second-order Froude-Krylov term is then given by

$$\frac{F_{z,c}^{FK(2)}}{\rho_w h g A_z} = \sum_{m=-N}^{N} \sum_{n=-N}^{N} \hat{\hat{B}}_m \hat{\hat{B}}_n e^{i((\omega_m+\omega_n)t-(k_m+k_n)x)} (\mathscr{F}_{z1,c}^{(FK)} + \mathscr{F}_{z2,c}^{(FK)}) \tag{5.18}$$

$$\mathscr{F}_{z1,c}^{(FK)} = \frac{\mathcal{T}_\Phi(\Omega_m + \Omega_n) \cosh\left((\kappa_m + \kappa_n)(1 - \frac{d}{h})\right)}{\cosh(\kappa_m + \kappa_n)} \tag{5.19}$$

$$\mathscr{F}_{z2,c}^{(FK)} = \frac{1}{4} \kappa_m \kappa_n \frac{\cosh\left((\kappa_m - \kappa_n)(1 - \frac{d}{h})\right) + \cosh\left((\kappa_n - \kappa_m)(1 - \frac{d}{h})\right)}{\cosh \kappa_m \cosh \kappa_n} \tag{5.20}$$

The added mass term is the product of the heave added mass and the second-order wave particle vertical acceleration, $w_t^{(2)}$, which is

$$w_t^{(2)} = \left(w_t^{(2)} + u^{(1)} w_x^{(1)} + w^{(1)} w_z^{(1)} \right) \tag{5.21}$$

Again, from (5.21) two separate quadratic transfer functions are derived: one for the first term and another for the sum of the last two terms. The expression for the added mass component of the heave force is as follows:

$$\frac{F_{z,c}^{(AM)}}{\rho_w C_{m,z} V_z g} = \sum_{m=-N}^{N} \sum_{n=-N}^{N} \hat{\bar{B}}_m \hat{\bar{B}}_n e^{i(\omega_m+\omega_n)t-(k_m+k_n)x)} (\mathscr{F}_{z1}^{(AM)} + \mathscr{F}_{z2}^{(AM)}) \tag{5.22}$$

with,

$$\mathscr{F}_{z1}^{(AM)} = -\frac{\mathcal{T}_\Phi(\Omega_m + \Omega_n)(\kappa_m + \kappa_n) \sinh\left((\kappa_m + \kappa_n)(1 - \frac{d}{h})\right)}{\cosh(\kappa_m + \kappa_n)} \tag{5.23}$$

$$\mathscr{F}_{z2}^{(AM)} = \frac{1}{4} \kappa_m \kappa_n (\kappa_m + \kappa_n) \frac{\sinh\left((\kappa_m - \kappa_n)(1 - \frac{d}{h})\right) + \sinh\left((\kappa_n - \kappa_m)(1 - \frac{d}{h})\right)}{\cosh \kappa_m \cosh \kappa_n} \tag{5.24}$$

$F_{z2,c}^{(FK)}$ and $F_{z2}^{(AM)}$ have been modified to make them symmetric, necessary for the eigenvalue decomposition. Once are defined the QTFs corresponding to the Froude-Krylov and added mass terms, the load time series are obtained through (5.14).

5.1.3 Second-Order Loads on Horizontal Member with Longitudinal Axis Perpendicular to the Wave Propagation Direction

Herein, the formulation for the case of a fully submerged prism with the longitudinal axis perpendicular to the wave propagation direction, as shown in fig. 5.2, is given. The formulation is referred to the local reference frame with origin at $z = -d$ with coordinate systems Op.

In this case, it can be assumed that the force is uniformly distributed along the y-axis. As this method assumes the mid-point force representation at the longitudinal axis, no pitch moment is generated, thus, only the surge and the heave forces are formulated.

Surge and Pitch First- and Second-Order Loads

The first-order surge force based on the slender-body approach is a function of the first-order wave particle acceleration in the flow direction, $u_t^{(1)}$

$$F_{x,pp}^{(1)} = \int_L \rho_w A (C_{mc} + 1) u_t^{(1)} dy \tag{5.25}$$

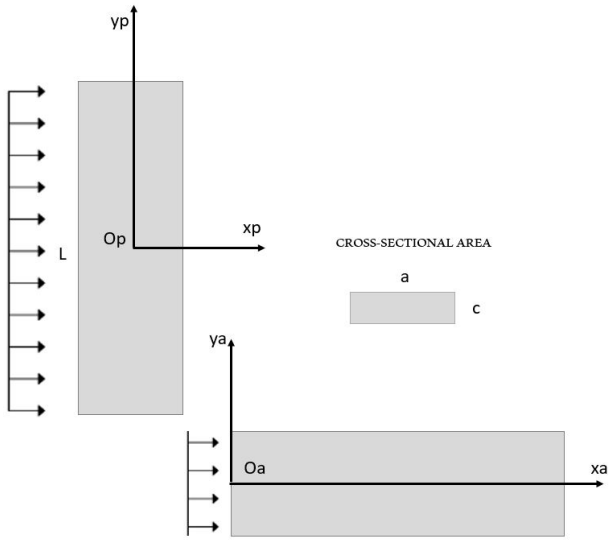

Figure 5.2: Horizontal members with the longitudinal axis perpendicular (left) and aligned (right) to the wave propagation direction.

where L is the pontoon length along the longitudinal axis, C_{mc} is the inertia coefficient corresponding to the motion along x-axis and A is the area projected on the plane perpendicular to the longitudinal axis, which corresponds to the cross-sectional area in fig. 5.2. Writing (5.25) in non-dimensional form:

$$\frac{F^{(1)}_{x,pp}}{\rho_w A L g} = (C_{mc}+1)\sum_{j=-N}^{N} \hat{\bar{B}}_j e^{i(\omega_j t - k_j x)} \mathscr{F}^{(1)}_{x,pp} \tag{5.26}$$

$$\mathscr{F}^{(1)}_{x,pp} = \Omega_j \kappa_j \frac{\cosh\left(\kappa_j(1-\frac{d}{h})\right)}{\cosh \kappa_j} \tag{5.27}$$

Considering the same surge components as described in (5.7) to (5.10), the axial divergence term is zero since $v = v_y = 0$ due to the assumption of uni-directional waves; and the free-surface force term is also zero because the body is fully submerged. The second-order force components are:

$$F^{(2)}_{x1,pp} = \int_L \rho_w A(C_{mc}+1) u^{(2)}_t dy \tag{5.28}$$

$$F^{(2)}_{x2,pp} = \int_L \rho_w A(C_{mc}+1)(u^{(1)}u^{(1)}_x + w^{(1)}u^{(1)}_z) dy \tag{5.29}$$

where the index *pp* denotes *pontoon perpendicular*. The equations above are given in the non-dimensional form as a function of the wave excitation and the quadratic transfer function:

$$\frac{F^{(2)}_{x,pp}}{\rho_w AgL} = (C_{mc}+1)i \sum_{m=-N}^{N} \sum_{n=-N}^{N} \hat{\bar{B}}_m \hat{\bar{B}}_n e^{i((\omega_m+\omega_n)t-(k_m+k_n)x)} (\mathscr{F}^{(2)}_{x1,pp} + \mathscr{F}^{(2)}_{x2,pp}) \tag{5.30}$$

The quadratic transfer functions corresponding to each of the surge components are given below.

$$\mathscr{F}^{(2)}_{x1,pp} = \frac{\mathcal{T}_\Phi(\Omega_m+\Omega_n)(\kappa_m+\kappa_n)}{\cosh(\kappa_m+\kappa_n)} \cosh(\kappa_m+\kappa_n)(1-\frac{d}{h}) \tag{5.31}$$

$$\mathscr{F}^{(2)}_{x2,pp} = \frac{1}{4}\kappa_m\kappa_n(\kappa_m+\kappa_n) \frac{\cosh((\kappa_m-\kappa_n)(1-\frac{d}{h})) + \cosh((\kappa_n-\kappa_m)(1-\frac{d}{h}))}{\cosh\kappa_m \cosh\kappa_n} \tag{5.32}$$

The pitch moment referred to the PoF from the contributions of the surge force becomes

$$M^{(2),PoF}_{y,pp} = -F^{(2)}_{x,pp} d \tag{5.33}$$

Heave First- and Second-Order Forces

The first-order heave force is obtained similarly to the surge force, but this time as a function of the vertical acceleration, $w^{(2)}_t$.

$$F^{(1)}_{z,pp} = \int_L \rho_w A(C_{ma}+1) w^{(1)}_t dy \tag{5.34}$$

Here C_{ma} is the inertia coefficient for the vertical motion. Writing the force in non-dimensional form, it is obtained

$$\frac{F^{(1)}_{z,pp}}{\rho_w ALg} = (C_{ma}+1)i \sum_{j=-N}^{N} \hat{\bar{B}}_j e^{i(\omega_j t - k_j x)} \mathscr{F}^{(1)}_{z,pp} \tag{5.35}$$

$$\mathscr{F}^{(1)}_{z,pp} = \Omega_j \kappa_j \frac{\sinh(\kappa_j(1-\frac{d}{h}))}{\cosh\kappa_j} \tag{5.36}$$

Regarding the second-order heave force, the formulation is based on the slender-body approximation and it is done in a similar way to the case of the isolated vertical cylinder.

$$F^{(2)}_{z,pp} = \int_L \rho_w A(C_{ma}+1)(w^{(2)}_t + u^{(1)} w^{(1)}_x + w^{(1)} w^{(1)}_z) dy \tag{5.37}$$

Again, two QTFs are derived from the equation above, one corresponds to the first term and the other, to the sum of the last two terms. The $\mathscr{F}_{z2,pp}$ has been modified to make it symmetric, as in the previous cases.

$$\frac{F^{(2)}_{z,pp}}{\rho_w A L g} = (C_{ma}+1)\sum_{m=-N}^{N}\sum_{n=-N}^{N}\hat{\bar{B}}_m\hat{\bar{B}}_n e^{i((w_m+w_n)t-(k_m+k_n)x)}(\mathscr{F}^{(2)}_{z1,pp}+\mathscr{F}^{(2)}_{z2,pp}) \tag{5.38}$$

where,

$$\mathscr{F}^{(2)}_{z1,pp} = -\mathcal{T}_{\Phi}\frac{(\Omega_m+\Omega_n)(\kappa_m+\kappa_n)\sinh\left((\kappa_m+\kappa_n)(1-\frac{d}{h})\right)}{\cosh(\kappa_m+\kappa_n)} \tag{5.39}$$

$$\mathscr{F}^{(2)}_{z2,pp} = \frac{1}{4}\kappa_m\kappa_n(\kappa_m+\kappa_n)\frac{\sinh\left((\kappa_m-\kappa_n)(1-\frac{d}{h})\right)+\sinh\left((\kappa_n-\kappa_m)(1-\frac{d}{h})\right)}{\cosh\kappa_m\cosh\kappa_n} \tag{5.40}$$

The resulting QTF from the sum in (5.38) is eigenvalue decomposed and the second-order heave force time series is obtained by means of (5.14).

5.1.4 Second-Order Loads on Horizontal Member with Longitudinal Axis Aligned to the Wave Propagation Direction

Herein, the formulation of a fully submerged prism with its longitudinal axis aligned to the wave propagation direction, as shown in fig. 5.2, is given. This member required the analytical integration of the forces along the x-axis since the wave kinematics change along the pontoon length. The pontoon member is rather long and, thus, it does not seem reasonable to approximate the surge force by the mid-point force representation. Instead, in this case the surge force formulation is based on the pressure difference at the two end surfaces. The heave force and pitch moment formulations, however, are based on the slender-body approach, as has been done in the previous cases. The formulation given below is referred to each of the local reference frames with origin at $z=-d$ with coordinate system Oa.

Surge Second-Order Force

The second-order surge force is formulated using the second-order hydrodynamic pressure expression:

$$F^{(2)}_{x,pa} = -\rho_w A\left(\phi^{(2)}_t+\phi^{(1)}_x\phi^{(1)}_x+\phi^{(1)}_z\phi^{(1)}_z\right)\Big|_L^0 \tag{5.41}$$

From the velocity potential time derivative, one QTF is obtained, and from the quadratic velocity sum term, another QTF, as shown as follows:

$$\frac{F^{(2)}_{x,pa}}{\rho_w A h g} = (C_{mb}+1)\sum_{m=-N}^{N}\sum_{n=-N}^{N}\hat{\bar{B}}_m\hat{\bar{B}}_n e^{i((w_m+w_n)t-(k_m+k_n)x)}(\mathscr{F}^{(2)}_{x1,pa}+\mathscr{F}^{(2)}_{x2,pa}) \tag{5.42}$$

with,

$$\mathscr{F}^{(2)}_{x1,pa} = \mathcal{T}_{\Phi}\frac{(\Omega_m+\Omega_n)\cosh\left((\kappa_m+\kappa_n)(1-\frac{d}{h})\right)}{\cosh(\kappa_m+\kappa_n)}(1-e^{-ikL}) \tag{5.43}$$

$$\mathscr{F}^{(2)}_{x2,pa} = \frac{1}{4}\kappa_m\kappa_n\frac{\cosh\left((\kappa_m-\kappa_n)(1-\frac{d}{h})\right)+\cosh\left((\kappa_n-\kappa_m)(1-\frac{d}{h})\right)}{\cosh\kappa_m\cosh\kappa_n} \tag{5.44}$$

Heave and Pitch Second-Order Loads

The heave force and the pitch moment are similarly obtained, with the difference that the latter is the product of the former and the arm in the x-direction. The second-order loads are given by

$$\begin{pmatrix}F^{(2)}_{z,pa}\\M^{(2)}_{y,pa}\end{pmatrix} = \rho_w A\int_L\left((C_{ma}+1)(w^{(2)}_t+u^{(1)}w^{(1)}_x+w^{(1)}w^{(1)}_z)+C_{ma}u^{(1)}_x w^{(1)}\right)\begin{pmatrix}1\\-x\end{pmatrix}dx \tag{5.45}$$

By solving (5.45), the following integral functions $I_{z1}(k)$ and $I_{z2}(k)$ are obtained.

$$I_{z1}(k) = \frac{i}{k}(1-e^{-ikL}) \tag{5.46}$$

$$I_{z2}(k) = -\left(\frac{iL}{k}e^{-ikL}+\frac{1}{k^2}(e^{-ikL}-1)\right) \tag{5.47}$$

And from (5.45), three QTFs are derived: first for the second-order acceleration term, second for the quadratic velocity term and third for the axial divergence term.

$$\mathscr{F}^{(2)}_{z1,pa} = -\mathcal{T}_{\Phi}\frac{(\Omega_m+\Omega_n)(\kappa_m+\kappa_n)\sinh\left((\kappa_m+\kappa_n)(1-\frac{d}{h})\right)}{\cosh(\kappa_m+\kappa_n)} \tag{5.48}$$

$$\mathscr{F}^{(2)}_{z2,pa} = \frac{1}{4}\kappa_m\kappa_n(\kappa_m+\kappa_n)\frac{\sinh\left((\kappa_m-\kappa_n)(1-\frac{d}{h})\right)+\sinh\left((\kappa_n-\kappa_m)(1-\frac{d}{h})\right)}{\cosh\kappa_m\cosh\kappa_n} \tag{5.49}$$

$$\mathscr{F}^{(2)}_{z3,pa} = -\frac{1}{2}\kappa_m\kappa_n\frac{\kappa_m\cosh\kappa_m(1-\frac{d}{h}))\sinh\kappa_n(1-\frac{d}{h}))+\kappa_n\cosh\kappa_n(1-\frac{d}{h}))\sinh\kappa_m(1-\frac{d}{h}))}{\cosh\kappa_m\cosh\kappa_n} \tag{5.50}$$

The heave force and the pitch moment share the same transfer functions in (5.48), which are derived in the similar way as in the previous cases. The second-order loads referred to the local reference system located at Oa (see fig. 5.2) are given by

$$\begin{pmatrix} F^{(2)}_{z,pa} \\ M^{(2)}_{y,pa} \end{pmatrix} = \rho_w A g \sum_{m=-N}^{N} \sum_{n=-N}^{N} \hat{\bar{B}}_m \hat{\bar{B}}_n e^{i((w_m+w_n)t-(k_m+k_n)x)} \left((C_{ma}+1)(\mathscr{F}^{(2)}_{z1,pa} + \mathscr{F}^{(2)}_{z2,pa}) + C_{ma}\mathscr{F}^{(2)}_{z3,pa} \right) \begin{pmatrix} I_{z1}(k) \\ I_{z2}(k) \end{pmatrix} \tag{5.51}$$

The pitch moment is referred to the PoF of the isolated horizontal member by considering the surge and heave forces contribution.

$$M^{(2),PoF}_{y,pa} = M^{(2)}_{y,pa} + F^{(2)}_{z,pa}\frac{L}{2} + F^{(2)}_{x,pa}d \tag{5.52}$$

5.2 Validation of the Accelerated Method on Semi-Submersible Platforms

The validity of this method for the second-order hydrodynamic loads on semi-submersible platforms is here demonstrated. For that purpose, the method has been first implemented to the Nautilus semi-submersible floater, which is shown in fig. 5.1 and its characteristics are described in section 2.2.2.

The Nautilus platform is composed of four equal columns and a squared ring pontoon [2]. Therefore, the accelerated method was applied to the isolated column, and to each of the rectangular prisms that compose the pontoon. In both cases, the position of each of the members with respect to the PoF was considered. The validation of the method is carried out by comparing the results with those obtained through the radiation-diffraction approach. The radiation-diffraction analysis was performed in ANSYS-AQWA for the calculation of the QTFs, where, for consistency with the formulation given in section 5.1, the floater was fixed and the first-order motion was not included [64]. ANSYS-AQWA uses the Pinkster approximation [82], where the free surface contribution to the QTF is neglected. The Morison drag force was not considered since the results are compared against radiation-diffraction analysis. Then, the generated loads were evaluated for each of the sea states defined in table 4.1 by the double frequency sum (3.21). This conventional approach is hereinafter referred to as $AQWA$.

The difference between the assumption of slender-body and the radiation-diffraction analysis, in addition to the modal truncation associated with the

accelerated method, can lead to significant differences. For this reason, the second-order loads were been compared to those obtained from the matrix product formulation (5.12), which is the step before the eigenvalue decomposition of the QTF. It is here referred to this approach as *Slender* since it is the application of the Morison and Rainey force models, based on slender-body theory. In this way, the discrepancies due to the slender-body assumption can be separated from those due to the modal truncation in the accelerated method.

To quantify the accuracy of the results, the same error definition used for the validation of the *HAAC* method is here used, which is based on the standard deviation ratio (4.12). This time, σ_x is the standard deviation of the load time series obtained through the accelerated method and σ_{ref} is that of the reference signal (*AQWA* or *Slender*). The error that compares the *Slender* with the *AQWA* results, which would be equivalent to use of an infinite number of modes in the accelerated method, is here referred to as the *non-diffraction error*. This error will be further analysed since it measures the limitation of the method due to the slender-body assumption. Throughout the paper, the standard deviation used for the error measurement is calculated for filtered time series, where the energy content above the wave peak frequency for each sea state has been removed from the Fourier amplitudes of the given signal. A filter cut-off frequency equal to the peak frequency for each sea state was used, although it was observed that the error is very sensitive to the filter cut-off frequency.

First, the results corresponding to the parametric studies regarding the vertical cylinder are shown and discussed. Then, the second-order loads for the Nautilus pontoon segments, both perpendicular and aligned configurations, are compared to those from *AQWA*. Also, the error values with respect to the *AQWA* loads and to the *Slender* loads are given. In all figures, the time series, PSD, and exceedance probability plots of the surge and heave forces and of the pitch moment are given. The window shown in the time series plot is always centred around the event where the error is maximum, while both the PSD and the exceedance probability analysis are always obtained from the entire corresponding signal, after the application of the filter.

5.2.1 Parametric Studies and Results for the Columns

The motivation for carrying out these parametric studies is based on the different accuracy of the method for different vertical cylinders. As mentioned before, the accelerated method is based on the slender body assumption, which holds when the diameter-to-wave-length ratio is smaller than 0.2 and assumes an infinitely long cylinder. In [63] and [64] a spar and a monopile

were validated, which both meet the slender-body criterion. However, it was observed that the diameter-to-draft ratio of the cylinder also had an important effect on the method's accuracy. For this reason, the influence of the variability of these parameters on the accuracy of the method was assessed.

Diameter-to-Draft Ratio

For the same incident sea state, the second-order hydrodynamic loads were obtained for several cylinders of equal diameters but different drafts, which enabled to analyse the influence of the diameter-to-draft ratio without being biased by the diameter-to-wave-length ratio. In order to analyse also the sensitivity of the modal truncation for the different diameter-to-draft ratios, different number of modes were used for the second-order load calculation.

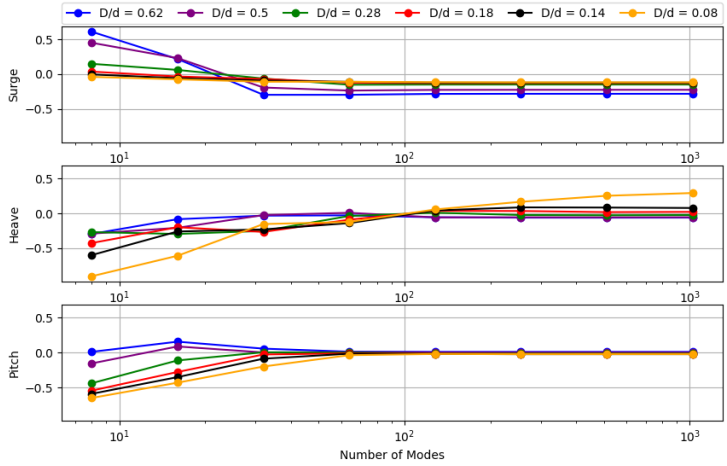

Figure 5.3: Standard deviation error. Accelerated method vs $AQWA$. Analysis of the error using different number of modes in the modal truncation and different diameter-to-draft ratio (see legend) under SS2 conditions.

In fig. 5.3, the error (4.12) with respect to $AQWA$ signal of the second-order loads is shown, where each colour corresponds to a different diameter-to-draft ratio. In table 5.1 and following tables, two measures of error are given: the error due to the modal truncation, where the loads from the accelerated method are compared to the loads obtained using the *Slender* approach (5.12); and the error when compared to the $AQWA$ approach, which includes errors due to the modal truncation and those associated with the slender-body assumption.

The estimation of the surge force was significantly influenced by the

diameter-to-draft ratio, especially for $\frac{D}{d} < 0.2$, where the accuracy improved notably achieving non-diffraction errors below 10%. Taking a look at fig. 5.3, the higher the values of diameter-to-draft ratios, the larger the error with respect to *AQWA*. The error converged with 64 modes for all cases, although the error for the case with the highest diameter-to-draft ratio was 10% and for the case with the lowest ratio increased to 28%. Initially, this observation led to believe the error was partly caused by end effects; therefore, the Rainey correction [78] that accounts for an additional point load at the cylinder ends was applied. However, the addition of this extra force did not make any significant change in the surge force. Looking at table 5.1, the error with respect to the *Slender* surge force was below 1% for both cylinders using 128 modes. This led to conclude that the inaccuracies of the surge force on vertical cylinders were mainly due to the slender-body approach, which results in larger errors for cylinders with diameter-to-draft ratio above 0.2. The modal truncation on the surge QTF seemed to be accurate using 128 modes, regardless of the diameter-to-draft ratio. It was noticed that the *Slender* surge loads were smaller than the *AQWA* results. The discrepancies can thus not be explained by the standard $\frac{D}{\lambda}$ effect as covered in MacCamy-Fuchs theory. As will be explained later, a reference calculation with *WAMIT* showed a reduction of the error of 28% to a value of 16%.

The heave force does not show the same dependence on the diameter-to-draft ratio as the surge force does. However, it was observed that cylinders with very large drafts receive small loads at the bottom end and, consequently, the differences in the loads with respect to *AQWA* were higher, causing larger errors. As a matter of fact, the case study with the highest diameter-to-draft ratio corresponds to a draft of 137 m, which showed very low heave forces. What can be observed in both fig. 5.3 and table 5.1 is that

		$\frac{D}{d} = 0.62$						$\frac{D}{d} = 0.14$					
Nº Modes		8	32	128	256	1024	∞	8	32	128	256	1024	∞
Surge	*Slender*	150	-1.4	-0.3	0.01	0	0	160	-5.7	-0.01	-0.002	0	0
	AQWA	60	-29	-28	-28	-28	-28	-0.3	-9	-12	-12	-12	-12
Heave	*Slender*	-27	2.8	-1.7	-0.4	0	0	-66	-35	-9	-4	-0.2	0
	AQWA	-29	-3	-5	-6	-6	-6	-60	-23	4	8	7	7
Pitch	*Slender*	1.5	6.4	0	0	0	0	-60	-7.2	0.3	0.04	0	0
	AQWA	-0.09	5	-0.9	-0.9	-0.9	-0.9	-59	-8	-2	-2.3	-2.3	-2.3

Table 5.1: Accelerated method error (%) for different number of modes with respect to the loads from *Slender* (5.12) and from *AQWA*. Cylinders of D = 10.5 m and drafts 17 m and 77 m under SS2 conditions.

this force component required a larger number of modes than the surge force for a good representation, reaching convergence with 256 modes, although 128 modes provided the same error with respect to *AQWA*. In table 5.1 it can be observed that the assumption of slender-body would introduce some disagreement with respect to the radiation-diffraction analysis but still the highest value of error found is of 7%, which seems reasonable for a preliminary design phase.

The results for the pitch moment showed that the modal truncation also influences the accuracy of the second-order load prediction, and the correct choice of the number of modes provided very good agreement with the *AQWA* loads. All cases show *non-diffraction errors* below 3% and convergence is reached for 64 modes, regardless of the diameter-to-draft ratio. It is interesting that the formulation for the surge and the pitch moment are very similar and, despite the rather large error found in the surge force for high diameter-to-draft ratios, the same tendency was not observed for the pitch moment. For this reason, this error in surge is related to some effect near the free surface that the radiation-diffraction analysis might be considering and the Morison and Rainey models are not.

Diameter-to-Wave-Length Ratio

The same cylinder was subjected to the three sea states defined in table 4.1. Additionally, three different diameter-to-draft ratio cases were used to assess this effect. The diameter was 10.5 m in all cases and the draft was changed to evaluate different aspect ratios: a Nautilus-size column with a ratio of 0.62, a high-draft column with a ratio of 0.14, and a spar-size column with a ratio of 0.08. It was expected to find a better agreement with the *AQWA* results as the diameter-to-wave-length ratio decreased since a Morison-based approach is the basis of the present method, where the range of applicability is for ratios $\frac{D}{L_{pw}} < 0.2$. This is because diffraction loads can be ignored for bodies that are slender compared to the incident wave length. The expected tendency was only observed for $\frac{D}{d} < 0.2$, as happens in plots (b) and (c) in fig. 5.4, which is clearly observed for the surge and the heave forces. The pitch moment was obtained with high accuracy for all the sea states, therefore there sems to be negligible influence of the diameter-to-wave-length ratio. However, in plot (a), which corresponds to a cylinder with $\frac{D}{d} = 0.62$, there is not a clear correlation of the error to the diameter-to-wave-length ratio and the accuracy on the load prediction. The surge force is the most influenced by this ratio, while the remaining loads show similar agreement for the three diameter-to-wave-length ratios.

Taking into account the results of these parametric studies, it can be concluded that the surge force was the most influenced by the diameter-

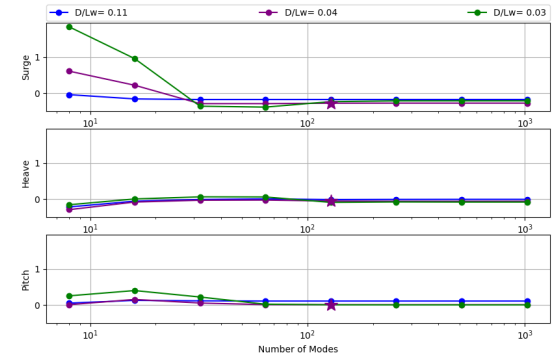

(a)

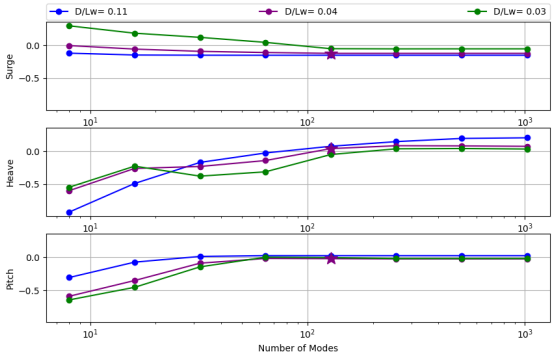

(b)

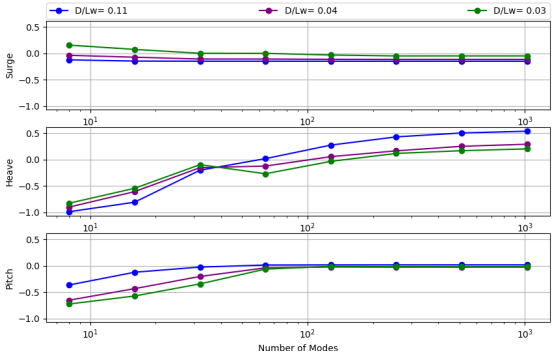

(c)

Figure 5.4: Standard deviation error. Accelerated method vs *AQWA*. Analysis of the error using different number of modes in the modal truncation and different diameter-to-wave-length ratio studied for three cylinders with a diameter of 10.5 m and a draft of (a) 17 m (b) 77 m. (c) 137 m.

to-draft ratio. For $\frac{D}{d} < 0.2$, an error with respect to *AQWA* below 10% is achieved when using 128 modes. In addition, since the method is a Morison based force model, the smaller the diameter-to-wave-length ratio, the better prediction of the hydrodynamic load, provided that the $\frac{D}{d} < 0.2$. The pitch moment was generally well predicted with error values lower than 10% in all cases using again 128 modes. The heave force did not seem to be influenced by any of the parameters and its calculation required at least 128 modes to reach error convergence. The *non diffraction error* achieved for the worst case is 11%, as long as the draft is less than 100 m.

In fig. 5.5 and 5.6, are given the results for the second-order hydrodynamic loads from the accelerated method using 128 modes and from the *AQWA* approach, for the cases marked with a star in fig. 5.4. The former corresponds to the Nautilus single column (D= 10.5 m and d = 17 m) and the latter, to a longer cylinder with the same diameter (d = 77 m) both under SS2 conditions ($\frac{D}{L_{pw}} = 0.04$). The most remarkable difference between these two cases regarding the accuracy resides in the surge force, consistent with the results of table 5.1. The number of modes required for the good prediction of the second-order loads on vertical cylinders is determined by the stabilisation of the error due to the modal truncation. For the Nautilus columns, this corresponds to 128 modes with an error of 28% with respect to the radiation-diffraction analysis for the second-order surge force, 7% for the heave force and 0.9% for the pitch moment. Regarding the case in fig. 5.5, the error in surge decreases as the diameter-to-draft ratio does, where the heave force had a deviation below 6% and the pitch moment wass accurately estimated with an error of 2.3%. Thus, the accelerated method agrees very well with the *Slender* solution and generally well with the *AQWA* solution, with the errors attributed mainly to diffraction effects, which are not accounted for in the present method. As a further check of the surge error, it was performed an independent check with *WAMIT* where the *non-diffraction error* for the isolated Nautilus column was 16 %, almost half the error than that obtained when comparing to *AQWA*. This difference between both radiation-diffraction panel codes is likely related to the free-surface integral in the second-order loads. This would also explain that the highest errors were found in surge, whereas the pitch moment was predicted with high accuracy. The *AQWA* solver uses the Pinkster approximation [82], which neglects the integral on the free surface for the second-order loads, whilst *WAMIT* does not.

5.2.2 Results for the Pontoon Members

The pontoon was decomposed into four equal rectangular prisms, as shown in fig. 5.2. Two of the members have the longitudinal axis perpendicular

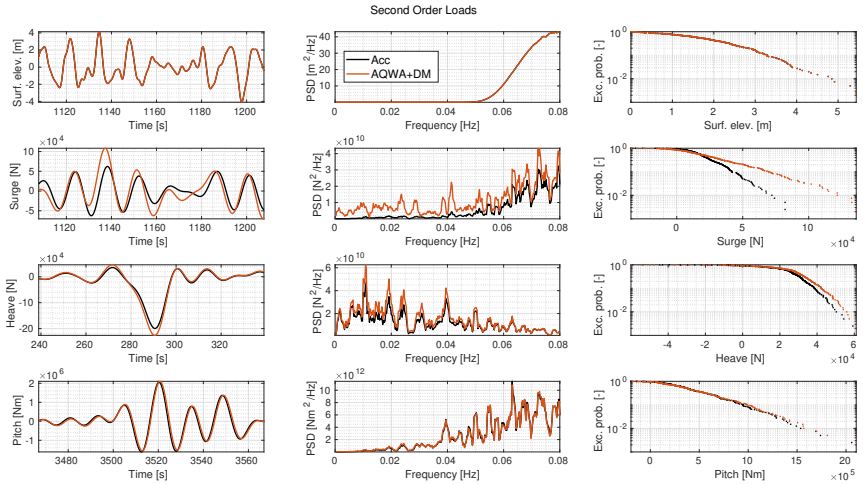

Figure 5.5: SS2 - Second-order loads on cylinder D = 10.5 m and draft = 17 m *AQWA* and Accelerated Method (128 modes).

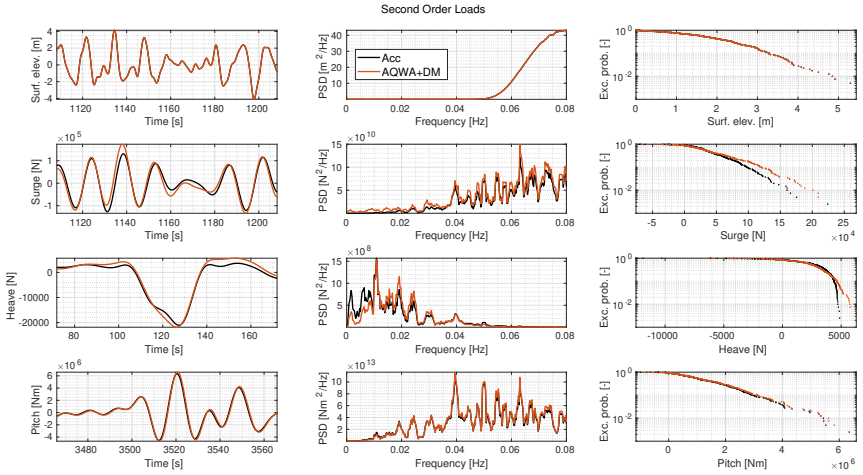

Figure 5.6: SS2 - Second-order loads on cylinder D = 10.5 m and draft = 77 m. *AQWA* and Accelerated Method (128 modes).

to the incident wave direction and the formulation given in section 5.1.3 was applied. The remaining pontoon segments have their longitudinal axis aligned to the wave propagation direction and the second-order loads were obtained through the formulation described in section 5.1.4. In order to verify the formulation, pontoon members with the dimensions of the pontoon corresponding to the original Nautilus platform described in section 2.2.2 were used.

The results for the first- and second-order wave loads on the pontoon segments are shown in fig. 5.7 for the member with the longitudinal axis

perpendicular to the wave propagation direction and in fig. 5.8 for the member with the longitudinal axis aligned under SS2 (see table 4.1). The three sea states were evaluated but since the results of the moderate sea state are representative of the general method's accuracy applied to the pontoon members, the results for SS1 and SS3 are not presented here. This time, results for the first-order loads are relevant to support the discussion on the second-order results.

The first-order loads in fig. 5.7 show very good agreement with the *AQWA* results, achieving errors below 5% for the three DoFs. Second-order loads, due to the complex non-linear effects, show larger error values in table 5.2 but still the *non-diffraction error* is of 10% and 11% for surge force and heave force, respectively, likely due to the slender-body approximation. The modal truncation worked well, needing 128 modes or less to reach convergence with the *Slender* approach. Therefore, this error can not be improved further while using a slender-body approach. Thus the accelerated method showed to work accurately for the surge and the heave forces calculation under the assumption of slender body. The conditions of SS2 are representative of the set of sea states in table 4.1, although it was observe slightly better agreement of the surge force with the radiation-diffraction analysis as the wave peak period increased.

Nº Modes		8	32	128	256	1024	∞
Surge	*Slender*	-67	6	0.02	0	0	0
	AQWA	-62	15	10	10	10	10
Heave	*Slender*	29	1.9	-0.4	0	0	0
	AQWA	22	16	11	11	11	11

Table 5.2: SS2 - Pontoon perpendicular member second-order loads error (%) vs number of modes using the loads from the *Slender* (5.12) and the *AQWA* as reference signals.

In fig. 5.8 and table 5.3 the results corresponding to the first- and second-order loads for the pontoon member aligned to the wave propagation direction and the error for different number of modes are shown, respectively. The first-order surge and heave forces show very good agreement with respect to *AQWA*, with deviations lower than 3%. The pitch moment, however, showed an error of 11%. This larger error in pitch is related to the constant $C_m a$ value assumed constant along the pontoon length. It would be more accurate to consider a $C_m a$ value for each point along the x-axis, with lower values towards the pontoon ends. This would explain the over prediction of the first-order pitch moment.

Nº Modes		8	32	128	256	1024	∞
Surge	*Slender*	-84	-2.8	0.2	0	0	0
	AQWA	-83	-10	-9	-9	-9	-9
Heave	*Slender*	-87	-28	-1.9	-0.3	-0.05	0
	AQWA	-85	-23	-2.8	4.2	5.1	5.1
Pitch	*Slender*	-30	-9.1	-0.4	0	0	0
	AQWA	-26	9	14	14	14	14

Table 5.3: SS2 - Pontoon aligned member second-order loads error (%) vs number of modes using the loads from the *Slender* (5.12) and the *AQWA* as reference signals.

Regarding the second-order pitch moment, a similar conclusion can be reached, where the *non-diffraction error* was quantified as a 14% over estimation. The second-order surge and heave forces showed errors below 10% which are also linked to the slender-body approximation. The number of modes that accurately represent the second-order hydrodynamic loads on this horizontal member were 128, although the heave force would be even more accurately obtained with more modes. As for the influence of the wave length on the accuracy of the method, it were observed only minor differences between the results. Again better agreement could be achieved for the severe sea state.

5.2.3 Results for the Nautilus Semi-Submersible Floater

The results obtained for the second-order hydrodynamic loads on the original Nautilus semi-submersible floater are here presented and discussed. The first-order loads are also shown since they allow to quantify the influence of neglecting the cross-member interaction on the accuracy of the method, due to apply load superposition.

In order to compute the loads on the full Nautilus floater, superposition of the loads on the different members was applied. The wave surface elevation and the pitch moment need to be referred to the PoF for the full floater. In fig. 5.9 the first- and second-order loads obtained through the accelerated method using 128 modes and through *AQWA* are shown for the moderate sea state (see table 4.1). Looking at the first-order loads, the slender approach agreed quite well with *AQWA* for the surge force, while a noticeable under estimation was observed for the heave force and the pitch moment, which is related to the cross-interaction between the members. Nevertheless, the time series and the exceedance probability showed very

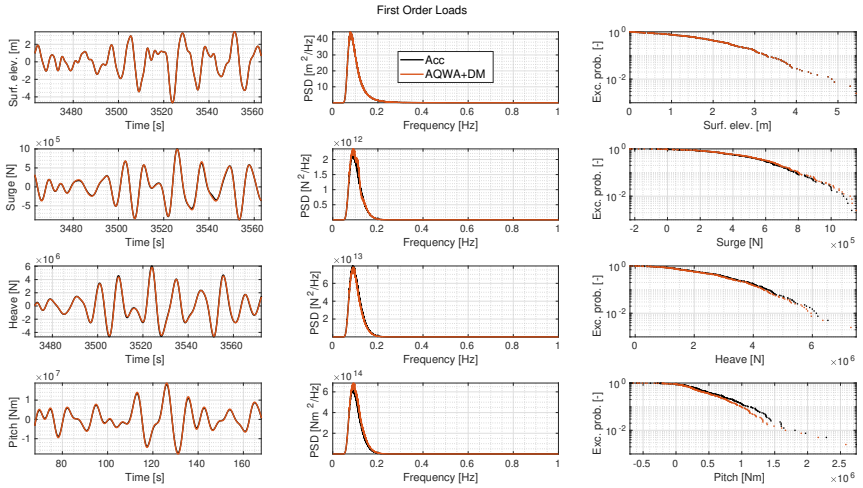

(a)

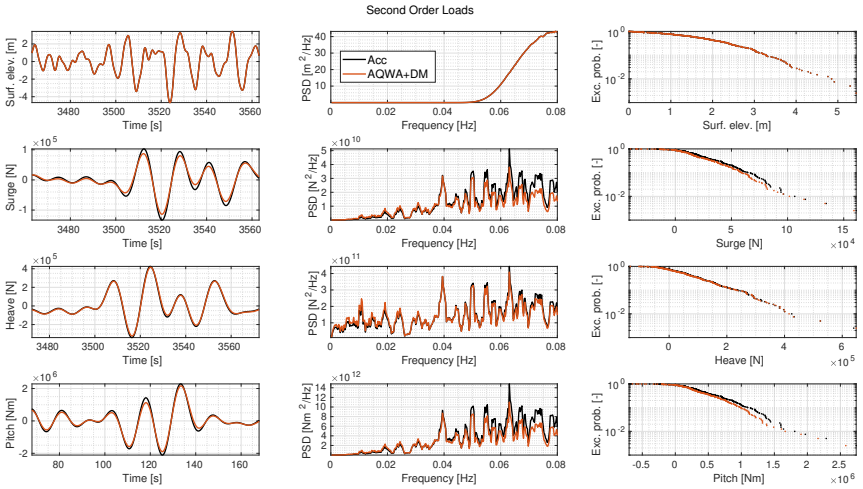

(b)

Figure 5.7: SS2 - Hydrodynamic loads on pontoon member with the longitudinal axis perpendicular to wave propagation direction. *AQWA* and Accelerated Method (128 modes) .(a) first-order, (b) second-order.

good agreement between the two signals at least for pitch. The second-order load statistics showed very good agreement for the heave force and the pitch moment. The surge force PSD seemed to agree well for the high frequencies but the low frequencies show substantial differences. The source of discrepancy here is the application of the slender-body assumption on cylinders with diameter-to-draft ratio above 0.2. In addition, the phases on the time series of the surge force did not match as well as for the other

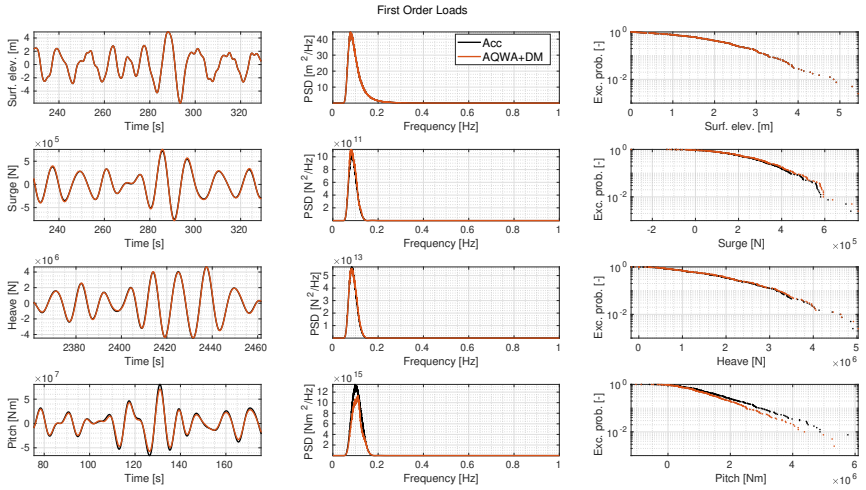

(a)

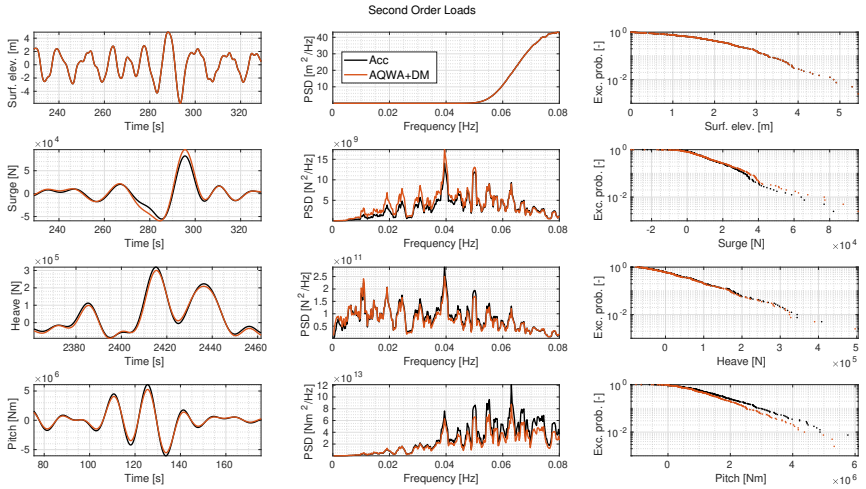

(b)

Figure 5.8: SS2 - Hydrodynamic loads on pontoon member with the longitudinal axis aligned to wave propagation direction *AQWA* and Accelerated Method (128 modes) .(a) first-order, (b) second-order.

components. This is due also to the slender-body approach, since the interaction between the columns seemed negligible in surge, as can be observed in the first order. As the findings for the three sea states were similar, only SS2 is shown and discussed in this section.

In order to understand the results obtained for the full Nautilus floater, table 5.4 is given, where the errors obtained for each of the separate members and for the full floater using 128 modes are compared. Here *Column*,

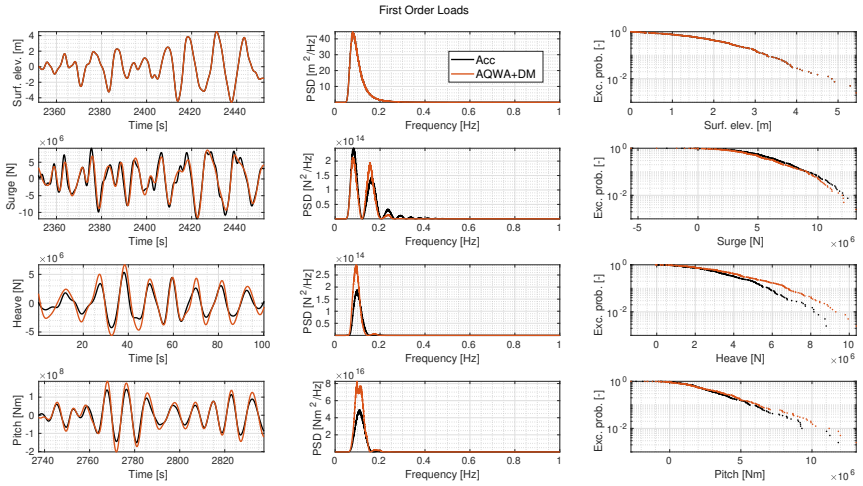

(a)

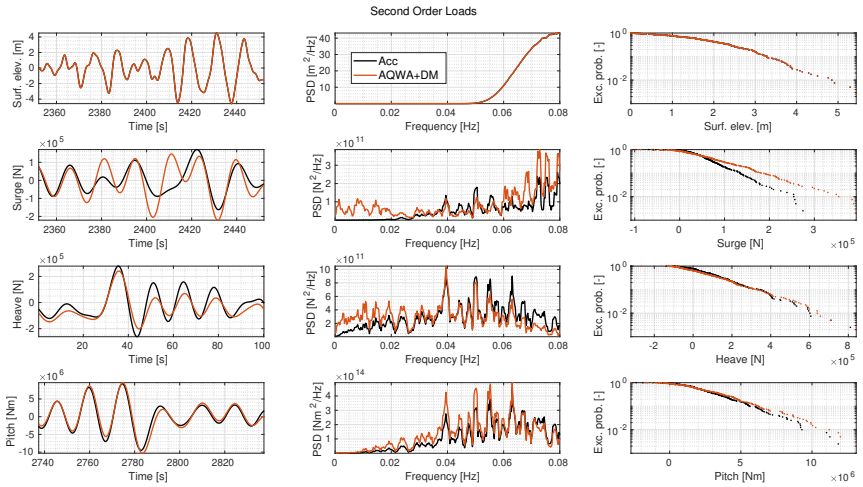

(b)

Figure 5.9: SS2 - Hydrodynamic loads for the full floater.(a) first-order, (b) second-order (128 modes).

PP and *PA* correspond to the error (4.12) of the accelerated method with respect to *AQWA* for the isolated Nautilus column, the isolated pontoon member perpendicular, and the pontoon member aligned to the wave propagation direction, respectively. 128 modes were chosen since with that number of modes, errors similar to the *non-diffraction error*, associated to the slender-body simplification, were achieved.

The surge force for the full floater showed a similar outcome to what was already observed for the single column in fig. 5.5. For cylinders with

DoF	Column	PP	PA	Nautilus
Surge	-28	10	-9	-22
Heave	-5	11	5.1	0
Pitch	-0.9	-	14	-10

Table 5.4: SS2 - Second-order loads error (%) for each member separately and for the full Nautilus floater with 128 modes.

diameter-to-draft ratios above 0.2, like the Nautilus columns, the surge force was underestimated and, since the columns were the main contributors to the surge force, the second-order loads on the full floater followed the same trend as the single columns with a deviation of 22%. In addition, it was observed from the first-order results that the interaction between the columns can be neglected for this case, or in other words, that superposition works well. Therefore, the accelerated method gives the same error as a conventional slender-body approach since the error was mainly driven by differences between radiation-diffraction analysis and slender-body theory. The second-order heave force for the full floater was obtained with almost perfect accuracy, despite missing the inclusion of the cross-interaction between members. This seems to be due to compensation between the under estimation of heave loads on the columns (-5%), the over estimation of heave loads on the pontoons (11% and 5%), and the under estimation associated to superposition. Finally, the pitch moment was under estimated with a deviation of 10%. Here it is more difficult to identify which member dominates the error, since the total pitch moment is also affected by contributions from the surge and the heave forces. It was apparent that compensation occurred between the over prediction on the pontoon member (associated to the constant $C_m a$ along the pontoon length) and the cross-interaction between the members. Despite these sources of error, the *Slender* approach was equivalent to the accelerated method with just 128 modes and the error relative to the radiation-diffraction solution was only 10% for the entire floater.

5.2.4 Computational Cost

The main advantage of the accelerated method is the significant reduction in computational cost achieved, when compared to that required by the *AQWA* approach, which first requires a radiation-diffraction analysis to obtain the QTFs and later involves a double sum to obtain the load time series for a specific sea state.

For the full Nautilus floater, the computational time needed to obtain

load time series by means of the full *AQWA* approach for a given floater geometry and sea state was 16900 s, using four cores through parallel technique in a computer with two Intel Xeon E5-2630 CPUs and Hyper-Threading active. This execution time is significantly longer than that employed by the accelerated method, as shown in table 5.5, which was 6.7 seconds for 128 modes.

Number of modes	8	16	32	64	128	256	512	1024
Time (s)	0.82	1.02	1.53	2.74	6.72	24.69	145	1262

Table 5.5: Computational time (s) for the accelerated method to calculate second-order loads on the Nautilus floater for a 1-hour sea state, using different number of modes.

5.2.5 Sensitivity of the Method with the Platform Design Parameters

In the previous section, the original Nautilus platform has been used as the case study for the method validation. Now, the second-order hydrodynamic loads on the different platform designs defined in table 3.8 are compared.

The second-order hydrodynamic loads due to the three sea states defined in table 4.1 have been calculated and compared against those derived from the direct method using the QTFs from *AQWA*, and further double summation for the specific wave spectrum. Since it has been demonstrated that for these type of structures 128 modes are enough to achieve the method's stability, the same number has been used to analyse all the platform design space. The error definition used for this validation is the same as in the previous section, using the expression (4.12).

Among the design space defined for the validation of this work, there is a wide range of diameter-to-draft values, from 0.5 to 1.36. It is noticeable that the columns currently used for FOW semi-submersible structures are relatively short compared to the spar-buoy foundations. According to the error values observed in the previous section for this range of diameter-to-draft ratios, it is expected to have deviations in the second-order surge force of around 22%.

In fig. 5.10 the standard deviation of the second-order surge and heave forces and pitch moments resulting from the accelerated method and from the *AQWA+DM* under SS2 conditions are shown. It is observed that the surge force is in all cases under predicted, as occurred with the Nautilus platform. The best approximation is found for the design with the smallest diameter and largest draft and largest distance between the columns, which is D12 and shows a deviation of 9.5%. This is coherent with the conclusions

made during the method validation in section 5.2. For all cases, as the draft increases, the surge force is better approached, which is mainly related to the contribution of the columns to this force component. This situation was explained in section 5.2.1, where it was shown that the accelerated method generally under estimates the second-order surge force. Align with this, as the columns diameter increases, there is also an increased in the error, which is associated to the increase in the D/d ratio, and also to the mid-point force representation, which leads to a better agreement with the $AQWA{+}DM$ method as the $D/$Ł$_w$ decreases. Thus, for the same peak period, the smaller the diameter, the lower the error.

The second-order heave force shows a very clear relationship with the platform diameters and also a very good agreement between both methods. Here, the interaction effects between the platform members has a more relevant influence on the method's accuracy since the pontoon takes an important roll in this DoF. In fact, throughout all the design space, as the columns become larger in terms of draft, a better match between the standard deviations is observed. This does not occur as the diameter increases. This is explained because in this study, the diameter and the width of the pontoon have been set equal. Thus, a larger diameter means also a larger pontoon, and less separation between the pontoon members, increasing the interaction effects, and therefore, increasing the error. Similarly, the second-order heave force is better predicted as the separation between the columns increases, due to the lower interaction effects.

As for the second-order pitch moment, again a clear tendency is observed and a general under prediction of load is obtained through the accelerated method. Following the same reasoning as for the previous loads, the estimated pitch moment shows better agreement as the draft increases and as the diameter decreases. This is very related to the surge component, where a strong relationship with the D/d and D/L_w was observed in the parametric studies in section 5.2.1.

In order to see how the time series and the spectra of designs corresponding to the best and worst second-order load prediction, fig. 5.11 is given. In view of the results obtained for each of the different platform designs and taking into account the conclusions observed in the parametric studies, the best estimation of the loads through the accelerated method is achieved for the lowest D/d and D/λ_w, and the largest separation between the columns. The worst estimation will be observed for the contrary case. Having a look at the design space, the former would be given by D12, with 10 m diameter, 20 m draft and 70 m of separation between columns. The latter would be observed with D28, with 15 m diameter, 11 m draft and 50 m of distance between the columns. Both under SS3 conditions, which

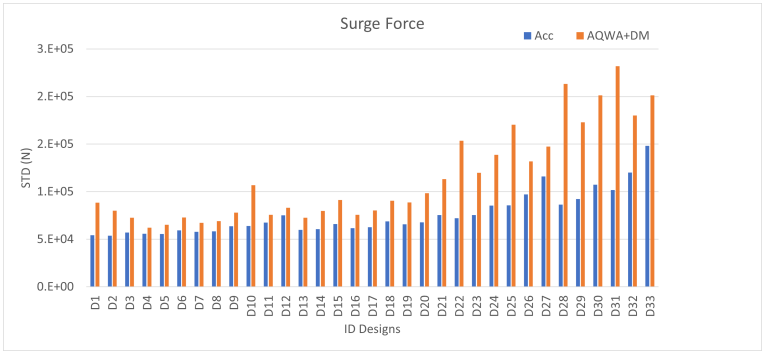

(a)

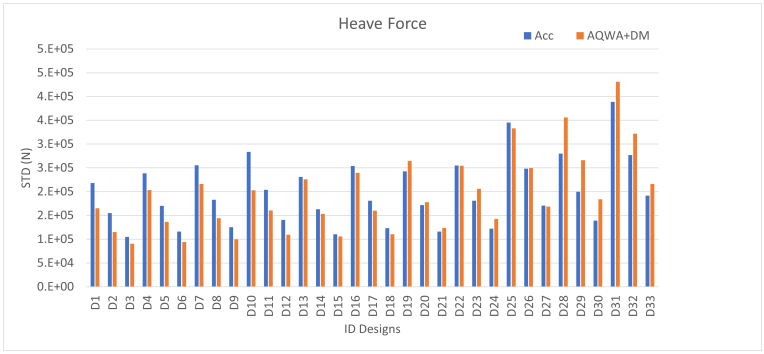

(b)

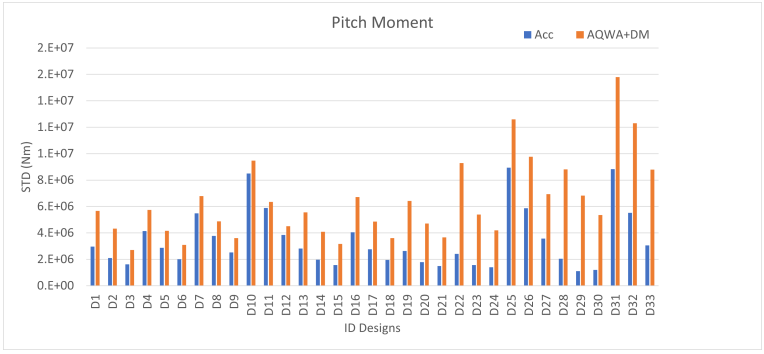

(c)

Figure 5.10: Second-order loads standard deviation on each platform design under SS2. *AQWA+DM* and *Accelerated Method* (128 modes). (a) Surge force [N] (b) Heave force [N] (c) Pitch moment [Nm]

correspond to the longest wave length.

In fig. 5.11, the second-order hydrodynamic loads corresponding to the maximum and minimum deviation in the pitch moment calculation are

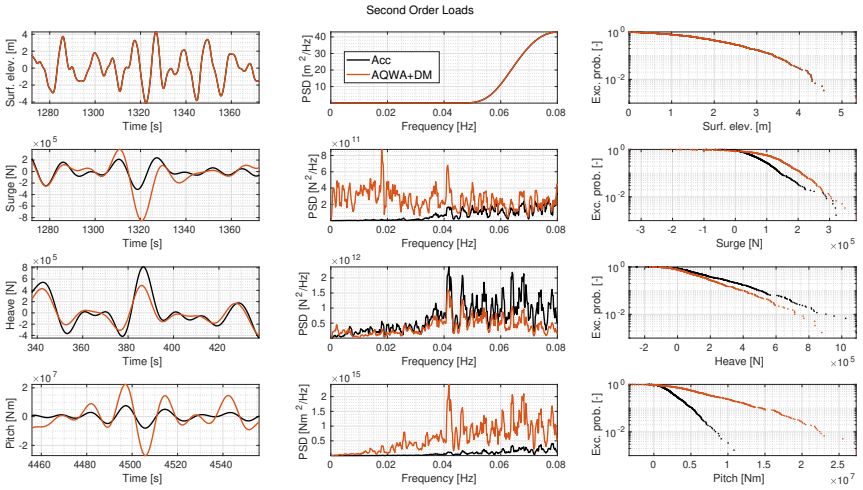

(a)

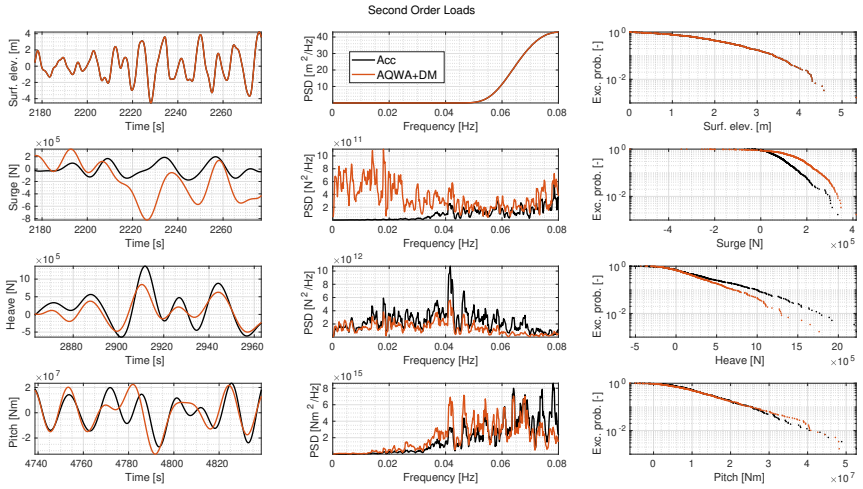

(b)

Figure 5.11: SS2 - Second-order hydrodynamic loads for the designs: (a) D23 (b) D25

shown. These designs are the D8 and D10, respectively. The surge force does not seem to differ significantly from one design to the other, showing an important under estimation at very low frequencies and a better agreement at higher frequencies. The heave force is reasonably accurately predicted, where a slightly over estimation is observed. And, finally, the pitch moment can be very well estimated through the accelerated method achieving deviations of 4% and in the worst case, D8, it can be substantially underestimated, which is related mainly to the superposition and negligible

interaction between the members, since the first-order loads obtained using the Morison and Rainey force model to each of the platform members showed similar error values in this DoF.

5.3 Integration of the Accelerated Method on the Frequency Domain Model

The main objective of the methodology proposed in this Thesis is to include the second-order hydrodynamic loads on the preliminary design of the FOWT substructures design. In a manner similar to the approach employed in section 4.3 to assess the impact of the accuracy of the *HAAC* method on the analysis of FOWT responses, the current section incorporates the *Accelerated Method* into the frequency domain response model outlined in chapter 3. This involves comparing the response motions with results obtained from the same frequency domain model when supplied with second-order loads generated by *AQWA+DM*. The hydrodynamic loads input to the model are those resulting from *AQWA*, in order to evaluate in an isolate way the accuracy of the here proposed method. An overview of this exercise is given in fig. 5.12.

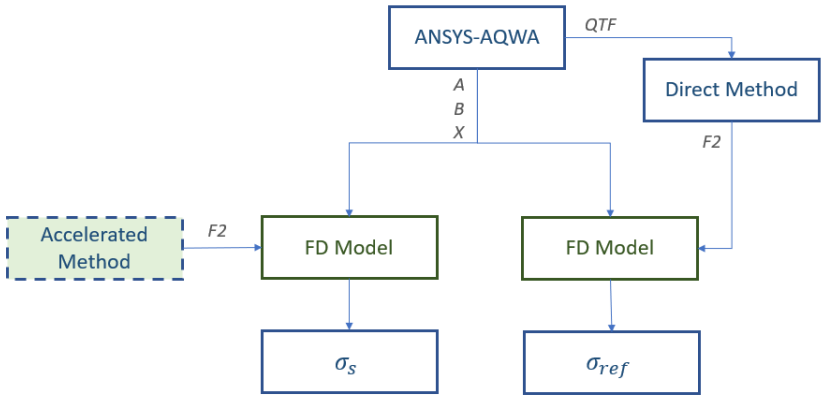

Figure 5.12: Scheme diagram for *Accelerated Method* validation process.

Again, the response under the different sea states defined in table 4.1 is evaluated, using the frequency domain simplified response model described in chapter 3. As done in the previous chapter chapter 4, first the response under the single action of wave is compared and then, the response including wind is given. The error expression to measure the accuracy of the *Accelerated Method* through the FOWT response motions is the same as in

the previous chapter, (4.12). The standard deviations of the FOWT surge, heave and pitch displacements, and the nacelle acceleration are compared below.

In fig. 5.13 the standard deviation corresponding to the surge, heave and pitch platform motions, and the nacelle acceleration for each design are given under SS2 conditions. This is a moderate sea state, thus the hydrodynamic loads are reasonably relevant. The surge force shows an important difference for the case where no wind action is considered, leading to significantly larger surge displacement if the *AQWA+DM* compared to the results using the second-order loads from the *Acc.* The platform designs with the columns with small diameter, such as 10-12 m, a better approach is observed. This is again very related to the D/d ratio, which increases with the diameter. Furthermore, again it can be observed how for larger drafts, the surge displacement is better predicted with the *Accelerated Method*. It appears that there is a substantial increase in deviation for columns when the ratio D/d exceeds 1, with particularly notable effects observed in designs D22, D26, D28, and D31. However, it's important to consider that this scenario may not provide a comprehensive representation, as these wave conditions would likely coincide with wind forces, potentially offsetting the error to some extent.

The pitch angle is predicted with reasonable accuracy, since it shows slight deviations and a similar tendency throughout the whole design space. Nevertheless, this time the interaction effects take an important roll on the method's accuracy. It is observed that, not only a low D/d ratio leads to better agreement with *AQWA+DM*, but also the interaction between the members. For instance, the larger the separation between columns, which also means larger separation between the pontoon members, the better estimation is observed.

The heave displacement and the nacelle acceleration are very well predicted either using the conventional method *AQWA+DM* or either the present approach *Acc.* This is also related to the less dependency of these DoFs on the second-order hydrodynamic loads.

In fig. 5.14, now the response motions under SS3, which corresponds to a severe sea state, are shown. The heave displacement and the nacelle acceleration are not shown, since it has been previously observed the low dependence on the second-order hydrodynamic loads. Therefore, they do not contribute to any substantial knowledge regarding this topic. This time better agreement can be observed in the surge motion between the *AQWA+DM* and the present method. This is related to the slender-body assumption, where the larger the D/λ_w, the better is approximated to slender, and therefore, the higher is accuracy is achieved. This explains the

better match observed in the surge standard deviations and also, how the larger is the column diameter, the differences become more important.

The pitch angle now shows larger standard deviation values, due to the higher and longer wave acting on the structure. It seems that, except for the designs D1 and D2, the *Accelerated Method* provides a very good approximation of the FOWT pitch angle, with a general under estimation of the response related to the previously observed under prediction of the load. This under prediction is very related to two factors: on one hand, the not very slender columns characteristic on the semi-submersible platforms, and on the other hand, the superposition which does not account for the cross-member interaction effects. This also explains the results for the surge response.

Ignoring the wind action might not be realistic, so in fig. 5.15 the response under DLC8 is given. This DLC consists of the wave conditions corresponding to SS3 and a turbulent wind with a mean speed of 12 m/s. Now, it can be observed that the response obtained feeding the frequency domain response model with the second-order loads from the conventional method or from the *Accelerated Method* does not lead to significant differences. This is explained by the major contribution of the aerodynamic load, compared to the non-linear hydrodynamic loads. Still, it meets the main goal of the study, which is to provide a similar dynamic behaviour of the FOWT under different wind and wave conditions. While it is certainly valuable to assess and discuss the results in scenarios involving wave excitation alone, it is more practical to evaluate the outcomes under realistic conditions where both wind and wave forces are at play. Furthermore, it is equally important to gauge the method's appropriateness based on the accuracy it offers in response analysis. The approach to measuring accuracy aligns with the central aim of this Thesis.

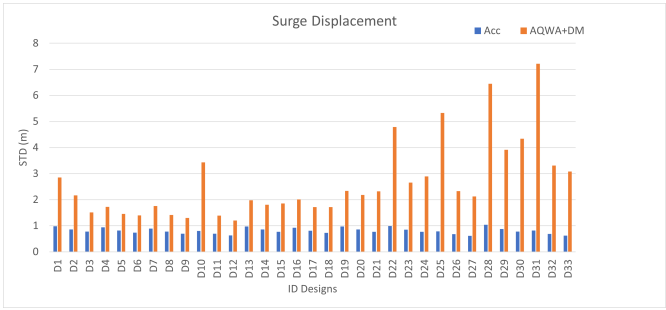

(a)

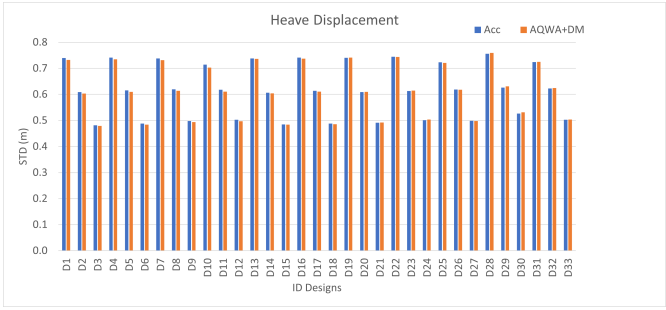

(b)

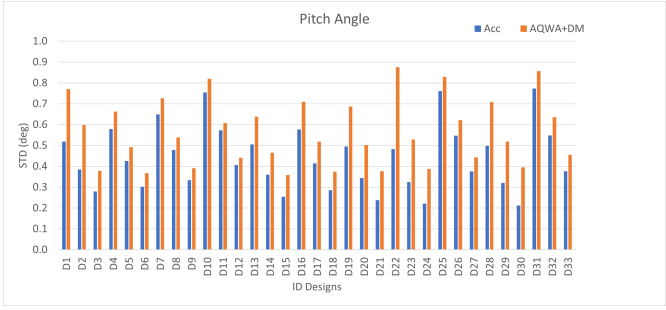

(c)

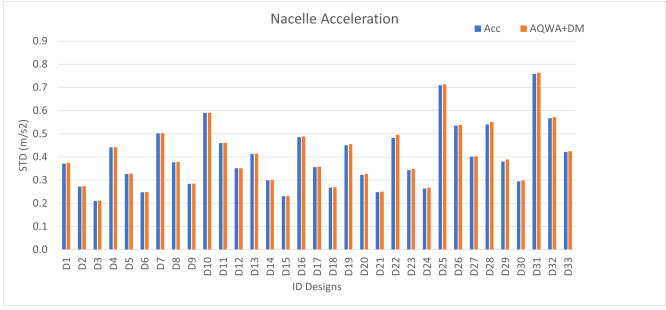

(d)

Figure 5.13: Response standard deviation for each design under SS2. (a) Surge (b) Heave (c) Pitch (d) Nacelle Acceleration

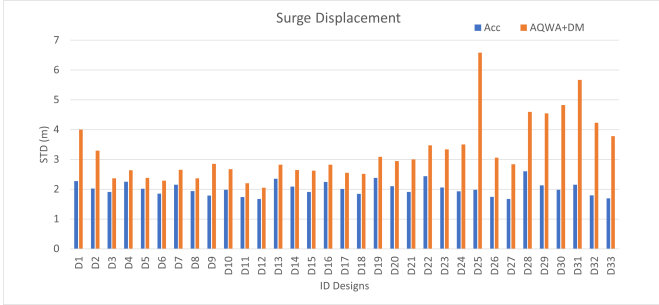

(a)

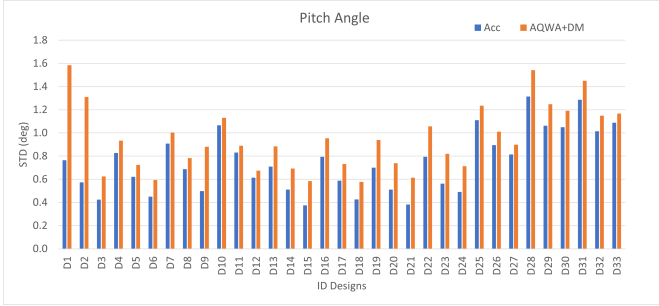

(b)

Figure 5.14: Response standard deviation for each design under SS3. (a) Surge (b) Pitch

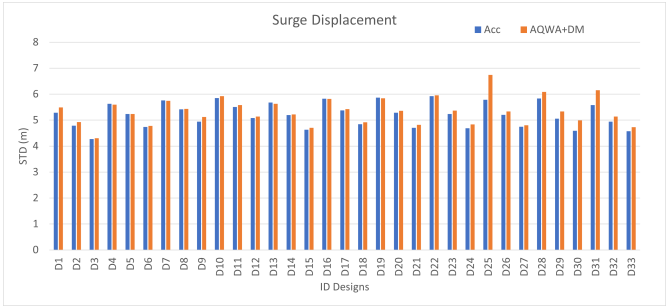

(a)

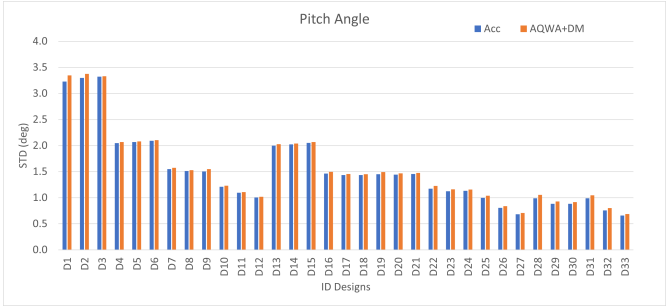

(b)

Figure 5.15: Response standard deviation for each design under DLC8. (a) Surge (b) Pitch

Chapter 6

Validation of the Preliminary Design Tool for FOWT

In this chapter, the validation of the proposed *FD Tool*, the simplified frequency domain modelling approach described in chapter 3 is given. The frequency domain simplified model is integrated with the two developed standalone methods for the calculation of the linear hydrodynamic coefficients and second-order hydrodynamic wave loads calculation presented in chapter 4 and chapter 5, respectively. The suitability of these methods during the preliminary design stages is here evaluated and discussed, as well as it is demonstrated the significant utility of the complete *FD Tool* and its advantages compared to the state-of-the-art (SoA) tools regarding the computational cost. To achieve this, the results obtained from the proposed tool with those obtained from the SoA reference tool, OpenFAST, have been compared. Therefore, in section 6.1, the procedure followed for the validation of the proposed tool is described. Then, in section 6.2, the response of motion from time domain and frequency domain are compared for the whole platform design space used in this study. Since one of the motivations of this work is to improve the efficiency of the existing design methods, in section 6.3 the computational cost reduction achieved through this method is highlighted.

6.1 Description of the Validation Procedure

This section provides a detailed explanation of the procedure employed to validate the *FD Tool*. As case study, it was explored a wide design space of semi-submersible platforms to support the DTU 10 MW WT, whose

characteristics are given in table 3.8. The *FD Tool* serves a dual purpose. Firstly, it is considered successful if it can pinpoint the same preliminary designs as the SoA methods, thereby narrowing down potential solutions for more in-depth analysis in the advanced stages of design. Secondly, it is crucial to obtain accurate predictions of the response of different platforms under a wide range of design load cases, with a particular focus on the most critical conditions.

In fig. 6.1, an overview of the validation procedure is shown. FD refers to frequency domain and TD, to time domain. As it can be observed, the response derived from the *FD Tool* is compared against the response from the TD SoA tool. The former, is fed with the hydrodynamic data obtained by means of the novel methods: $HAAC$ for the first-order hydrodynamic coefficients and Acc for the second-order hydrodynamic wave loads. The SoA tool, however, integrates the hydrodynamic linear coefficients and the Quadratic Transfer Functions (QTFs) derived from radiation-diffraction analysis, that for this study has been adopted in the commercial panel code tool ANSYS-AQWA. Both the FD and TD models utilise identical mooring stiffness and viscous damping matrices, which ensures that any discrepancies between the two modelling approaches arise solely from differences in the hydrodynamic model, eliminating other potential sources of error.

From each of the models, the static component, ξ_{st}, and the standard deviation, σ_ξ, of the response were determined. These parameters were utilised to compute the maximum response, ξ_{max}, which is subsequently adjusted using a dynamic factor, C_{dyn}. Regarding the response signals derived from the OpenFAST simulations, the mean and the standard de-

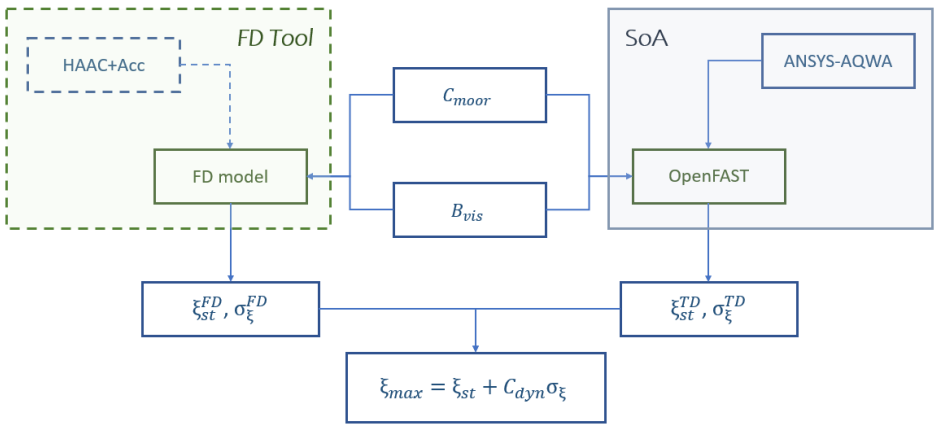

Figure 6.1: Overview of the validation procedure.

viations were directly obtained from the time series. As for the frequency domain response, the standard deviation was calculated through the Power Spectral Density (PSD), whereas the mean response was obtained by means of an static calculation, as shown in eq. (6.1):

$$\xi_{st}^{FD} = \frac{F_{st}}{C_{st}} \tag{6.1}$$

being ξ_{st} the static response vector, F_{st} the static load vector, whose components have been explained in chapter 3 and C_{st} is the restoring matrix at the equilibrium position for each Design Load Case (DLC).

To assess the accuracy of the results, an error measurement defined in (6.2) was employed. It is referred to the threshold value for each Degree of Freedom (DoF) since it is a way of pondering the accuracy of the prediction as the maximum response obtained is closer to the maximum response allowed. Similarly, this error becomes less important as the maximum response of the structure is further from the design limit values.

$$\epsilon = \frac{\xi_{max}^{FD} - \xi_{max}^{TD}}{threshold} \tag{6.2}$$

where ξ_{max}^{FD} and ξ_{max}^{TD} are the maximum response derived from the *FD Tool* and from OpenFAST, respectively. The thresholds defined for each DoF have been already given in section 3.2.3.

In view of this procedure, in the following sections how the time domain analysis has been set is described in section 6.1.1. It should be noted that, in order to compare the time domain results against the response of the frequency domain, the former should have a slightly linear behaviour, or in other words, should not be very non-linear. Therefore, the level of non-linearity of the present TD model is assessed in section 6.1.2. Then, the adjustment of the dynamic factor is explained in section 6.1.3.

6.1.1 Set-up of the Time Domain Simulations in OpenFAST

The time domain simulations were conducted using the reference tool for wind turbine response analysis, OpenFAST, developed by NREL [14]. The maximum simulation duration was set at 5400 seconds, with a time step of 0.025 seconds. However, for the purpose of comparing results with the frequency domain model, the initial 1800 seconds of the time series data were excluded to eliminate transient effects.

The structural model was defined in ElastoDyn module input file, which was set with the same values of mass, inertia and structural stiffness that were used for the frequency domain model described in chapter 3. In table 6.1, the output parameters required for the comparison are indicated.

Parameter	Description
PtfmSurge	Platform translational surge displacement
PtfmHeave	Platform translational heave displacement
PtfmPitch	Platform rotational pitch displacement
TwHt1ALxt	Yaw bearing x acceleration

Table 6.1: OpenFAST ElastoDyn output parameters corresponding to the DoFs considered in the simplified structural model in section 3.3.1.

Wind speed time series data were generated using TurbSim [17]. The turbulence model utilised was the Kaimal spectrum model. The wind velocity distribution was modelled using a power law, with the hub height of 119 meters serving as the reference height, as indicated in section 3.2.1. The power law exponent was set to 0.14, and a surface roughness length of 0.03 was employed. The analysis area for the wind data covered a 210x280 meter region (width x height) to encompass a sufficient area for capturing the wind turbine's motion. The wind speed time series obtained from TurbSim simulations were then used for aerodynamic load calculations, which were subsequently integrated into the frequency domain simplified model. For processing the wind time series data from TurbSim, InflowWind module was employed, and the AeroDyn module, also developed by NREL, was used for the time domain calculation of the aerodynamic loads on the wind turbine blades and tower. For that purpose, the publicly available data from the LIFES50+ project [2] regarding the DTU 10 MW WT was used, such as the airfoil characteristics. The input files for the wind speed time series and wind turbine data were the same for the full platform design space assessed in the validation. The controller applied in the OpenFAST simulations was the basic DTU controller, which is described also in the LIFES50+ project [2]. The fact of having the controller active, allows to maximise the thrust force, and consequently, the power generation.

The hydrodynamic model was configured using the HydroDyn module, developed by NREL. This module relies on hydrodynamic coefficients provided in the WAMIT output file format. In this study, radiation-diffraction analyses were conducted for each platform of the design space using ANSYS-AQWA. However, to make these results compatible with the HydroDyn module, the output files were converted from their original format to WAMIT format using the open-source tool BemRosetta [83]. In addition, the simulations run in ANSYS-AQWA were referred to the Point of Flotation (PoF) of the FOWT, since both, the linear hydrodynamic coefficients and the QTFs need to be referred to the WAMIT reference point, which is located at the Mean Sea Level (MSL). The wave excitation was modelled with the Peirson-Moskowitz (PM) spectrum for the given wave

significant height and wave peak period. In this study, a single wave direction was assessed, propagating along the x-axis in the positive direction, and no current was considered. To ensure consistency with the simplified model, the same viscous damping was incorporated as linear additional damping matrix within the HydroDyn file, with no consideration for quadratic damping. Any other sources of drag affecting the platform were set to zero. The viscous damping matrix was calculated as defined in Equation (3.24) for each of the platform concepts and sea states. Similarly, the mooring stiffness is introduced in the HydroDyn file as linear additional stiffness matrix instead of utilising the MoorDyn module. This approach was taken to eliminate any potential sources of error originating from the mooring system, as the primary objective is to validate the developed hydrodynamic methods, particularly focusing on their accuracy in predicting the dynamic behaviour of FOWT. As before mentioned, the mooring stiffness was defined as as function of the mean wind speed, thus, a specific stiffness matrix was associated to each reference wind speed. Contrary to the viscous damping, the mooring stiffness does not depend on the platform.

6.1.2 Assessment of the Non-Linearity Level of the Fully-Coupled Model

As before briefly mentioned, so as to compare the response signals obtained from the OpenFAST fully coupled aero-servo-hydro-elastic non-linear model against the response from a frequency domain linear model, it is necessary that the former could be, to a certain extent, approximated to a Gaussian distribution, as the excitation, meaning that it has not a purely non-linear behaviour. In order to check this, a few designs from the design space defined in table 3.8 were chosen, considering different diameter-to-draft ratios and with different distance between the columns; and simulations using different seeds were performed in OpenFAST. These were the designs D2, D11 and D18, which cover the total range values of the design space assessed in this study. Also, from mild to severe metocean conditions were examined for this verification, corresponding to the operational condition DLC2 and to the ultimate condition DLC9 from table 3.1.

Although FOWT design standards [69] recommend six random seeds, here a sensitivity analysis of the variation of the maximum response value with the number of seeds was performed. The results showed that three random seeds provide a similar maximum response to that with six random seeds, with deviations below 1% for mild conditions, and below 5% for extreme conditions. The representative maximum value to which is referred to in this analysis was modelled using the method of moments estimator of the Gumbel distribution. This method leads to a maximum value, $\tilde{\mu}$,

as a function of the mean, $\bar{X}$, and standard deviation, σ, of the registered peak values from each of the simulations corresponding to different seeds. In view of these results, three seeds were considered to assess the level of non-linear nature of the time domain model.

$$\tilde{\mu} = \bar{X} - 0.45\sigma \tag{6.3}$$

Since the frequency domain response does not account for transient effects, the first 1800 s were removed from the time series extracted from OpenFAST. Then, the histogram of the signal were obtained and compared to a normal distribution, using the mean and standard deviation of the time series. This procedure was applied for each DoF and using three different seeds in the time domain simulations. As the results obtained derived to similar conclusions, in fig. 6.2 only the histogram of the surge and pitch platform motions and the nacelle acceleration for the design D2 under the operational conditions of DLC2 are shown, with the corresponding normal distribution overlaid.

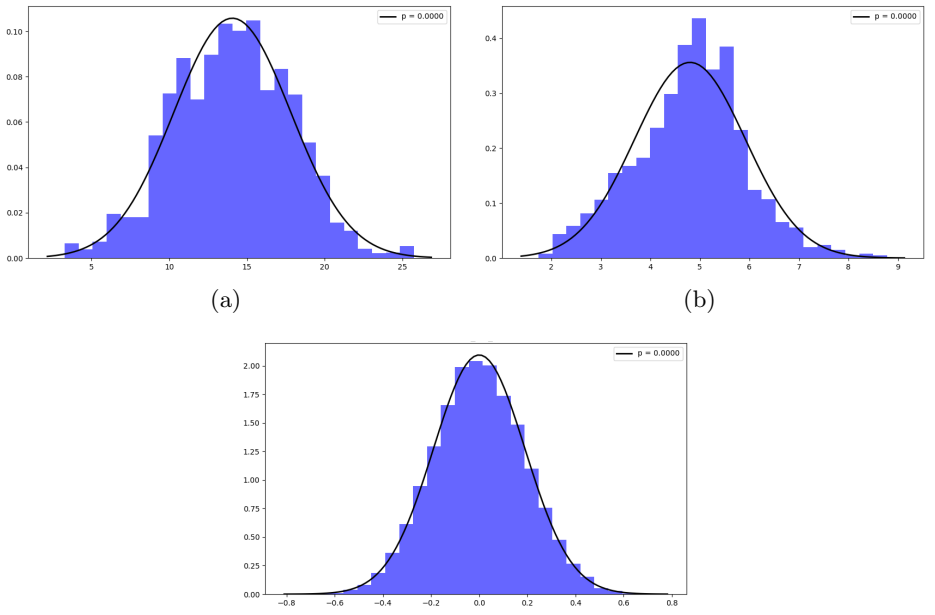

(a) (b)

(c)

Figure 6.2: Frequency distribution for D2 under DLC1 conditions (a) Surge, (b) Pitch, (c) Nacelle acceleration.

The figure fig. 6.2 provides a visual check weather the signal histogram follows a normal distribution or not. However, there are few methods for testing normality numerically. In this case, the D'Agostino-Pearson test [84]

has been applied, which returns a p-value that quantifies the null hypothesis that the values were sampled from a Gaussian distribution. A insignificant p-value means the normality test has passed. The p-value corresponding to each signal is given in the legend, and it can be observed that it is negligible, leading to the assumption that the time domain system response can be assumed to follow a Gaussian distribution.

The conclusion above enables to compare the responses from frequency domain model with those from the time domain model. From the time domain model, time series were extracted, whereas from the frequency domain model, the FFT signals and PSD are extracted. The static response was obtained by means of a static analysis, whilst the mean value of the time series was taken from the time domain model. The maxima aimed to be compared, but, since these signals follow a random process, and statistic measures were required.

6.1.3 Maximum Dynamic Response Factor Calibration

Once it was confirmed that the time domain model had a slightly non-linear behaviour and, thus, it was reasonable to assume that the response followed a Gaussian distribution, the response from the time domain model and from the frequency domain model can be compared. In fig. 6.1, the definition of the maximum response is given as a function of the mean and the standard deviation of the response, where the latter is multiplied by a dynamic factor. This factor was adjusted taking into account the distribution of the maximum response values derived from the OpenFAST simulations.

There are several ways of extracting a maximum distribution from a time series, but the key is to have a good analysis of the peak threshold that should be considered to fit the distribution. In view of the main goal of this tool, which is to provide similar tendency regarding the FOWT dynamic behaviour and enable to identify the most cost-competitive preliminary platform designs in the same way as the SoA tools, just a few simulations in the time domain were performed. The lack of a massive set of simulation data does make it nonsense to apply a complex extreme value analysis. Therefore, in this Thesis it was considered a simple approach to estimate the maximum response as a function of the mean and standard deviation, which demonstrates to be enough for the required accuracy in the initial phase of the platform design. For that purpose, first, the maximum values for each DoF and DLC resulted from the Gumbel distribution as given in eq. (6.3) were obtained.

Table 6.2 shows the maximum response for each DoF resulted from the Gumbel distribution corresponding to the most critical condition, DLC9.

ID	Surge	Heave	Pitch	Nac.Acc
D2	27.42	5.19	9.83	1.51
D11	29.50	5.13	4.02	3.12
D18	33.04	4.33	4.12	2.72

Table 6.2: Gumbel maximum response under DLC9 conditions from the OpenFAST simulations. (Units: m, deg, s)

ID	Surge	Heave	Pitch	Nac.Acc
D2	28.50	5.40	10.08	1.40
D11	30.41	5.23	3.95	2.69
D18	33.31	4.53	3.75	2.45

Table 6.3: Maximum response under DLC9 conditions using eq. (6.4) with the mean and standard deviation derived from the SoA tool. (Units: m, deg, s)

ID	Surge	Heave	Pitch	Nac.Acc
D2	27.25	5.51	9.91	1.36
D11	29.21	4.74	4.43	2.45
D18	29.04	4.21	5.01	2.42

Table 6.4: Maximum response under DLC9 conditions using eq. (6.4) with the mean and standard deviation from the *FD Tool*. (Units: m, deg, s)

For the values given in table 6.2, the dynamic factor C_{dyn} described in fig. 6.1 was extracted for each of the DoF, DLC and design, and it was concluded that it can be reduced to a unique factor, resulted from the average. The definition of the maximum response as a function of the mean and standard deviation that best represents the time domain model is given as:

$$\xi_{max} = \xi_{st} + 3.6\sigma_{\xi} \tag{6.4}$$

Table 6.3 shows the maximum response values for each DoF under DLC9 conditions, resulted from the maximum response definition through (6.4). Having a look at both table 6.2 and table 6.3, one could say that this approach generally provides a very good estimate of the maximum response. The nacelle acceleration is the motion that showed the largest differences, with a maximum deviation of 21% using (6.2), although the tendency was maintained. Moreover, this adjustment seems conservative since it accepts designs that might be further discarded. The pitch motion showed very good agreement, with deviations below 4%, and the surge and heave maximum displacements showed differences below 2% with respect to the Gumbel maximum values. Therefore, it seems reasonable to use this C_{dyn} factor to represent the maximum response of the FOWT dynamic behaviour.

In table 6.4 the maximum response resulted from (6.4) using the mean and standard deviation values from the developed frequency domain design tool, *FD Tool*, are given. From this results, it was observed that the surge was underestimated, and it seems to be very dependent on the mooring stiffness, thus, it will be more affected by the static load. Furthermore, it has been observed in chapter 5 that there was a general underestimation of the second order load through the *Accelerated Method*, so the fact of setting a more conservative factor in the surge motion would favour the comparison. Despite, the maximum deviation observed regarding the maximum surge displacement with respect to the SoA tool was 10% for the larges D/s ratio. The most important motions to be here assessed are the platform pitch displacement and the nacelle acceleration, since these are critical for the platform design and cannot be fully compensated through the mooring system design. The former showed a general good match between the SoA tool and the proposed tool, except for the largest platform design, with a maximum deviation of 8.8%. The reason for this will be discussed in the following sections. Regarding the nacelle acceleration, as before mentioned, it was under predicted, which is considered a proper approach due to the conservative hypothesis, leading to accept rather than discard platform designs too early. Nevertheless, these results demonstrated that a dynamic factor $C_{dyn} = 3.6$ can be considered a good approach of the real peak response to be used for the tool validation.

6.1.4 Platform Cost Estimation

A simple cost estimation was carried out in order to compare the different platform concepts defined in table 3.8 aimed to support the same wind turbine. Similarly to the cost estimation procedure performed by Bachynski [30], the cost of the floating platform is proportional to the steel mass required. It is a rough number, leading to a general underestimation of the overall cost, but it provides a first idea of the relative contributions of the different platform designs. In fig. 6.3 the steel mass required for each of the platform designs is shown. Neither installation nor maintenance cost were here considered.

It can be observed that as the draft of the columns increases, the steel mass does it too. Also, as the separation between the columns increases, so does the pontoon length, and thus, more steel mass is required. Similarly, the larger the diameter (or pontoon width), the larger amount of steel. The difference between the lightest platform and the heaviest, considering only the platform steel mass, is of 35%.

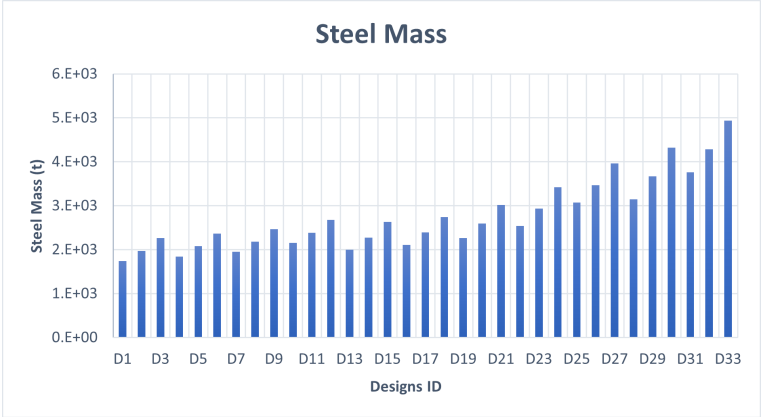

Figure 6.3: Steel mass for the different platform concepts from table 3.8.

6.2 Dynamic Response Analysis: *FD Tool* vs SoA Methods

In this section, the present *FD Tool* is validated against the SoA tool, following the scheme shown in fig. 6.1. The developed frequency domain based tool is considered successful if it is able to provide the FOWT dynamic response with the accuracy required for the substructures' preliminary design. This statement might seem rather general, however, in this Thesis it is measured through the maximum dynamic displacements of the FOWT, seeking the best agreement with the results derived from the SoA methods. Simultaneously, the tool's accuracy can be determined by the evaluation of the methodology's ability to streamline the initial design phase by identifying and discarding unsuitable platform designs, mirroring the decision-making process of SoA methods.

First, in section 6.2.1, the response of the FOWT motions along the four DoF considered in the simplified frequency domain simplified model (see section 3.3.1) are presented and discussed. Then, in section 6.2.2, the platform solutions that meet the design requirements are identified, both based on the results from the *FD Tool* and from the SoA time domain method. The results obtained for the maximum response according to the expression (6.4) are here given, measuring the accuracy through the error referred to the threshold values defined in (6.2).

6.2.1 Comparative Analysis of the FOWT Maximum Response

Herein, the FOWT surge, heave, and pitch displacements, as well as the nacelle acceleration for the different substructures defined in table 3.8 supporting the DTU 10 MW WT are shown. The viability of the method's

application is evaluated, by assessing the variability of the accuracy along the different platform designs.

Similarly to the validation of *HAAC* and *Accelerated Method*, in chapter 4 and chapter 5, respectively, the thirty-three platform solutions were subjected to a comprehensive set of DLCs, characterised by certain wind and wave conditions, which are detailed in table 3.1. These DLCs primarily encompass operational scenarios, although a few ultimate conditions were also included for examination. The thrust curve characteristic of a wind turbine increases with the mean wind speed until it reaches the maximum value at the called rated wind speed, and then it starts to decrease. The rated wind speed for the DTU 10 MW WT is 11.4 m/s. In this context, the focus is set on the most representative DLCs, namely DLC2, DLC8, and DLC9. These selected DLCs effectively span a wide spectrum of wind and wave conditions, ranging from mild to severe sea states and encompassing evaluations at low, rated, and high wind speeds. This approach allows for a thorough assessment of various combinations of wind and wave loads, highlighting instances where hydrodynamic loads may outweigh aerodynamic loads, and vice versa. In the following subsections, the results regarding each combination of wind and wave loads are discussed.

Maximum Thrust and Mild Sea State

This case corresponds to DLC2, which represents a scenario characterised by a mean wind speed of 10.3 m/s, a value very close to the maximum thrust, and relatively mild sea conditions with a wave peak period of 8 seconds. Consequently, in this scenario, the primary contribution to the overall loads experienced by the FOWT comes from wind forces.

From fig. 6.4 to 6.7, the maximum response under DLC2 for each DoF is given. The platform's behaviour in terms of surge displacements appeared to align with expectations given the thrust force in this particular context. This statement refers to the significant influence of the aerodynamic load on the surge response when the hydrodynamic loads are barely noticeable. This case particularly, the surge displacement is dominated by a mean component that is mainly on the thrust force and on the mooring stiffness, both constant along the whole design space for a given DLC. There are some noteworthy observations regarding the trend observed under these conditions. The mean response, which was well-predicted across all platform designs with deviations below 4%, suggested that the methodology effectively captures the average behaviour. However, when considering the dynamic response, as represented by the standard deviation, there were relatively noticeable larger errors, especially in cases where the platforms feature columns with 10 m diameter and 11 m draft. Despite this, it is

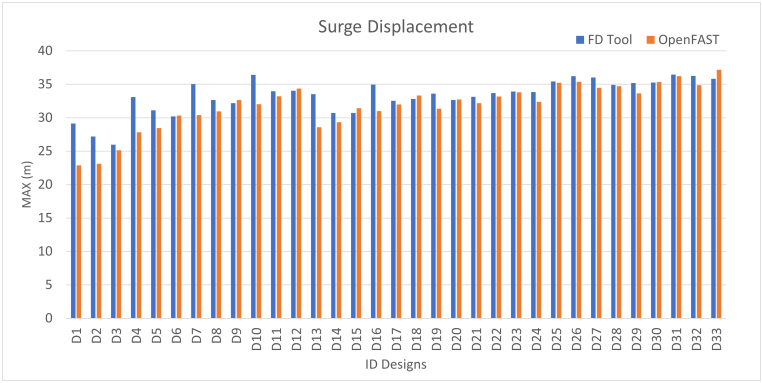

Figure 6.4: Surge maximum displacement under DLC2 for the different platform designs supporting the DTU 10 MW WT.

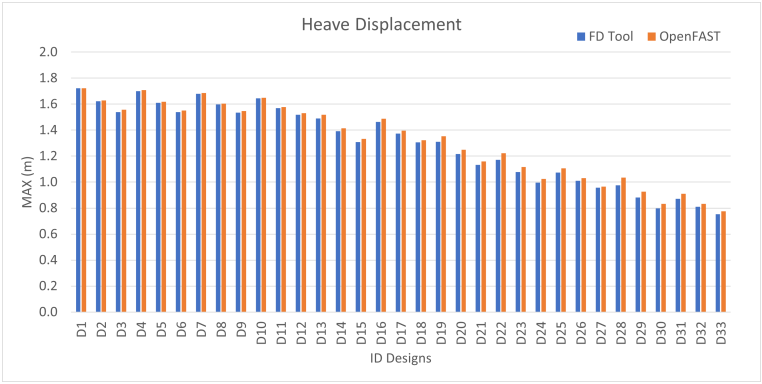

Figure 6.5: Heave maximum displacement under DLC2 for the different platform designs supporting the DTU 10 MW WT.

worth emphasising that even in these instances, the differences observed are reasonably small. Furthermore, it is interesting to note that these particular designs exhibited the smallest surge displacements compared to the other designs under examination. The maximum deviation obtained for the maximum surge displacement corresponds to D1, with 16% of error.

The heave motion stands out as the DoF that exhibited the most favourable agreement with almost zero error, displaying a consistent trend even as the platform dimensions vary. In the context of this particular DLC, the primary heave displacement was primarily attributed to the static component, resulting from aerodynamic loads. However, it is important to note that the vertical displacement of the FOWT resulted relatively insignificant in this scenario. The observed differences among responses primarily stem from the underestimation of the dynamic response, which was consistently underestimated in all cases, albeit with a similar level of accuracy. Notably,

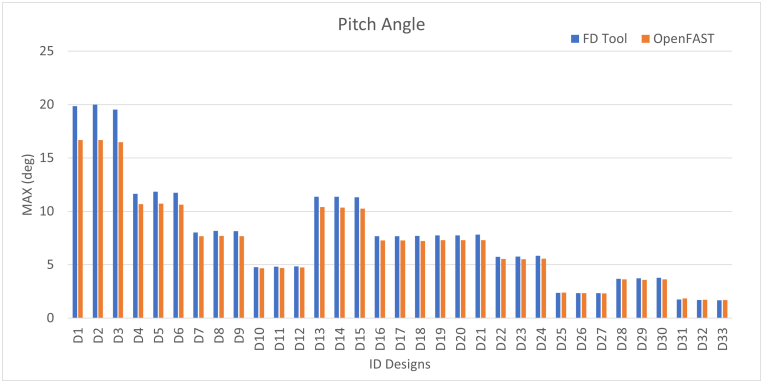

Figure 6.6: Pitch maximum angle under DLC2 for the different platform designs supporting the DTU 10 MW WT.

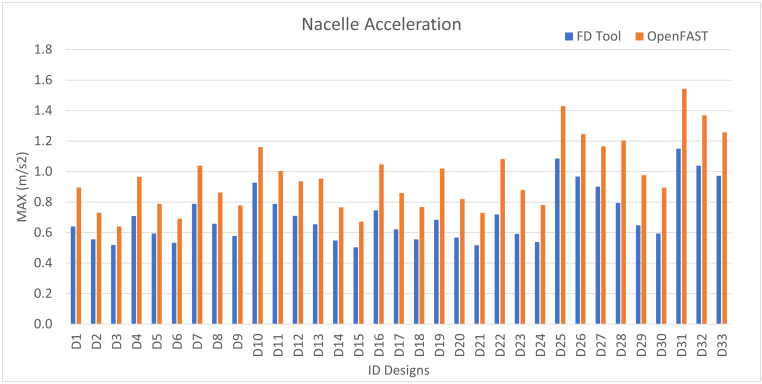

Figure 6.7: Nacelle maximum acceleration under DLC2 for the different platform designs supporting the DTU 10 MW WT.

platforms with closer column spacing tend to exhibit slightly larger deviations. Nevertheless, it is worth mentioning that the heave motion may not be a particularly critical signal for floater designers, given its relatively less pronounced significance in this context.

In the context of this DLC, the maximum pitch angle becomes particularly critical due to the very high thrust force involved, placing a substantial load on the rotor and the structure as a whole. Interestingly, it was observed that the *FD Tool* tends to overestimate the pitch angle across all cases, with a more pronounced overestimation occurring in designs featuring a smaller separation between the columns. This behaviour can be attributed primarily to two key factors. Firstly, the assumption of negligible interaction between members becomes increasingly significant when the columns are closer to each other. This assumption leads to a more accurate approximation when the platforms have a larger distance between

the columns, contributing to the observed differences. Secondly, the relevance of hydrodynamic loads versus aerodynamic loads plays a significant role in determining the method's accuracy. For smaller platform designs, the hydrodynamic loads were comparatively small, and the underestimation of the added mass and radiation damping factors contribute to an overestimation of the response motion, for a given aerodynamic load. The maximum deviation observed correspond to 30% of error for D1. However, as the platforms increase in size, these hydrodynamic loads also increase, thereby compensating for the previously mentioned differences, achieving a general deviation of 5%, and even 1% for larger platforms. This combination of factors provides an explanation for the observed results, with platform size and column spacing influencing the accuracy of the *FD Tool*'s predictions regarding pitch angles.

The nacelle acceleration showed a very good match between the proposed tool and SoA tool regarding the tendency and it was observed a relatively stable underestimation for all the designs. This DoF depends mainly on the surge and the pitch motions. If the deflection was compared, a better agreement would be achieved. However, due to the double derivative with respect to time of the estimated signal, the differences between both signals increased. The trend observed regarding the dynamic behaviour agreed very well with the SoA tool. The larger platform designs, which presented higher stiffness, suffered larger nacelle accelerations, and vice-versa. Due to the influence of the surge motion, this time, a better prediction was achieved as the draft of the columns increased. The platform design that provided the worst nacelle acceleration estimation is D28 with 23% of error, whereas the best approach was achieved for D3 with 7% of error. This is related to the contribution of the columns with respect to the full platform, where the better estimation of the hydrodynamic coefficients was obtained as the volume of the columns increase with respect to that of the pontoon.

Maximum Thrust and Severe Sea State

Now, the results corresponding to DLC8 are herein presented and discussed. This time, instead of a mild sea state, the FOWT is subjected to a severe sea state with a wave peak period of 16 s, which is a very close value to some of the platform's natural periods in heave and pitch motions, as was mentioned in section 3.3.6.

From fig. 6.8 to 6.11, the maximum response under DLC8 conditions are depicted for all thirty-three substructures supporting the DTU 10 MW Wind Turbine. Contrary to what happened under DLC2 conditions, the predicted maximum surge displacement showed a general over prediction

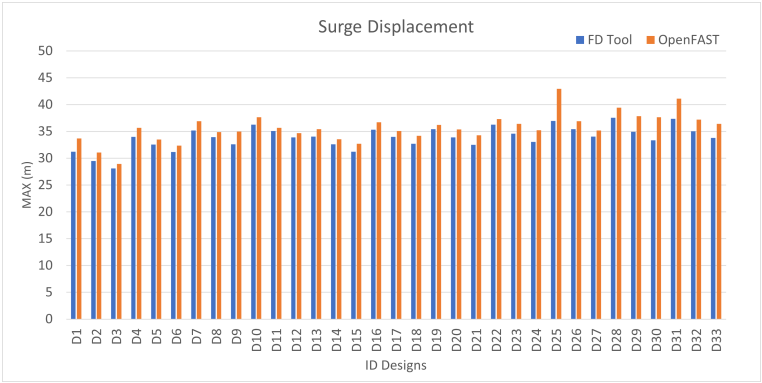

Figure 6.8: Surge maximum displacement under DLC8 for the different platform designs supporting the DTU 10 MW WT.

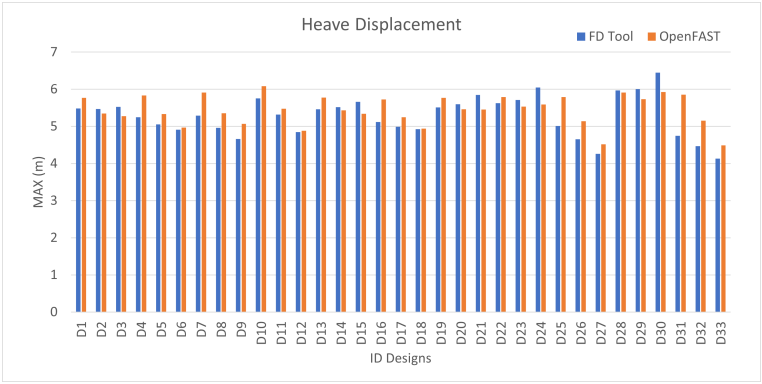

Figure 6.9: Heave maximum displacement under DLC8 for the different platform designs supporting the DTU 10 MW WT.

when the wave excitation increases, despite that the aerodynamic loads had not changed. Moreover, due to the higher contribution of the hydrodynamic loads acting on the substructure, it was observed a better prediction on the smaller platform designs, and however, larger deviations on the larger floaters. This can be mainly related to the interaction effects, which become less important when the platform members are small, and are more separated between each other. In addition, the second-order hydrodynamic loads showed to be relevant for this sever sea state, introducing the inaccuracies derived from the *Accelerated Method*, which provided very good results when the platform columns had smaller diameter-to-draft ratios. This would explain the larger deviations observed for the platform designs with larger size, such as D26 to D33. Still, the maximum deviation of the surge displacement was of 13% for D25.

The heave motion, while appeared to be somewhat more varied, still

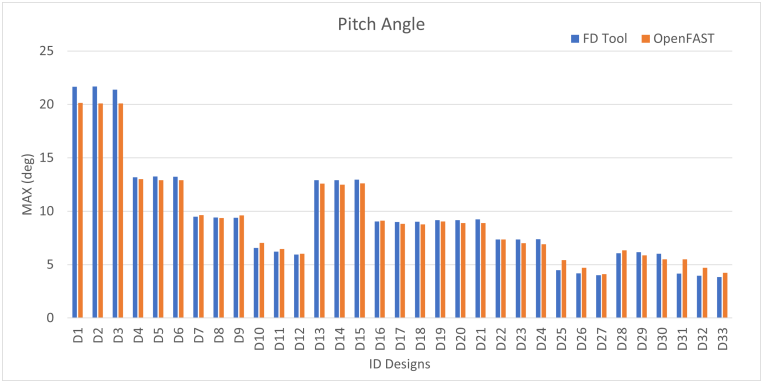

Figure 6.10: Pitch maximum angle under DLC8 for the different platform designs supporting the DTU 10 MW WT.

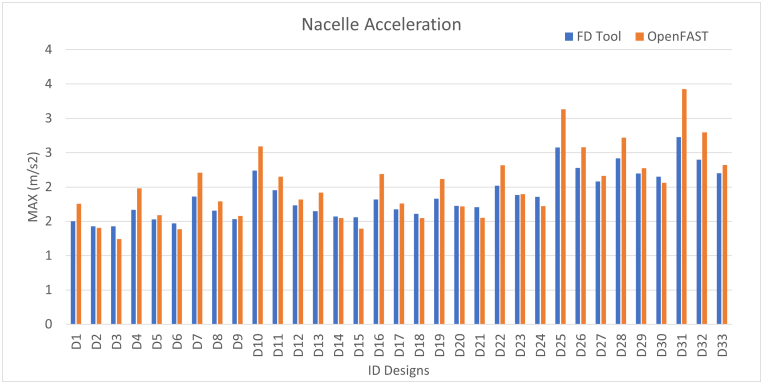

Figure 6.11: Nacelle maximum acceleration under DLC8 for the different platform designs supporting the DTU 10 MW WT.

maintained deviations below 5% across all cases. This level of accuracy provides reasonable confidence in the obtained results, despite the variability observed. Moreover, this time the heave displacement showed values that could become more significant for other design parameters, although in this Thesis it has not been deeply assessed.

Regarding the maximum pitch angle, DLC8 offered a high degree of accuracy in the response estimation, particularly for intermediate-sized platforms. It is worth noting that there was observed a general trend of over prediction of the pitch angle by the *FD Tool*, although as the platform size increases, the methodology tended to slightly under predict the response. The maximum deviation achieved was of 14% for the designs D1, with decreasing error for D2 and D3, but it was nearly isolated cases. The rest of platform designs showed deviations below 5%. The present frequency domain tool demonstrated to provide a very similar dynamic behaviour to

the SoA methods across the whole design space.

With a better prediction of the surge motion, there were found slight differences in the nacelle acceleration compared to the maximum values obtained with the SoA tool. Notably, the maximum values recorded under these conditions were generally higher than those observed in the previous case DLC2, and some of them even surpassed the defined thresholds. It could be identified the critical nature of DLC8 in assessing the FOWT's dynamic behaviour. However, some similarities were observed to DLC2, such as the general under estimation of the nacelle acceleration along the whole platform design space. The *FD Tool* again provided better estimation of the nacelle acceleration as the draft increased, related to the length of the platform columns. Also, explained by the significant influence of the second-order hydrodynamic loads when stronger waves act on the FOWTs, the platforms with smaller diameter showed better agreement with the results from the SoA tool.

Low Thrust and Severe Sea State

For the previous DLCs, the aerodynamic loads still have an important contribution to the overall load to which the FOWT is subjected. Moreover, the pitch angle, especially, and the nacelle acceleration are highly dependent on the thrust force, thus, the results leaded to relatively similar conclusions. Now, the case where the hydrodynamic loads contribution dominate over the aerodynamic loads is assessed. This condition, DLC9, was characterised by a mean wind speed of 22 m/s and a severe sea state (SS3 in table 4.1) with a 16-second wave peak period, as in DLC8. It is crucial to remember that one of the principal contributions of this study lies in the independently developed methods for estimating hydrodynamic coefficients and second-order hydrodynamic wave loads, denoted as *HAAC* and *Accelerated Method*, respectively. Therefore, DLC9 offered a valuable test case to validate and showcase the effectiveness of these unique approaches in accurately modelling and predicting the behaviour of FOWTs under conditions where hydrodynamic forces take the lead.

From fig. 6.12 to 6.15, the maximum response motions under DLC9 conditions are depicted. As expected, there were found slightly higher discrepancies between the results obtained with the proposed *FD Tool* and the SoA tool (see fig. 6.1). However, it is important to note that both signals exhibited a similar general trend, what led to consider that the *FD Tool* provides a reasonably accurate understanding of the dynamic behaviour of various platforms supporting the same wind turbine. Ultimately, achieving this level of consistency is precisely what substructure designers aim for in their quest to attain the optimal solution for their projects.

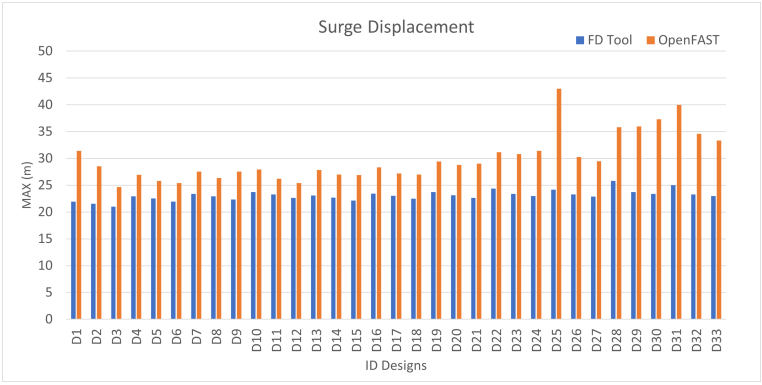

Figure 6.12: Surge maximum displacement under DLC9 for the different platform designs supporting the DTU 10 MW WT.

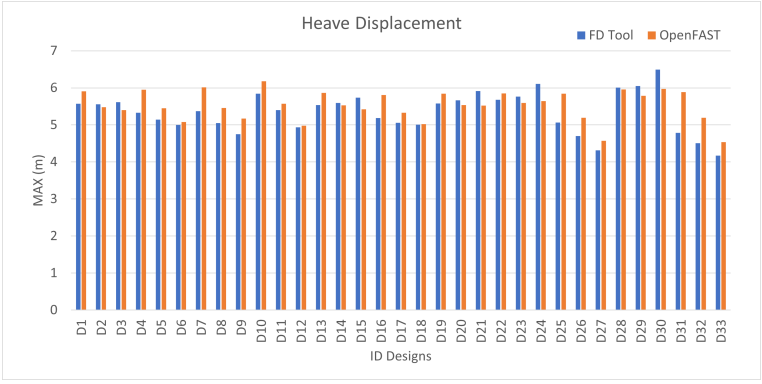

Figure 6.13: Heave maximum displacement under DLC9 for the different platform designs supporting the DTU 10 MW WT.

The most notable differences pertained to the maximum surge displacement, where a distinct underestimation of the response became evident. This outcome is was directly attributed to the significant role played by hydrodynamic loads with respect to the overall loads and, particularly by the second-order wave loads, in the context of severe sea states. As previously demonstrated in chapter 5, it was observed that the accuracy of the *Accelerated Method* was less robust for shorter columns, or in simpler terms, for platforms with a lower diameter-to-draft ratio (D/d). This trend was further illustrated in the dynamic response, where an increase in draft for the same diameter resulted to show lower errors, achieving deviations of 10% for these cases. Conversely, platforms with columns of larger diameters exhibited more substantial errors in their predictions, with deviations up to 30%. Despite this, the trend of the dynamic behaviour of the different FOWT seemed reasonably well represented by the proposed method.

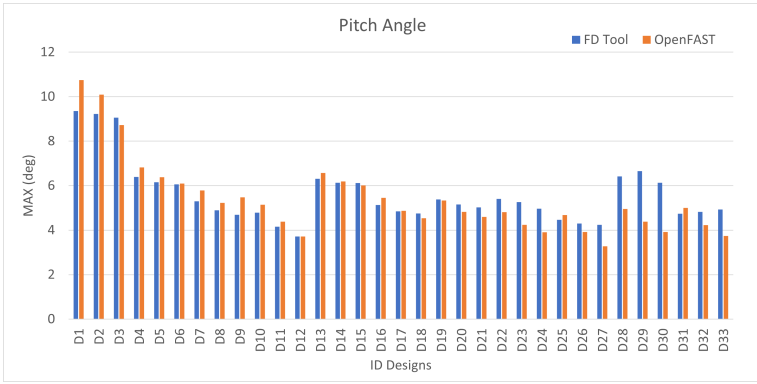

Figure 6.14: Pitch maximum angle under DLC9 for the different platform designs supporting the DTU 10 MW WT.

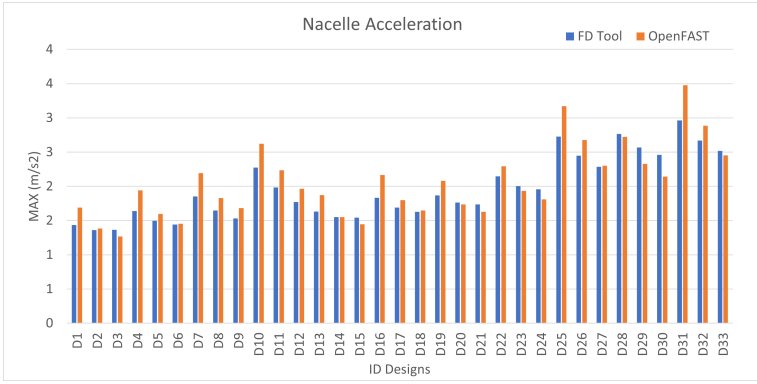

Figure 6.15: Nacelle maximum acceleration under DLC9 for the different platform designs supporting the DTU 10 MW WT.

The heave displacement derived from the FD Tool showed very good agreement with the response from the SoA tool. The maximum heave displacements for the different designs is predicted with deviations below 7%. Regarding the tendency observed, both signals matched well in overall and followed an expected tendency.

Under the current wind conditions, platform pitch angles were generally lower than in previous cases due to the lower value of the thrust force. The accuracy on the pitch angle prediction was found to slightly decrease as the platform gets bigger due to the significant contribution of the hydrodynamic loads, leading to occasional overestimation and underestimation of response. This effect was similar to that observed in chapter 5. Platforms with smaller diameters, indicating lower hydrostatic stiffness, tend to have higher pitch angles, and they were estimated with good accuracy, showing deviations below 10%. Conversely, platforms with lower pitch angle

displacements were less accurately predicted, with errors of up to 20%. Importantly, these inaccuracies in pitch angle are not considered critical as they involve relatively small thrust forces. Moreover, the platform designs that achieved the largest pitch angle showed low error values.

Lastly, but certainly not less importantly, the nacelle acceleration appeared to be accurately predicted. The maximum values obtained from OpenFAST did not exhibit significant variations when compared to those obtained under DLC8 conditions. This suggests that nacelle acceleration is primarily influenced by the sea state. Moreover, concerning the accuracy of its determination, it remained relatively consistent compared to DLC8.

6.2.2 Selection of Set of Suitable Designs

In this section, the most cost-effective preliminary platform designs were identified, taking into account the maximum response discussed in the section 6.2.1. Additionally, the relationship between the parameters and the platform cost estimation was discussed.

Among the DLCs studied in this Thesis, DLC8 stands out as the most critical one. It subjects the FOWT to a high thrust and a severe sea state, closely aligning with some platform natural periods. With this in mind, the results from DLC8 were used to identify and discuss the most appropriate platform solutions. These findings allowed to determine which platform configurations were the most suitable, focusing on their ability to meet design requirements and on the cost-competitiveness. The possibility to efficiently narrow-down the number of platform solutions enables to accelerate the whole design process, taking fewer designs to the more advanced design stage.

In fig. 6.16 and fig. 6.17, the same results as in fig. 6.10 and fig. 6.11 are shown, but this time the threshold value is given with a red dashed line and the the 10 % of threshold value upwards in order to also accept in this preliminary design stage those designs that have the maximum response inside that area. The surge and heave displacements are not here discussed since the former is mainly influenced by the mooring stiffness, which it is out of the scope of the Thesis. The influence of the mooring stiffness on the substructure design will be later discussed in chapter 7, though. Regarding the latter, it was not considered of interest in first place for the platform design.

Having a look at the pitch angle for the different designs, there were several cases that over-passed the threshold of 10 deg. These were those with the platforms of lowest diameter and lowest separation between the columns. This can be explained by the low hydrostatic stiffness value, which leads to a high tilt angle due to the thrust load. The most important idea

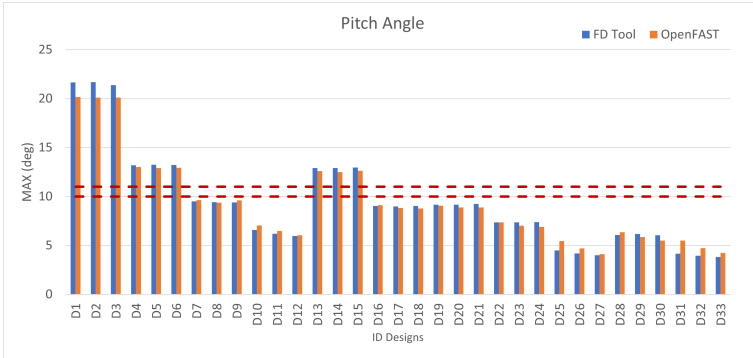

Figure 6.16: Pitch maximum angle under DLC8 for the different platform designs supporting the DTU 10 MW WT and threshold range.

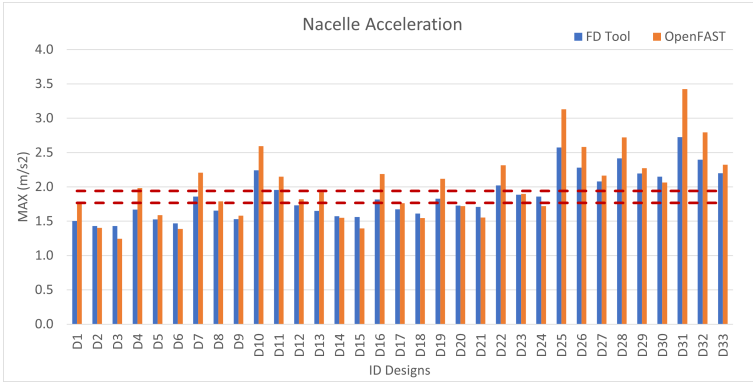

Figure 6.17: Nacelle maximum acceleration under DLC8 for the different platform designs supporting the DTU 10 MW WT and threshold range.

from these results, was that both the *FD Tool* and the SoA tool discarded the same platform designs. This could be expected in view of the low errors already discussed in the previous section. Furthermore, there was no disagreement found for any design, which provides substantial confidence to the present methodology, and consequently, to the application of the proposed hydrodynamic methods, *HAAC* and *Accelerated Method*, for the FOWT response analysis.

As for the nacelle acceleration, this time there were several platforms that did not meet the design requirement and this is mainly related to the excitation wave peak period, that was very close to the first fore-aft tower natural period. It could be noticed that those designs with 11 m draft generally were above the thresholds, and particularly, the platforms with diameter 13 m and 15 m achieved very high values of nacelle acceleration. Again, very good agreement was found between the *FD Tool* and the SoA tool, although a few designs were discarded by the latter and accepted by

the proposed tool. These were D4, D8, D12, and D13, which did not show a clear relationship, only that they corresponded to the platforms with columns of 10 m and 11 m diameter. Still, it is preferable to accept in this stage platform solutions that will be later disregarded, rather than remove potential optimal designs.

Taking these results into consideration, the viable designs to be considered for the next design stage are listed in table 6.5. It was found a very good match between the selected designs based on the results from the SoA tool and those from the new *FD Tool*. There was only one platform design that was removed by the latter, while it would be accepted by the conventional method. This was D24, which is due to the over estimation of the nacelle acceleration with an 8% of deviation. Regarding the maximum pitch angle, both methods provided the same conclusion.

ID	Steel Mass	Pitch TD	Pitch FD	Nac. Acc TD	Nac. Acc FD
D8	2.179×10^6	9.36	9.42	1.79	1.66
D12	2.385×10^6	6.03	5.96	1.82	1.73
D17	2.387×10^6	8.83	8.99	1.76	1.67
D9	2.469×10^6	9.60	9.38	1.58	1.53
D20	2.594×10^6	8.89	9.17	1.72	1.73
D18	2.739×10^6	8.78	9.02	1.55	1.61
D21	3.012×10^6	8.88	9.24	1.55	1.71

Table 6.5: Sorted list of platforms that meet design requirements and the response from the FD Toll and TD SoA tool. (Units: kg, m, deg, s)

In view of these results, it can be concluded that the most cost-competitive designs were those with columns of 10-11-12 m diameter. Those platforms with 11 m draft showed not to be suitable for supporting the DTU 10 MW WT, since none of them met with the design requirements. Additionally, for these diameter values for the columns, 50 m of separation seemed only appropriate for the 12 m diameter columns, for lower diameter values the structure did not introduce the enough hydrostatic stiffness to withstand the thrust force.

Once that the platforms that meet the design requirements are identified, it is up to the designer to set the next criterion to considered. For instance, if the steel mass is regarded, there is not substantial difference between the chosen platforms, except for the design D21. In real practice, more factors would be taken into account, although this tool showed to give a quick glance of the dynamic behaviour of the different FOWT substructures.

6.3 Computational Cost Reduction

In this section, the computational cost reduction achieved by means of the proposed methodology is discussed. The main motivation of this Thesis is the reduction of the FOWT cost. As mentioned in the chapter 2, the floating substructures are one of the main costs drivers, thus, by their optimisation, a substantial reduction of the Levelised Cost of Energy (LCOE) could be achieved. Nevertheless, the optimisation process can become very time consuming, when tens of solutions are assessed with multiple combinations of their design parameters (diameter of the columns, distance between them, draft, freeboard, ballast, etc). It is common to reduce the number of platform designs to be evaluated in order to save computational time, disregarding some intermediate solutions. This study has pursued to accelerate this preliminary design process by developing efficient methods that enable even to increase the floater's design space. As the analysis time for the calculation of the hydrodynamic characteristics is, to some extent, proportional to the assessed number of platforms, this Thesis has focused on improving the efficiency of these type of analyses, through *HAAC* and *Accelerated Method*, described and validated in chapter 4 and chapter 5, respectively. In the corresponding chapters, the saving in computational cost compared to that required in the radiation-diffraction analysis by means of panel codes, has been quantified. As the *FD Tool* integrates both methods, the overall analysis time results from the sum of the time required by each of the methods. Regarding the computational time of the accelerated method, 128 modes were used, although it has been already explained that the time required was for the database creation. The total time required for the analysis of the eighteen platforms supporting the DTU 10 MW WT, without considering the 60.000 s to build the database, was 183 s, what means less than 10 s of analysis per design. This is 2500 times faster than the time required by SoA method, which was performed in the time domain and with the radiation-diffraction analysis for each of the platform designs. If the database is considered, the *FD Tool* improved the efficiency with respect to the SoA tool 14 times.

In fig. 6.18, the chart illustrates the improved efficiency of analysing the dynamic response of FOWTs as a function of the number of platform designs being evaluated. The *FD Tool* exhibits enhanced efficiency in comparison to the SoA tool, particularly as the design space grows larger. This improvement can be attributed to two key factors. Firstly, the SoA tool necessitates performing a radiation-diffraction analysis for each floater design to obtain hydrodynamic loads, which are subsequently fed into OpenFAST. In contrast, the *FD Tool* streamlines this process. Secondly, it was observed that the developed *HAAC* method consistently took 60,000 seconds to build

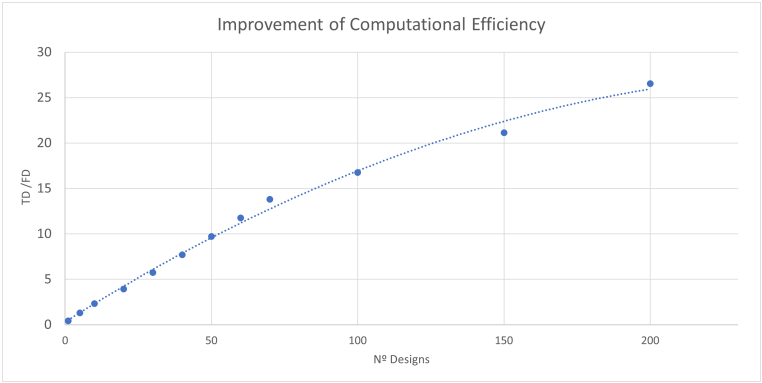

Figure 6.18: Improvement of the computational efficiency for the dynamic response analysis through the *FD Tool* with respect to the SoA tool.

the database, regardless of the number of platform designs being evaluated. Consequently, the *HAAC* method becomes more efficient as the number of platform solutions increases, resulting in an overall enhancement of the *FD Tool* efficiency.

To put this into perspective, employing the conventional SoA tool for dynamic response analysis, which involves radiation-diffraction analysis in ANSYS-AQWA followed by time-domain simulation in the fully coupled OpenFAST tool, for each of the thirty different platforms supporting the DTU 10 MW WT would take 480 hours. However, the *FD Tool* can complete the same analysis in just 83 hours while providing reasonably accurate results.

Furthermore, in a scenario where a hundred platform solutions need to be assessed, not far from a real-world situation, the computational cost is reduced from 1800 hours with the SoA tool to just 168 hours using the *FD Tool*. This significant reduction in computational time underscores the effectiveness of the *FD Tool* in handling a large number of platform designs.

Chapter 7

Sensitivity Studies with the *FD Tool*: Defining Design Guidelines

In the preceding sections of this Thesis, the frequency domain tool developed here has been validated and has demonstrated its ability to draw conclusions consistent with state-of-the-art (SoA) tools when examining the dynamic behaviour of the Floating Offshore Wind Turbine (FOWT). Furthermore, it has proven its suitability for the initial design phases of FOW substructures by providing reasonably accurate estimates of response trends when various platform design parameters are modified. The primary advantage of this tool is its computational efficiency in dynamic analysis. This improvement of the efficiency allows for the evaluation of numerous platform designs, facilitating the pursuit of optimal solutions from a very early design stage. Additionally, the tool's efficiency permits the analysis of different conditions and supports sensitivity analysis, which may be pertinent to floater designers.

Within this Thesis, two sensitivity analyses were conducted with the primary aim of extracting insights into the platform design process and the factors influencing it. Firstly, in section 7.1, the up-scaling of the platform when it aims to accommodate the IEA 15 MW WT was investigated. Similar to the comparative analysis conducted for the DTU 10 MW WT, the the most cost-effective platforms for supporting the larger turbine were identified, and subsequently presented the scaling relationships. Secondly, in section 7.2, a second sensitivity study was conducted, focusing on the influence of the mooring system on platform design. Typically, this is a subsequent step in the process, but it has a significant impact, particularly concerning second-order hydrodynamic loads.

7.1 Designing Platforms to Support Larger Wind Turbines

Within this sensitivity study, a qualitative analysis was undertaken to assess the influence on substructure design when scaling up wind turbine size. Particularly, the DTU 10 MW WT was used as the reference and how platform dimensions evolve when tasked with supporting larger turbines was examined, comparing the previously identified solutions. If a larger turbine is installed, the supporting platform is expected to increase in size with respect to a less powerful wind turbine. Not only because of the size of the rotor, but mainly because of the higher thrust force. This increase in loads, requires a larger platform that provides stability to the wind turbine. First the suitability of the platforms defined in table 3.8 that were used to support the DTU 10 MW WT was evaluated and it was found that most of the platforms that were in the small size range were not even stable under static loads. Therefore, a new design space was defined for the IEA 15 MW WT including platforms with dimensions within the large size range. Then, the dynamic analysis was performed, where again, a comparative analysis of the different FOWT under several DLCs was carried out. Finally, similarly to the procedure followed in the section 6.3, the most suitable and cost-effective platform solutions were identified and their design parameters were compared with respect to those platforms selected for the 10 MW WT wind turbine. The primary goal of this study is to determine specific design guidelines that provide insights into how platform dimensions change as the size of wind turbines increases.

7.1.1 Platform Design Space for the IEA 15 MW WT

The platforms used for the DTU 10 MW WT were first assessed, by means of a simple static analysis. The static loads composed of the mean wind loads and gravitational loads, and most of the floater solutions seemed not to be suitable for the scaled IEA 15 MW WT. This is reasonable, since a larger wind turbine is expected to require a larger sub-structure, thus new platform designs were defined and their characteristic dimensions can be found in table 7.1. In order to differentiate the scaled up designs from the original ones used for the DTU 10 MW WT, now the identification index is denoted with S instead of D. Throughout this Thesis, as described in chapter 3, the FOWT draft was defined as a design parameter, which was set prior to the calculation of the platform mass, including ballast. In other words, the mass of water ballast was derived from the equilibrium between the displaced water mass and the total FOWT mass. This procedure might not be realistic, but it is a simple assumption that enables a clear compar-

ative analysis to show the validity of the present tool. Therefore, the same draft values as for the DTU 10 MW WT were again evaluated, and new values for the columns' diameter and the distance between them were given. The new design space increased the number of designs within the range of the large substructures. The platforms corresponding to the low range of diameter and separation between the columns needed to be removed, since they did not meet even the static stability under the maximum thrust conditions.

ID	**S1**	**S2**	**S3**
D	10	10	10
s	70	70	70
d	11	15	20

ID	**S4**	**S5**	**S6**
D	11	11	11
s	70	70	70
d	11	15	20

ID	**S7**	**S8**	**S9**	**S10**	**S11**	**S12**
D	12	12	12	12	12	12
s	60	60	60	70	70	70
d	11	15	20	11	15	20

ID	**S13**	**S14**	**S15**	**S16**	**S17**	**S18**	**S19**	**S20**	**S21**
D	13	13	13	13	13	13	13	13	13
s	50	50	50	60	60	60	70	70	70
d	11	15	20	11	15	20	11	15	20

ID	**S22**	**S23**	**S24**	**S25**	**S26**	**S27**
D	14	14	14	14	14	14
s	50	50	50	70	70	70
d	11	15	20	11	15	20

ID	**S28**	**S29**	**S30**	**S31**	**S32**	**S33**
D	15	15	15	15	15	15
s	50	50	50	70	70	70
d	11	15	20	11	15	20

Table 7.1: New platform design space for IEA 15 MW WT. Values of diameter 'D', separation between columns 's' and draft 'd' (Units: m).

7.1.2 Dynamic Response Assessment

The new set of FOWT were subjected to the DLCs described in table 3.1. In this section, again situations with different combinations of low to high wind speeds and mild to severe sea states are evaluated. In addition, since the platform selection criteria in this work was mainly dependent on the pitch angle and nacelle acceleration, whose maximum values following the standards for FOWT design indicated in section 3.2.3, only the maximum pitch angle and the maximum nacelle acceleration are shown. The maximum definition used for this results is the same as that defined in section 6.1.3 through the expression (6.4). Particularly, the DLC2, DLC5, DLC8, and DLC9 are presented and discussed below.

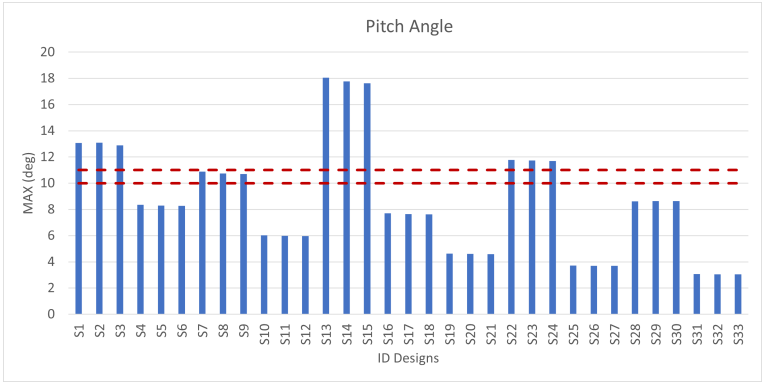

Figure 7.1: Pitch maximum angle under DLC2 for the different platform designs supporting the IEA 15 MW WT and threshold range.

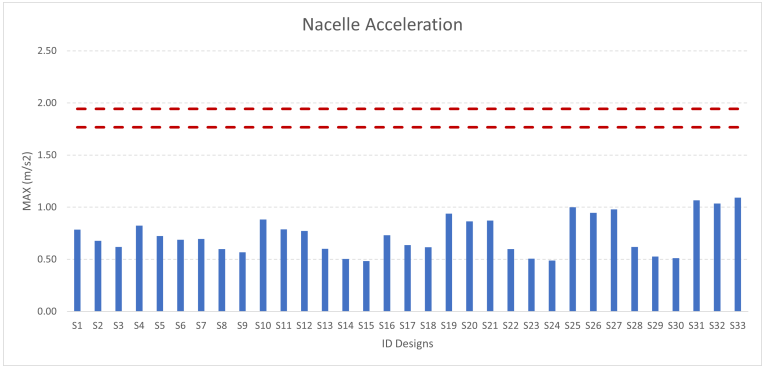

Figure 7.2: Nacelle maximum acceleration under DLC2 for the different platform designs supporting the IEA 15 MW WT and threshold range.

In fig. 7.1 and fig. 7.2, the results for the new FOWT are shown. This condition corresponds to a major contribution of the aerodynamic loads, since the incident wind speed is very close to the rated mean wind speed. Therefore, this DLC is critical for the pitch motion. Here, two important relationships between the dynamic behaviour and the platform dimensions were well observed. On one hand, the platforms with small diameter ($D = 10 - 12$ m) were still close to the threshold value, and some of them even over-passed it for short distances between the columns. Larger separation between the columns also implies larger pontoons which provides more hydrostatic stiffness, although it seemed not to be enough to withstand the thrust force. On the other hand, platforms with large diameter, such as $D = 13 - 15$ m, showed to provide more stability to the structure, although for the lower range of distance between the columns they over-passed the threshold. The draft, again, did not seem to have a significant effect on this motion, although the low contribution of the hydrodynamic loads is

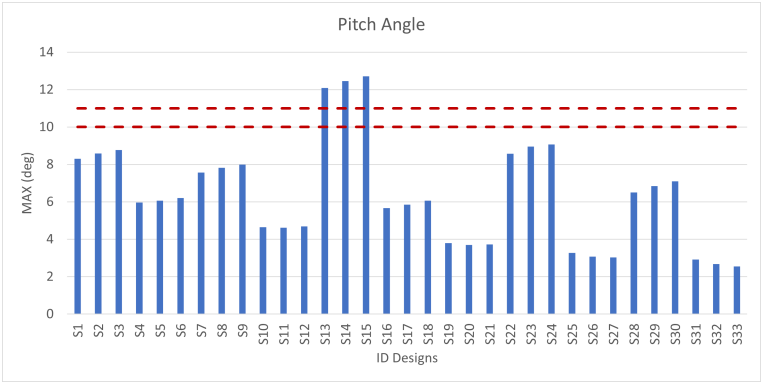

Figure 7.3: Pitch maximum angle under DLC5 for the different platform designs supporting the IEA 15 MW WT and threshold range.

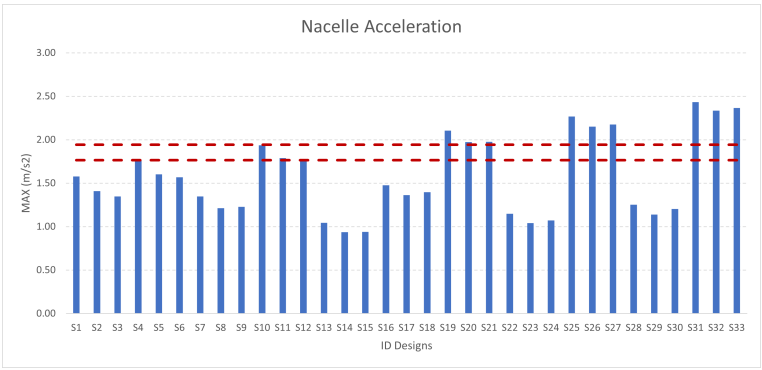

Figure 7.4: Nacelle maximum acceleration under DLC5 for the different platform designs supporting the IEA 15 MW WT and threshold range.

one of the reasons for this. The nacelle acceleration, which is mainly influenced by the sea conditions, showed maximum values relatively far from the threshold, thus this DLC would not discard any platform solution considering this motion.

In fig. 7.3 and fig. 7.4, the results under DLC5 are given. This DLC corresponds to a turbulent wind characterised by a mean wind speed of 22 m/s and a moderate sea state. Now, the thrust force is lower, thus the aerodynamic loads are not dominating the excitation on the FOWT. It is remarkable the high pitch angle suffered on the designs S13-S15, which correspond to the platforms with $D = 13$ m and $s = 50$ m, leading to the conclusion that this poor distance between columns resulted in a very low hydrostatic stiffness, making the structure not very stable. These designs would be discarded in this initial design stage. Regarding the nacelle acceleration, under a moderate sea state with a wave peak period $T_s = 12.5$ s, it was found that some of the floating substructures were not suitable

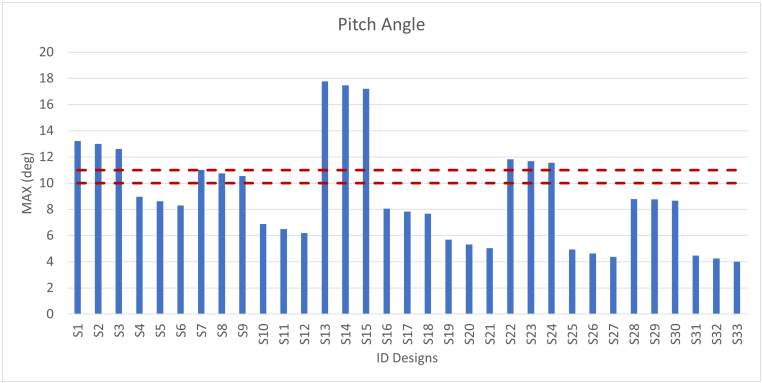

Figure 7.5: Pitch maximum angle under DLC8 for the different platform designs supporting the IEA 15 MW WT and threshold range.

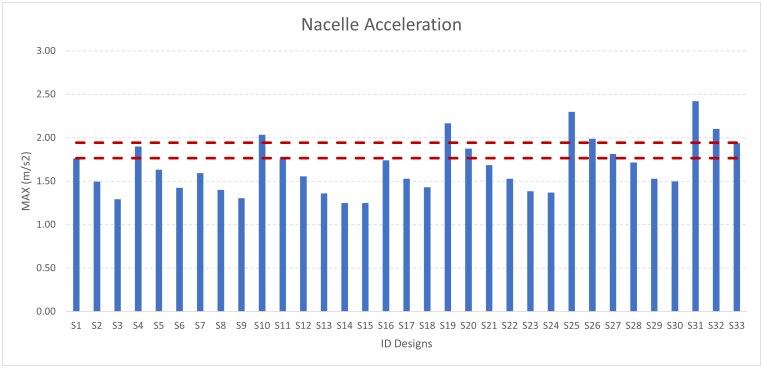

Figure 7.6: Nacelle maximum acceleration under DLC8 for the different platform designs supporting the IEA 15 MW WT and threshold range.

for support this powerful wind turbine. In fact, the nacelle acceleration showed the contrary effect as the pitch angle, being those platforms with larger column diameter and larger distance between the columns the ones that provided higher acceleration value, presumably due to its higher pitch hydrostatic stiffness. This would lead to a balance between the pitch stability and the loads on the tower base due to the nacelle acceleration, in order to keep the maximum values below the threshold line.

In fig. 7.5 and fig. 7.6, the most critical DLC is given, which corresponds to maximum thrust and severe sea state. The results obtained for the pitch angle were barely the same as those for DLC2, highlighting the importance of the thrust force on this motion. Compared to the results of the designs supporting the DTU 10 MW WT, some of them did not meet the design requirements. For instance, the solutions with $D = 10$ m and $s = 70$ m, were suitable for the 10 MW WT, whereas were not for the 15 MW WT, and this is mainly because of the higher thrust force of the latter.

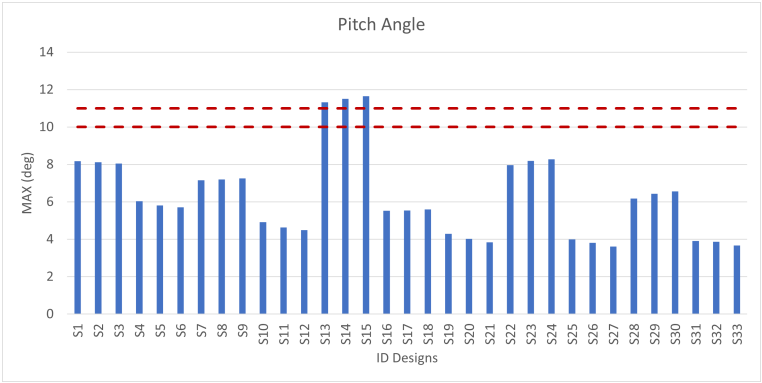

Figure 7.7: Pitch maximum angle under DLC9 for the different platform designs supporting the IEA 15 MW WT and threshold range.

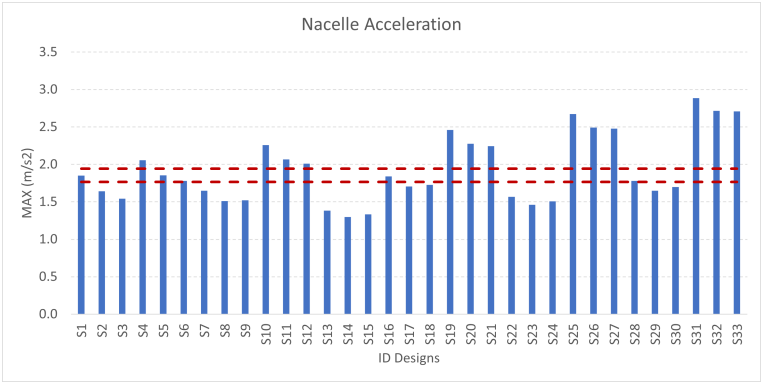

Figure 7.8: Nacelle maximum acceleration under DLC9 for the different platform designs supporting the IEA 15 MW WT and threshold range.

Similar situation happened with the designs with columns of $D = 13$ m and $s = 50$ m. On the contrary, the nacelle acceleration showed a more relevant influence on the draft, which was related to the importance of the hydrodynamic load contribution to the total excitation acting on the FOWT.

In fig. 7.7 and fig. 7.8 the maximum pitch and nacelle acceleration of the different FOWT under DLC9 conditions are depicted. Since the aerodynamic loads were less relevant than the hydrodynamic loads, lower pitch angle motions were generally observed. Except for the platform designs with columns of 13 m diameter separated 50 m between them, generally pitch angles below the limit value were observed, although they showed higher values than for the 10 MW WT. The accelerations of the nacelle for the IEA 15 MW WT are significantly lower too. In fact, the designs with columns of $D = 13 - 15$ m and $s < 60$ m seem to be suitable, whilst they

were not for the DTU 10 MW WT.

7.1.3 Selected Platform Solutions

Taking into account the results observed in the previous section, from fig. 7.1 to 7.8, the most cost-competitive platform designs that meet with the design requirements were identified. Furthermore, they were compared against the platform solutions selected for the DTU 10 MW WT. In this section the results obtained and how the variation of the platform dimensions are discussed.

ID	Steel Mass	D	s	d	Pitch	Nac. Acc
S29	3.667×10^6	15	50	15	8.77	1.53
S18	3.692×10^6	13	60	20	7.68	1.43
S30	4.321×10^6	15	50	20	8.67	1.50

Table 7.2: Sorted list of platforms that meet design requirements and the maximum response estimated by the *FD Tool* for the IEA 15 MW WT. (Units: kg, m, deg, s)

The designs that resulted to be the most suitable to support the IEA 15 MW WT are given in table 7.2. Compared to the designs that seemed the most cost-effective to support the DTU 10 MW WT, the present designs correspond to larger platforms as expected. Essentially, the dimension that appeared to be the most influencing one is the diameter, which was initially constrained to be equal to the pontoon width. Therefore, columns of bigger diameter also mean to have wider pontoons. However, the distance between the columns did not show a clear influence, since the values for the present designs were similar to those for the smaller turbine, which are between 50-60 m. Regarding the draft of the new designs, it generally increased, being from 15-20 m more suitable than the smaller ones. A larger draft provides stability especially in terms of the nacelle acceleration. It would be decision of the designer whether to prioritise the response or the platform dimensions, since factors such as installation or construction are not here taken into account.

The surge natural periods were between 135-155 s, the heave and pitch natural periods showed slightly low values, with 16 s and 30 s, respectively. The heave motion was not here discussed, although the natural period seemed susceptible to resonance under severe sea conditions. The tower displacement according to the first fore-aft mode shape did not compromise the 1P-3P region in the Campbell Diagram from fig. 3.14. Compared to the natural periods for the most suitable platform designs to support the DTU 10 MW WT, when scaling up to more powerful turbines, the surge

natural periods decrease a little bit, although this depends significantly on the mooring stiffness, which is different in these two cases. In this tool, the mooring system was represented by a stiffness matrix and the one used for the IEA 15 MW WT almost doubles that employed for the DTU 10 MW WT. Therefore, the natural period for larger turbines, in this case, would decrease slightly. The heave natural periods also showed lower values for the larger turbine, becoming more susceptible to resonance. The natural period values on the heave motion could be adjusted by adding heave plates, which increase the added mass. Now that the dimensions of the preliminary platform design that appeared to be the most cost-effective, heave plates can be added in the next stage of design. The pitch natural periods, however, resulted to be very similar among the different designs, with variations below 5%.

The platforms resulting from this analysis required very similar amount of steel mass. Compared to the platforms selected for the DTU 10 MW WT, the platform designs aimed to support the IEA 15 MW WT showed an increased of steel mass between 1.5-2 times. As a reference, the amount of steel mass per megawatt for this wind turbine scaling-up increases between 1-1.3 times.

7.2 Influence of the Mooring System on the Floaters Design

This section introduces the second sensitivity study, which focuses on evaluating the impact of mooring effects within the context of platform design and identifying the key factors to consider. In the design of FOWT substructures, mooring pretension plays a pivotal role as a design parameter. Due to the nature of the frequency domain tool developed in this Thesis, where the mooring system is represented by a stiffness matrix that varies with the wind conditions, the definition of the mooring lines was not here evaluated nor defined. Therefore, the type of mooring line, length, material, chain diameter, or any other mooring design parameter were not here considered. However, the developed frequency domain design tool can be useful for mooring design through the analysis of the needed mooring stiffness to keep the FOWT within certain offset values from the structure's equilibrium position without excitation. For instance, through the estimation of the minimum mooring system stiffness required for a given floating platform design, the minimum pretension required in the mooring lines can be estimated. This enables concurrent development of the mooring system and platform design. The subsequent discussion focuses on how the mooring system influences the dynamic behaviour of FOWTs.

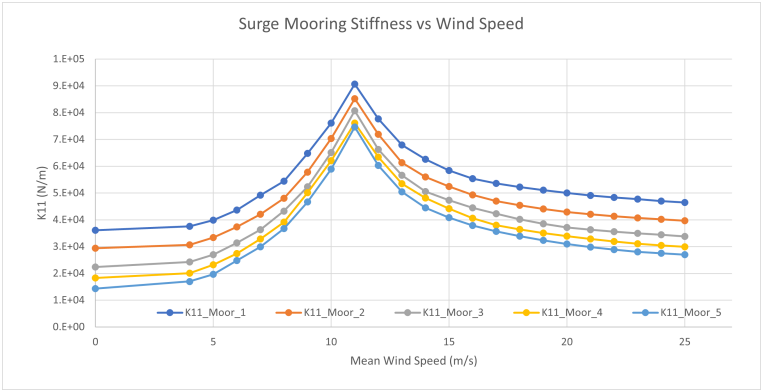

(a)

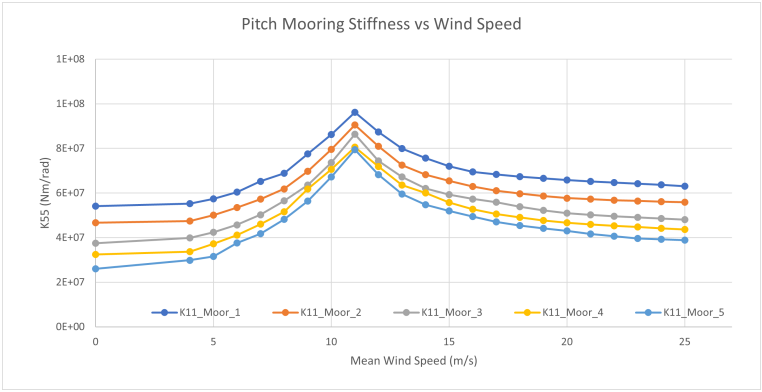

(b)

Figure 7.9: Stiffness for five mooring systems as a function of the mean wind speed at equilibrium position under no excitation. (a) Surge (b) Pitch

This study was applied to the DTU 10 MW WT supported by the different platform designs described in table 3.8. Five mooring systems were defined, represented by stiffness matrices, covering a wide range of values, from softer to stiffer systems. In fig. 7.9, the surge and pitch mooring stiffness as a function of the mean wind speed are shown, since, as explained in section 3.3.4, the mooring stiffness is associated to a specific thrust force based on the wind turbine performance curves. The grey curve ($Moor_3$) corresponds to the mooring system used for the validation of the present *FD Tool* described in section 3.2.4, and four other matrices have been defined with lower and higher stiffness values. The stiffness of the surge DoF is given by the mooring system, making the response in this motion highly sensitive to these stiffness values. In contrast, the system pitch stiffness matrix is predominantly affected by hydrostatic stiffness, with mooring stiffness in

this DoF being one or two orders of magnitude lower, resulting in minimal impact on pitch response motion. Similarly occurs with the heave DoF, although it is now here shown.

The various mooring stiffness matrices were utilised as inputs for the *FD Tool*, and the behaviour of the thirty-three floaters described in table 3.8 was assessed across a broad spectrum of environmental conditions. Initially, the natural frequencies associated with the four degrees of freedom within the *FD Tool* were compared across the five different mooring matrices. Following this, the motion responses of each of the FOWT designs were analysed, with a particular focus on examining how the mooring system affected these responses. Ultimately, the benefits of incorporating second-order hydrodynamic loads in the early stages of designing FOW substructures were identified.

It should be borne in mind that the optimal design of the mooring system falls outside the purview of this thesis. However, this section is dedicated to quantify the impact of mooring on platform design. The primary goal is to refine the preliminary platform design by taking the mooring system into more precise consideration. To simplify matters, this study exclusively concentrated on differences in stiffness among various mooring system designs and did not factor in alterations in mass.

7.2.1 Assessment of the Response for the Different Mooring Systems

Herein, the results from the comparative analysis of the different FOWT designs response under different DLCs from table 3.1, and for the five mooring systems shown in fig. 7.9 is discussed. The main goal is to quantify the effect of the mooring system on the dynamic response of the full FOWT. For that purpose, the *FD Tool* is used to analyse the FOWT response, by introducing the five different mooring systems, represented by stiffness matrices. The results for most representative cases DLC2, DLC8 and DLC9 are here shown and discussed. In addition, the influence of the mooring system on the FOWT natural periods is previously examined.

Natural Periods

In fig. 7.10, the surge natural periods for each of the platform designs are shown. These natural frequencies were obtained by solving the eigenvalue problem using the mass and stiffness matrices of the system described in section 3.3.1. For the calculation of the natural periods, the position with no excitation was considered. It is noticeable that the variation of the natural periods with the mooring stiffness is nearly a constant factor, proportional

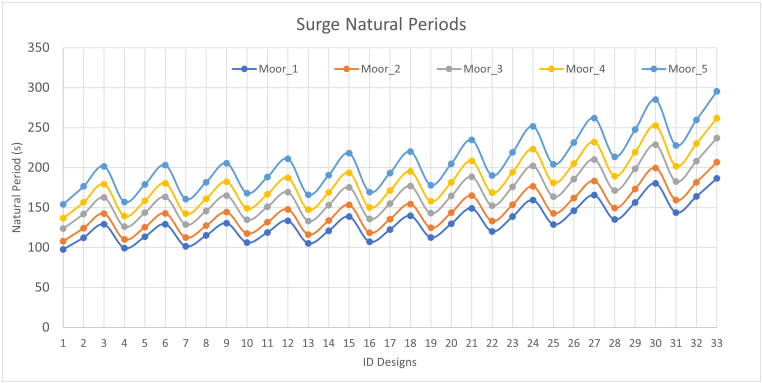

Figure 7.10: Natural periods (s) for the different platform designs and mooring systems.

to the square root of the stiffness ($T_n \sim \sqrt{m/k}$).

The heave and pitch natural periods are not given since it was observed to have negligible influence from the mooring system, since both are dominated by the hydrostatic stiffness. Similarly occurs with the tower first fore-aft deflection natural period due to its high dependency on the pitch angle. Regarding the surge natural periods, the peaks observed in fig. 7.10 follow the expected trend: on one hand, as the stiffness increases, the natural period decreases. And, in the other hand, as was observed in the previous chapters, the platforms with larger drafts, due to longer columns, and larger diameter of the columns, showed a higher value of the natural period since they have a higher mass. These high natural periods on the large substructures makes them more sensitive to resonance excited by second-order hydrodynamic loads.

Maximum Surge Displacement

The maximum response under some relevant DLCs was evaluated for each of the platform design space. Regarding the response motion, again no substantial differences were observed in the heave and pitch motions, nor in the nacelle acceleration despite the contribution of the surge motion to the latter. Therefore, herein only the results obtained for the surge displacement are shown and discussed. This fact is definitely an important conclusion regarding the mooring design, particularly for the semi-submersible platforms. Conversely, in case Tension Leg Platforms (TLP) were assessed, the influence of the mooring system stiffness on heave and pitch motions would be critical, and through the proposed tool a quick estimation of its influence could be achieved.

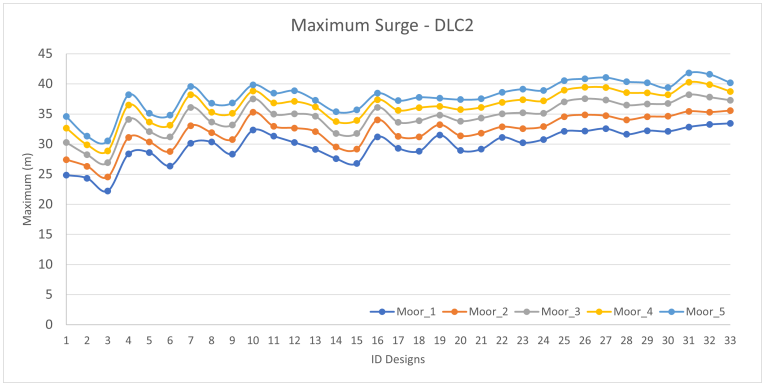

(a)

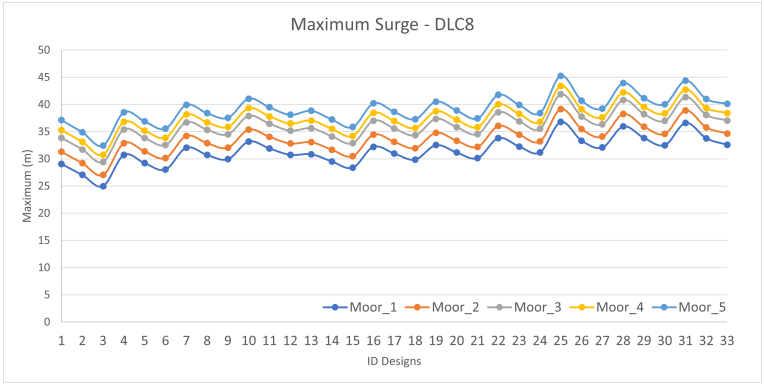

(b)

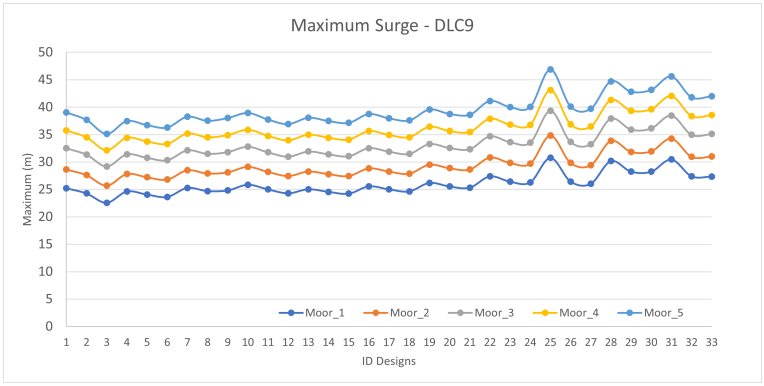

(c)

Figure 7.11: Stiffness for five mooring systems as a function of the mean wind speed at equilibrium position under no excitation. (a) Surge (b) Pitch

In fig. 7.11 the maximum surge displacement obtained using the definition of maximum from (6.4) is given, for DLC2, DLC8 and DLC9. These conditions represent maximum thrust and mild sea state, maximum thrust and severe sea state, and low thrust and severe sea state, respectively. This way, three different situations were assessed, where the aerodynamic loads dominate over the hydrodynamic loads, and vice versa. Therefore, the influence of the mooring under several metoceanic conditions was evaluated. As expected, the stiffer mooring system considered, the lower maximum surge displacement was achieved for all DLCs and all designs. Furthermore, the higher the thrust force, the higher maximum horizontal displacement were observed, due to the dominance of this force in this direction. It was also noticeable that the cases where the aerodynamic loads dominate over the hydrodynamic loads, as for DLC2, the maximum response showed more variation with the change of draft, especially for the smallest platform designs, and as the diameter of the columns increase, the influence of the draft was reduced. However, when hydrodynamic loads dominate the excitation on the FOWT, as for DLC9, the maximum surge displacement of the different FOWT did not show barely influence of the draft, except for the largest platform designs. This behaviour can be related to the added mass and radiation damping, where both are proportional to the length of the columns, and consequently, to the platform draft.

Estimation of the Minimum Mooring Stiffness

As mentioned at the beginning of the chapter, the pretension of the mooring lines is a useful parameter for the design of the mooring system, together with other indicators such as the platform offset, the FOWT natural periods, the fatigue life of the lines, and the costs associated with mooring installation and required vessels. Although this Thesis primarily focuses on substructure design for FOWT, it is essential to recognise that all structural components are interrelated. The optimisation of platform designs is achieved by accounting for these interactions right from the outset of the design process. The proposed frequency domain tool, *FD Tool*, enables to gain a deeper understanding of how each component influences the others in order to establish a more precise and comprehensive initial design. In this study, one of the suitable selected designs in section 6.3 (see table 6.5) was used as a case study and the response under the most critical conditions using the different mooring stiffness matrices were compared. For this example it was used the platform design D8 supporting the DTU 10 MW WT, which features columns with a diameter of 10 meters, spaced 60 meters apart from their axes, and a draft of 15 meters. The study considered the response of this design under the most critical conditions, comparing res-

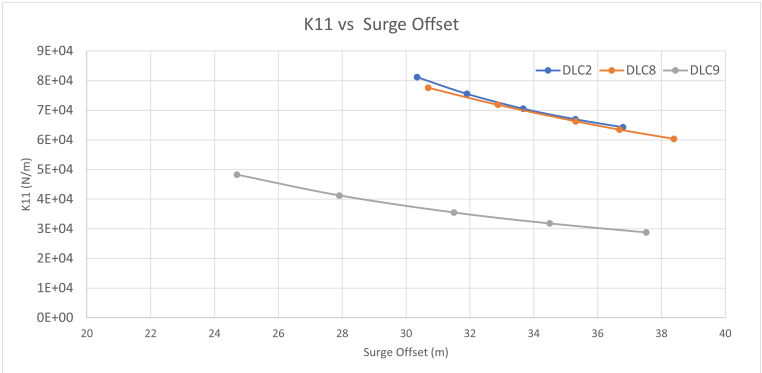

Figure 7.12: Surge mooring stiffness vs FOWT horizontal displacement for three DLCs.

ults using different mooring stiffness matrices. The three DLCs for which the results have been previously shown are here discussed. In fig. 7.12, the mooring stiffness in the surge DoF corresponding to the offset along the x-axis is given for the DLC2, DLC8 and DLC9.

It was observed that the mooring stiffness and the surge displacement of the FOWT followed a nearly linear relationship for the given offset range values. Since the *FD Tool* uses a mooring stiffness for a specific mean wind speed, as explained in section 3.3.4, in fig. 7.12, the surge mooring stiffness corresponding to the maximum horizontal displacement is given. The mean wind corresponding to DLC2 and DLC8 are very similar, with values of 10.3 m/s and 12 m/s, respectively, resulting in not substantial difference between both signals. However, DLC9 features a 22 m/s mean wind speed, which produced low thrust, leading to lower offsets and, thus, reducing the mooring stiffness. Looking at fig. 7.12, assuming a certain threshold for the platform maximum offset, one could determine the minimum mooring stiffness required in the surge DoF associated to the pretension in the lines. In this case, it would be interesting to use the most critical DLC, such as DLC8, in order to identify the minimum stiffness requirement in the surge DoF. In case the mooring stiffness had a more relevant influence on the pitch response, a similar study could be carried out, and thus, a more constrained mooring pretension would be obtained.

7.2.2 Effect of the Second-Order Hydrodynamic Loads on the Platform Response

Furthermore, this research delved into the impact of second-order hydrodynamic loads on the response of FOWTs. A distinctive aspect of this study is the introduction of second-order hydrodynamic loads during the

initial stages of designing floating substructures, which sets it apart from many other design tools found in the literature. Additionally, a highly computationally efficient method, referred to as the *Accelerated Method* is employed, and its description and validation are provided in chapter 5. Notably, this study aims to make the effects of introducing non-linear loads into the response analysis clear. Conditions where hydrodynamic loads take precedence over aerodynamic loads are highlighted, particularly in the case of DLC9, which corresponds to a mean wind speed of 22 m/s and the severe sea state defined in table 4.1.

In fig. 7.13, the mooring stiffness associated to the surge displacement is shown, where the signals using only the first-order hydrodynamic loads and including the second-order hydrodynamic loads are compared. As could be expected, the inclusion of the second-order loads leads to a higher FOWT surge displacement, and it is mainly due to the mean drift loads. The surge displacement was increased 10% when the second-order loads are considered.

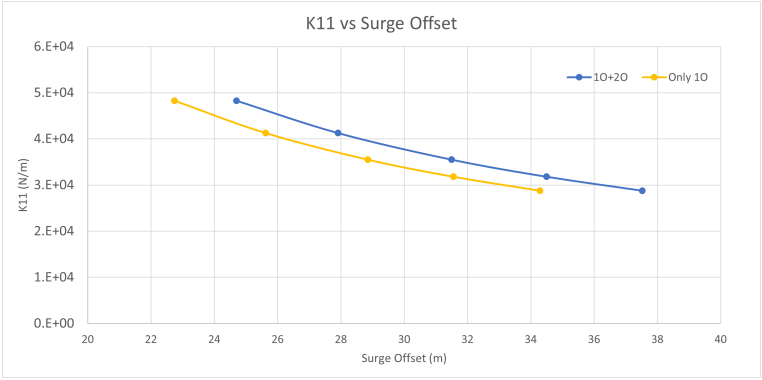

Figure 7.13: Mooring stiffness versus FOWT offset in the surge DoF with (blue) and without (yellow) second-order hydrodynamic loads.

In fig. 7.14, fig. 7.15, and fig. 7.16, the maximum surge response for the whole design space is shown, for three of the five mooring systems assessed, $Moor_1$, $Moor_3$, and $Moor_5$, respectively. The one in the middle corresponds to the same mooring system matrix used for the validation of the *FD Tool* in chapter 6. The surge and pitch stiffness values of each corresponding matrix are given in fig. 7.9.

The maximum offset limit value, is plotted with the red dashed line, whose value were obtained as the 30% of the water depth, following the recommended standards from [72] and described in section 3.2.3. The maximum surge displacement derived from the analysis where only fist-order loads were obtained resulted in all cases lower than that including the second-order loads, which means that including second order loads at

a preliminary platform design stage contributes to a better estimation of the platform maximum offset expected. Moreover, as the mooring stiffness matrix became stiffer, as for $Moor_1$, the surge response was smaller, achieving surge displacements very far from the threshold value. However, for the case where the least stiff mooring system was used, $Moor_5$, there were found several designs that overpass the threshold, leading to discard from the initial stage of design some of the platforms assessed. It was observed, that the platforms with low draft values and a given diameter showed a substantial increase of the surge displacement when second-order loads were considered. This could be explained by the lower mass, among other factors. The platforms with the largest diameters showed the highest offset values, which is explained by the large hydrodynamic loads. It is remarkable that the main differences were observed as the platform size increase, and particularly for lower draft values.

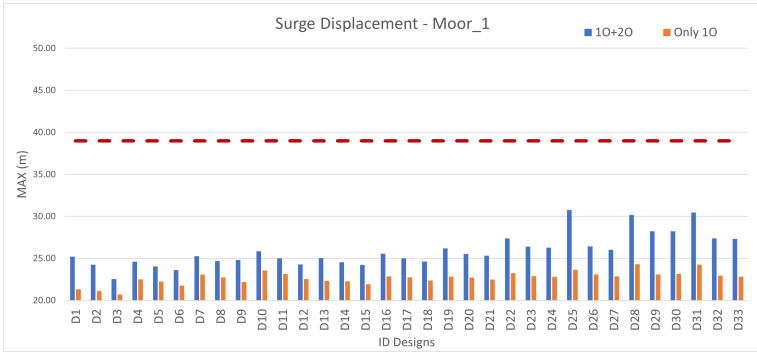

Figure 7.14: Surge maximum displacement for the different designs using the stiffest mooring system $Moor_1$ under DLC9.

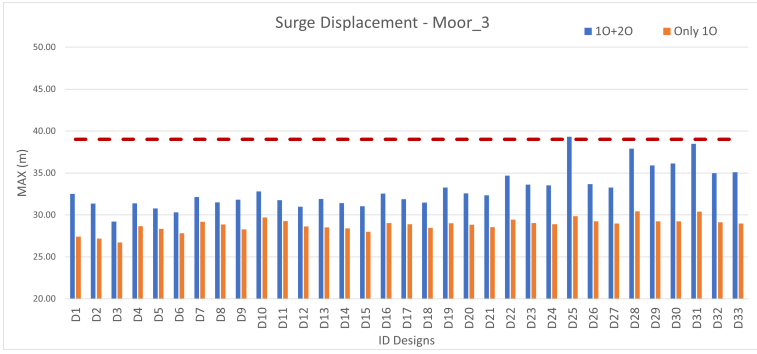

Figure 7.15: Surge maximum displacement for the different designs using the original mooring system from section 3.2.4 $Moor_3$ under DLC9.

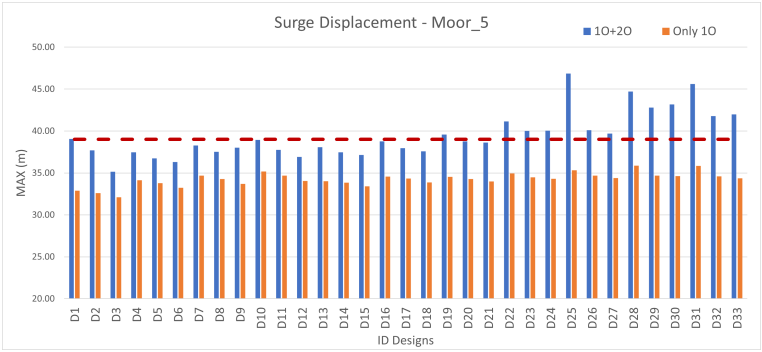

Figure 7.16: Surge maximum displacement for the different designs using the softest mooring system $Moor_5$ under DLC9.

Chapter 8

Conclusion and Future Work

In this section, the main conclusions are presented related to the new floating offshore wind platform preliminary design methodology and tools developed, as well as the primary steps envisaged for related future developments.

8.1 Conclusions

This Thesis introduces a novel frequency domain based design tool (*FD Tool*) tailored to Floating Offshore Wind (FOW) substructures, particularly emphasising semi-submersible platforms which is the current preference of the industry. The *FD Tool* simplifies the complex dynamics of Floating Offshore Wind Turbines (FOWT) under wind and wave loads and is designed to expedite the preliminary design phase. Simplified models, often used in this context, benefit from cascading techniques, incorporating high-fidelity tools' input to account for complex effects on structural responses. These techniques are essential because certain parameters, such as aerodynamic loads and aerodynamic damping, are usually pre-computed due to the simplified model's nature. In this Thesis, novel methods that improve the efficiency of hydrodynamic analysis are presented, since conventional radiation-diffraction analysis can become very time consuming when evaluating numerous platform designs in the quest to streamline FOW substructure pre-design.

From this research work it can be highlighted two main contributions related to the development of two standalone methods alternative to radiation-diffraction analysis. The *Hydrodynamic Analysis on Aggregated Components*, referred to as *HAAC*, estimates the hydrodynamic added mass, radiation damping and wave excitation coefficients based on the radiation-diffraction results but with a significant reduction of computational cost.

The conclusions regarding this method are exposed in section 8.1.1. Conversely to most of the tools for the platform's preliminary design, this study includes the second-order hydrodynamic wave loads through the developed *Accelerated Method*, since they have relevant influence on catenary moored structures. Similarly, the conclusions related to this method are highlighted in section 8.1.2. Both methods share common characteristics, which can also translate into limitations. The floater is split into simple isolated members and the hydrodynamic coefficients and loads are obtained for each of them separately. Then, superposition is applied, neglecting any possible cross-interaction between the platform members. Furthermore, both methods were validated against radiation-diffraction analysis and their accuracy was assessed through the impact of the estimated results on the FOWT response.

As case study, the DTU 10 MW WT was used, supported by thirty-three different semi-submersible platforms based on the original Nautilus floater, where the draft, columns diameter and distance between them were modified within a certain range. In order to reduce the number of design parameters, and considering the objective of the study, some platform dimensions were set equal across the platform design space. Additionally, the pontoon and deck width were established to match the diameter of the columns.

Then, both new developed methods were included into the frequency domain simplified model, denoting the integrated tool as *FD Tool*. The tool was validated and the conclusions are given in section 8.1.3. Due to the high efficiency of the developed tool obtaining the response of FOWT, sensitivity studies can be carried out in order to gain knowledge on FOW platform design. In particular, in this Thesis two different sensitivity analyses were performed and the conclusions achieved are explained in section 8.1.4.

8.1.1 Conclusions Related to *HAAC*

Despite the fact that the *HAAC* method does not consider the interaction between the platform members, a parametric study was carried out in order to assess the influence of the interaction between the columns on the method's accuracy. It was observed that this assumption was reasonable for the added mass and for the wave excitation coefficient within the range of aspect ratios of the case study platform designs. However, the radiation damping showed to be significantly influenced by this interaction. In order to improve the accuracy of its prediction through the proposed method, it was developed a novel formulation that accounts for the presence of the adjoining cylinders. Array of multiple vertical partially submerged cylinders located along the wave propagation direction were assessed and a rela-

tionship between the distance between the cylinders and results accuracy was found. This formulation provided a better prediction of the radiation damping as the cylinders were further from each other and there is a minimum number of cylinders. It can be considered the following valid region which ensures results have reasonable accuracy, and it resulted to be for platforms with columns separated between 2.5 and 7.5 times the diameter. This region includes most of reasonable platform designs aimed to support offshore wind turbines.

Regarding the estimation of the hydrodynamic coefficients on fully submerged members, which generally represent the pontoon of the platforms, the influence of the variation of depth at which they are submerged on the hydrodynamic coefficients calculation was also assessed. Moreover, based on linear wave theory, two expressions for the prediction of the added mass and the radiation damping, respectively, were developed. The application of these expressions to the hydrodynamic coefficients notably improved the accuracy of the results.

The results obtained through *HAAC* agree very well with those from the radiation-diffraction analysis adopted in the panel code *AQWA*, showing a slight under prediction in heave and pitch, which is mainly related to the superposition approach, assuming no cross-interaction between members. The surge motion's added mass reveals interaction effects, causing signal peaks that were not captured by the *HAAC*. However, the prediction of values at zero and infinite frequencies appeared to be accurate.

The proposed method for the calculation of the hydrodynamic coefficients showed to achieve an important reduction of the computational cost. For the database setting were required 60,000 s, which was approximately equivalent to the time required for the radiation-diffraction analysis for 2 to 5 full semi-submersible platforms, depending on the dimensions. The three basic steps implied a negligible simulation time, below 1s per design. In the preliminary design phase of the substructures for FOW, tens of platforms are often assessed, with multiple combinations of the defined design parameters. Therefore, this makes the *HAAC* method suitable for the estimation of the hydrodynamic coefficients in the early stages of design, especially when more than 5 platforms aim to be evaluated.

Furthermore, the utilisation of *HAAC* allows for a precise estimation of the natural periods for various FOW substructures. The results indicated minimal errors in the surge direction and maximum errors of 9% and 5.5% for heave and pitch motions, respectively. When applying the dynamic response from the frequency domain model with *HAAC* results, it closely aligned with the response obtained using hydrodynamic coefficients from *AQWA*. Initially, the response under wave action alone was examined

across a broad range of sea states. It was noted that the intensity of the sea state did not substantially affect the accuracy of response estimation. However, the accuracy was influenced by the aspect ratio of the platform designs, where the platforms with lower diameter-to-separation-between-columns ratio showed the best agreement. This relationship is linked to interaction effects between the platform members. The contribution of the columns played a crucial role in the method's accuracy. The higher the contribution of the columns relative to the full platform, the more accurate the predictions were achieved. Additionally, the evaluation of response under both wind and wave actions resulted in significantly reduced errors, as expected, owing to the contribution of aerodynamic loads. This scenario represents a more realistic operational condition.

HAAC demonstrated to provide accurate results of the hydrodynamic coefficients of structures with aggregated components, such as the semi-submersible platforms used in FOWT, with the main advantage of requiring a significantly lower computational cost, compared to the radiation-diffraction analysis. It showed that, despite assuming some small errors in the calculation of the hydrodynamic coefficients, it still enabled to identify the designs that meet the defined thresholds in a comparative analysis. Its high efficiency makes it suitable to be integrated into platform design optimisation routines and for platforms' preliminary design stages.

8.1.2 Conclusions Related to the *Accelerated Method*

The accelerated method is based on the slender-body assumption but, as a semi-submersible platform is not slender, the structure was decomposed into simpler, individual members, for which the first- and second-order loads were calculated. The overall loads on the full floater were obtained by superposition, assuming negligible cross-interaction between members. In [63] the validation of the method for the surge force and the pitch moment on a monopile was presented. To treat the full semi-submersible floater, the formulation of the heave forces on a vertical cylinder was developed and validated, achieving reasonable accuracy. In addition, the method was extended to horizontal members with their longitudinal axes perpendicular and aligned to the wave propagation direction, so that the full semi-submersible platform can be modelled. For these pontoon members, the formulation for the surge and heave forces and for the pitch moment was developed and validated. The results for the pontoons showed generally a good match, achieving the worst prediction for the pitch moment with a deviation of 14% with 128 modes. The surge force showed very good agreement for both pontoon members, with a non-diffraction error of 10% for the perpendicular case and 9% for the aligned case. The results for the heave force

were as accurate as for the columns and showed an over prediction for both the perpendicular and aligned pontoon members, with error levels of 11% and 5%, respectively.

Furthermore, it was observed that the accuracy of the method on the vertical columns was significantly influenced by the diameter-to-draft ratio and, since it is based on the slender-body theory, it was also affected by the diameter-to-wave-length ratio. Parametric studies assessing the influence of these two parameters were carried out, so as to quantify the accuracy. On one hand, the diameter-to-draft ratio seemed to be the main driver of the error in the surge force, when compared to the loads from the diffraction approach. It was observed that for diameter-to-draft ratios below 0.2 the method was able to predict the surge force with less than 10% of error, with 128 modes used in the truncation. The heave force, however, showed less dependency to the diameter-to-draft ratio, while a larger number of modes were needed to achieve errors lower than 10% relative to the solution without modal truncation, which did not significantly increase the computational cost. The pitch moment was generally well predicted with errors below 3%, with 128 modes too. On the other hand, the diameter-to-wave-length ratio also had an influence on the surge force, as discussed in [64]. Aligned with classical diffraction theory for cylinders, it was noticed that the smaller the ratio, the better estimation of the load, as long as the diameter-to-draft ratio was below 0.2.

The second-order hydrodynamic loads on the full Nautilus semi submersible floater were obtained by means of superposition of the loads on each of the members. The results showed that the interaction between columns did not significantly affect the accuracy, even for the mild sea states. In fact, the error found for the loads corresponding only to the columns was similar to that of isolated column with the same dimensions, thus a good prediction of the surge force on the full semi-submersible floater depends on the diameter-to-draft ratio of the columns. When analysing the results for the three sea states, an under prediction of the surge force of 22% was observed, mainly due to the slender-body approach. For a single column of the same geometry, this error was 28%, although a reference computation with *WAMIT* lead to a value of 16%. The heave force showed very good agreement with almost perfect accuracy, which was due to compensation of the over-prediction of the pontoon heave forces and the cross-interaction effects. The pitch moment agreed well with an under prediction of 10%. Having a good prediction of the pitch moment is probably the most important achievement in this study, since the pitch motion plays a key role in the floater design, especially in the initial stages. Thus, despite the rather large error values obtained for the surge force, its contribution

to the pitch moment still provided good approach. On the computational cost side, the accelerated method enabled the calculation of second-order hydrodynamic loads 2500 times faster than the conventional approach for the semi-submersible floater configuration considered.

Similarly to the *HAAC* method, the impact on the response analysis was assessed in order to evaluate the accuracy of the method. For that purpose, again the response under certain DLCs for the thirty-three platform designs was obtained and compared. For the cases where no wind is considered, only wave conditions, the surge displacement was the DoF that showed the largest errors, which could be expected since the surge second-order force showed the worst approach. It was underestimated for all the platform designs and, similarly to the second-order force results, the designs with lower diameter-to-draft ratio showed in general better agreement. The pitch angle was also under estimated for all the designs, although it seemed to be better predicted. When wind loads were included, these differences were reduced, and the response obtained from the frequency domain tool fed with the accelerated method showed very similar results as if it were fed with the second-order loads resulting from the conventional approaches.

8.1.3 Conclusions Related to the *FD Tool*

In this section, the main conclusions related to the *FD Tool* are presented. The primary goal was to provide an efficient tool for the preliminary design of FOW substructures. It is clear that the frequency domain models outperform time domain models in terms of efficiency, but this is not considered part of the research contribution. Instead, the novelty lies in the inclusion of the newly developed methods for hydrodynamic analysis, which have demonstrated the ability to provide accurate results with a significant reduction in computational cost compared to conventional radiation-diffraction analysis. Consequently, the integration of these methods in the frequency domain models, lead to a general improvement of efficiency of the design tools.

The current tool underwent validation against results generated by the SoA tool, OpenFAST, which is a time domain fully coupled aero-hydro-servo-elastic model for analysing FOWT response. To facilitate a comparison between results obtained from frequency domain and time domain tools, the non-linearity level of the latter was initially assessed. Analysing the histograms of various time series from OpenFAST, it was observed that the time domain model exhibited slight non-linearity. Consequently, the maximum response could be approximated as the sum of the mean component and the standard deviation multiplied by a dynamic factor. This factor was calibrated using time domain simulations in OpenFAST to de-

termine the most representative value for the evaluated FOWTs. Using the mean and standard deviation from the time series derived from OpenFAST, it resulted that using a factor of 3.6 provided very good estimation of the maxima in all DoFs, especially regarding the surge and heave motions with deviations below 2%. The maximum pitch angle showed a slightly worse representation with deviations below 4%. The nacelle acceleration displayed the most significant variation in comparison to the Gumbel maximum value, with a maximum deviation of 21%, leaning towards a conservative estimation. When comparing the maximum response resulted from the mean and standard deviation derived by the *FD Tool*, similar values were achieved, although with a slightly larger differences. This could be expected, due to the developed hydrodynamic methods, which led to deviations around 10% and 8.8% for surge and pitch, respectively. The heave motion was nearly neglected throughout the response analysis, since it is not considered of critical interest for the platform design.

Once the dynamic factor was calibrated, then several DLCs were analysed both with the *FD Tool* and SoA tool. Those DLCs where the aerodynamic loads dominate over the hydrodynamic loads, showed a better prediction of the FOWT response, especially the surge maximum displacement due to the important contribution of the mean thrust force. The whole design space showed similar surge displacements and the maximum error observed was for the platform design with the columns of smallest diameter, smallest draft and smallest separation between the columns (D1), with a value of 16%. Pitch was generally overestimated, especially for platforms with small separation between columns, mainly related to the interaction effects. As for the nacelle acceleration, the simple fact of performing the double derivative of the deflection with respect to time introduces an error, thus leading to general under estimation of the signal. Despite, platforms with larger drafts showed a better approach, due to the higher contribution of the columns compared to the pontoon. It was observed that the hydrodynamic loads acting on the columns were predicted with higher accuracy than those on the pontoon. The contrary case, where the hydrodynamic loads dominate over the aerodynamic loads showed larger deviations, which was an expected conclusion since the main source of inaccuracy are the developed methods for the hydrodynamic loads calculation. Particularly, for severe sea states the *FD Tool* showed higher accuracy in predicting the dynamic response when the platforms have long columns, small diameter-to-draft ratios, and the separation between the columns is sufficiently large in order to have negligible interaction effects. These results are also very related to the relevance of the second-order hydrodynamic loads under strong sea states. The nacelle acceleration was found to be significantly influenced

by the sea state, as expected.

It was observed, that for cases where both aerodynamic loads and hydrodynamic loads were important, the surge motions included the effect of the relevant second-order wave loads leading to a slightly worse agreement with respect to the cases with mild sea states. Still, the maximum deviation found was of 15%. Regarding the maximum pitch angle, due to the under estimation of the hydrodynamic loads, it was observed a general under prediction but very similar tendency as the response obtained through the SoA tool.

In general, the results obtained through the proposed *FD Tool* showed better agreement with the SoA tool as the draft of the platform increased, which is equivalent to increased length of the platform columns, and also when the separation between them increased. This is related to the interaction effects between members, which becomes less significant as the distance between them gets larger. Additionally, the larger the columns of the platform compared to the pontoon, the better estimation of the FOWT motions was achieved.

The most important conclusion regarding these results is that the *FD Tool* is able to provide similar results as the SoA tools and shows the same sensitivity with the platform design parameters, although with some lost of accuracy due to the limitations of the developed hydrodynamic methods. Moreover, the present tool allows to identify those platform preliminary designs that meet the design requirements, regarding some recommended threshold values for the maximum surge, pitch and nacelle acceleration, in a similar way as those obtained with the much more time consuming SoA tools. Among the selected designs, the most cost-competitive support structures for the DTU 10 MW WT resulted to be those platforms with columns of diameters between 10-12 m. In addition, platforms with low draft also were found not to be very suitable designs, especially regarding the high values achieved of acceleration on the RNA. The selected platform solutions were the same as those identified by the SoA tool, giving to the *FD Tool* the confidence enough to be used for the preliminary design of the FOW substructures. Furthermore, the main advantage of the present tool, and also corresponding to one of the main contributions of this Thesis, is the reduction of the computational cost achieved. For the case studies used for the validation of the *FD Tool*, where thirty three designs were assessed, the dynamic response of the whole design space was obtained 14 times faster than the SoA tool. Furthermore, a sensitivity analysis on the size of the platform design space with the wind turbine power was assessed and the efficiency increase of the proposed method with the number of platforms to be evaluated. This trend is related to the need to perform

a radiation-diffraction analysis for each floater design when the SoA tool is used, whereas the proposed methodology starts with 60,000 s required to build the database which is independent of the size of the design space. Therefore, as the number of platforms to examine increase, so does the efficiency of the present tool.

8.1.4 Conclusions Related to the Sensitivity Studies

Taking advantage of the efficiency of the present *FD Tool*, it enables to quickly perform dynamic analysis in order to assess different aspects regarding FOWT design. This includes the ability to conduct multiple sensitivity studies, thereby enhancing our understanding of FOWT behaviour and the most influential parameters related to substructure design. Furthermore, it supports co-design of FOWT components by facilitating interaction among them.

This Thesis explores two instances where the *FD Tool* was harnessed. First, it investigates how the up-scaling of wind turbines impacts platform dimensions and design. Second, it delves into the influence of the mooring system on platform design.

Increasing the Size of the Wind Turbines Effect

Regarding the initial sensitivity analysis, which involved examining the impact of up-scaling wind turbines on platform design, the focus was on identifying the most suitable platform designs to support the IEA 15 MW WT. To achieve this, a comparative analysis of various platform designs was conducted. Initially, a static analysis was carried out, subjecting the platforms to the maximum thrust force within the design space used to validate the *FD Tool*. This analysis revealed that a significant portion of the floaters with small-diameter columns and short distances between them did not meet the prescribed threshold values for pitch angles and therefore had to be excluded from consideration. Consequently, a new design space was established, with a heightened resolution within the larger size range.

The dynamic response assessed through the proposed frequency domain tool was examined under a wide range of wind and wave excitation. A comparison of the results was made with the DTU 10 MW WT. It was generally observed that structures supporting larger wind turbines experienced higher maximum displacements, while simultaneously showing lower maximum nacelle accelerations.

Within the newly assessed design space for the IEA 15 MW WT, only three structures satisfied the design criteria related to maximum platform pitch angle and maximum nacelle acceleration. In comparison to the plat-

forms designed for the DTU 10 MW WT, these structures featured larger column diameters, ranging from 13 to 15 meters. Likewise, greater drafts were observed, discarding all platforms with an 11 m draft. Notably, it was interesting to find that the distance between columns was not a highly influential parameter, as even a 50 m separation still yielded acceptable maximum values for the 15 MW WT.

Additionally, the sensitivity of the natural periods of the selected designs was also examined. It resulted that, as the platform's size increased, the surge natural period also increased. The heave natural period showed values very close to wave excitation, thus it could be that heave plates were required. This would be evaluated in a more detailed stage of design. The pitch natural periods, however, resulted to be very similar among the different designs, with variations below 5%. It was calculated a rough number of how the steel mass scales with the increasing wind turbines, resulting that the mass per megawatt required for the 15 MW WT was 1-1.3 times that of the DTU 10 MW WT.

Mooring System Influence on the Platform Design

In a subsequent study, an investigation was conducted to gauge the impact of the mooring system on the platform design. To achieve this, five different mooring systems, each represented by stiffness matrices, were integrated into the *FD Tool* to obtain the dynamic response. Notably, the surge displacement proved to be the most significantly affected DoF, although heave and pitch motions were also evaluated. The sensitivity analysis employed the same case study used to validate the *FD Tool*, involving the platform designs outlined in table 3.8 supporting the DTU 10 MW WT. Initially, the study examined the effect on the variation of natural periods, revealing that only the natural periods associated with surge motion were influenced. Natural periods for heave and pitch, along with the tower's first fore-aft mode, exhibited no variation with the mooring systems analysed. This is explained by the high contribution of the hydrostatic stiffness in those DoF. The surge motion, however, showed an increase of the natural period proportional to the decrease of the mooring stiffness, since no variation of the mass with the mooring system was assumed.

Moreover, the response was assessed across a wide spectrum of DLCs, yielding similar findings to those observed for the natural periods. Notably, the surge motion was the sole component that displayed variations with changes in the mooring stiffness matrix. While the maximum surge displacement across different designs was not notably affected by mooring stiffness, it did show sensitivity to both aerodynamic and hydrodynamic contributions. Specifically, platforms featuring columns with smaller dia-

meters (in the 10-11 m range) exhibited more significant differences in surge displacement when aerodynamic loads predominated, especially in DLCs associated with very high thrust forces. Conversely, when hydrodynamic loads took precedence over aerodynamic forces, greater variations in surge displacement were observed among designs within the larger platform size range.

This study illustrated the utility of the *FD Tool* in estimating the minimum stiffness required for a given platform, ensuring it remains below a specific platform offset threshold. This information proves invaluable to mooring system designers as it assists in determining appropriate line pretension. Furthermore, the study underscored the significance of incorporating second-order loads in the initial design phase. In the case of the platform design space under examination, the maximum surge displacement increased by approximately 10% when second-order loads were considered. Indeed, depending on the contribution of mooring stiffness to the system and the nature of excitation loads, particularly in challenging conditions, second-order loads can become pivotal in the decision-making process for accepting or rejecting a platform design. The inclusion of second-order loads is therefore crucial for preliminary design considerations. Although fatigue analysis has not been conducted in this study, these results suggest that it will be an important component for enhancing the accuracy of mooring system design.

8.2 Future Work

Several research topics have not been covered in this thesis, and some have not undergone an in-depth analysis, presenting intriguing and promising avenues for future research. Furthermore, exploring these areas could greatly enhance the precision of results, ultimately leading to a more reliable tool and enabling more accurate designs from the very initial stages.

- In relation to the proposed method for estimating hydrodynamic coefficients, the utilisation of *HAAC* to account for member cross-interaction effects would significantly enhance result accuracy. While it has been shown to have a minor impact on FOWT response, especially in comparative analyses, its implementation would lead to more precise hydrodynamic coefficient estimates, which are crucial for proper Response Amplitude Operator (RAO) comparisons. Additionally, the potential to divide the pontoon into isolated prisms would increase the method's versatility, allowing for the use of the same database for platform designs featuring pontoon with rectan-

gular shaped cross-sections. This modification would streamline the methodology and broaden its applicability.

- Aligned to the previous point, to account for the cross-member interaction would also improve the estimation of the second-order hydrodynamic loads obtained thought the second proposed novel method *Accelerated Method*. Furthermore, a more in-depth investigation on the influence of the diameter-to-draft ratio on the calculation of the surge loads through the Morison and Rainey force model would correct the under estimation observed in the second-order hydrodynamic surge force on cylinders.

- The *FD Tool* presents several limitations, such as the ability to assess only aligned wind and wave excitation, and it is developed for a four DoF model. It could be studied the possibility to wider the wind and wave incident directions, in order to assess wind and wave misalignment conditions, which can become critical for some structures. Additionally, to improve the efficiency of calculating the aerodynamic loads and aerodynamic damping would lead to an even quicker analysis.

- The current tool has demonstrated significant capabilities that can be valuable for FOW substructure designers. The logical next step for this tool is its integration into optimisation loops. In this scenario, instead of pre-defining the design space, the optimisation process would only require specifying a range for the platform dimensions to be explored, and the optimiser itself would determine the characteristics of the most cost-effective platform. Naturally, expanding the number of design parameters would also be a suitable progression.

Bibliography

[1] WindEurope. windeurope.org. 2023.

[2] W Yu, K Müller, F Lemmer, H Bredmose, M Borg, G Sanchez, and T Landbo. Public definition of the two lifes50+ 10mw floater concepts. *LIFES50+ Deliverable*, 4, 2017.

[3] Qun Cao, Longfei Xiao, Zhengshun Cheng, Mingyue Liu, and Binrong Wen. Operational and extreme responses of a new concept of 10mw semi-submersible wind turbine in intermediate water depth: An experimental study. *Ocean Engineering*, 217:108003, 2020.

[4] Zhixin Zhao, Wei Shi, Wenhua Wang, Shengwenjun Qi, and Xin Li. Dynamic analysis of a novel semi-submersible platform for a 10 mw wind turbine in intermediate water depth. *Ocean Engineering*, 237:109688, 2021.

[5] Nautilus floater. nautilus floating solutions. In *https://www.nautilusfs.com/*.

[6] P Gonzalez, G Sanchez, A Llana, and G Gonzalez. Deliverable 1.1 oceanographic and meteorological conditions for the design. *LIFES50*, 2015.

[7] Mareike Leimeister, Athanasios Kolios, and Maurizio Collu. Critical review of floating support structures for offshore wind farm deployment. In *Journal of Physics: Conference Series*, volume 1104, page 012007. IOP Publishing, 2018.

[8] WindEurope. Getting fit for 55 and set for 2050. In *Tech.rep., WindEurope*, 2021.

[9] Markus Lerch, Mikel De-Prada-Gil, Climent Molins, and Gabriela Benveniste. Sensitivity analysis on the levelized cost of energy for floating offshore wind farms. *Sustainable Energy Technologies and Assessments*, 30:77–90, 2018.

[10] DNV. Floating offshore wind: the next five years. february, 2022. In *Tech.rep., DNV*, 2022.

[11] BVG Associates. Guide to a floating offshore wind farm. 2023.

[12] Daniel Nilsson and Anders Westin. Floating wind power in norway-analysis of opportunities and challenges. *CODEN: LUTEDX/TEIE*, 2014.

[13] Jose V Taboada. Comparative analysis review on floating offshore wind foundations (fowf). In *Proceedings of the 54th Naval Engineering and Maritime Industry Congress, Ferrol, Spain*, pages 14–16, 2015.

[14] M. Sprague J. Jonkman. Openfast. an open source wind turbine simulation tool. nrel.

[15] Torben J Larsen and Anders Melchior Hansen. *How 2 HAWC2, the user's manual*. Risø National Laboratory, 2007.

[16] EA Bossanyi. Gh bladed theory manual. *GH & Partners Ltd*, 2:56–58, 2003.

[17] BJ Jonkman. Turbsim user's guide v2. 00.00. *Natl. Renew. Energy Lab*, 2014.

[18] Jose V Taboada. Comparative analysis review on floating offshore wind foundations (fowf). In *Proceedings of the 54th Naval Engineering and Maritime Industry Congress, Ferrol, Spain*, pages 14–16, 2015.

[19] Paul Musial, Walter amd Spitsen, Patrick Duffy, Philipp Beiter, Melinda Marquis, RObert Hammond, and Matt Shields. Offshore wind maret report: 2022 edition. Technical report, National Renewable Energy Lab. (NREL), Golden, CO (United States, 2022.

[20] Yichao Liu, Sunwei Li, Qian Yi, and Daoyi Chen. Developments in semi-submersible floating foundations supporting wind turbines: A comprehensive review. *Renewable and Sustainable Energy Reviews*, 60:433–449, 2016.

[21] Christian Bak, Frederik Zahle, Robert Bitsche, Taeseong Kim, Anders Yde, Lars Christian Henriksen, Morten Hartvig Hansen, Jose Pedro Albergaria Amaral Blasques, Mac Gaunaa, and Anand Natarajan. The dtu 10-mw reference wind turbine. In *Danish Wind Power Research 2013*, 2013.

[22] NY Sergiienko, LSP da Silva, EE Bachynski-Polić, BS Cazzolato, Maziar Arjomandi, and Boyin Ding. Review of scaling laws applied to floating offshore wind turbines. *Renewable and Sustainable Energy Reviews*, 162:112477, 2022.

[23] Md Touhidul Islam. Design, numerical modelling and analysis of a semi-submersible floater supporting the dtu 10mw wind turbine. Master's thesis, NTNU, 2016.

[24] Dominique Roddier, Christian Cermelli, Alexia Aubault, and Alla Weinstein. Windfloat: A floating foundation for offshore wind turbines. *Journal of renewable and sustainable energy*, 2(3), 2010.

[25] Xu Yingyu, Hu Zhiqiang, and Liu Geliang. Kinetic characteristics research of the 10 mw-level offshore floating wind turbine. *the Ocean Engineering*, 35(3):44–51, 2017.

[26] Zhixin Zhao, Xin Li, Wenhua Wang, and Wei Shi. Analysis of dynamic characteristics of an ultra-large semi-submersible floating wind turbine. *Journal of Marine Science and Engineering*, 7(6):169, 2019.

[27] Mareike Leimeister, Erin E Bachynski, Michael Muskulus, and Philipp Thomas. Rational upscaling of a semi-submersible floating platform supporting a wind turbine. *Energy Procedia*, 94:434–442, 2016.

[28] Michael Borg, Anders Melchior Hansen, and Henrik Bredmose. Floating substructure flexibility of large-volume 10mw offshore wind turbine platforms in dynamic calculations. In *Journal of physics: Conference series*, volume 753, page 082024. IOP Publishing, 2016.

[29] H Bredmose and A Pegalajar-Jurado. An efficient frequency-domain model for quick load analysis of floating offshore wind turbines. 3(2):693–712, 2018.

[30] Erin Elizabeth Bachynski. Design and dynamic analysis of tension leg platform wind turbines. 2014.

[31] Coupled Modes. User's guide to bmodes. Technical report, Colorado: National Renewable Energy Laboratory, 2007: 1- 24, 2007.

[32] Meysam Karimi, Brad Buckham, and Curran Crawford. A fully coupled frequency domain model for floating offshore wind turbines. *Journal of Ocean Engineering and Marine Energy*, 5:135–158, 2019.

[33] Frank Sandner, David Schlipf, Denis Matha, Robert Seifried, and Po Wen Cheng. Reduced nonlinear model of a spar-mounted floating wind turbine. 2012.

[34] Hermann Glauert. Airplane propellers. *Aerodynamic theory*, 1935.

[35] Emrah Kulunk. Aerodynamics of wind turbines. In *Fundamental and Advanced Topics in Wind Power*. IntechOpen, 2011.

[36] David J Laino and A Craig Hansen. User's guide aerodyn. 2002.

[37] Patrick J Moriarty and A Craig Hansen. Aerodyn theory manual. Technical report, National Renewable Energy Lab., Golden, CO (US), 2005.

[38] Benjamin Sanderse, SP Van der Pijl, and Barry Koren. Review of computational fluid dynamics for wind turbine wake aerodynamics. *Wind energy*, 14(7):799–819, 2011.

[39] Matthew Hall, Brad Buckham, and Curran Crawford. Hydrodynamics-based floating wind turbine support platform optimization: A basis function approach. *Renewable Energy*, 66:559–569, 2014.

[40] Chang-Ho Lee. *WAMIT theory manual*. Massachusetts Institute of Technology, Department of Ocean Engineering, 1995.

[41] AQWA Ansys. Aqwa user's manual release 17.0. *USA. Canonsburg (PA): ANSYS Inc*, 2016.

[42] R Kurnia and G Ducrozet. Nemoh v3. 0 user manual. 2022.

[43] JR Morison, Joseph W Johnson, and Samuel A Schaaf. The force exerted by surface waves on piles. *Journal of Petroleum Technology*, 2(05):149–154, 1950.

[44] Jorgen Fredsoe and B Mutlu Sumer. *Hydrodynamics around cylindrical structures (revised edition)*, volume 26. World Scientific, 2006.

[45] RC MacCamy and R Aam Fuchs. *Wave forces on piles: a diffraction theory*. Number 69. US Beach Erosion Board, 1954.

[46] Odd Faltinsen. *Sea loads on ships and offshore structures*, volume 1. Cambridge university press, 1993.

[47] Matthew Hall, Brad Buckham, and Curran Crawford. Evaluating the importance of mooring line model fidelity in floating offshore wind turbine simulations. *Wind energy*, 17(12):1835–1853, 2014.

[48] SINTEF. Marintek. sima. 2016. *www.windbench.net/models-offshore/sima*, accessed April 28, 2020.

[49] Aldert Otter, Jimmy Murphy, Vikram Pakrashi, Amy Robertson, and Cian Desmond. A review of modelling techniques for floating offshore wind turbines. *Wind Energy*, 25(5):831–857, 2022.

[50] John Marius Hegseth and Erin E Bachynski. A semi-analytical frequency domain model for efficient design evaluation of spar floating wind turbines. *Marine Structures*, 64:186–210, 2019.

[51] Meysam Karimi. *Frequency domain modeling and multidisciplinary design optimization of floating offshore wind turbines*. PhD thesis, 2018.

[52] Kristine Bøyum Riste. Development of a frequency-domain model for dynamic analysis of the floating wind turbine concept-windfloat. Master's thesis, NTNU, 2016.

[53] Meysam Karimi, Matthew Hall, Brad Buckham, and Curran Crawford. A multi-objective design optimization approach for floating offshore wind turbine support structures. *Journal of Ocean Engineering and Marine Energy*, 3:69–87, 2017.

[54] Giulio Ferri, Enzo Marino, Niccolò Bruschi, and Claudio Borri. Platform and mooring system optimization of a 10 mw semisubmersible offshore wind turbine. *Renewable Energy*, 182:1152–1170, 2022.

[55] WM Hicks. *On the motion of two cylinders in a fluid*. 1879.

[56] AN Williams and Z Demirbilek. Hydrodynamic interactions in floating cylinder arrays—i. wave scattering. *Ocean Engineering*, 15(6):549–583, 1988.

[57] AN Williams and AG Abul-Azm. Hydrodynamic interactions in floating cylinder arrays—ii. wave radiation. *Ocean Engineering*, 16(3):217–263, 1989.

[58] John Nicholas Newman. Second-order slowly varying forces on vessels in irregular waves. In *Proceedings of the international symposium on dynamics of marine vehicles and structures in waves. London, UK, 1974*, 1974.

[59] Alexander J Coulling, Andrew J Goupee, Amy N Robertson, and Jason M Jonkman. Importance of second-order difference-frequency

wave-diffraction forces in the validation of a fast semi-submersible floating wind turbine model. In *International Conference on Offshore Mechanics and Arctic Engineering*, volume 55423, page V008T09A019. American Society of Mechanical Engineers, 2013.

[60] Tiago M. Duarte, António Jna Sarmento, and Jason Jonkman. Effects of second-order hydrodynamic forces on floating offshore wind turbines. In *Proc. 32nd ASME Wind Energy Symposium*, 2014.

[61] Stephen H Crandall and William D Mark. *Random vibration in mechanical systems*. Academic Press, 2014.

[62] Takeshi Ishihara and Shining Zhang. Prediction of dynamic response of semi-submersible floating offshore wind turbine using augmented morison's equation with frequency dependent hydrodynamic coefficients. *Renewable energy*, 131:1186–1207, 2019.

[63] H Bredmose and A Pegalajar-Jurado. Second-order monopile wave loads at linear cost. *Coastal Engineering*, 170:103952, 2021.

[64] Antonio Pegalajar-Jurado and Henrik Bredmose. Accelerated hydrodynamic analysis for spar buoys with second-order wave excitation. In *International Conference on Offshore Mechanics and Arctic Engineering*, volume 84416, page V009T09A067. American Society of Mechanical Engineers, 2020.

[65] Carlos López-Pavón, Rafael A Watai, Felipe Ruggeri, Alexandre N Simos, and Antonio Souto-Iglesias. Influence of wave induced second-order forces in semisubmersible fowt mooring design. *Journal of Offshore Mechanics and Arctic Engineering*, 137(3):031602, 2015.

[66] Lixian Zhang, Wei Shi, Madjid Karimirad, Constantine Michailides, and Zhiyu Jiang. Second-order hydrodynamic effects on the response of three semisubmersible floating offshore wind turbines. *Ocean Engineering*, 207:107371, 2020.

[67] Kun Xu, Zhen Gao, and Torgeir Moan. Effect of hydrodynamic load modelling on the response of floating wind turbines and its mooring system in small water depths. In *Journal of Physics: Conference Series*, volume 1104, page 012006. IOP Publishing, 2018.

[68] Srinivasan Chandrasekaran. *Dynamic analysis and design of offshore structures*, volume 761. Springer, 2015.

[69] IEC. Wind energy generation systems - part 3-2: Design requirements for floating offshore wind turbines. In *IEC 61400-3-2 ED1*, 2022.

[70] Evan Gaertner, Jennifer Rinker, Latha Sethuraman, Frederik Zahle, Benjamin Anderson, Garrett E Barter, Nikhar J Abbas, Fanzhong Meng, Pietro Bortolotti, Witold Skrzypinski, et al. Iea wind tcp task 37: definition of the iea 15-megawatt offshore reference wind turbine. Technical report, National Renewable Energy Lab.(NREL), Golden, CO (United States), 2020.

[71] Christopher Allen, Anthony Viscelli, Habib Dagher, Andrew Goupee, Evan Gaertner, Nikhar Abbas, Matthew Hall, and Garrett Barter. Definition of the umaine volturnus-s reference platform developed for the iea wind 15-megawatt offshore reference wind turbine. Technical report, National Renewable Energy Lab.(NREL), Golden, CO (United States); Univ. of . . . , 2020.

[72] DNV. Coupled analysis of floating wind turbines. dnvgl-rp-0286. may, 2019. In *Recommended practice, DNV*, 2019.

[73] Alberto Ghigo, Lorenzo Cottura, Riccardo Caradonna, Giovanni Bracco, and Giuliana Mattiazzo. Platform optimization and cost analysis in a floating offshore wind farm. *Journal of Marine Science and Engineering*, 8(11):835, 2020.

[74] M Collu and M Borg. Design of floating offshore wind turbines. In *Offshore wind farms*, pages 359–385. Elsevier, 2016.

[75] HC Guo, GQ Li, Xiong Liu, et al. Influence of aerodynamic damping on tubular tower of offshore horizontal axis wind turbines. *Acta Energiae Solaris Sinica*, 34(8):1450–1457, 2013.

[76] Xiong Liu, Cheng Lu, Gangqiang Li, Ajit Godbole, and Yan Chen. Effects of aerodynamic damping on the tower load of offshore horizontal axis wind turbines. *Applied Energy*, 204:1101–1114, 2017.

[77] Yanfei Deng, Sara Ying Zhang, Mingming Zhang, and Peng Gou. Frequency-dependent aerodynamic damping and its effects on dynamic responses of floating offshore wind turbines. *Ocean Engineering*, 278:114444, 2023.

[78] RCT Rainey. Slender-body expressions for the wave load on offshore structures. *Proceedings of the Royal Society of London. Series A: Mathematical and Physical Sciences*, 450(1939):391–416, 1995.

[79] Eli Bressert. Scipy and numpy: an overview for developers. 2012.

[80] Henrik Bredmose and Antonio Pegalajar-Jurado. An nlog n method for second-order wave loads on a vertical pile. In *35th International Workshop on Water Waves and Floating Bodies (IWWWFB 2020)*, 2020.

[81] Harald Hanche-Olsen. Buckingham's pi-theorem. *NTNU: http://www. math. ntnu. no/˜ hanche/notes/buckingham/buckingham-a4. pdf*, 2004.

[82] Johannes Albert Pinkster. Low frequency second order wave exciting forces on floating structures. 1980.

[83] Inaki Zabala, Yerai Pena-Sanchez, Thomas Kelly, João Henriques, Markel Penalba, Nicolás Faedo, John Ringwood, and Jesús M Blanco. Bemrosetta: An open-source hydrodynamic coefficients converter and viewer integrated with nemoh and foamm. 2021.

[84] RB d'Agostino and M Stephens. Tests for normal distribution in goodness-of-fit techniques. *Marcel Decker*, 1986.

Main Outcome of the Thesis

Articles Indexed in Journal Citation Reports

The following articles have resulted from the development of the present Thesis:

- Alonso Reig, Maria; Pegalajar-Jurado, Antonio; Mendikoa, Iñigo, Petuya, Victor; Bredmose, Henrik. Accelerated second-order hydrodynamic load calculation on semi-submersible floaters. Marine Structures, 2023, vol. 90, p. 103430.

- Alonso Reig, Maria; Mendikoa, Iñigo; Touzon, Imanol; Petuya, Victor. Efficient hydrodynamic analysis for preliminary design of Floating Offshore Wind substructures. Ocean Engineering, 2023, vol. 285, p. 115318.

- Alonso Reig, Maria; Mendikoa, Iñigo; Petuya, Victor. A novel tool for floating offshore wind substructures design: Validation and definition of design guidelines. Applied Ocean Research. Submitted.

Conference Publications

In addition to the above mentioned articles, during the development of this Thesis conference publications related with the work here presented have been published. Also, a conference article resulted from collaborations with Offshore Renewable Energy Area in TECNALIA:

- Alonso Reig, Maria; Mendikoa, Iñigo; Petuya, Victor. Fast Frequency-Domain Based Tool for FOWT Platforms Preliminary Design. En International Workshop IFToMM (International Federation for the promotion of Mechanism and Machine Science) for Sustainable Development Goals. Cham: Springer Nature Switzerland, 2023. p. 37-44.

- Touzon, Imanol, Petuya, Victor; Nava, Vincenzo, Alonso-Reig, Maria; Mendikoa, Iñigo. Numerical Approaches for Loads and Motions Assessment of Floating WECs Moored by Means of Catenary Mooring Systems. En International Workshop IFToMM for Sustainable Development Goals. Cham: Springer International Publishing, 2021. p. 59-69.

Participation in Seminars

The work carried out in this thesis has also been disseminated through several seminars:

- Fast Comparative Tool for Foating Offhore Wind Substructures. 7^{th} Marine Energy Conference. Euskampus Fundazioa. 2021. Awarded for the best video presentation.
- Development and validation of a frequency domain methodology for conceptual design of floating offshore wind semi submersible platforms. 8^{th} Marine Energy Conference. Euskampus Fundazioa. 2022
- Herramienta para el prediseño de plataformas de eólica flotante. IV Jornadas de Divulgación Científica G-9. University of the Basque Country (UPV-EHU). 2022
- Fast Frequency Domain based Tool for Floating Offshore Wind Platforms Preliminary Design. I4SDG - IFToMM for Sustainable Development Goals (SDG) Workshop 2023.
- Methodologies for the quick estimation of hydrodynamic coefficients: a comparative study. International Offshore Wind Technical Conference (IOWTC) 2023 Abstract accepted.